

UNCLASSIFIED

AD NUMBER
AD295489
NEW LIMITATION CHANGE
TO Approved for public release, distribution unlimited
FROM Distribution authorized to U.S. Gov't. agencies and their contractors; Administrative/Operational Use; DEC 1962. Other requests shall be referred to Aeronautical Systems Div., Flight Dynamics Lab., Wright-Patterson AFB, OH 45433.
AUTHORITY
Air Force Flight Dynamics Lab ltr dtd 21 Oct 1974

THIS PAGE IS UNCLASSIFIED

UNCLASSIFIED

AD 295 489

*Reproduced
by the*

ARMED SERVICES TECHNICAL INFORMATION AGENCY
ARLINGTON HALL STATION
ARLINGTON 12, VIRGINIA



UNCLASSIFIED

NOTICE: When government or other drawings, specifications or other data are used for any purpose other than in connection with a definitely related government procurement operation, the U. S. Government thereby incurs no responsibility, nor any obligation whatsoever; and the fact that the Government may have formulated, furnished, or in any way supplied the said drawings, specifications, or other data is not to be regarded by implication or otherwise as in any manner licensing the holder or any other person or corporation, or conveying any rights or permission to manufacture, use or sell any patented invention that may in any way be related thereto.

ASD-TDR-62-702

PART II

295489
INVESTIGATION TO DETERMINE THE FEASIBILITY OF USING
INFLATABLE BALLOON TYPE DRAG DEVICES FOR RECOVERY
APPLICATIONS IN THE TRANSONIC, SUPERSONIC,
AND HYPERSONIC FLIGHT REGIME

Part II. Mach 4 to Mach 10 Feasibility Investigation

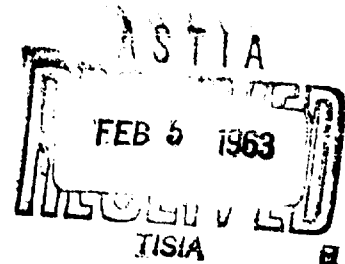
TECHNICAL DOCUMENTARY REPORT ASD-TDR-62-702

PART II

December 1962

Flight Accessories Laboratory
Aeronautical Systems Division
Air Force Systems Command
Wright-Patterson Air Force Base, Ohio

Project No. 6065, Task No. 606506



(Prepared under Contract No. AF33(616)-8015 by Goodyear Aircraft
Corporation, Akron 15, Ohio. Author: W. C. Alexander)

NO OTS

CATALOGED BY ASTIA
AS AD NO.

295 489

NOTICES

When Government drawings, specifications, or other data are used for any purpose other than in connection with a definitely related Government procurement operation, the United States Government thereby incurs no responsibility nor any obligation whatsoever; and the fact that the Government may have formulated, furnished, or in any way supplied the said drawings, specifications, or other data, is not to be regarded by implication or otherwise as in any manner licensing the holder or any other person or corporation, or conveying any rights or permission to manufacture, use, or sell any patented invention that may in any way be related thereto.

ASTIA release to OTS not authorized.

Qualified requesters may obtain copies of this report from the Armed Services Technical Information Agency, (ASTIA), Arlington Hall Station, Arlington 12, Virginia.

Copies of this report should not be returned to the Aeronautical Systems Division unless return is required by security considerations, contractual obligations, or notice on a specific document.

Aeronautical Systems Division, Dir./Aeronautics, Flight Accessories Lab, Wright-Patterson AFB, Ohio.
 Rpt Nr ASD-TR-62-702, Pt II. INVESTIGATION TO DETERMINE THE FEASIBILITY OF USING INFLATABLE BALLOON TYPE DRAG DEVICES FOR RECOVERY APPLICATIONS IN THE TRANSONIC, SUPERSONIC, AND HYPERSONIC FLIGHT REGIME. Mach 4 to Mach 10 Feasibility Investigation. Final report, Dec 62, 1969. Incl illus., tables, 28 refs.
 Unclassified Report

Analytical and experimental data was obtained on a number of inflatable balloon type drag device configurations in the subsonic, super-

(over)

sonic and hypersonic flight regime. On the basis of this data it has been concluded that an inflatable conical balloon is a feasible stabilization and deceleration device for recovery from high-altitude, high-speed flight regimes (up to Mach 10 at 200,000 feet). The practicality of these inflatable decelerators was based on satisfactory performance for a given weight and bulk penalty, technique of manufacturing, and availability of structurally compatible materials within a temperature regime up to 1500°F. The Ballute (res-air inflated conical balloon) configuration was selected as optimum for best meeting the contract requirements.

1. Space capsules
2. Re-entry aerodynamics
3. Drag
4. Balloons
5. Recovery
1. AFSC Project 6065.
- Task 606506
- II. Contract AF 33 (616)-8015
- III. Goodyear Aircraft Corp., Akron, Ohio
- IV. W. C. Alexander
- V. Not avail for OTS
- VI. In ASTIA collection

Aeronautical Systems Division, Dir./Aeronautics, Flight Accessories Lab, Wright-Patterson AFB, Ohio.
 Rpt Nr ASD-TR-62-702, Pt II. INVESTIGATION TO DETERMINE THE FEASIBILITY OF USING INFLATABLE BALLOON TYPE DRAG DEVICES FOR RECOVERY APPLICATIONS IN THE TRANSONIC, SUPERSONIC, AND HYPERSONIC FLIGHT REGIME. Mach 4 to Mach 10 Feasibility Investigation. Final report, Dec 62, 1969. Incl illus., tables, 28 refs.
 Unclassified Report

Analytical and experimental data was obtained on a number of inflatable balloon type drag device configurations in the subsonic, super-

(over)

sonic and hypersonic flight regime. On the basis of this data it has been concluded that an inflatable conical balloon is a feasible stabilization and deceleration device for recovery from high-altitude, high-speed flight regimes (up to Mach 10 at 200,000 feet). The practicality of these inflatable decelerators was based on satisfactory performance for a given weight and bulk penalty, technique of manufacturing, and availability of structurally compatible materials within a temperature regime up to 1500°F. The Ballute (res-air inflated conical balloon) configuration was selected as optimum for best meeting the contract requirements.

1. Space capsules
2. Re-entry aerodynamics
3. Drag
4. Balloons
5. Recovery
1. AFSC Project 6065.
- Task 606506
- II. Contract AF 33 (616)-8015
- III. Goodyear Aircraft Corp., Akron, Ohio
- IV. W. C. Alexander
- V. Not avail for OTS
- VI. In ASTIA collection

FOREWORD

The work presented in this report was performed by Goodyear Aircraft Corporation, Akron, Ohio, under the authority of Project 6065, Task 606506 entitled "Feasibility Study for a Balloon Type Stabilization and Deceleration System for High-Altitude and High-Speed Recovery, " and Air Force Contract No. AF33(616)-8016.

This is Part II of the contract. Part I of this report has the subtitle "Functional and Performance Demonstration."

Mr. S. Metres, Flight Accessories Laboratory, Aeronautical Systems Division, served as contract monitor.

The authors and contributing personnel of Goodyear Aircraft Corporation who cooperated in the research and the preparation of this report were F. R. Nebiker, project engineer; W. C. Alexander, associate project engineer; W. A. Barr, design head; J. W. Bezbachenko, aerodynamic analysis; J. D. D'Allura, aerodynamic analysis; L. M. Cerreta, thermodynamic analysis; J. J. Graham, design; N. E. Houtz, structural analysis; R. W. Nordlie, materials; Dr. R. S. Ross, consultant; and F. Bloetscher, consultant.

ABSTRACT

Analytical and experimental data was obtained on a number of inflatable balloon type drag device configurations in the subsonic, supersonic and hypersonic flight regime. On the basis of this data it has been concluded that an inflatable conical balloon is a feasible stabilization and deceleration device for recovery from high-altitude, high-speed flight regimes (up to Mach 10 at 200,000 feet).

The practicality of these inflatable decelerators was based on satisfactory performance for a given weight and bulk penalty, technique of manufacturing, and availability of structurally compatible materials within a temperature regime up to 1500°F.

The Ballute (ram-air inflated conical balloon) configuration was selected as optimum for best meeting the contract requirements. Included in the report are wind tunnel test data that present drag and stability information of various decelerator configurations placed in a towed position behind a forebody.

PUBLICATION REVIEW

This report has been reviewed and is approved.

FOR THE COMMANDER:

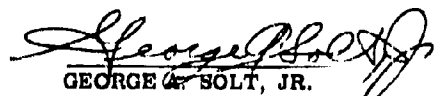

GEORGE A. SOLT, JR.
Chief, Retardation and Recovery
Branch
Flight Accessories Laboratory

TABLE OF CONTENTS

Section	Page
1 INTRODUCTION.	1
A. General	1
B. Background	1
C. Objectives	1
2 DISCUSSION OF INFLATABLE STRUCTURE DEVICES FOR DRAG RE-ENTRY. .	3
3 PRELIMINARY STUDY PROGRAM	5
A. General	5
B. Trajectory Analysis	5
C. Aerodynamic Analysis	6
D. Thermodynamic Analysis.	6
1. Objective.	6
2. Method of Analysis	17
3. Results	20
4. Conclusions	20
E. Wind Tunnel Model Design Concept.	27
1. Pressurized Types	27
2. Ram-Air Inflation Types	27
F. Wind Tunnel Model Stress Analysis	29
1. Langley Unitary Plan Wind Tunnel (First Series).	29
2. Langley Unitary Plan Wind Tunnel (Second Series)	38
3. Arnold Tests	43
G. Subsonic Wind Tunnel Tests	54
4 SUPERSONIC WIND TUNNEL TESTS AT NASA LANGLEY RESEARCH CENTER .	55
A. General	55
B. Test Program	55
C. Summary of Results	58
5 HYPERSONIC WIND TUNNEL TESTS	73
A. General	73
1. Description of Von-Kármán Tunnel "C"	73
2. Description of Test Setup and Models	73
3. Pressure Model Instrumentation	74
4. Temperature Model Instrumentation	82
5. Drag Model Instrumentation	82
6. Test Procedure	82
E. Discussion of Results and Conclusions	82
6 MATERIALS INVESTIGATION	91
A. Introduction	91
1. Review of Available Materials	91
2. Formulation of Work Outline	91
B. Material Procurement	92
C. Material Evaluation	93
1. Cloth A Evaluation	93
2. Cloth B Evaluation	97
3. René Cable (1/32 and 3/32) Tension Tests (Standard Aircraft Cable Configuration).	104
4. Stainless Steel Cloth Evaluation	104
5. CS-105 Coating Evaluation	104
D. Welding Investigation	108
1. Equipment	108
2. Equipment Evaluation	108

TABLE OF CONTENTS (Continued)

Section	Page
3. Joint Design	109
4. Weld Strength Evaluation (Cloths A and B)	109
E. Fabrication Techniques	111
F. Summary of Results	111
7 INFLATION SYSTEMS STUDY	117
A. General	117
B. Compressed Air in Pressure Vessels	117
C. Residual Air within the Ballute	117
D. Gas Generation by Burning Solid Fuel	117
E. Chemically Generated Gas	118
F. Airborne Compressors	118
G. Ram-Air Inflation	118
H. Package Bulk Factors for the Various Inflation Systems	120
8 CONFIGURATION INVESTIGATION	121
A. General	121
B. Stress	121
1. Spherical Ballutes with Meridian Cable Suspension System	121
2. Hemispherical Ballutes with Tucked Back	125
3. Optimum Design Ballutes	129
4. Conical Ballutes	130
5. Eighty-Degree Airmat Cone	134
6. Torus with Curtain	137
7. Weight Analysis	139
C. Thermodynamic Configuration Analysis	141
1. General	141
2. Method of Analysis	142
3. Conclusions and Recommendations	148
D. Aerodynamics	148
1. General	148
2. Flow Behavior	151
3. Drag Results	151
E. DESIGN	153
1. Design Conditions and Assumptions	153
2. Configuration Weight and Bulk Comparison	154
3. Design Curves	157
9 CONCLUSIONS AND RECOMMENDATIONS	161
A. General	161
B. Design Requirements (Considered Optimum)	161
C. Reasons for Design Parameter Selections	161
D. Recommendations	161
Appendix	
I RAM-AIR BALLUTE SHAPE STABILITY ANALYSIS	163
II VARIABLE DRAG BALLUTES	167
A. General	167
B. Variable Riser Line Ballutes	167
C. Clustered Ballutes	167
D. Variable Geometry Ballutes	169

TABLE OF CONTENTS (Continued)

Appendix	Page
III VARIOUS SPHERE DRAG SHAPES	173
IV	177
V REFERENCES	181
VI BIBLIOGRAPHY	183
A. Thermodynamics	183
B. Aerodynamics	184

LIST OF ILLUSTRATIONS

Figure		Page
1	Speed and Altitude Envelope for Development of Inflated Balloon Type Drag Devices in Mach 4 to Mach 10 Flight Regime	7
2	Altitude versus velocity from Mach 10 and 200,000 Feet	7
3	G versus Time from Mach 10 and 200,000 Feet	8
4	Altitude versus Time from Mach 10 and 200,000 Feet	8
5	Altitude versus Total Pressure (P_T) from Mach 10 and 200,000 Feet	9
6	Altitude versus Velocity from Mach 10 and 120,000 Feet.	9
7	G versus Time from Mach 10 and 120,000 Feet	10
8	Altitude versus Time from Mach 10 and 120,000 Feet	10
9	Altitude versus Total Pressure (P_T) from Mach 10 and 120,000 Feet	11
10	Altitude versus Velocity from Mach 4 and 70,000 Feet.	11
11	G versus Time from Mach 4 and 70,000 Feet	12
12	Altitude versus Time from Mach 4 and 70,000 Feet	12
13	Altitude versus Total Pressure (P_T) from Mach 4 and 70,000 Feet	13
14	Altitude versus Velocity from Mach 4 and 120,000 Feet	13
15	G versus Time from Mach 4 and 120,000 Feet	15
16	Altitude versus Time from Mach 4 and 120,000 Feet	15
17	Altitude versus Total Pressure (P_T) from Mach 4 and 120,000 Feet.	16
18	Graphical Solution for ϕ of 90-Degree Cone with Other Conditions Same as for the Sphere.	18
19	Heat Flux Ratio versus Location for Spiked and Non-Spiked Body	19
20	Stagnation Temperature versus Time from 200,000 Feet (Sphere)	21
21	Stagnation Temperature versus Time from 120,000 Feet (Sphere).	21
22	Temperature Profile from 200,000 Feet (Sphere)	22
23	Temperature Profile from 120,000 Feet (Sphere)	22
24	Maximum Temperature at $\theta = 4.4$ Seconds versus Location from 200,000 Feet (Sphere)	23
25	Maximum Temperature at $\theta = 0$ Seconds versus Location from 120,000 Feet (Sphere)	23

LIST OF ILLUSTRATIONS (Continued)

Figure		Page
26	Maximum Temperature versus Location from 200,000 Feet (90-Degree Cone) . .	24
27	Maximum Temperature versus Location from 120,000 Feet (90-Degree Cone) . .	24
28	Maximum Temperature versus Location at Various W/C_{DA} 's from 200,000 Feet (Cone)	25
29	Maximum Temperature versus Location at Various W/C_{DA} 's from 120,000 Feet (Cone)	25
30	Temperature versus Drag Body Radius	26
31	Wind Tunnel Model Design Concepts	28
32	Ram-Air Ballute ($2\beta = 80$ and 100 Degrees)	32
33	Tucked Ballute Stresses	33
34	Airmat Cone Stresses	33
35	Torus with Curtain Radial Loading	35
36	Eccentric Application of Load to Torus	35
37	Sphere	36
38	Hemisphere Model under Load	37
39	Radial Loads at Rear Fitting	38
40	Second-Series Wind Tunnel Models a and b	40
41	Second-Series Wind Tunnel Model c	40
42	Second-Series Wind Tunnel Model d	41
43	Second-Series Wind Tunnel Model e	42
44	Second-Series Wind Tunnel Model f	43
45	Metal Cloth Drag Model	44
46	Cross Section of Nose Fitting	46
47	Web Cross Section	47
48	Rigid Temperature Model	48
49	Rigid Pressure Model	49
50	Bending Moment at Rear Wall	49
51	Model Support Sting	51

LIST OF ILLUSTRATIONS (Continued)

Figure		Page
52	Strut Cross Section Dimensions	51
53	Rod Spacing	52
54	Wall Loading	52
55	Radial Loads at Rear Fitting	53
56	Sevety-Five Degree Cone Balloon with 6.3-Percent Fence in GAC Subsonic Tunnel.	54
57	Typical Supersonic Wind Tunnel Installation	60
58	Supersonic Wind Tunnel Support Systems	60
59	Sphere with 6.2-Percent Fence Trailing Payload in Supersonic Wind Tunnel . . .	61
60	Torus and Curtain Trailing Payload in Supersonic Wind Tunnel.	61
61	Eighty-Degree Airmat Cone Model Trailing Payload in Supersonic Wind Tunnel	61
62	Seventy-Five Degree Cone Balloon with 6.3-Percent Fence Trailing Payload in Supersonic Wind Tunnel	61
63	Proinflated Sample Supersonic Wind Tunnel Test Models.	62
64	Ram-Air Sample Supersonic Wind Tunnel Test Models	63
65	Detailed Sketches of Typical Ballute Models	64
66	Schlieren Photograph of Sphere with 6.25-Fence at $M = 2.5$	65
67	Schlieren Photograph of 75-Degree Cone Balloon at $M = 2.87$	65
68	Schlieren Photograph of Sphere with 6.25-Fence at $M = 2.87$	65
69	Schlieren Photograph of 80-Degree Ram-Air Ballute at $M = 2.5$	65
70	Effect of the Tow-Cable Length on the Drag Coefficient of a Sphere with 6.25 Percent Fence, 75-Degree Balloon, and 80-Degree Airmat Cone behind the Forebody	66
71	Effect of Tow-Cable Length on the Drag Coefficient of a Hemisphere	67
72	Effect of Tow-Cable Length on the Drag Coefficient of a 75-Degree Cone Balloon with 6.3-Percent Fence	67
73	Effect of Tow-Cable Length on the Drag Coefficient of an 80-Degree Airmat Cone ($M = 1.63$ to 2.75)	68
74	Effect of Tow-Cable Length on the Drag Coefficient of an 80-Degree Ballute without Fence (Ram-Air Inflated).	68

LIST OF ILLUSTRATIONS (Continued)

Figure		Page
75	Effect of Tow-Cable Length on the Drag Coefficient of an 80-Degree Ballute with 3.9-Percent Fence (Ram-Air, Side Inlets)	69
76	Effect of Tow-Cable Length on the Drag Coefficient of a 75-Degree Cone Balloon with 6.3-Percent Fence	69
77	Effect of Tow-Cable Length on the Drag Coefficient of a Sphere with 6.25-Percent Fence	70
78	Effect of Tow-Cable Length on the Drag Coefficient of a 75-Degree Ballute with 6.3-Percent Fence with Side Inlets	70
79	Effect of Tow-Cable Length on the Drag Coefficient of an 80-Degree Alrmat Cone ($M = 2.50$ to 4.65)	71
80	Effect of Mach No. on the Drag Coefficient (Ballutes)	71
81	Effect of Mach No. on the Drag Coefficient (Closed Pressure Vessel)	72
82	Side Inlet Pressure Recovery for 75-Degree Ballute with 6.3-Percent Fence	72
83	Ballute Geometry, Thermal and Pressure Tap Locations	74
84	Heat Transfer Model	75
85	Pressure Model	75
86	Partially Inflated Ballute	75
87	Typical Nose Configurations	76
88	Front and Side Pitot Tubes	76
89	Pressure and Temperature Model Installation	77
90	Drag Model Installation	77
91	Pressure Model in Tunnel Installation Chamber	78
92	Water-Cooled Support Strut (Side View)	79
93	Water-Cooled Support Strut (Bottom View)	79
94	Eighty-Degree Ballute Model at $T_g = 1428^{\circ}\text{F}$ during Test Run (Front Inlets)	83
95	Eighty-Degree Ballute Model at $T_g = 1375^{\circ}\text{F}$ during Test Run (Side Inlets)	83
96	Eighty-Degree Ballute Model at $T_g = 1400^{\circ}\text{F}$ during Test Run (Bladder Inflated)	83
97	Ballute Pressure Tap Locations	84
98	Ballute Longitudinal Pressure Distribution behind the Forebody (Plugged Inlet), $L/d = 18$	85

LIST OF ILLUSTRATIONS (Continued)

Figure		Page
99	Ballute Longitudinal Pressure Distribution behind the Forebody (Ram-Air Inflation), $L/d = 9$	85
100	Ballute Longitudinal Pressure Distribution behind the Forebody (Ram-Air Inflation), $L/d = 11$	86
101	Ballute Longitudinal Pressure Distribution behind the Forebody (Ram-Air Inflation), $L/d = 12$	86
102	Ballute Longitudinal Pressure Distribution behind the Forebody (Ram-Air Inflation), $L/d = 18$	87
103	Ballute Longitudinal Pressure Distribution behind the Forebody (Ram-Air Inflation), Various L/d 's	87
104	Heat Transfer Coefficients Obtained without the Presence of the Forebody and Strut Assembly (Plugged Inlet)	88
105	Heat Transfer Coefficients on the Ballute when Mounted behind the Forebody and Strut Assembly (Plugged Inlet)	88
106	Effect of the Tow-Cable Length on the Drag Coefficient of an 80-Degree Ballute (Ram-Air Inflated)	89
107	Effect of the Tow-Cable Length on the Drag Coefficient of an 80-Degree Ballute (Bladder Inflated and Rigid Tested behind a Forebody).	89
108	Cloth A Typical Stress-Strain Diagrams for René Wire and Cloth (Six-Inch Gage Lengths)	98
109	Cloth B Typical Stress-Strain Diagrams for René Wire, Strand, and Cloth (Six-Inch Gage Lengths).	105
110	Leak Rates	107
111	Fabrication Templates	112
112	Clamping Goro in Coating Frame	112
113	Indexing Attachment	113
114	Welding Subassemblies.	113
115	Joining Ballute Halves	114
116	Thirty-Six Inch Diameter Stainless Steel Ballute Model	114
117	Welding Two Cloth B Gores	115
118	Inflation System Weights for Various Types of Systems	119
119	Parameters Affecting Drag Device Design	122
120	Sphere Geometry with No Drag Load	123

LIST OF ILLUSTRATIONS (Continued)

Figure		Page
121	Structural Model with Cables Partially Replaced by External Loads	124
122	Deflected Shape of a Spherical Drag Body under Various Loadings	126
123	Cable Tension Parameters versus Drag to Pressure Force Ratio for Four Drag Body Configurations	126
124	Hemisphere Model Geometry	127
125	Profile Curve for $\rho = 0$ for Various Values of x/R and k	128
126	Equilibrium Shape of Hemisphere for Various Values of j	128
127	Tailored Geometry of Plain Back 80-Degree Cone.	130
128	Equilibrium Shape of Plain Back 80-Degree Cone for Various Values of j	132
129	Tailored Geometry of 80-Degree Tucked Cone	133
130	Equilibrium Shape of Tucked 80-Degree Cone for Various Values of j	134
131	Airmat Cone Dimensions	135
132	Loads Acting on a Segment of an Airmat Cone	135
133	Taking Element from Free Body	136
134	Profile Curve of Torus with Curtain Drag Body	138
135	Effect of Forebody on Heat Fluxes.	143
136	Transition from Laminar to Turbulent Flow	143
137	Laminar Heat Flux and Temperature Distribution on a Blunted Cone	144
138	Heat Flux and Temperature Distribution on a Sphere Laminar Flow	144
139	Turbulent Heat Flux and Temperature Distribution on a Blunted Cone	145
140	Heat Flux and Temperature Distribution on a Sphere Turbulent Flow	145
141	Laminar and Turbulent Heat Fluxes	146
142	Laminar and Turbulent Temperatures	146
143	Mach 10 Ballute Trajectory and Temperature Limit Parameters (Sphere in Laminar Flow)	149
144	Mach 10 Ballute Trajectory and Temperature Limit Parameters (Blunt Cone in Turbulent and Laminar Flow, Sphere in Turbulent Flow)	149
145	Reynold's Number Range in Performance Envelope	150
146	Towed Blunt Body Drag Data	152

LIST OF ILLUSTRATIONS (Continued)

Figure		Page
147	Towed Cone, Fence Drag Data	152
148	Decelerator Weight-to-Total-Weight Ratio (W_D/W) versus Ballistic Coefficient ($W/C_D A$).	156
149	Projected Weight Range for 80-Degree Ballute of Coated René 41 at 1500°F . .	156
150	Vertical Trajectories within the 1500°F Limit for 10-Foot-Diameter Ballute in Turbulent Flow	158
151	Weight of 80-Degree Ballute versus Diameter at One Pressure for Two Material Conditions	158
152	Weight of 80-Degree Ballute versus Diameter at Various Dynamic Pressures .	159
153	Membrane Stress in 80-Degree Ballute at Various Inflation Pressures	159
154	Water Table Test Setup	166
155	Dual-Chambered Inflated Variable-Drag Cone (Smallest Drag)	169
156	Dual-Chambered Inflated Variable-Drag Cone (Intermediate Stage)	170
157	Dual-Chambered Inflated Variable-Drag Cone (Maximum Drag Area Shown)	170
158	Ram-Air Double-Skin Ballute (Inner Chamber Inflated)	171
159	Ram-Air Double-Skin Ballute (Outer Chambers Inflated)	171

LIST OF TABLES

Table		Page
1	Maximum Stagnation Temperatures	20
2	Wind Tunnel Models Fabric Materials	30
3	Summary of Aerodynamic Data	31
4	Summary of Minimum Margins of Safety (Based on Limit Loads)	31
5	Summary of Aerodynamic Loading, Fabric Materials, and Minimum Margins of Safety	39
6	Minimum Margins of Safety (Based on Ultimate Loads)	44
7	Subsonic Performance Data	54
8	Supersonic Wind Tunnel Test Models	55
9	Log Sheet of Supersonic Tests	56
10	Log Sheet of Mach 10 (± 0.187) Tests	80
11	Cloth A Evaluation Test Conditions (Instron Machine)	93
12	0.0021-Inch-Diameter René Wire Tensile Tests	94
13	Cloth A Breaking Tests (Warp Direction)	95
14	Cloth A Breaking Tests (Fill Direction)	95
15	Structural Efficiency Data (Cloth A)	97
16	Cloth B Evaluation Test Conditions (Instron Machine)	99
17	0.0015-Inch-Diameter René Wire Tensile Tests	99
18	René Strand Tensile Tests (Seven 0.0015-Inch-Diameter Wires)	100
19	Cloth B Breaking Tests (Fill Direction)	101
20	Cloth B Breaking Tests (Warp Direction)	102
21	Structural Efficiency Data (Cloth B)	103
22	Summary of Stainless Steel Cloth Tension Tests	106
23	Hot Roc Tests	106
24	Permeability Tests	106
25	Welded Strengths of 0.0016-Inch-Diameter, 200 x 200 Mesh René 41	109
26	Spot Weld Strengths in Stainless Steel Cloth (Fill)	109
27	Summary of Weld Strength Evaluation Test Results	110

LIST OF TABLES (Continued)

Table		Page
28	Summary of Strength Tests	115
29	Summary of Weld Results	115
30	Summary Comparison of Weights	118
31	Weights of Various Concepts for One Trajectory Condition	154
32	Water Table Test Log - Series I Configuration	164
33	Water Table Test Log - Series II Configuration	164

SECTION 1

INTRODUCTION

A. GENERAL

Under contract AF33(616)-8015 with Aeronautical Systems Division, Goodyear Aircraft Corporation (GAC) has conducted a detailed study and test program to determine the feasibility of using inflatable balloon type drag devices at speeds up to Mach 10 and altitudes up to 200,000 feet for applications such as first-stage decelerators of missile components, emergency escape capsules, booster assemblies, and others. This program is an extension of an applied research study. Specifically it is the continuation of the work conducted under contract AF33(616)-6010. The "6010" program showed the feasibility of the spherical inflatable drag device at speeds up to Mach 4 and altitudes up to 200,000 feet.

B. BACKGROUND

With the advent of high-speed, high-altitude flight, new methods of stabilization and deceleration must be developed for successful recovery of such payloads as manned space capsules, rocket boosters, nose cones, and instrument data packages. Initial stabilization is required so that protective re-entry devices (heat shields, ablation shields, drag producing devices) of a payload tumbling or disoriented in space can be aligned with the flight path. Initial deceleration is required to reduce aerodynamic heating and loading and to gradually reduce the velocity of the payload through a varying dynamic loading regime.

C. OBJECTIVES

The main objective of this program was to determine the optimum drag device system that would perform satisfactorily along a vertical downward flight path following deployment within the Mach number versus altitude envelopes as shown in Figure 1. An optimum system is defined as a system that provides the largest stable drag area at a minimum weight and bulk penalty. Satisfactory drag device performance is defined as providing a payload adequate deceleration with attitude stability for aligned flight (near zero angle of attack) and for the subsequent safe landing in a designated target area. In addition to the main objective, it was necessary to determine the performance capabilities and limitations of the applicable drag devices investigated in order to define the requirements for a follow-up Mach 10 captive and free-flight test program. The summary of the scope of the required work of this program is as follows:

Task 1 - Conduct a preliminary study program to determine performance and design requirements with respect to aerodynamics, thermodynamics, bulk, and fabrication limitations of various drag device configurations. The configurations include spheres, hemispheres, and cones at various apex angles.

Task 2 - Utilizing the performance requirements of Task 1, conduct a gas storage hardware study to determine weight and bulk of various inflation systems to maintain inflation of the drag device throughout the descent trajectory down to sea level.

Task 3 - Conduct a material requirement study with respect to weight, bulk, strength, flexibility, gas tightness, and fabrication techniques. The operational temperature limit requirement of the material is 1500°F.

Task 4 - Conduct functional and laboratory tests as required to support the analytical work of tasks 1, 2, and 3.

Task 5 - Utilizing the results of tasks 1, 2, 3 and 4, conduct an optimum configuration design study. Assemble results with applicable tables, graphs, and drawings.

This report presents the results of Tasks 1 through 5.

Manuscript released by the author October 1962 for publication as an ASD Technical Documentary Report.

SECTION 2

DISCUSSION OF INFLATABLE STRUCTURE DEVICES FOR DRAG RE-ENTRY

This research and development program was conducted to obtain additional design and performance information to verify the feasibility of utilizing inflatable balloon type drag devices to improve flight vehicle performance for safe and successful re-entry and recovery from space.

Experimental performance data was obtained at speeds up to Mach 10. The data consists of the results of wind tunnel tests conducted at subsonic, supersonic, and hypersonic speeds. The majority of the decelerator models were flexible fabric inflatable models which were towed behind a forebody at the end of a flexible riser cable. The tests supported the major program requirements of obtaining aerodynamic, thermodynamic, and structural data on various inflatable decelerator configurations for the subsequent optimum system design in an expanded flight regime not previously investigated to any degree of completeness.

Per contract requirements, closed pressure-vessel spheres, hemispheres, and cones were investigated. In addition self-inflated configurations called Ballutes were investigated. As the name implies, it is a combination balloon and parachute. It is similar to a parachute by method of ram-air inflation and over-all external shape. It differs from a chute because of its near-zero porosity coated fabric structure and its enclosure of multiple suspension lines. Because of the coating the Ballute forms a more rigid inflatable structure and a resulting finite aerodynamic shape (dimensional stability) which gives predictable, repeatable performance. This type of performance was demonstrated during the wind tunnel tests.

This over-all program, supported by laboratory tests, consisted of aerodynamic, thermodynamic, material, and design studies. The major result of the material study was the development of a strong lightweight foldable metal cloth woven with stranded wires. The significant wind tunnel results are as follows:

- (1) Trailing towed conical decelerators with burble fences have the capability of obtaining drag coefficients of one or greater over the entire supersonic speed range. Drag coefficients were based on the fully inflated model design diameters of either 7 or 8 inches. The burble fence outside diameters were greater than their respective inflated design diameters.
- (2) Trailing towed conical decelerators which have apex nose angles of 80 degrees or less are stable (little or no coning) in the infinite payload mass condition throughout the range of speeds tested.
- (3) Ram-air(self-inflating) Ballute models performed satisfactorily throughout the range of speeds tested.
- (4) The use of the metal cloth fabricated models performing under dynamic loads in a wind tunnel at Mach 10 and at temperatures of approximately 1500°F for an exposure time of over one minute was demonstrated.

The significant results of the configuration design study are as follows:

- (1) Of all of the zero-porosity balloon configurations the ram-air Ballute configurations offer the most promise for providing the best performance at speeds ranging from extremely low subsonic up to and including hypersonic at the least weight and bulk penalty.
- (2) Along vertical trajectories from 250,000 feet down to sea level aerodynamic heating limits Dacron-neoprene type fabric decelerators in the order of 10 feet in diameter to operation at speeds up to Mach 2 to 2.5.
- (3) It is feasible to utilize Ballute decelerators made of present-day coated metal cloth for actual free flight tests in the Mach 4 to Mach 10 flight regime.

SECTION 3

PRELIMINARY STUDY PROGRAM

A. GENERAL

The purpose of the preliminary study program was to determine the type of inflatable blunt body configurations to be investigated. The three basic geometric shapes to be studied under contractual requirements were the sphere, hemisphere, and cone.

Basic shape variations determined worthy of consideration were the ram air Ballute (cone balloon), the ram air tucked Ballute, and the torus skirt.

The preliminary study program included a trajectory analysis, aerodynamic analysis, thermodynamic analysis, wind tunnel model design study, wind tunnel model stress analysis, and subsonic wind tunnel tests.

B. TRAJECTORY ANALYSIS

The definition of the vertical trajectories, required at the earliest date possible for initial design purposes, was fulfilled to some extent by the work of Reference 1. The desire for explicit trajectories beginning at each corner of the design Mach number-altitude trapezoid (Figure 1) and covering the range of W/C_{DA} from 1.0 to 100 required the computation of the trajectories.

The equation defining the vertical acceleration is

$$\dot{V} = g \left(1 - \frac{\rho V^2}{2(W/C_{DA})} \right)$$

and the velocity and altitude equations are

$$V = \int_0^t \dot{V} dt$$

$$h = \int_0^t V dt.$$

The IBM 650 digital computer was utilized for the calculation of the trajectories. The 1959 ARDC atmosphere was adopted, and the time increment in the solution was varied as acceleration changed.

A constant (W/C_{DA}) was assumed in this trajectory analysis rather than a rigorous consideration of its variation with Mach number for a specific configuration. This assumption was concluded after observing only a slight change in the interested trajectory quantities of an 80-degree cone using both a constant value of W/C_{DA} and a variable value with Mach number.

The computer print-out listed time, altitude, velocity, Mach number, dynamic pressure, and acceleration in terms of gravity(g). These quantities are plotted defining each trajectory for the specified initial altitude-Mach number.

An additional quantity, stagnation pressure (P_T) is also of interest for design. This quantity is the pressure behind a normal shock as a total head tube would measure in a supersonic stream. It was calculated by the following equation:

$$P_T = \left(\frac{P_T}{q_\infty} - \frac{P_\infty}{q_\infty} \right) q_\infty + P_\infty.$$

The quantity $(P_T - P_\infty)/q_\infty$ is solely a function of Mach number which is a modification of the Rayleigh pitot-tube formula. The dynamic pressure (q) was obtained from the computer print-out and P_∞ was obtained from the 1959 ARDC atmosphere table for the altitude in question. All this trajectory data is described in Figures 2 through 17.

It will be noted from observation of the acceleration and stagnation pressures that their maxima occur at time zero for the initial case of $M = 4.0$ and altitude = 70,000 feet and at $W/C_D A$'s from 1.0 to 100. These maxima occur later in the trajectory as altitude is increased and $W/C_D A$ is increased. At Mach 10 and 120,000 feet, however, this is still the case for $W/C_D A$'s of 1 and 10.

C. AERODYNAMIC ANALYSIS

The superiority of a given decelerator over any other conceivable configuration lies not only in the evaluation of its drag effectiveness behind a payload but also on its aerodynamic stability, structural integrity which affects its weight, and upon the nature of the inflation mechanism and its weight. Of aerodynamic concern is the drag effectiveness of the decelerator behind a given payload size (diameter of d) and decelerator size (diameter of d'), so that the tethered length (L) may be optimally set at a given L/d . The effect of Mach number must also be concerned since compromises in this length may be in order.

The state of the analytical art does not permit the solution of these problems. Experimental techniques must then be utilized.

A search of the literature indicated only a minor contribution of experimental data except that collected under the previous contract (reference 2), and this work did not extend to the $M = 4$ to 10 zone. Further, it was desired to suspend the inflatable decelerator behind the payload on a cable so that the stability characteristics could be observed. The ram-air principle of inflation was also a new area to be investigated. It was therefore concluded that wind tunnel tests were quite necessary.

The NASA Langley Unitary wind tunnel was made available for the tests covering the Mach number range of 1.57 to 4.85. The Arnold Engineering Development Center, Tunnel "C" of the Von Karman Gas Dynamics Facility was made available for the $M = 10$ tests. These tests are completely discussed in their respective sections of this report.

In the initial phases of this contractual effort, drag estimates and pressure estimates were made of various configurations to establish further consideration. This was also done for wind tunnel model design purposes. For this effort, existing data was exploited, and theoretical calculative methods such as Newtonian theory and conical flow theory were employed.

D. THERMODYNAMIC ANALYSIS

1. Objective

Aerodynamic heating of spheres and 90-degree cones with spherical noses as re-entry blunt drag bodies were studied in a Mach number range of 10 to 2 and in an altitude range of 200,000 to 40,000 feet. Temperature histories were determined for spheres without flow separation spikes and correlated to spheres with flow separation spikes. Analyses were made to determine temperature distributions over spheres, spheres with flow separation spikes, 90-degree cones, and 80-degree cones with flow separation spikes.

The objective of this preliminary thermal study was to establish thermodynamic requirements for the specified performance envelope (see Figure 1) and to provide temperature data to establish functional, structural, and environmental design requirements.

Re-entry trajectories within the flight envelope shown in Figure 1 were obtained from computer studies conducted by GAC aerodynamicists in which various drag body sizes and ballistic coefficients were used.

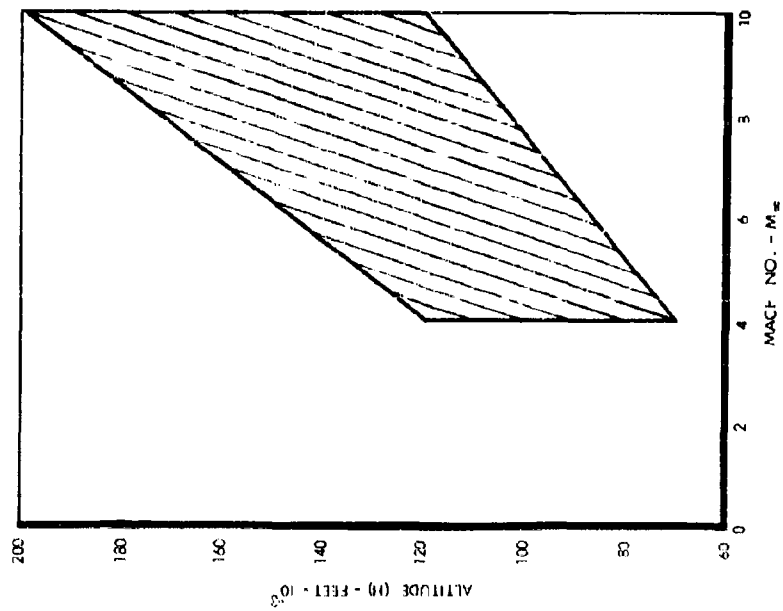


Figure 1. Speed and Altitude Envelope for Development of Inflated Balloon Type Drag Devices in Mach 4 to Mach 10 Flight Regime

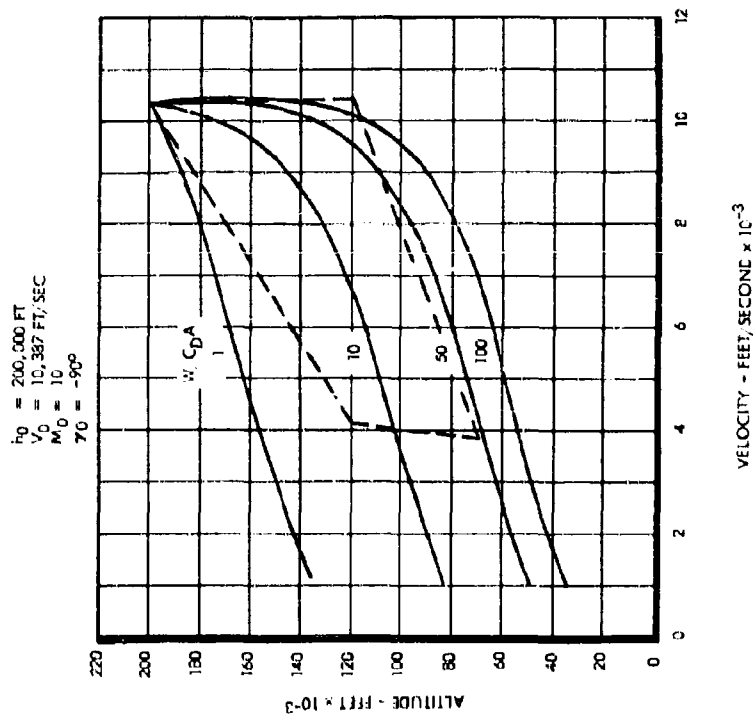


Figure 2. Altitude versus Velocity from Mach 10 and 200,000 Feet

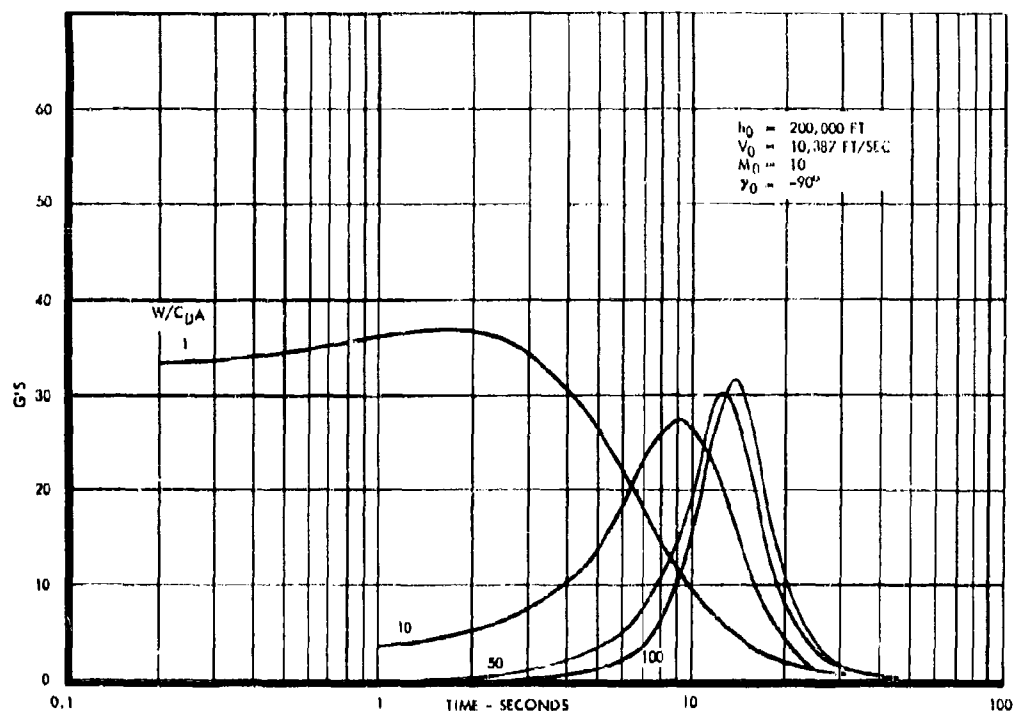


Figure 3. G versus Time from Mach 10 and 200,000 Feet

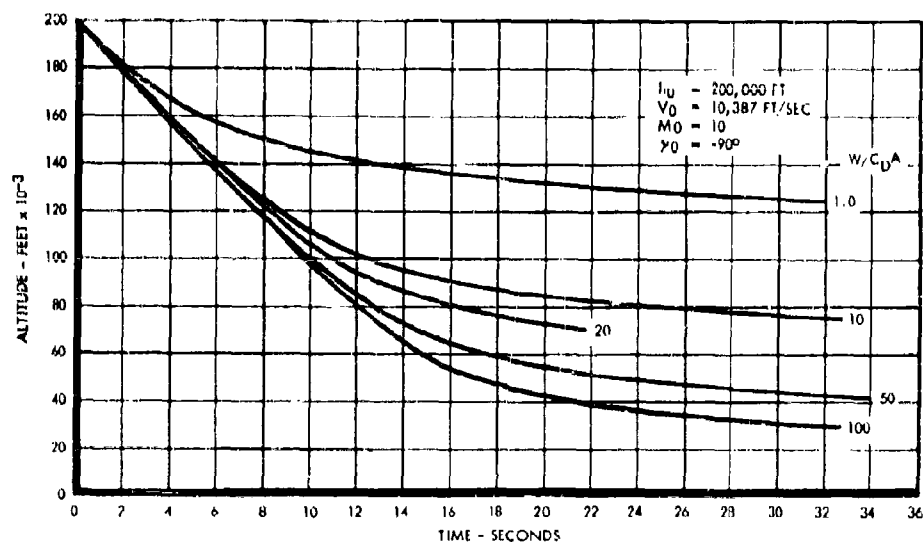


Figure 4. Altitude versus Time from Mach 10 and 200,000 Feet

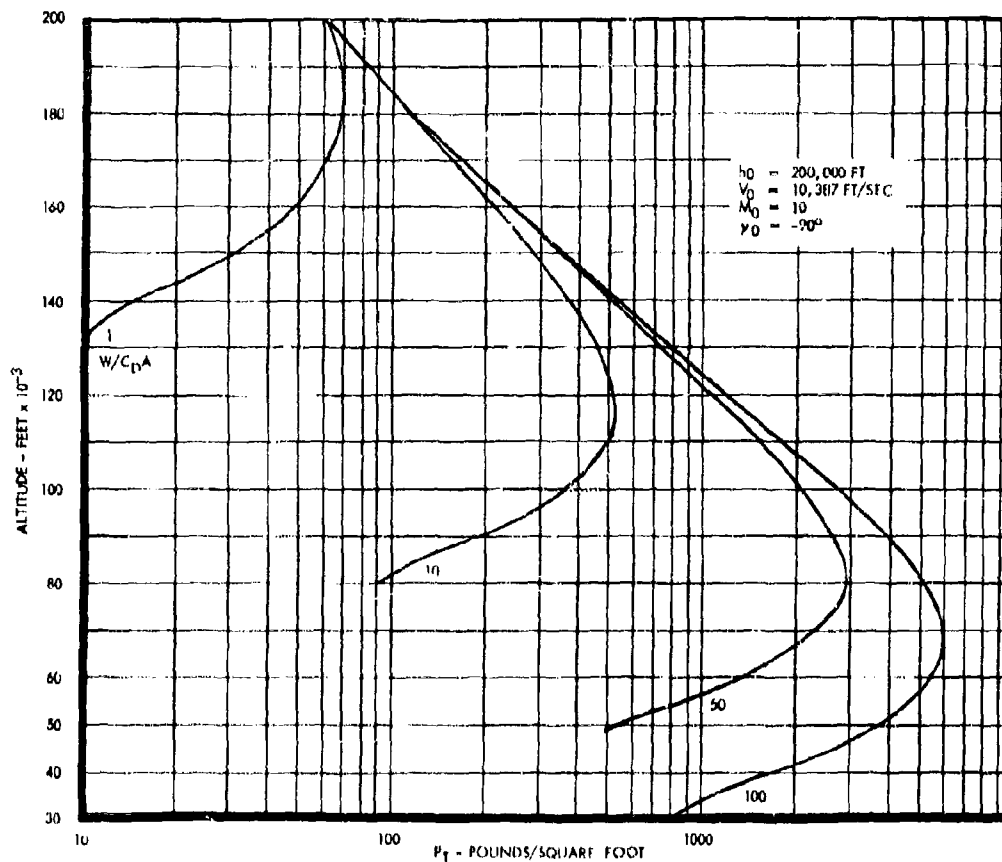


Figure 5. Altitude versus Total Pressure (P_t) from Mach 10 and 200,000 Feet

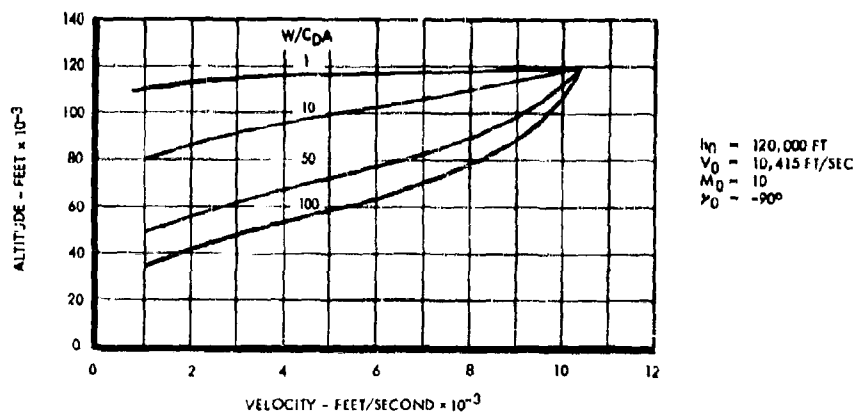


Figure 6. Altitude versus Velocity from Mach 10 and 120,000 Feet

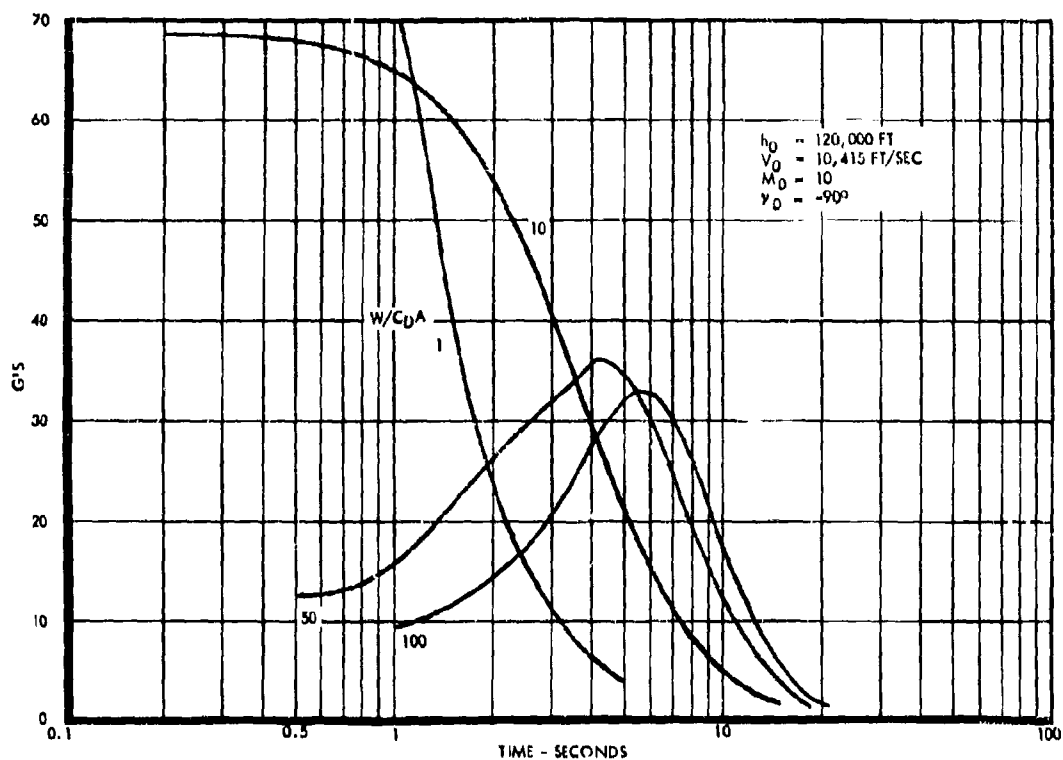


Figure 7. G versus Time from Mach 10 and 120,000 Feet

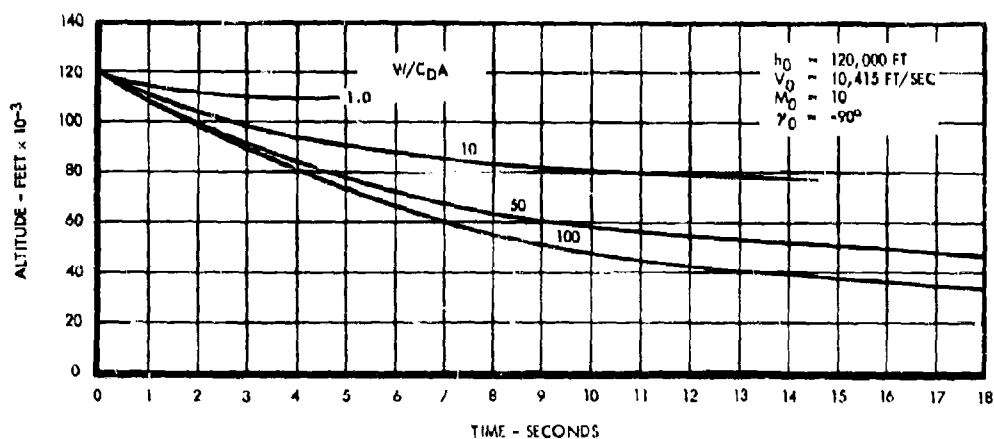


Figure 8. Altitude versus Time from Mach 10 and 120,000 Feet

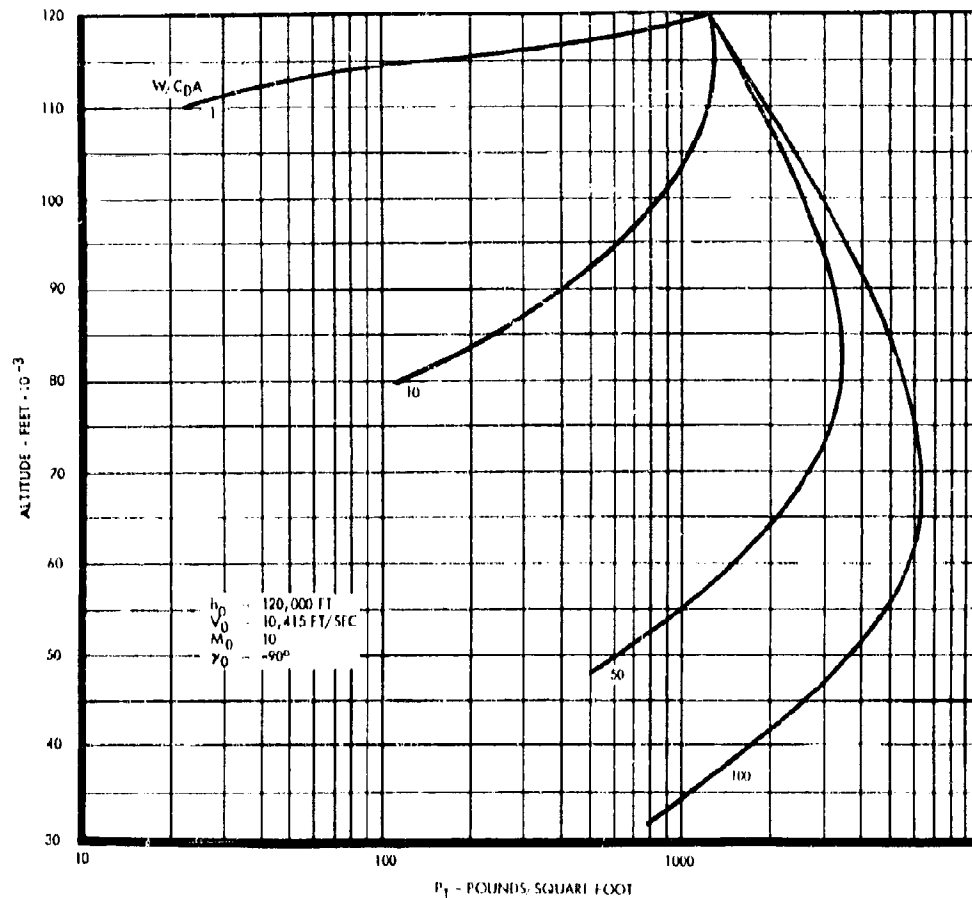


Figure 9. Altitude versus Total Pressure (P_T) from Mach 10 and 120,000 Feet

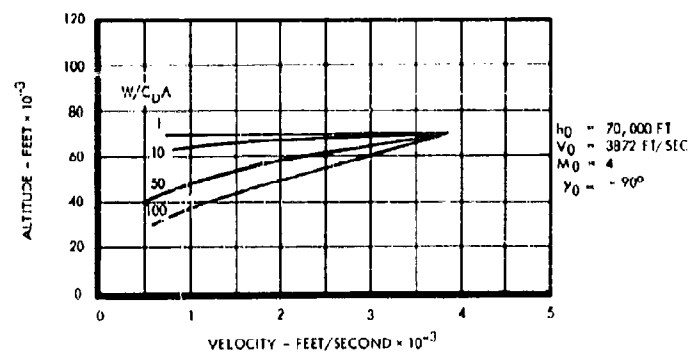


Figure 10. Altitude versus Velocity from Mach 4 and 70,000 Feet

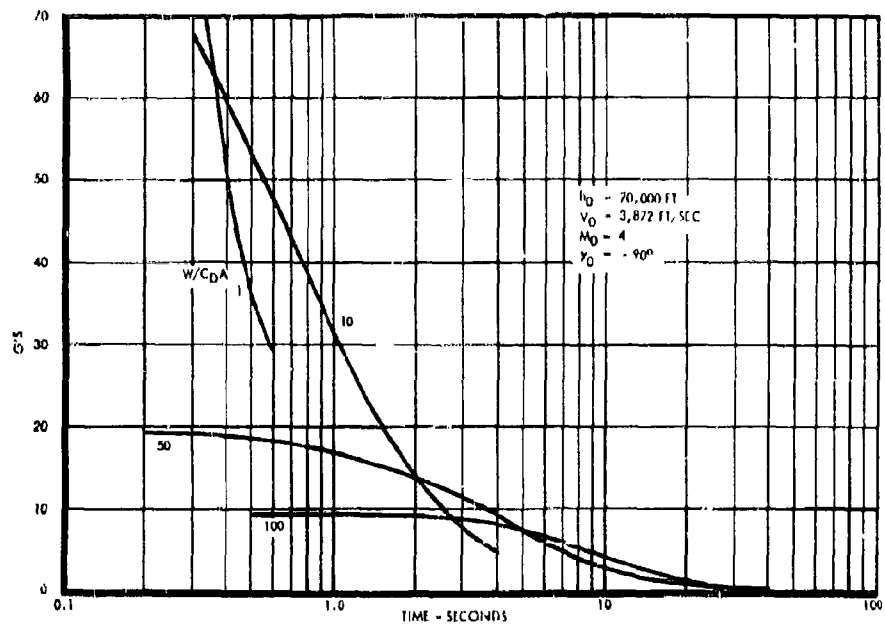


Figure 11. G versus Time from Mach 4 and 70,000 Feet

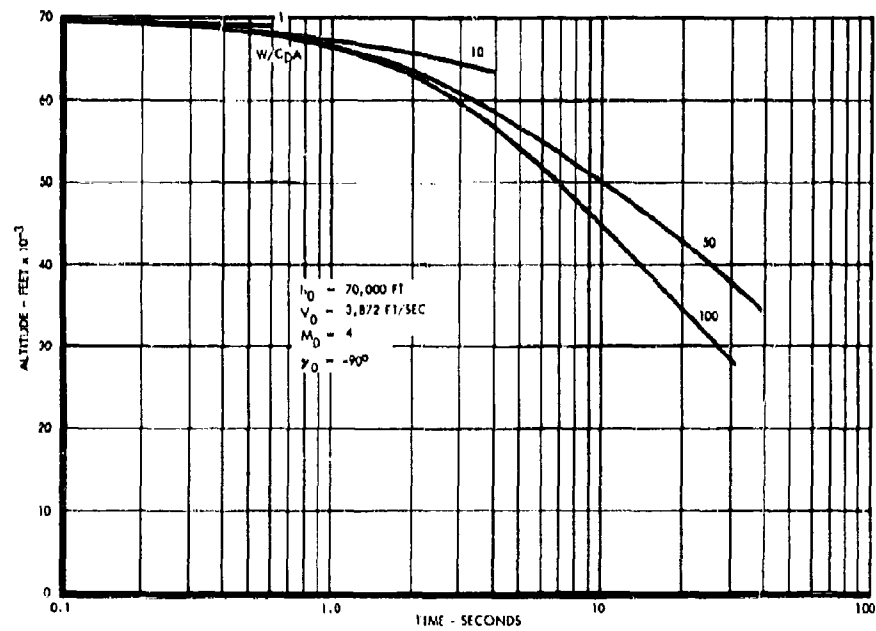


Figure 12. Altitude versus Time from Mach 4 and 70,000 Feet

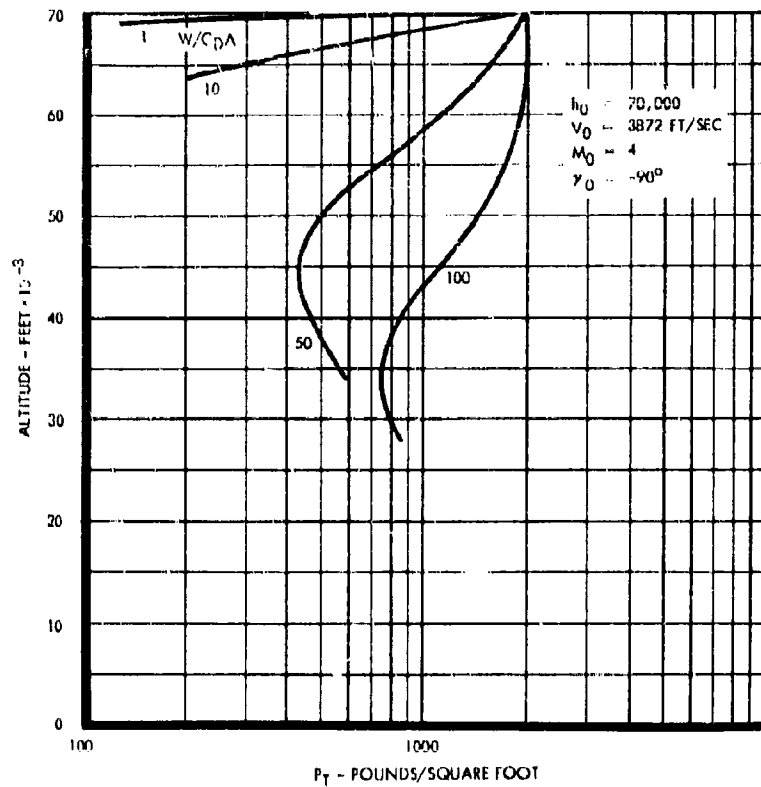


Figure 13. Altitude versus Total Pressure (P_T) from Mach 4 and 70,000 Feet

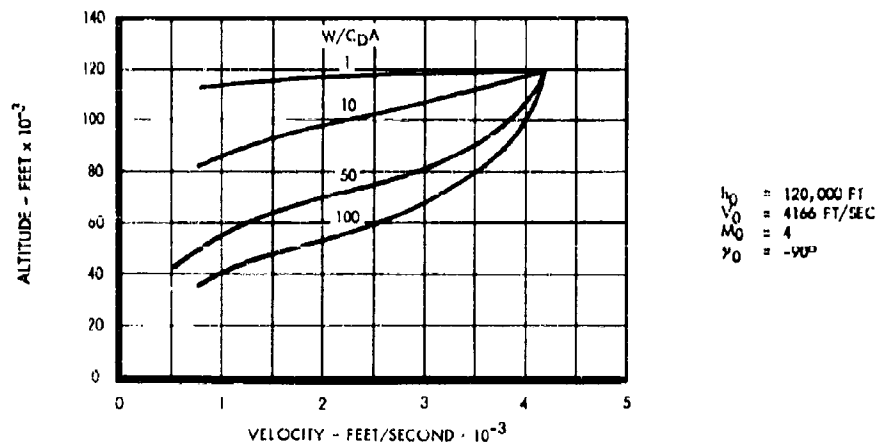


Figure 14. Altitude versus Velocity from Mach 4 and 120,000 Feet

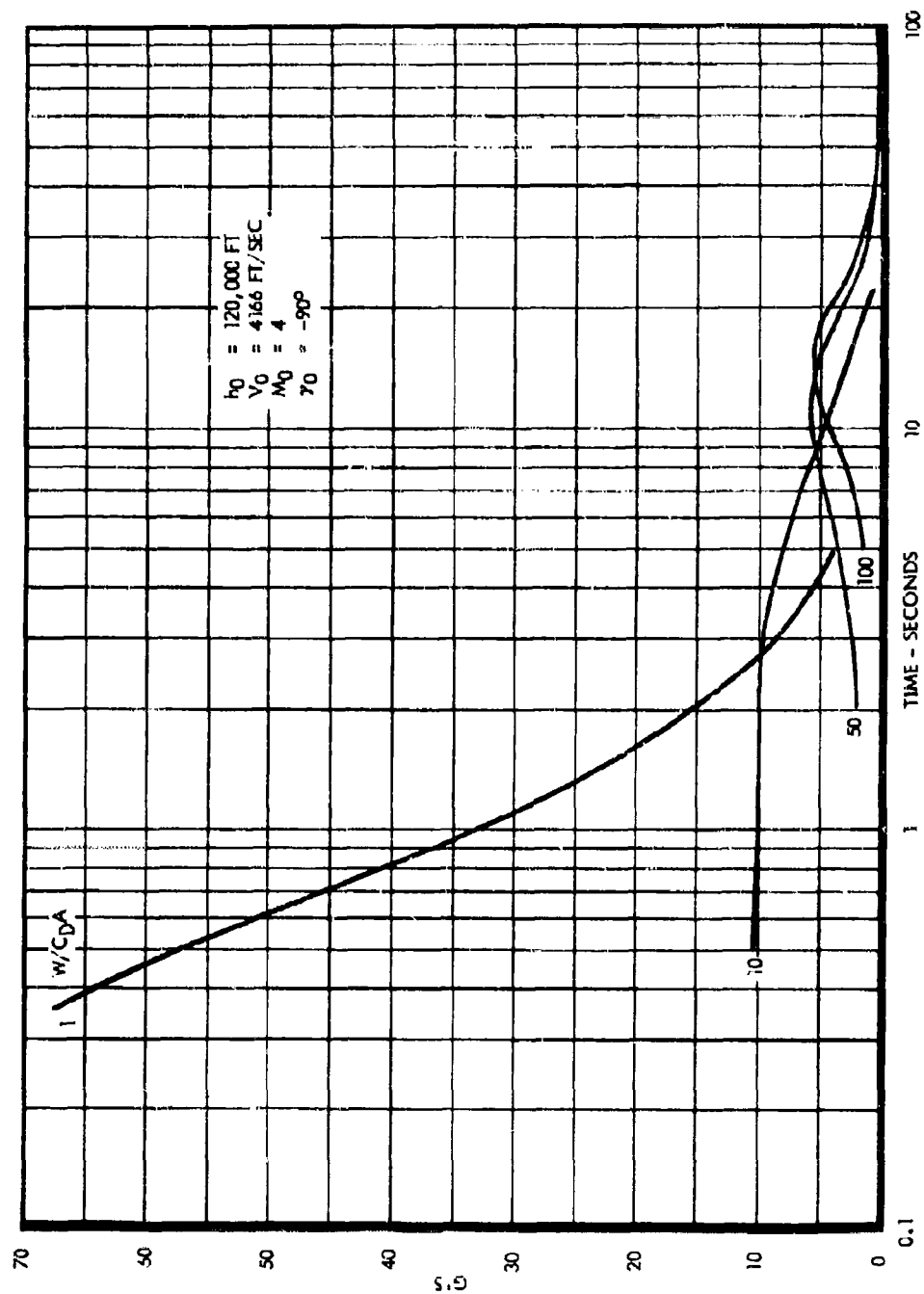


Figure 15. G versus Time from Mach 4 and 120,000 Feet

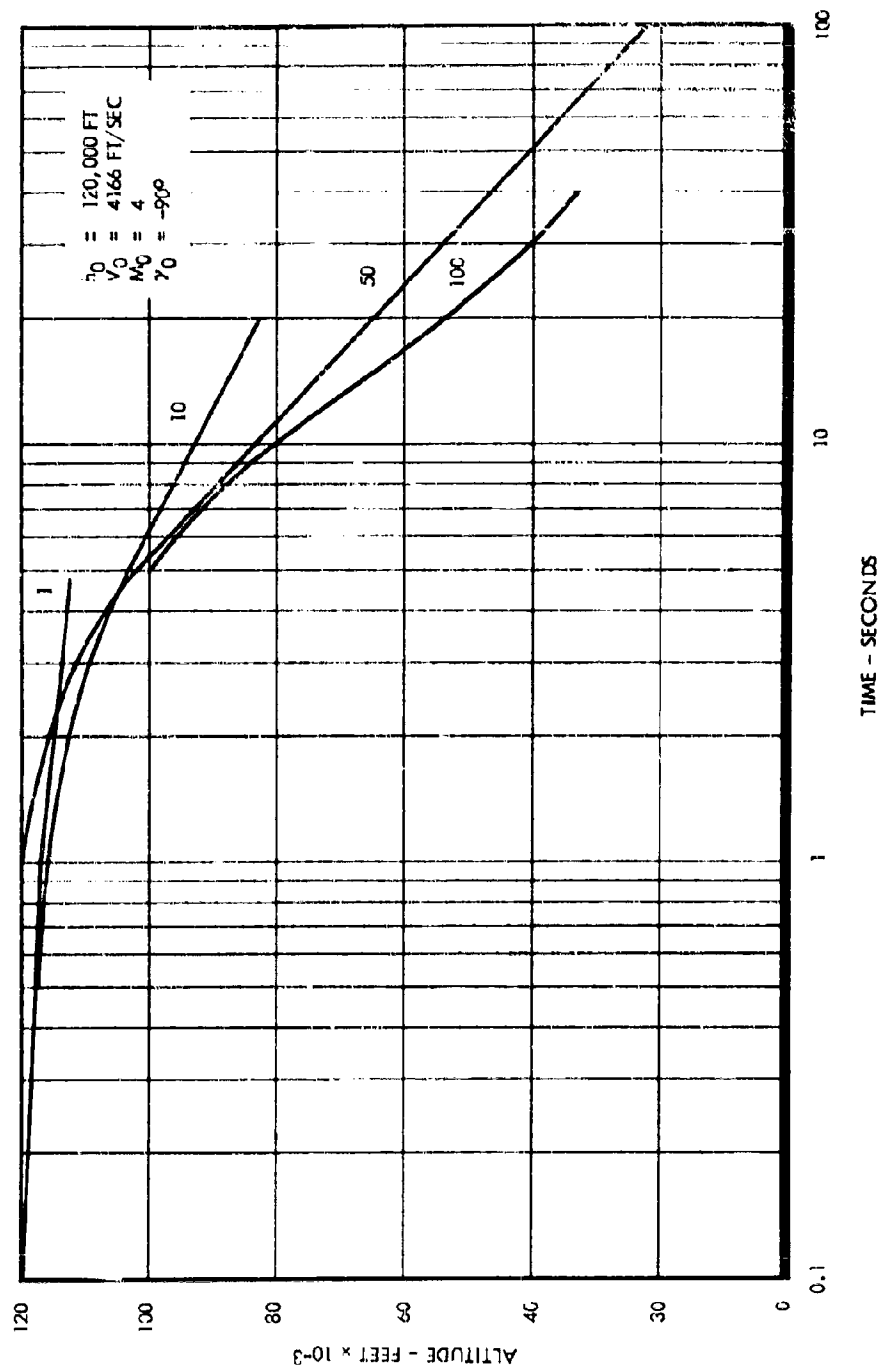


Figure 16. Altitude versus Time from Mach 4 and 120,000 Feet

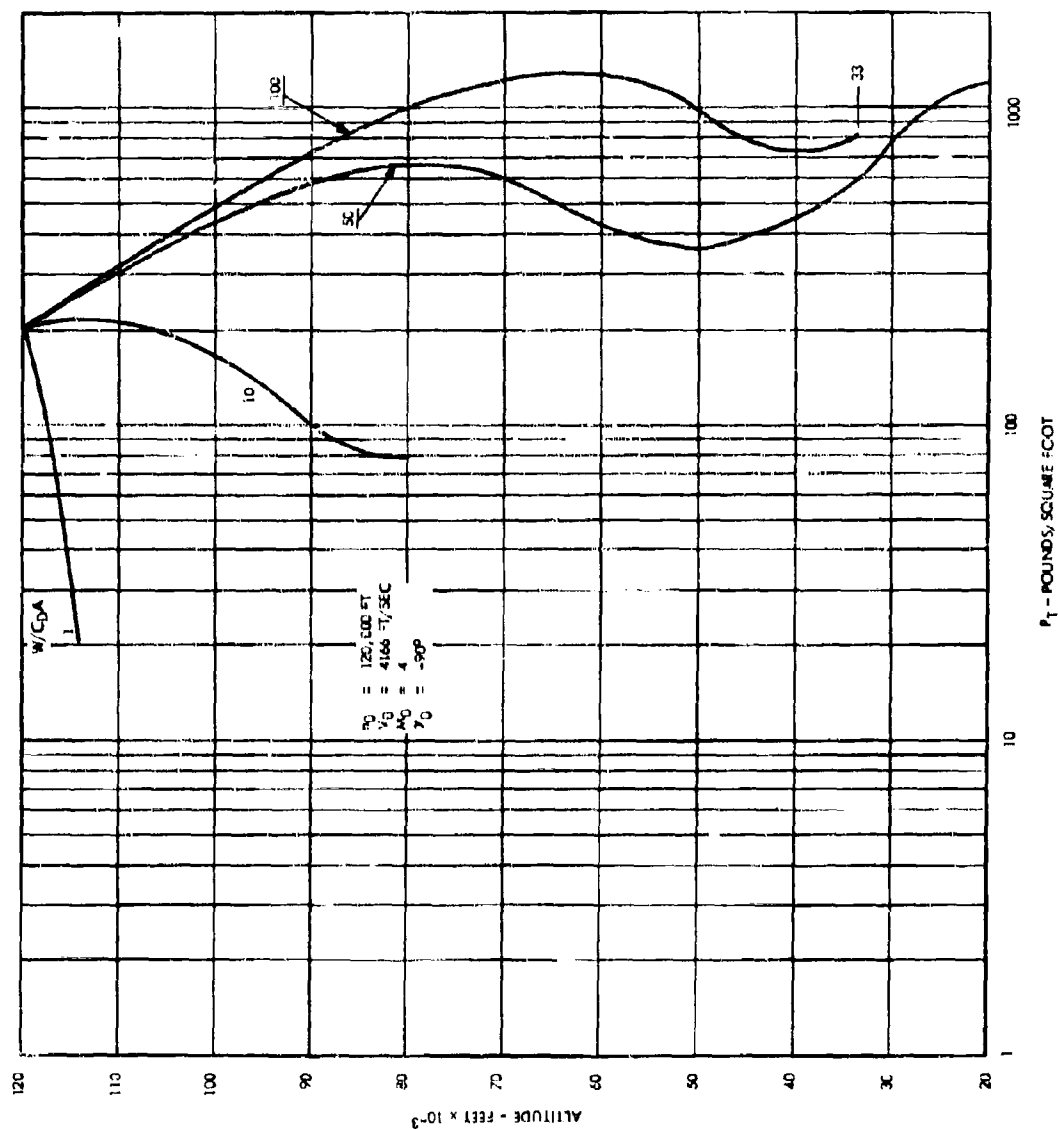


Figure 17. Altitude versus Total Pressure (P_T) from Mach 4 and 120,000 Feet

Re-entry trajectories with ballistic coefficients (W/CDA) of 1, 10, 20, 50, and 100 and initial drag body deployment at 200,000 foot and 120,000-foot altitudes with freestream Mach number 10 were utilized in this thermodynamic analysis. Herein, drag bodies with or without flow separation spikes are called out as spiked or non-spiked bodies respectively.

2. Method of Analysis

Laminar or turbulent flow conditions, whichever results in the most critical condition, were used to calculate temperature distributions over the blunt bodies. Continuum flow theory was applied throughout the flight envelope. The 1959 ARCD Model Atmosphere was used in all calculations.

a. **Stagnation Point Heat Transfer.** Stagnation temperatures were determined from the expression for heat flux to the forward stagnation point of an axisymmetric blunt body (Eq 1).

$$\dot{q}_{SP} = \frac{0.793}{(Pr_{w,SP})^{0.6}} (\rho_e \mu_e)^{0.4} (\rho_w \mu_w)^{0.06} \left(\frac{dU_x}{dX} \right)_{SP}^{0.5} (1r-1w)_{SP} \left[1 + (1.052 - 1.1 \frac{1d}{1e}) \right]_{SP} \quad (1)$$

Equilibrium dissociation flow properties were assumed throughout, with Lewis Number (L) = 1.4 and viscosity as a function of temperature. This expression is a result of the boundary layer theory of Fay and Riddell (Reference 3) with the ionization term omitted since it is negligible at velocities less than 30,000 fps.

The calculated heat flux was then equated to the formula for reradiation equilibrium temperatures to obtain the stagnation temperature

$$\dot{q}_{SP} = \epsilon \sigma T_0^4. \quad (2)$$

Emissivity (ϵ) = 0.9 was used in the calculation.

b. **Blunt Body Heat Transfer Distribution.** Temperature distribution over the axisymmetric blunt body was determined from the heat flux ratio Equation (3) proposed by Lees (Reference 4) for laminar flow.

$$\frac{\dot{q}}{\dot{q}_{SP}} = \frac{0.5(P/P_0)(U_e/U_\infty)S \left[(\rho\mu/P)_e / (\rho\mu/P)_{e,SP} \right]}{\int_0^X (P/P_0)(U_e/U_\infty)S^2 \left[(\rho\mu/P)_e / (\rho\mu/P)_{e,SP} \right] dX}^{0.5} \sqrt{U_\infty / \left(\frac{dU_x}{dX} \right)_{SP}} \quad (3)$$

Turbulent flow temperatures over the axisymmetric blunt body were calculated by Van Driest's method (Eq 4, Reference 5).

$$\dot{q} = 0.175 \rho_\infty U_\infty C_P \left(\frac{D}{U_\infty} \frac{dU_e}{dX} \right)_{SP}^{0.8} R_\infty D^{-0.2} \left(\frac{\rho_e}{\rho_\infty} \right)^{0.8} \left(\frac{\mu_e}{\mu_\infty} \right)^{0.2} \left(\frac{X}{D} \right)^{0.6} Pr^{-2/3} (1r-1w) \quad (4)$$

Ideal gas properties and the Sutherland viscosity law were applied to evaluate temperatures using Van Driest's method.

c. **Spiked Blunt Body Heat Transfer Distribution.** The total heat transfer to a blunt body, equipped with a flow separation spike, has been increased under some conditions (Reference 6) and decreased under other conditions (Reference 7). Theoretically, an increase in heat transfer might be expected for transitional or turbulent flow in the boundary layer over the separated region, since prediction

shows here a large increase for the lower Mach number. According to Reference 8, a decrease in heat transfer should be expected for laminar flow over the entire separated region. With these conditions in mind, Crawford's investigation of spiked hemispheres (Reference 9) was used in conjunction with calculated temperatures for spheres to predict the temperature distribution over a spiked sphere. The following correlations were used to determine the temperature distribution of the spiked sphere (Reference 9):

$$\phi = 22.5^\circ, \quad \dot{q} = 0.8 \dot{q}_{SP}, \text{ NS}$$

$$\phi = 45^\circ, \quad \dot{q} = 2.0 \dot{q}_{SP}, \text{ NS}$$

$$\phi = 67.5^\circ, \quad \dot{q} = 0.6 \dot{q}_{SP}, \text{ NS}$$

$$\phi = 90^\circ, \quad \dot{q} = 0.15 \dot{q}_{SP}, \text{ NS}$$

For the spiked sphere with L/D of 4 or greater, the shock reattachment location on the sphere is approximately 49 degrees from the center-line of the spike as shown in Figure 18 and has an average separation angle of 11 degrees (Reference 9).

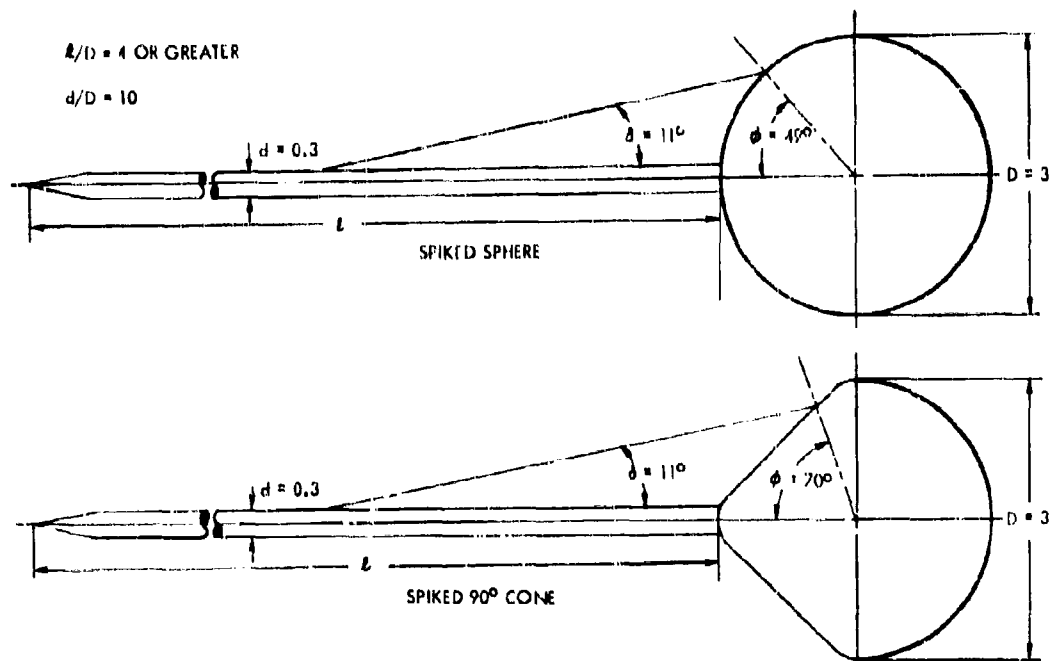


Figure 18. Graphical Solution for ϕ of 90-Degree Cone with Other Conditions Same as for the Sphere

An approximation method was used in obtaining the temperature distribution for the spiked 90-degree cone. Assuming the separation angle is the same as that of a spiked sphere when L/D , d/D , and diameter of the spiked cone are equal to that of the spiked sphere, the shock reattachment location was determined graphically for the spiked cone. Using this method of correlation between the spiked sphere and spiked cone, a heat flux ratio versus location curve was obtained for the spiked cone (Figure 19).

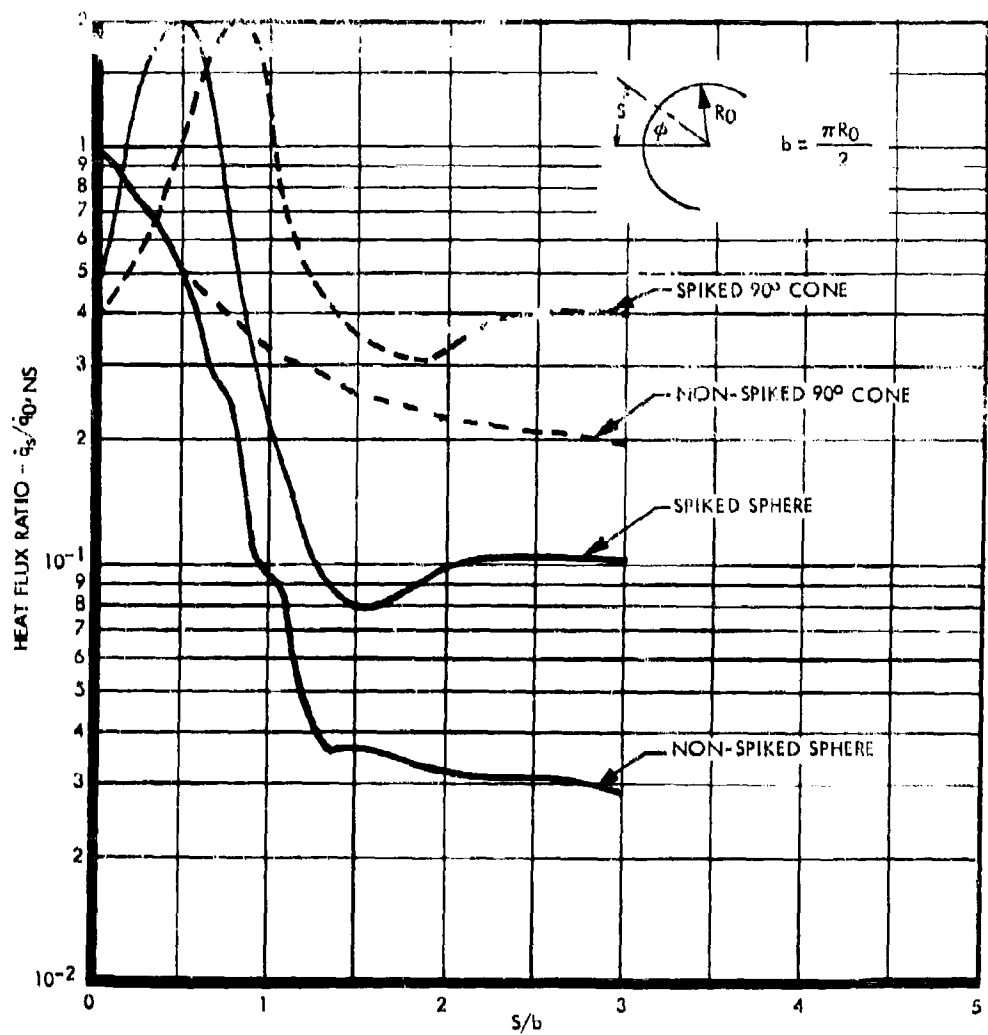


Figure 19. Heat Flux Ratio versus Location for Spiked and Non-Spiked Body

3. Results

Stagnation temperature histories during the various flight trajectories of a sphere with radius of one foot are shown in Figures 20 and 21. Maximum stagnation temperature for the various trajectories are given in Table 1.

Table 1. Maximum Stagnation Temperatures

W/C _D A	INITIAL CONDITION		MAXIMUM STAGNATION TEMPERATURE CONDITION			
	M _∞	H(ft)	U _∞ (fps)	H(ft)	θ (sec)	T _{0,max} (°R)
1	10	200,000	10,350	200,000	0	2310
10	10	200,000	9500	155,000	4.4	2460
20	10	200,000	9350	140,000	6.5	2610
50	10	200,000	9550	120,000	7.8	2980
100	10	200,000	9730	105,000	9.6	3270
1	10	120,000	10,400	120,000	0	3240
10	10	120,000	10,400	120,000	0	3240
50	10	120,000	10,100	113,500	0.6	3250
100	10	120,000	9,530	99,000	2.5	3380

From the stagnation temperature histories, the flight trajectory with a ballistic coefficient of 10 was chosen as the most probable trajectory for the drag devices. Therefore, surface temperature versus time calculations were made using this trajectory. Surface temperature results for spiked and non-spiked spheres are presented in Figures 22 and 23. The maximum surface temperature distribution curves for spiked and non-spiked spheres are shown in Figures 24 and 25. The maximum surface temperature of the spiked sphere is approximately 20 percent higher than the stagnation temperature of the non-spiked sphere.

Maximum temperature distribution over a spiked 90-degree cone for a ballistic coefficient of 10 type trajectory, with initial deployment altitudes at 200,000 and 120,000 feet, is presented in Figures 26 and 27. Calculated temperature distribution over a non-spiked 90-degree cone having the same conditions as the spiked 90-degree cone is shown in Figures 26 and 27 for comparison. Temperature distribution over a 90-degree cone for various trajectories is shown in Figures 28 and 29.

The decreasing heat transfer rate with increasing radius of curvature at the stagnation point of a blunt body has long been recognized. The temperature decrease with radius increase of a blunt body can be obtained from the following expression:

$$T_s = T_1 R_0^{-0.125} \quad (5)$$

Temperatures presented in Figures 19 through 29 are for blunt bodies with one-foot radii. Temperatures for spheres or 90-degree cones having radii greater than one foot, can be easily determined from Eq 5 or from the temperature conversion chart of Figure 30.

4. Conclusions

As was previously stated, the effect on heat transfer rates to blunt bodies with flow separation spikes may vary considerably with length and diameter of spike, tunnel Reynolds number, and Mach number. The available data does not lend itself to predicting heat transfer rates to a drag balloon system in that little if any similarity exists between the spiked blunt bodies and a drag balloon system.

SPHERICAL SHAPE WITHOUT SPIKE
FOR $R_0 = 1$ FT

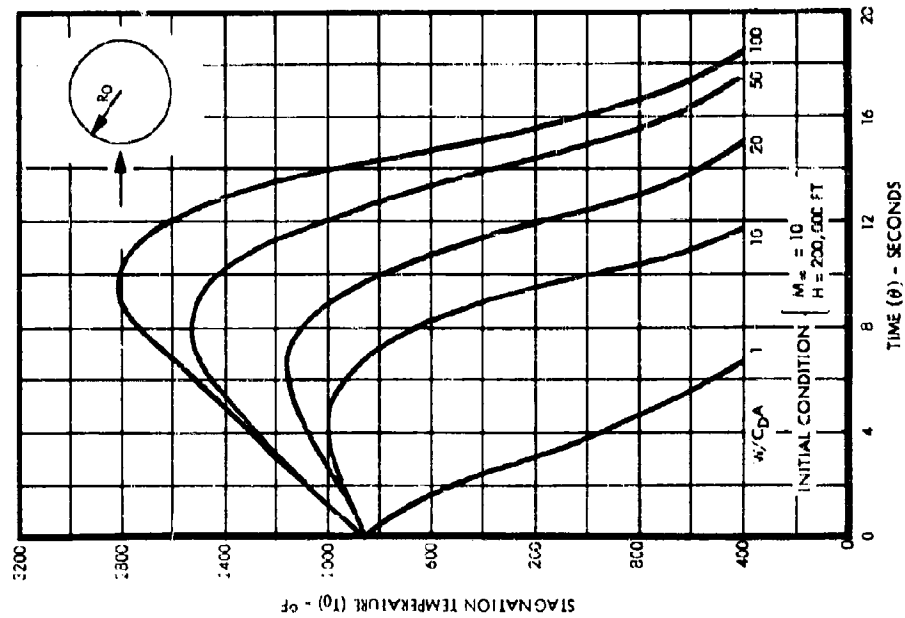


Figure 20. Stagnation Temperature versus Time from 200,000 Feet (Sphere)

SPHERICAL SHAPE WITHOUT SPIKE
FOR $R_0 = 1$ FT

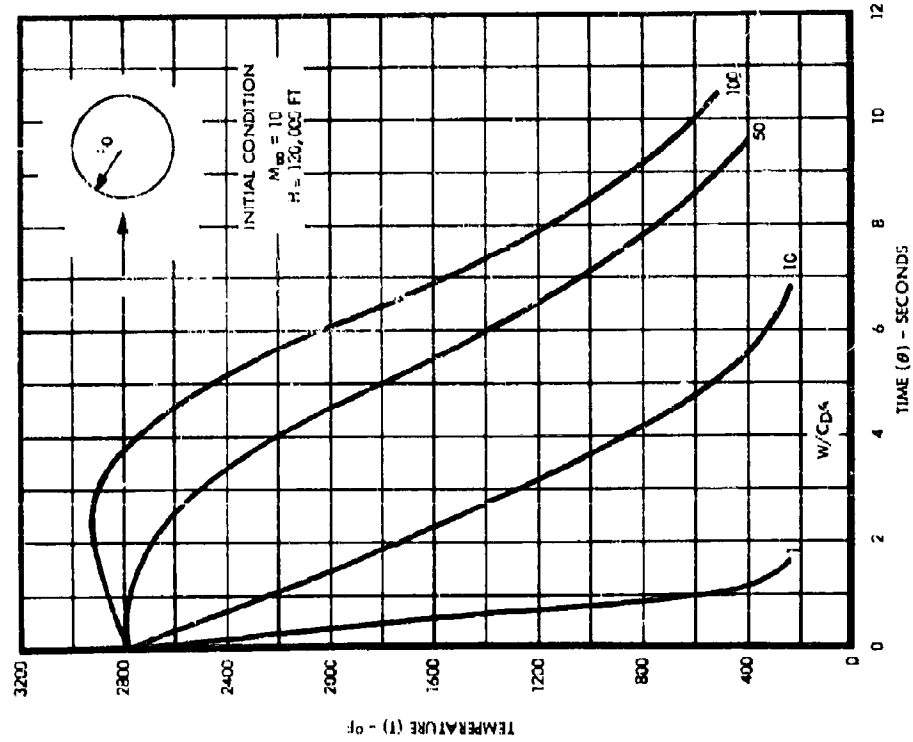


Figure 21. Stagnation Temperature versus Time from 120,000 Feet (Sphere)

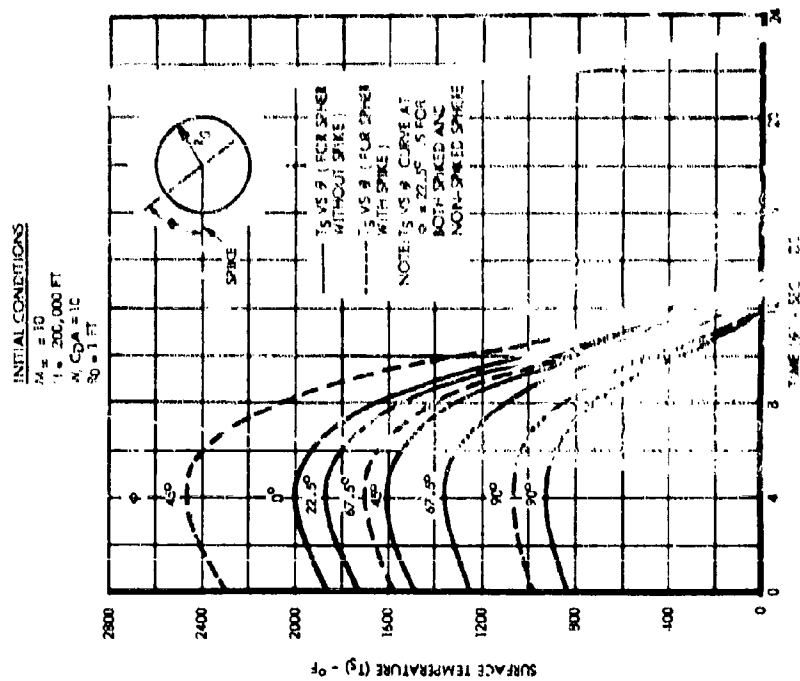


Figure 21. Temperature Profile from 200,000 Feet (Sphere)

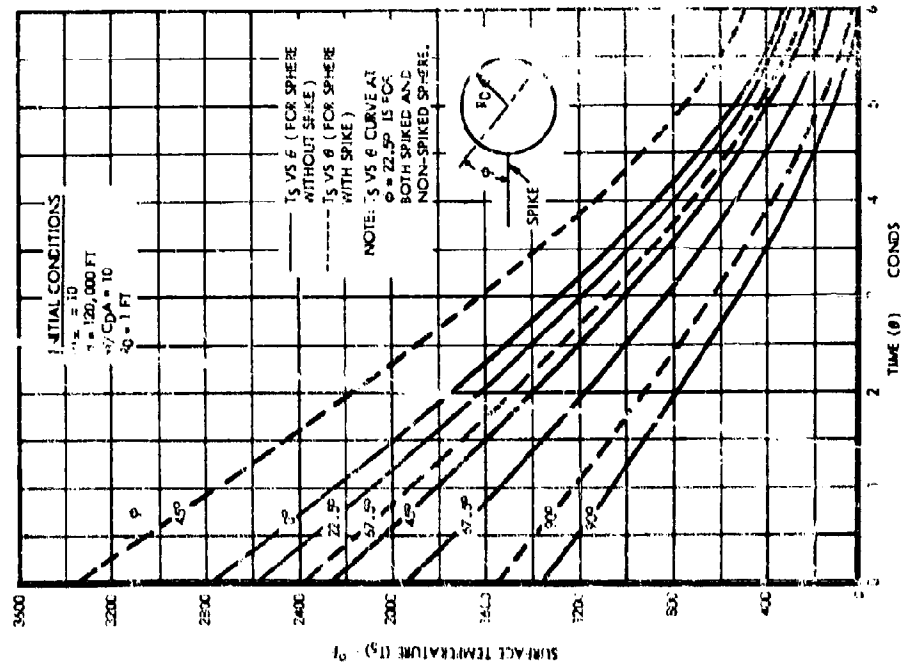


Figure 23. Temperature Profile from 120,000 Feet (Sphere)

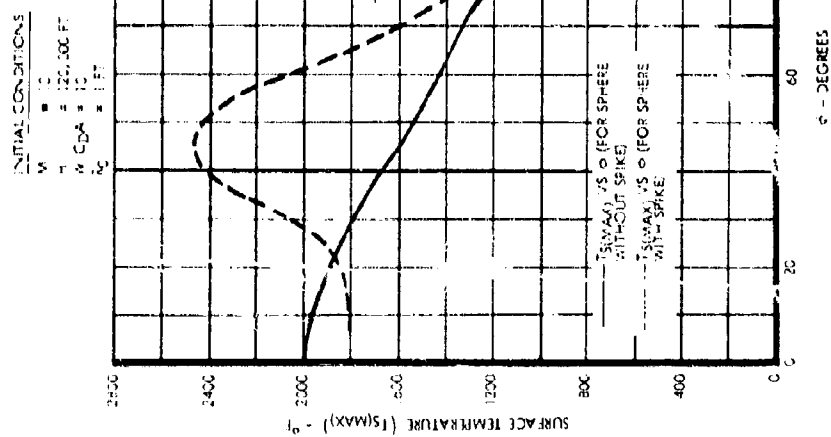


Figure 24. Maximum Temperature at $\theta = 4.4$ Seconds versus Location from 200,000 Feet (Sphere)

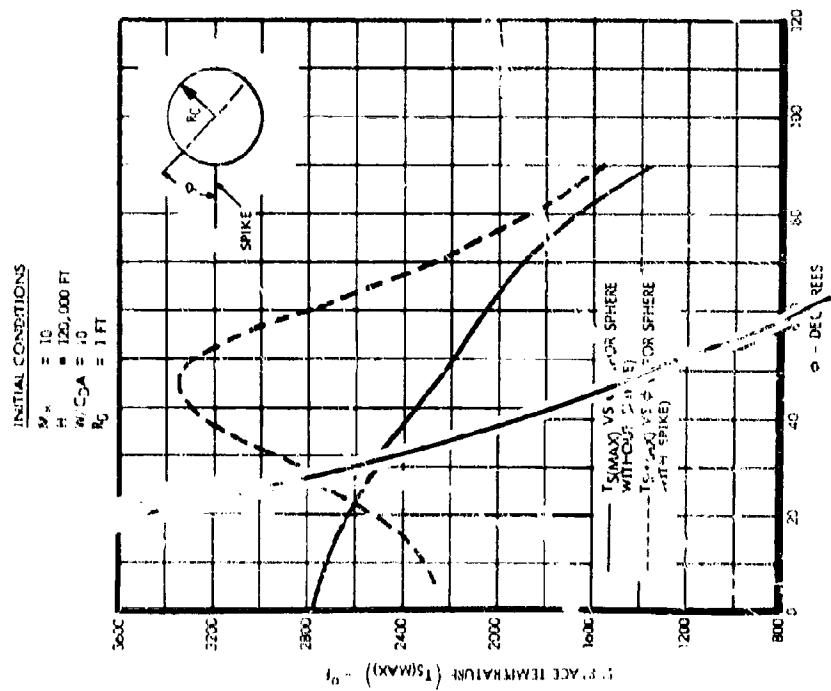


Figure 25. Maximum Temperature at $\theta = 0$ Seconds versus Location from 120,000 Feet (Sphere)

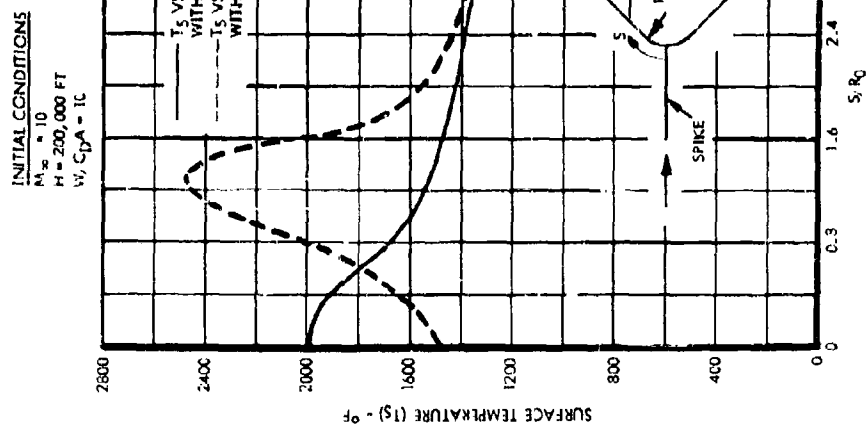


Figure 26. Maximum Temperature versus Location from 200,000 Feet (90-Degree Cone)

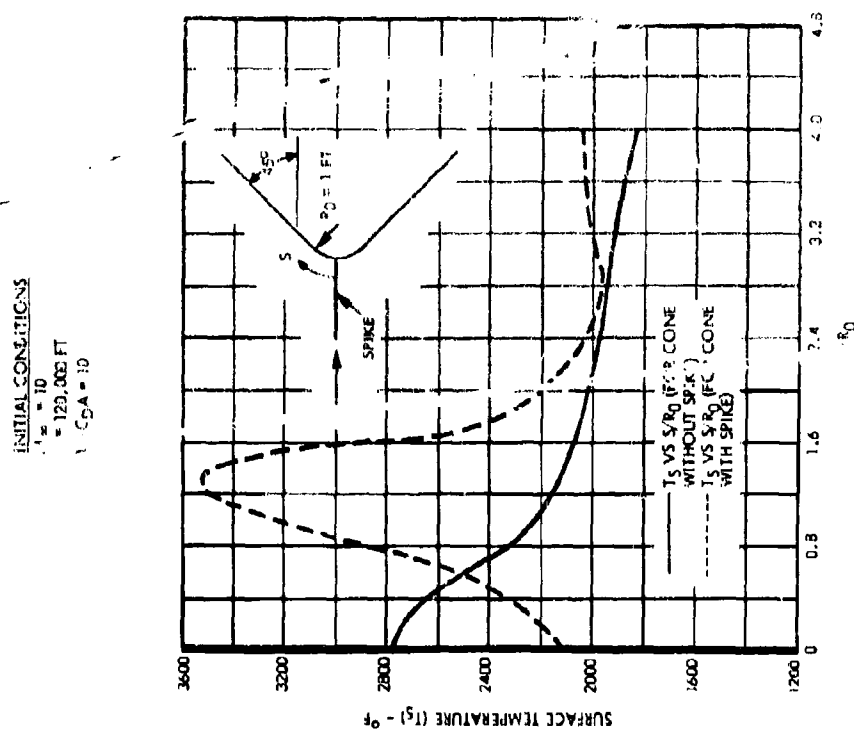


Figure 27. Maximum Temperature versus Location from 120,000 Feet (90 Degree Cone)

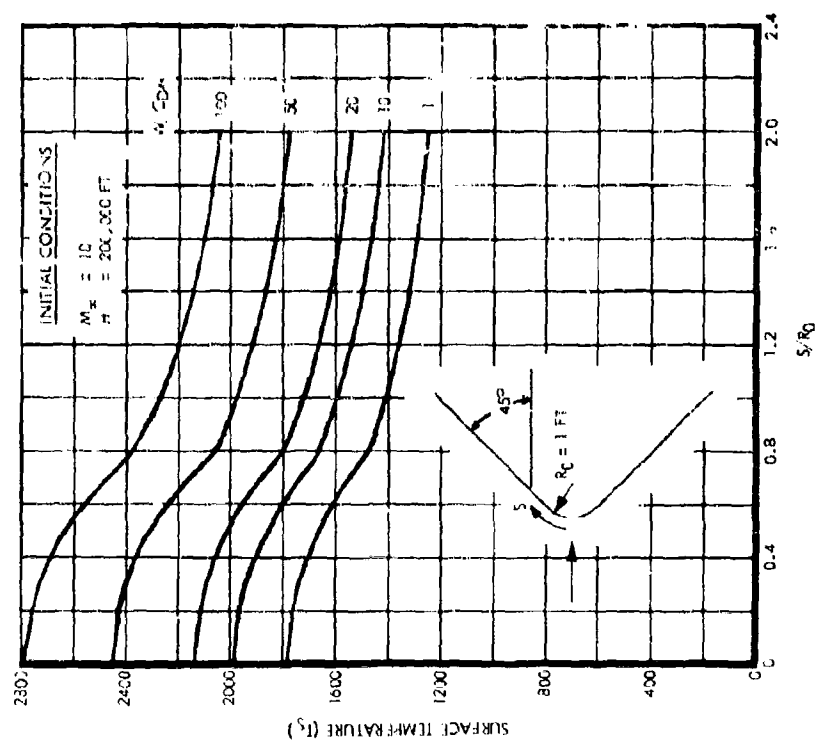


Figure 28. Maximum Temperature versus Location at Various W/CDA 's from 200,000 Feet (Cone)

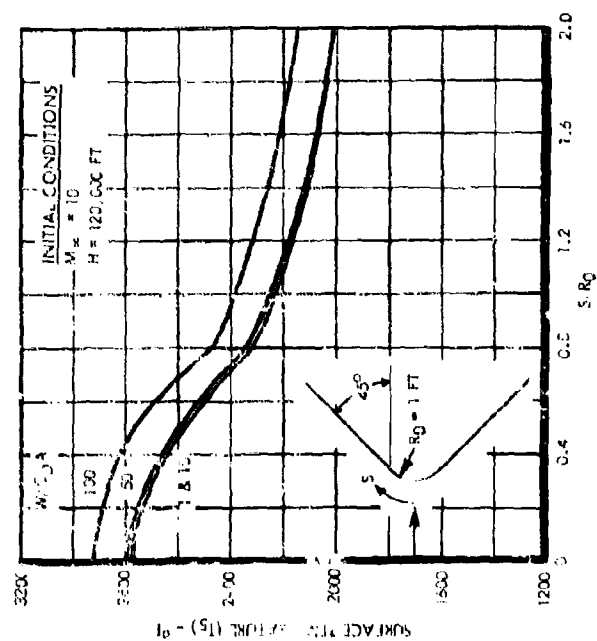


Figure 29. Maximum Temperature versus Location at Various W/CDA 's from 120,000 Feet (Cone)

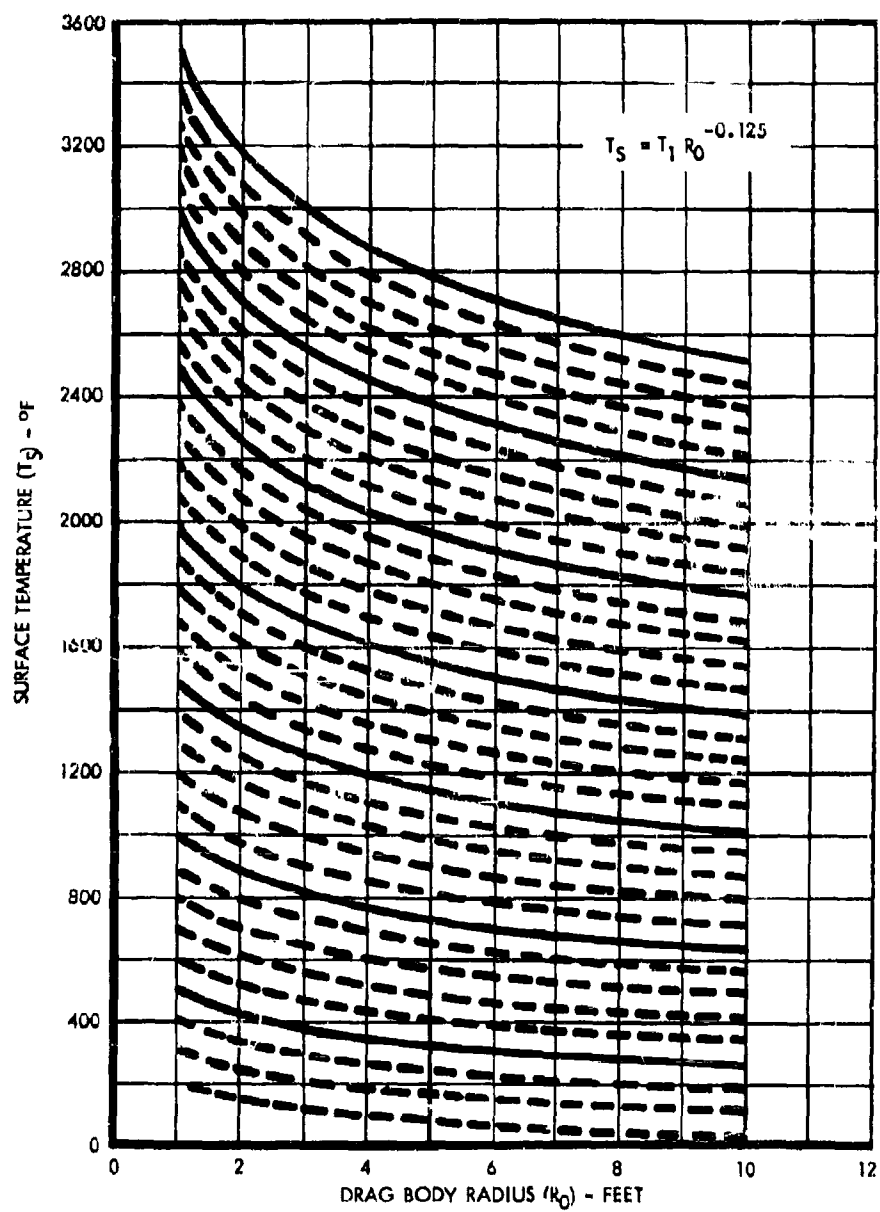


Figure 30. Temperature versus Drag Body Radius

E. WIND TUNNEL MODEL DESIGN STUDY

A preliminary design study was made to determine the types of inflatable blunt body configurations to be investigated. A large number of configurations were conceived, and each was evaluated on the basis of packageability, weight and structural stability, methods and cost of manufacture, and aerodynamic performance. Most of the concepts were eliminated quickly by these considerations, with no numerical analysis, leaving a smaller number of concepts (see Figure 31) to be investigated further. The remaining, most promising, concepts fell into two basic categories: (1) pressurized types, or those that are inflated by a self-contained pressure source and (2) ram-air inflated types.

1. Pressurized Types

The pressurized type of inflated structure (inflated by a self-contained pressure source) provides a wide range of possible shapes. The concepts selected for further consideration were chosen for their relative simplicity, low weight, structural stability, and ease of manufacture. Their shapes fell into areas of known good aerodynamic performance: sphere and hemisphere.

a. Sphere. The sphere, with a fence 15 degrees aft of the equator (Figure 31a), had already undergone considerable development as a decelerator (Reference 2), and it warranted further test work.

b. Hemisphere. The hemisphere concept (Figure 31b) has a hemispherical front, and the attachment to the fabric structure is made entirely to the back membrane by passing the tow cable through a slide fitting at the front. Thus, the shape of the front is never distorted from its hemispherical shape by attachments to the fabric or by meridional cables, as is the case with the sphere. The advantages of this concept over the sphere were believed to be

- (1) Frontal shape would remain hemispherical, smooth and free of protrusions.
- (2) Inflated volume is reduced and is variable as the back membrane moves in and out, thus reducing the complexity of pressure regulation during changes of altitude.
- (3) The possibility that no fence would be required for subsonic stability due to the sharper radius of the profile at the equator.

c. Cone Balloon. The cone balloon (Figure 31c) has a structural advantage over the sphere because the drag forces are applied directly to the frontal cone and distributed back toward the equator through suitable fabric reinforcements. The 75-degree cone with the fence at the equator was selected for this program because a wind tunnel model of this particular configuration existed for use.

d. Airmat Cones. The pure cone is known to be an ideal drag body shape. The Airmat cone (Figure 31d) comes closest to providing the pure cone of all the inflated structures. Other means of obtaining a cone which were considered and then discarded were

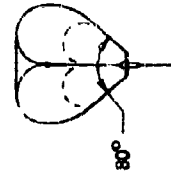
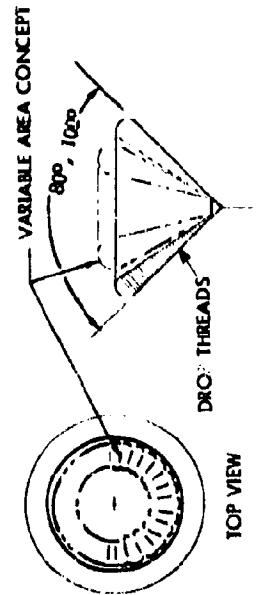
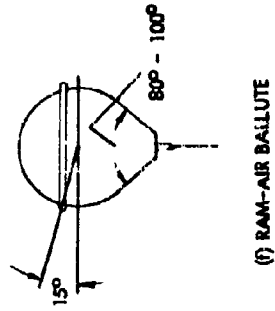
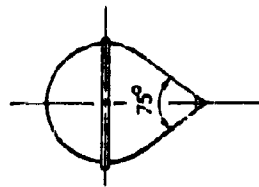
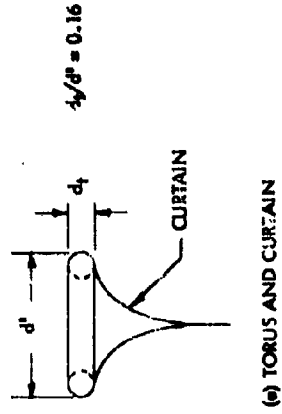
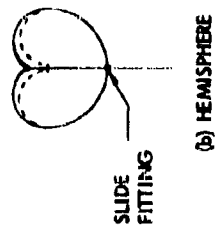
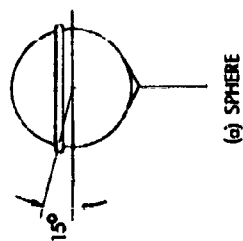
- (1) A series of concentric tori, which would have presented a rippled contour in the flow direction, and probably would be heavier and more difficult to build.
- (2) A constant thickness Airmat, which would have required a special weaving technique not yet developed, to produce the curved panels.
- (3) A series of flat, triangular Airmat panels, which was not considered a desirable contour.

The Airmat cone with tapered gores (Figure 31d) is a modified type of Airmat which is feasible to manufacture economically with proper tooling. An added feature of this concept was the possibility of use as a variable area device by reducing the inflation pressure and causing the gores to be shortened in the hoop direction, thus forcing the cone into a smaller angle.

e. Torus with Curtain. In this concept (Figure 31e) a torus, which is a well-known inflated shape, is towed by a contoured curtain of uncoated fabric. The curtain is contoured in the shape of a flared cone and was expected to have aerodynamic characteristics similar to a blunt cone.

2. Ram-Air Inflation Types

The concept of ram-air inflation, which inflates the body with pressure obtained by the



*T.M., Goodyear Aircraft Corp., Akron 15, Ohio
Figure 31. Wind Tunnel Model Design Concepts

energy of motion, automatically compensates for change in altitude and changes in dynamic conditions. Thus, the concept promises to greatly simplify and lighten the device by

- (1) Eliminating the weight and bulk of the pressure generating system.
- (2) Eliminating the need for pressure programming.
- (3) Reducing structure weight by reducing the pressure differential required through large changes in altitude.

In addition, the ram-air concept eliminates the need for maintaining a positive pressure seal in the membrane of the pressure body, for a considerable amount of leakage can be tolerated. At high temperature, the leakage in the closed (pressurized) types may become prohibitive.

The ram-air concepts selected during this preliminary phase were:

a. Cone Ballute with Hemispherical Back. This was the first-conceived ram-air Ballute. It is a sphere with a tangent cone at the front and with the inlet at the apex. The fence is located 15 degrees aft of the equator to give maximum subsonic stability. Two cone angles, 80 degrees and 100 degrees, were selected for the test program in order to bracket the known limiting angle of approximately 90 degrees for supersonic stability of pure cones. This concept is shown in Figure 31f.

b. Cone Ballute with Tucked Back. In this concept (Figure 31g) the fabric stress in the rear of the Ballute is reduced by attaching a center cable to the rear portion and carrying a part of the drag force by this cable. The resulting reduction in radius of curvature and the addition of radial reinforcing straps to the center fitting cause the membrane stress to be reduced. Another advantage anticipated in this concept was the possibility of varying the drag area by shortening the center cable and thus tucking the back into a smaller diameter.

c. Eighty-Degree Isotenoid Ballute with Plain Back. This concept is a refinement of the cone Ballute with hemispherical back and was developed for the second wind tunnel program after it became apparent that the membrane stress in the back of the Ballute could be reduced. In this concept the membrane envelope is held within a cage of meridian cables or straps extending from the nose to a ring in the back. The cables then carry a portion of the pressure load, thereby reducing the membrane stress. A method of design and analysis of this type of structure is presented in Section 8-C. At this stage in the program the 80-degree cone angle had been determined to be approximately the maximum limit for supersonic stability.

F. WIND TUNNEL MODEL STRESS ANALYSIS

1. Langley Unitary Plan Wind Tunnel (First Series)

Stress analysis of the models was based on the maximum loads anticipated in the tests. Fabric materials descriptions of the wind tunnel models are presented in Table 2. Models throughout this section are identified the same as in Table 2.

a. General Analysis. All models were analyzed for the conditions of maximum theoretical drag coefficient, as given in Table 3. Using these values, the drag is given by the equation

$$D = C_D q R^2,$$

and the pressure at any point is given by

$$P = C_p q.$$

In the case of the meridian cable balloon (Model h), the no-load condition can probably be slightly more critical to the fabric stresses than the maximum drag condition. In this case, however, the static pressure during operation of the tunnel is lower than the minimum pressure to which the tunnel is evacuated before the flow is started. The maximum load condition, therefore, is the most critical for the meridian cable balloon model, as it is for all the other models.

[illegible]

Table 3. Summary of Aerodynamic Data

Critical Wind Tunnel Conditions: $q = 150$ psf, $P = 95.2$ psf, $M = 1.5$				
MODEL	C_D	C_p (aft)	C_p (inside)	C_p (max)
a	1.33	-0.22	1.52	**
b	1.60	-0.17	1.52	**
c	*	*	*	**
d	*	*	*	*
e	1.33	-0.22	----	**
f	1.60	-0.17	----	**
g	1.26	-0.17	----	**
h	1.05	-0.25	----	2.0
i	1.05	-0.25	----	2.0
j	1.33	-0.22	1.52	**

*Porous Models c and d have lighter loads and pressures than similar coated models a and b. Therefore, no analysis is performed and no aerodynamic data is needed.

**Maximum pressure coefficient data is used only in analysis of models h and i.

----Internal pressure coefficient applies only to ram-inflated Models a, c, d, and j.

Table 4. Summary of Minimum Margins of Safety (Based on Limit Loads)

MODEL	FABRIC MARGIN	TAPES AND/OR STRAPS MARGIN	REAR FITTING RING MARGIN
a	*	*	**
b	*	2.88	**
c	Less critical than Model a or b.		**
d	Less critical than Model a or b.		**
e	> (f)	**	**
f	3.02	**	**
g	*	*	**
h	*	**	**
i	*	1.7	1.71
j	*	*	**

* Margins of safety are greater than four.

** These models are not equipped with the respective structural elements.

In all the pressurized models except h, the pressure is determined by the criterion of first wrinkling, and to insure against wrinkling this pressure is multiplied by a factor of 1.5 to obtain the actual pressure desired for the test. Using this actual pressure, the maximum stresses are obtained and are compared to the quick-break strengths of the materials. The results are presented as margins of safety (Table 4), which are defined as follows:

$$\text{Margin of Safety} = MS = \frac{\text{quick-break strength}}{\text{maximum design stress}} - 1.$$

In Model h, the pressure is arbitrarily chosen large enough to prevent the deflection under load from becoming excessive, as indicated by the analysis of Reference 10, and the stresses are based on this pressure as described above.

b. Analysis of Models a, b, and j. The ram-air Ballute model shown in Figure 32 consists of a conical front part and hemispherical rear part. The drag load is transmitted through an inlet fitting to the fabric and straps at the front of the Ballute. The straps reinforce the fabric, spreading the drag load. These straps have the threads running parallel and perpendicular to the direction of the tape, as opposed to the gores which have the threads 45 degrees to the center line of the gore. Since the tapes are straight-cut, they are much stiffer in the meridian direction than the gores. They, therefore, carry most of the drag load away from the drag fitting. At the end of the straps the drag load is spread out so that fabric can carry the additional meridian stresses. The stress analysis is based on the Ballute with $2\beta = 100$ degrees, since the load in the conical part is more critical.

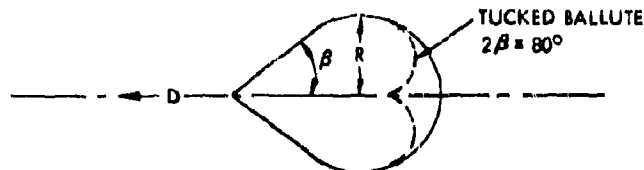


Figure 32. Ram-Air Ballute ($2\beta = 80$ and 100 Degrees)

The maximum drag is given by the equation

$$D = C_D q \pi R^2$$

$$D = 1.33 \times 150 \times 0.349 = 70 \text{ pounds.}$$

The maximum stress in the hemispherical part is

$$P = (1.52 + 0.22)q = 1.74q = 1.74 \times \frac{150}{144} = 1.81 \text{ psi}$$

$$\frac{PR}{2} = \frac{1.81 \times 4}{2} = 3.62 \text{ ppl.}$$

The hemispherical part fabric strength is 38 lb/in, giving a large margin of safety.

Load carried by the straps and tapes:

$$nT_m = \frac{D}{\cos 50^\circ} = \frac{70}{0.643} = 109 \text{ pounds.}$$

$$\text{Strength of straps} = 100 \times 0.12 = 12.0 \text{ pounds.}$$

$$\text{Strength of tapes} = 38 \times 0.38 = 14.5 \text{ pounds.}$$

No. of straps = 16 inside and 16 outside.
 No. of tapes = 8.

$$\begin{aligned} 32 \times 12.0 &= 384 \\ 8 \times 14.5 &= \frac{116}{500} \text{ pounds.} \end{aligned}$$

$$MS = \frac{500}{109} - 1 = 3.58.$$

The meridian fabric stress in the conical section (see Figure 33) where the straps end is

$$D + 1.52qw(R\cos 50^\circ)^2 = 1.11qw(R\cos 50^\circ)^2 + 2\pi R\cos 50^\circ t$$

or

$$t = 7.55 \text{ lb/in.}$$

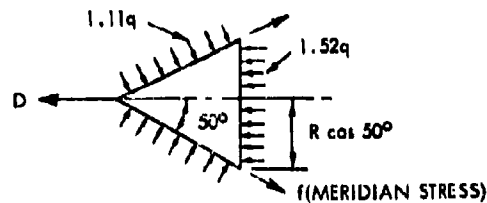


Figure 33. Tucked Ballute Stresses

The conical section fabric strength is 38 lb/in., giving a large margin of safety.

c. Analysis of Models c and d. The porous Ballutes are strong enough by inspection since loads are less than for Model a and b Ballutes and fabric strength is 90 ppl.

d. Analysis of Models e and f. The Airmat cones (Figure 34) have a nearly uniform pressure

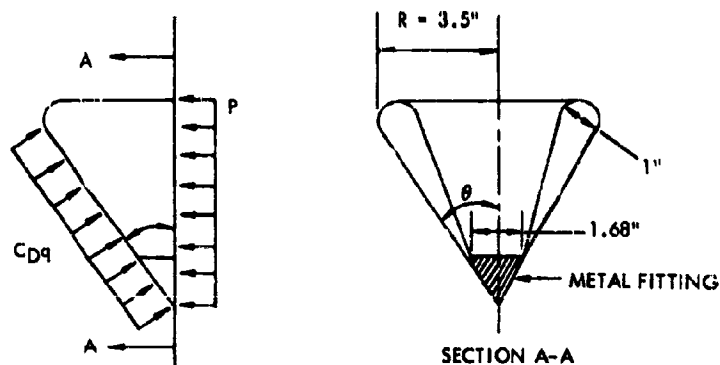


Figure 34. Airmat Cone Stresses

around the front side, giving a uniform pressure difference across the Airmat equal to $C_D q$. The load from the Airmat is transmitted to the main cable by means of a conical metal nose fitting. The external pressure loading tends to reduce the hoop stresses in the Airmat until wrinkling occurs.

The hoop stress in the cone due to the external loading is $(-C_D q R)/(\cos \theta)$

and the sum of the hoop stresses in the inner and outer skins due to internal pressure is $2Pr$, where $r = 1/2$ inch. Wrinkling occurs when $2PR = (C_D q R)/(\cos \theta)$.

When $\theta = 40$ degrees, $C_D = 1.33$:

$$P = \frac{(150/144) (3.5) (1.33)}{0.766} = 6.3 \text{ psi to wrinkle.}$$

Applying a factor of safety of 1.5 on wrinkling, the pressure required is 9.45 psi in the 80-degree cone.

When $\theta = 50$ degrees, $C_D = 1.60$:

$$P = \frac{(150/144) (3.5) (1.60)}{0.643} = 9.1 \text{ psi to wrinkle}$$

and the actual required pressure is $(1.5) (9.1) = 13.6$ psi in the 100-degree cone.

Taking the metal nose piece as a free body, static equilibrium yields the approximate relationship

$$(2) (2\pi) (0.84) f_1 \cos \theta = D$$

or

$$f_1 = \frac{D}{(2) (1.68 \pi \cos \theta)} = \frac{C_D q \pi R^2}{(1.68 \pi \cos \theta) (2)} = \frac{C_D (150/144) (3.5)^2}{(1.68 \cos \theta) (2)}$$

where

f_1 is the fabric stress in the meridian direction at the nose.

80-degree cone: $f_1 = 6.6$ lb/in.

100-degree cone: $f_1 = 9.45$ lb/in.

The largest pressure stress occurs in the inner diameter of the torus and is equal to

$$\frac{Pr}{2} \left[\frac{2 - (r/R - r)}{1 - (r/R - r)} \right]$$

Using the 100-degree cone pressure of 13.6 psi, the stress is 7.48 lb/in.

The highest fabric stress is 9.45 lb/in. The fabric strength is 38 lb/in, giving a margin of safety of 3.02.

e. Analysis of Model g. The curtain consists of eight gores of bias-cut fabric seamed together with straight cut tapes, which are assumed to carry the entire drag load. There are 16 tapes (8 inside and 8 outside) with a strength of 22.5 pounds each. The drag is

$$D = C_D q \pi R^2 = (1.28) (150/144) (3.5^2) \pi = 50.5 \text{ lb.}$$

The load in each tape is $50.5/16 = 3.16$ pounds. The margin of safety of the tapes is large.

The curtain is attached tangent to the front side of the torus, applying a nearly radial load of 50.5 pounds distributed uniformly around the torus, giving a unit load of $50.5/2\pi R = 2.3 \text{ lb/in.}$ The loading is shown in Figure 35.

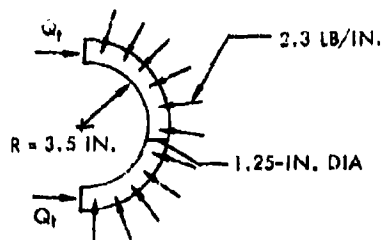


Figure 35. Torus with Curtain Radial Loading

From Figure 35

$$Q_t = (2.3)(3.5) = 8.05 \text{ lb}$$

which produces a compressive stress equal to $8.05 / \pi(1.25) = 2.05 \text{ lb/in.}$

In addition to the compression, the eccentric application of the load produces a bending moment in the torus shown in Figure 36.

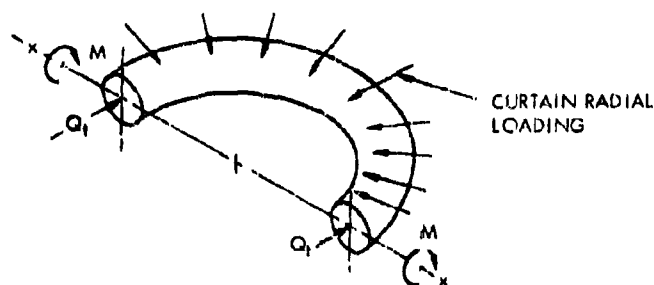


Figure 36. Eccentric Application of Load to Torus

Summing moments about the x-x axis

$$\frac{(7)(2.3)(1.25)}{2} = 2M_t,$$

$$M_t = 5.03 \text{ in-lb.}$$

The moment produces bending stress ($M_t c / I$) equal to

$$M_t \frac{(0.625)}{\pi(0.625)^3} = 0.814M_t = 4.1 \text{ lb/in.}$$

The total stress is $4.1 + 2.05 = 6.15 \text{ lb/in.}$

The thickness of the torus is about 0.020 inch, giving a stress of $\frac{6.15}{0.020} = 308$ psi and a very large margin of safety.

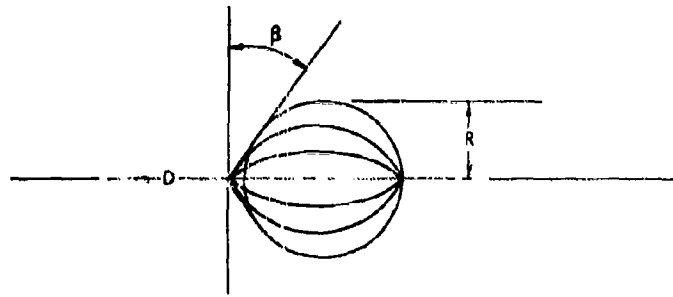


Figure 37. Sphere

f. **Analysis of Model h.** The spherical balloon in Figure 37 consists of a spherical pressure vessel suspended by a system of eight cables along the meridian circles of the sphere. The angle β is designed to be 30 degrees with no load on the balloon. Under load β increases slightly, but a conservative value of the meridian cable tension is obtained by neglecting any change in β . The maximum drag expected on the balloon is

$$D = C_D q R^2 = (1.05) (150) (0.349) = 55 \text{ lb.}$$

The meridian cable tension is given by the equilibrium of the juncture at the nose of the balloon: $8T_m \sin 30^\circ = 55 \text{ lb.}$, or $T_m = 13.74$ pounds. The meridian cables are 1/32 diameter non-flexible carbon steel with a breaking strength of 185 pounds (Reference 11, page 240). The margin of safety is large. The quantity nT_m (where $n = 8$) is equal to 110 pounds. Assuming a pressure of 10 psi, the quantity $P\pi R^2 = (10) (\pi) (16) = 503$ pounds. The ratio $nT_m/P\pi R^2$ is then equal to 0.219. A previous detailed analysis of meridian cable balloons indicates that this value results in only moderate distortion of the spherical shape (Reference 10).

The fabric stresses can be obtained conservatively by neglecting the effect of the meridian cables on the sphere, in which case the stress is everywhere equal to

$$\frac{PR}{2} = \frac{(10) (4)}{2} = 20 \text{ lb/in.}$$

The fabric strength is a minimum of 100 lb/in., giving a large margin of safety (refer to Table 2).

g. **Analysis of Model i.** Figure 38 shows the hemisphere model under load. This model consists of a hemispherical front half and a rear half whose profile varies under load. The drag load is transmitted through the rod to the rear fitting and from the fitting to the fabric at the rear of the balloon. In order to carry the drag load with a small circumference of fabric, the rear half of the balloon is reinforced with meridional tapes which pass inside a metal ring at the rear fitting and are cemented to the inside surface of the balloon. These tapes have the threads running parallel and perpendicular to the direction of the tape, as opposed to the fabric gores which are cut with the threads at 45 degrees to the center line of the gore. Because the tapes are straight-cut, they are much stiffer in the meridian direction than the gores. They, therefore, carry almost all the drag load away from the rear fitting in the form of meridian stresses, and the rear surface becomes a membrane with meridian stresses much larger than the hoop stresses. Assuming the hoop stress in the rear half of the balloon to be everywhere equal to zero, the rear-half profile is derived as a function of the parameter $D/P\pi R^2$. The derivation is lengthy and is not presented here, but the results are used in the following stress analysis.

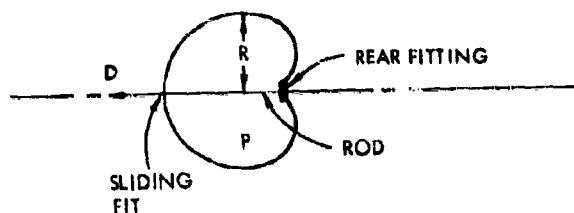


Figure 38. Hemisphere Model under Load

The maximum drag is given by the equation

$$D = C_D q \pi R^2,$$

and the maximum pressure on the front of the balloon is equal to $2.0 q$. (Refer to Table 3). Around the back side the pressure is $-0.25 q$. In order to prevent dimpling on the front under load, the pressure differences across the back surface must be $2.25 q = P$. The quantity $D/P\pi R^2$ is then equal to a maximum of

$$\frac{C_D q}{P} = \frac{C_D}{2.25} = \frac{1.05}{2.25} = 0.466.$$

The drag, D , is evaluated to be $D = (1.05) (150) (0.349) = 55$ pounds, and the required pressure becomes, inserting a safety factor of 1.5 on wrinkling,

$$\frac{(55) (1.5)}{P\pi R^2} = 0.466, P = \frac{(55) (1.5)}{(0.466) (16\pi)} = 3.52 \text{ psi.}$$

The maximum stress in the sphere is equal to

$$\frac{PR}{2} = \frac{(3.52) (4)}{2} = 7.04 \text{ lb/in.}$$

The fabric strength is 38 lb/in., giving a large margin of safety. Assuming the tapes carry all the stress in the meridian direction, the load in each of the 16 tapes at the equator is

$$\frac{P\pi R^2}{16} = 3.52\pi = 11.1 \text{ lb.}$$

The strength of each tape is 30 pounds, giving a margin of safety equal to

$$\frac{30}{11.1} - 1 = 1.7.$$

The tapes exert radial loads on the ring at the rear fitting, as shown in Figure 39.

The ring is Type 312 stainless steel annealed tubing; a cross section is shown in Figure 39. The cross-sectional area is

$$\pi/4 [(0.0625)^2 - (0.0385)^2] = 0.00191 \text{ in.}^2.$$

The tensile stress is $28.3/0.00191 = 14,800$ psi. Type 312 stainless steel hot rolled has a yield strength of 45,000 psi (Reference 11, page 17), and the yield strength in the annealed condition is estimated to be 38,000 psi, giving a margin of safety of $38,000/14,800 - 1 = 1.71$.

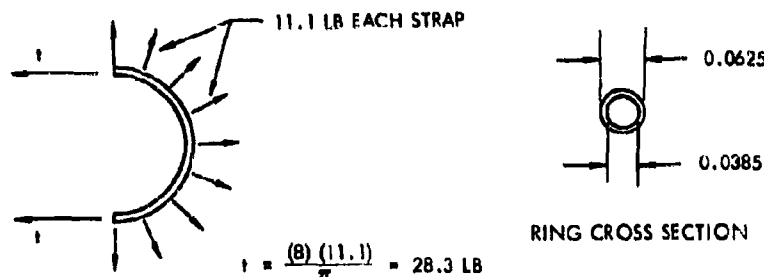


Figure 39. Radial Loads at Rear Fitting

2. Langley Unitary Plan Wind Tunnel (Second Series)

Six models, each eight inches in diameter, were analyzed for the wind tunnel conditions presented in Table 5. Models throughout this section are identified the same as in Table 5.

Each model had bias-cut gores seamed together along the meridian of the model. In all cases except the hemisphere, which has no outside tapes, the gores were butted together and tapes were cemented inside and outside. The outside tape on the cone balloon was N2582 nylon, a bias-cut tape with a strength of 50 lb/in. in warp and fill directions. The outside tape, where used, was 1/2-inch wide. The inside tape in every case was a 3/4-inch wide strip of Dacron fabric N337A15 cut on the bias. The outside tape on Model a through c was the same material, also cut on the bias. The straps were cut from the same fabric as the gores, with the warp threads running lengthwise. The straps were two plies in thickness and 1/4-inch wide.

a. General Analysis. Wind tunnel loads during supersonic operation arise from several sources, as indicated by previous experience with pressurized and ram-air models. The most critical condition appears to be the aerodynamic pulsing observed in the ram-air models (Reference 12). Additional instability occurs during starting or stopping the tunnel, when the air flow passes through the transonic speed range. Instability can also be encountered during steady-state operation of the tunnel if the drag body is close enough behind the forebody to be affected by its turbulent wake. The above loading conditions are, of course, superimposed upon the static drag loading, which is the only desired loading condition. The static loading condition is also the only one that can be predicted theoretically, because of the complicated nature of the various types of instability. The present models are therefore designed on the basis of the static loading, and large margins of safety are used in an effort to obtain a satisfactory operating life for the models.

The drag is given by the equation

$$D = C_D \rho V^2 R^2,$$

and the pressure at any point is given by the equation

$$P = C_p q.$$

The margins of safety (Table 5) are defined as $MS = \frac{\text{allowable stress}}{\text{applied stress}} - 1$ where allowable

$$\text{stress} = \frac{\text{ultimate stress}}{FS} = \frac{\text{allowable strength}}{FS} \text{ and applied stress} = \text{limit stress}.$$

As was the case for previous tests of 8-inch models under similar flow conditions, the analysis of the metal parts is not included.

Table 5. Summary of Aerodynamic Loading, Fabric Materials, and Minimum Margins of Safety

MODEL	DESCRIPTION	AERODYNAMIC DATA (q = 150 psf; M = 2.5 to 5.0)				MATERIAL PROPERTIES				MIN MARGINS OF SAFETY			
		Cp(1)	Cp(aft)	Cp(inside)	Cp(max)	Code No.	Material	Warp(2)	Fill(2)	Fabric	Straps	Metl Parts	Center Cord
a	80-degree Ballute with fence	0.780	-0.250(3)	1.81(5) 1.72(6)	0.90(5) 0.95(6)	N337A15	Dacron	120	100	4.87	1.22	----	----
b	80-degree Ballute without fence	0.780	-0.100(4)(5) -0.120(6)(4)	1.81(5) 1.72(6)	0.90(5) 0.95(6)	N228A230	Nylon	180	140	7.35	2.33	----	----
c	80-degree tucked Ballute	0.780	-0.100(4)(5) -0.120(6)(4)	1.81(5) 1.72(6)	0.90(5) 0.95(6)	N337A15	Dacron	120	100	4.80	1.78	----	0.61
d	Hemisphere	0.900	-0.250(3) -0.100(4)(5) -0.120(6)(4)	---	1.81(5) 1.72(6)	N337A15	Dacron	120	100	3.45	0.89	-0.195	----
e	75-degree cone Balloon	0.870	-0.250(3)	---	0.72(5) 0.78(6)	N337A15	Dacron	120	100	3.66	----	----	----
f	80-degree Air-mat cone	0.760	-0.030(5) -0.103(6)	---	0.90(5) 0.95(6)	Air-mat (see Table 2)				0.44	----	----	----

NOTES

(1) Expected at M = 2.5; lower values at M > 2.5
(2) Minimum tensile strength in pounds per inch.
(3) With burble fence.

(4) Without burble fence.
(5) At M = 5.0
(6) At M = 2.5.

During tunnel operation the maximum dynamic pressure is expected to be 150 psf. Reference 13 requires that the models be designed with a factor of safety of four based on the yield strength. Because fabrics do not have a yield strength in the same sense as metals, the quick-break strength is used in determining the margins for the fabric components.

b. **Analysis of Models a and b.** Models a and b are identical in design, except that Model b does not have a burble fence and different fabrics are used in the two models (see Figure 40). These models are equipped with meridian straps which run the full length of the Ballute. At the nose the straps are assumed to carry the entire drag load. The drag is given by

$$D = C_D \rho \pi R^2$$

$$D = (0.78) (150/144) \pi (16) = 39.8 \text{ lb.}$$

The load in each of the eight straps at the nose is equal to

$$\frac{D}{8 \cos 40^\circ} = 6.5 \text{ lb.}$$

On Model a, each strap is estimated to have a strength of about 60 pounds, giving a margin of safety of 1.31. On Model b, the estimated strap strength is 90 pounds, giving a margin of safety of 2.46.

The contour shape of the rear of the Ballute has been designed with the value of $k = nT_m / P\pi R^2 = 1/2$ (Reference 14, Figure 3A) where the pressure, P, is estimated to be 2.06 q. The strap load on the rear is then equal to

$$T_m = \frac{P\pi R^2}{2n} = \frac{(2.06) (150/144) (\pi) (16)}{(16)} = 6.75 \text{ lb.}$$

The strap margins of safety are 1.22 and 2.33 for Models a and b respectively.

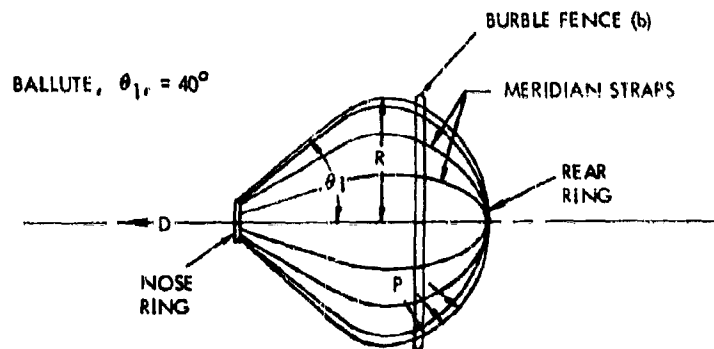


Figure 40. Second-Series Wind Tunnel Models a and b

The fabric stress for this contour is equal to $PR/4$ in any direction over the rear half of the Ballute, which gives a stress for this condition of

$$\frac{PR}{4} = (2.06) (150/144) = 2.14 \text{ lb/in.}$$

The fabric strength for Model a is 100 lb/in., giving a margin of safety of 10.7. For Model b, the strength is 140 lb/in., and the margin of safety is 15.3. On the Ballute front half, the largest stress occurs at the base of the conical surface at a radius of 3.38 inches. The hoop stress in the fabric is equal to $P(3.38)/\cos 40^\circ$ where P is the pressure difference across the front half of the Ballute, which is estimated to be $0.91q$. The fabric stress is therefore

$$\frac{(0.91) (150/144) (3.38)}{0.766} = 4.19 \text{ lb/in.}$$

The margin of safety for Model a is 4.97, and for Model b the margin is 7.35.

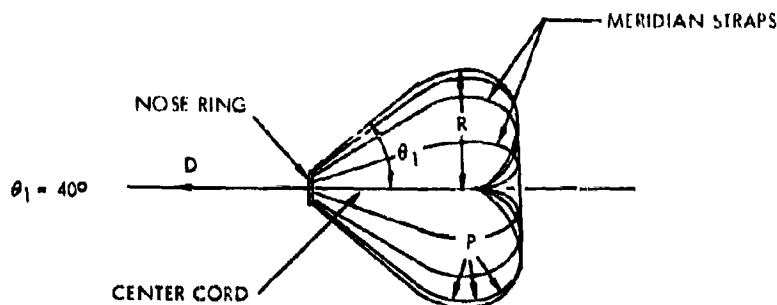


Figure 41. Second-Series Wind Tunnel Model c

c. Analysis of Model c (Figure 41). The rear surface of the Ballute is designed so that the strap load (for all eight straps together) is equal to $0.4 P \pi R^2$ (Reference 14, Figure 4A); the pressure pattern is the same as for Models a and b. The load in each strap is therefore

$$T_m = \frac{0.4 P \pi R^2}{8} = \frac{(0.4) (2.06) (150/144) (\pi) (16)}{8} = 5.40 \text{ lb.}$$

The margin of safety is 1.78. The load in the center cord is $0.3Pr^2 = 31.0$ pounds. The center cord is composed of two strands of MIL-C-5040A (ASG), Type I cord with a strength of 100 pounds/strand (Reference 15). The margin of safety is 0.61.

At the nose the portion of the load carried by the meridian straps is equal to the drag minus the center cable load, or

$$39.8 - 31 = 8.8 \text{ lb.}$$

The load in each strap is $(8.8)/(8 \cos 40^\circ) = 144$ pounds, and the margin of safety is 9.4.

The radius at the base of the conical nose portion is 3.6 inches. The hoop stress at this point is

$$\frac{3.6P}{\cos 40^\circ} = \frac{(3.6)(0.91)(150/144)}{0.766} = 4.45 \text{ lb/in.}$$

The margin of safety is $100/(4.45)(4) - 1 = 4.6$. The rear surface is designed for a fabric stress of $0.15 PR = (0.15)(150/144)(2.06)(4) = 1.29 \text{ lb/in.}$ The margin of safety is larger than at the front.

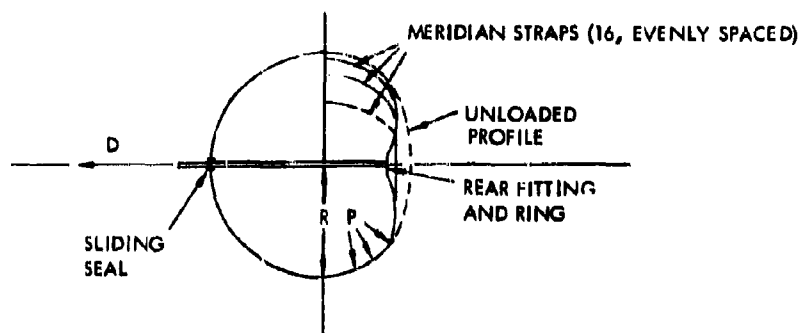


Figure 42. Second-Series Wind Tunnel Model d

d. Analysis of Model d. The hemisphere model (Figure 42) is a closed pressure vessel with a hemispherical nose and a rear surface from which the drag load is transmitted to the main cable. The rear surface is tailored to a profile shape which produces zero hoop stress; all the pressure load is carried by the meridional elements (Reference 14, Figure 6A). In order for such a shape to be stable under pressure, there must be an infinite number of meridional elements. If there is not an infinite number of meridional elements, there must be a finite radius of curvature in the fabric between the meridional elements, producing a fabric stress in both directions. The tailored shape is therefore unstable under pressure, and the meridional cross section tends to become more circular than the tailored shape. In this case there are 16 meridional straps made of material much stiffer than the gore fabric. The equilibrium shape is therefore slightly different from the tailored shape, resulting in a small fabric stress (smaller than in the spherical nose section) and a meridian strap load smaller than the theoretical value. It is therefore conservative to design the straps with the assumption that they carry all the pressure stress and to choose the fabric on the basis of the stresses in the spherical nose.

The drag is given by

$$D = C_D q \pi R^2 = (0.9)(150/144)(\pi)(16) = 47.0 \text{ lb.}$$

The internal pressure is arbitrarily chosen such that the quantity $D/PrR^2 = 1/3$. This gives $C_D q/P = 1/3$, or using $C_D = 0.9$, $P = 2.7$ and $q = 2.81$ psi. The maximum fabric stress is $PR/2 = 5.62$ lb/in., giving a margin of safety of $100/(5.62) (4) - 1 = 3.45$. The load in each strap is $PrR^2/16 = 2.81\pi = 8.85$ pounds. The strength of each strap is 60 pounds, giving a margin of safety of $60/(8.85) (4) - 1 = 0.69$.

On page 37 the rear ring was found to have a tensile stress of 14,800 psi with a strap load of 11.1 pounds. As the ring in this model is identical with the previous one, the stress can be obtained merely by multiplying by the ratio of the loads:

$$(8.85/11.1) (14,800) = 11,800 \text{ psi.}$$

The margin of safety is $38,000/(11,800) (4) - 1 = -0.195$. Although the margin is negative, the factor of safety is still greater than three (6.35 versus the estimated ultimate strength of 75,000 psi), and the strength is therefore considered adequate.

e. Analysis of Model e. The cone balloon is also a closed pressure vessel, consisting of a conical nose section tangent to a spherical aft section (see Figure 43). The model is seamed together from bias-cut gores with bias tapes. At the nose the fabric is clamped to a metal nose cone, to which the main cable is attached.

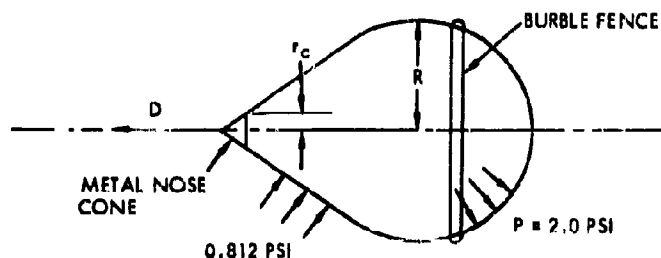


Figure 43. Second-Series Wind Tunnel Model e

The meridian stress in the fabric at the nose is obtained by summing forces on the nose cone:

$$D = 2\pi r f_1 \cos 35^\circ$$

$$f_1 = \frac{D}{2\pi r \cos 35^\circ} = \frac{(0.87) (150/144) \pi (16)}{2\pi (0.83) (0.819)} = 10.7 \text{ lb/in.}$$

where r is the radius of the nose cone. At the nose the seam tapes cover the full circumference of the balloon. The total fabric strength is then $(2 \times 50) + 100 = 200$ lb/in. The margin of safety is $200/(10.7) (4) - 1 = 3.66$.

The highest pressure on the front of the balloon is estimated to be $0.78q = 0.812$ psi. An internal pressure of 2 psi should be sufficient to maintain the shape of the balloon. The highest hoop stress occurs at the base of the conical nose section, at a radius of $R \cos 35$ degrees. The stress is

$$\frac{P(R \cos 35^\circ)}{\cos 35^\circ} = 8 \text{ lb/in.}, \text{ giving a margin of } 100/(8) (4) - 1 = 2.13.$$

The fabric stress in the spherical part is $PR/2 = 4$ lb/in., which is less than the stress in the nose section.

f. Analysis of Model f (Figure 44). The Airmat cone was analyzed in the first series of tests for similar loading conditions. In that analysis the maximum stress was found to be 6.6 lb/in. for the 80-degree cone, giving a margin of safety of $38/(6.6)(4) - 1 = 0.44$.

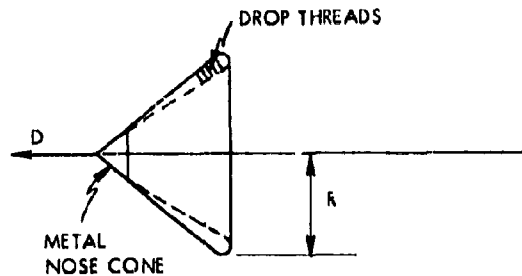


Figure 44. Second-Series Wind Tunnel Model f

3. Arnold Tests

a. General. The analysis included three 10-inch-diameter wind tunnel models and the model support sting. The three models included one inflatable model made of coated metal fabric, one rigid model designed for pressure measurements, and one rigid model designed for temperature measurements. All three models were the 80-degree plain Ballute configuration and were analyzed for the following critical wind tunnel conditions:

Mach number	= 10.25
Dynamic pressure	= 2.24 psi = q
Drag coefficient	= 0.7 = C_D
Internal pressure coefficient	= 1.85 = C_{Pi}
Rear pressure coefficient	= 0 = C_{Pr}

The fabric gores of the inflatable model were bias-cut, seamed along the meridians of the Ballute, and equipped with meridian cables which run the full length and were gathered at the front and rear by metal rings.

Various types of loads to which the models were subjected in supersonic operation are discussed in the second series of Langley tests.

During tunnel operation the drag is given by the equation

$$D = C_D q \pi R^2,$$

and the pressure at any point on the drag body is given by

$$P = C_p q.$$

The margins of safety (Table 6) are defined as

$$MS = \frac{\text{allowable stress}}{\text{limit stress}} - 1 \text{ where allowable stress} = \frac{\text{ultimate stress}}{FS}.$$

Reference 16, page 712, prescribes a factor of safety of 5 based on the ultimate strength or 2 based on the yield, whichever is more critical. In all cases herein the ultimate strength condition governs, except where otherwise stated.

Table 6. Minimum Margins of Safety (Based on Ultimate Loads)

DESCRIPTION OF STRUCTURAL COMPONENTS	MARGIN OF SAFETY
Metal Cloth Drag Model	
Meridian Cables	-0.265*
Main Cable	-0.38*
Fabric	0.15
Nose Piece	0.00
Rigid Temperature Model	
Shell	Large
Screws	0.16
Rigid Pressure Model	
Mounting Sleeve	0.94
Rear Wall	0.22
Model Support Sting	
Strain Link	0.24
Side Walls	0.13**

*Satisfactory to AEDC personnel.
 **Refer to 3F3a for discussion of yield margin.

b. Analysis of Metal Cloth Drag Model. The drag on the model (Figure 45) under the critical wind tunnel conditions is

$$D = C_D q \pi R^2 = (0.7) (2.24) (26\pi) = 123 \text{ lb.}$$

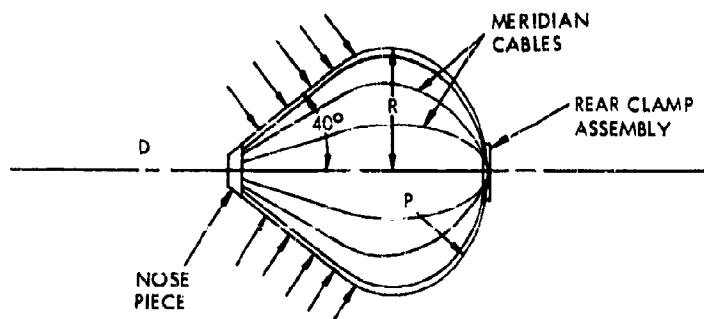


Figure 45. Metal Cloth Drag Model

If there are eight meridian cables, the load in each one is

$$T_m = \frac{D}{8 \cos 40^\circ} = 20.1 \text{ lb.}$$

at the nose of the Ballute. On the rear half the cable loads and fabric stresses are determined by the pressure difference, P , and the profile shape. In this case the Ballute is designed with a rear profile shape, which gives a total cable load equal to $0.5 P \pi R^2$ and a fabric stress of $PR/4$. (Derivation of the profile shape is given in Reference 14.) The pressure, P , is $1.85 q = 4.15$ psi during steady-state operation. The load in each cable is then

$$\frac{(0.5)(4.15)(25\pi)}{8} = 20.3 \text{ pounds in the rear half of the Ballute, and the fabric stress is}$$

$$\frac{(4.15)(5)}{4} = 5.19 \text{ lb/in.}$$

The fabric is estimated from tests run at GAC to have a strength of 30 lb/in. at 1400°F. The margin of safety is

$$\frac{30}{(5)(5.19)} - 1 = 0.15.$$

Tensile tests have also been run on the meridian cables at room temperature, yielding a value of 102 pounds. The meridian cable strength is estimated to be 74.5 pounds at 1400°F, and the main cable strength is 670 pounds. The margins of safety are -0.265* and 0.09 respectively.

In the wind tunnel the Ballute was to have been deployed a distance of 4 inches behind the payload in free fall. From there the actuator was used to move the Ballute to a total distance of 12 inches. During deployment it is assumed that the model does not have time to inflate. The drag area is therefore equal to the area of the three-inch-diameter disc on the rear of the Ballute. The drag is equal to

$$D = (1)(2.24)\pi/4(3)^2 = 15.8 \text{ lb.}$$

assuming a drag coefficient of 1. The energy applied to the Ballute is then $(15.8)(4) = 63.2$ in-lb. The main cable must absorb this energy by stretching under the snatch load that occurs when the cable is fully payed out. The main cable is composed of 49 strands of 0.0104-inch-diameter Rend 41 wire. The cross section area is $(49)(\pi/4)(0.0104)^2 = 41.6 \times 10^{-4} \text{ in.}^2$. The modulus of elasticity of this cable is assumed to be similar to that of carbon steel cable (Reference 11, page 241). A value of 14,000,000 psi is used. Using a total cable length of 82 inches, the elongation of the cable under load, P , is

$$\Delta L = \frac{P(82)}{(14 \times 10^6)(41.6 \times 10^{-4})} = 1.41 \times 10^{-3} P.$$

The strain energy is equal to $P\Delta L/2 = 0.705 \times 10^{-3} P^2$. This energy is equated to the Ballute kinetic energy:

$$0.705 \times 10^{-3} P^2 = 63.2$$

or

$$P = 300 \text{ lb.}$$

The room temperature strength of this cable is estimated to be 320 pounds, giving a margin of safety of -0.38.*

*Although a negative margin is obtained, the safety factor is greater than 3, and the strength is felt to be adequate by AEDC personnel since a possible failure of these lightweight models would not be detrimental to the operation of the tunnel.

At the rear of the Ballute the fabric is clamped between two metal rings by eight No. 4 screws. The root area of each screw is 0.0085 in.² (Reference 17, page 165), giving a total area of 0.068 in.². The screws are Type 316 stainless steel, which has a room temperature strength of 85,000 psi tension. If these screws are tightened to only 10,000 psi, they exert a total load of 520 pounds. Assuming a coefficient of friction of 0.3, the radial fabric load required to cause slippage is $(520)(2)(0.3) = 312$ pounds. The fabric stress times the circumference at the clamp is $(3.42 \text{ lb/in.})(2.375 \text{ in.}) = 25.5$ pounds. There are large margins of safety on both the screw stress and the clamp friction.

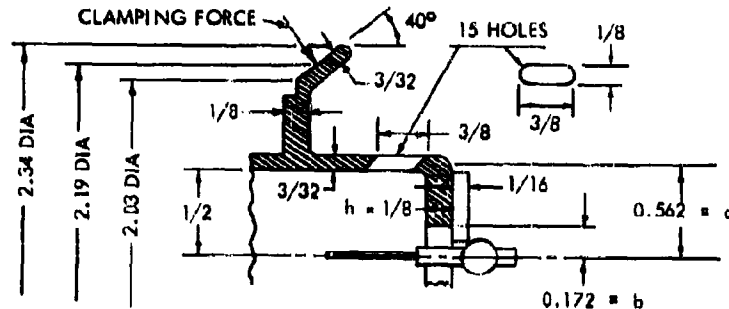


Figure 46. Cross Section of Nose Fitting

Figure 46 shows part of the cross section of the nose fitting. The load is applied through the ball on the main cable to the rear of the nose fitting. The rear face of the nose fitting can be conservatively analyzed as a circular plate simply supported at the outer edge and loaded by shear around the center hole. This is case 1, page 62, of Reference 18, which gives a table of values of the constant k for use in the equation

$$\sigma_{\max} = \frac{kq(a)^2}{h^2} \text{ (Reference 18)}$$

where σ_{\max} is the maximum bending stress, q the shear per unit length, a the outer radius, and h the plate thickness. The inner radius is defined as b . For this case $a = 0.562$ inch, $b = 0.172$ inch, $h = 0.125$ inch, and k is estimated to be 1.95. Using the drag of 123 pounds, (Reference 18)

$$q = \frac{123}{2\pi b} = 114.0 \text{ lb/in.}$$

The maximum stress is then

$$\sigma_{\max} = \frac{(1.95)(114)(0.562)^2}{(0.125)^2} = 4500 \text{ psi. (Reference 18)}$$

The nose piece is made of Type 321 stainless steel, with a tensile strength of 29,000 psi at 1400°F. (Reference 19, page 73, 700°F - 1200°F part), the margin of safety is 0.28.

The outer flange of the nose piece is used to clamp the fabric in place. The fabric stress was previously found to be 5.19 lb/in. At the outer diameter of the flange, this gives a total fabric load in the meridian direction of $(5.19)(2.34)\pi = 38.2$ pounds. Assuming a coefficient of friction of 0.3, the required normal force to prevent slippage is $38.2/(0.3)(2) = 63.5$ lb.

Using a factor of 2 on the normal force, the actual load is 127 pounds. For purposes of analysis the flange load is assumed to be resisted entirely by bending of the necked-down portion, as though the flange were a series of radial strips. The resultant of the flange load acts at approximately the diameter

$$\frac{2.03 + 2.34}{2} = 2.19 \text{ in.}, \text{ and the load per unit length is}$$

$$\frac{127}{2.19\pi} = 18.45 \text{ lb/in. The moment arm of the resultant about the necked-down section is}$$

$$\frac{2.19 - 2.03}{2 \sin 40^\circ} + 0.0804 = 0.204 \text{ inch, and the bending moment is } (18.45) (.204) = 3.77 \text{ in.-lb/in. The section modulus per unit width is}$$

$$\frac{1}{c} = \frac{1}{(6)(16)^2} = \frac{1}{1536} \text{ in.}^3$$

at the necked-down section. The bending stress is $(1536)(3.77) = 5780 \text{ psi}$, giving a margin of safety of

$$\frac{29,000}{(5)(5780)} - 1 = 0.00.$$

To allow for inflation of the Ballute, 15 equally spaced holes are cut in the cylindrical section of the nose piece. The webs between the holes then act as fixed ended columns through which the drag load is transmitted. The web cross section is shown in Figure 47.

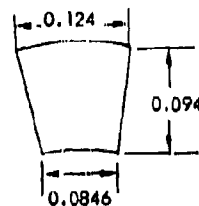


Figure 47. Web Cross Section

The cross section area is approximately

$$(0.094) \left(\frac{0.0846 + 0.124}{2} \right) = 0.0098 \text{ in.}^2, \text{ and the compressive stress is}$$

$$\frac{123}{(15)(0.0098)} = 840 \text{ psi.}$$

The cross section properties can be conservatively obtained by neglecting the taper and treating the webs as though they were rectangular in section, 0.0846×0.094 . The minimum moment of inertia is

$$\frac{(0.094)(0.0846)^3}{12} = 4.74 \times 10^{-8} \text{ in.}^4.$$

The load on the rectangular section is

$$(840)(0.094)(0.0846) = 6.70 \text{ lb.}$$

The equation for the critical load on a fixed-ended column (Reference 20) is

$$P_{cr} = \frac{4\pi^2 EI}{2}$$

Because the ends of the column are free to displace laterally, however, the length, l , must be twice the actual length of 0.375 inch. The critical load thus obtained is

$$P_{cr} = \frac{4\pi^2 (30 \times 10^6) (4.74 \times 10^{-6})}{(0.75)^2} = 9,980 \text{ lb.}$$

The margin of safety in buckling is very large.

c. Analysis of Rigid Temperature Model. The temperature measurement model (Figure 48) is fabricated from 0.050-inch stainless steel sheet and is supported at each end of the model by a shaft passing through the center. At the front support the cross section profile is at 40 degrees to the center line, whereas at the rear the profile is nearly perpendicular to the center line. Because the front support is much stiffer under axial loads than the rear, the entire drag load is assumed to be carried by the front. The radius at the welded joint between the skin and the nose plug is one inch. Using the same value of drag (123 pounds) as for the metal cloth drag model, the tensile stress is

$$S = \frac{123}{(2\pi) (0.050) \cos 40^\circ} = 511 \text{ psi.}$$

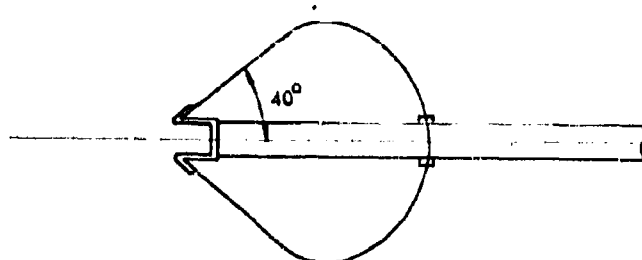


Figure 48. Rigid Temperature Model

At 1400°F the strength of 321 stainless steel is 29,000 psi. (Reference 19, page 73, 700° - 1200°F part). The margin of safety is large.

The maximum internal pressure is estimated to be 4.15 psi. Again neglecting the load picked up at the rear support, the entire pressure load is assumed to be carried by 8 No. 4 Type 316 stainless steel screws holding the front and rear halves together. The total pressure load is

$$(4.15) (25\pi) = 326 \text{ lb.}$$

The shear load in each screw is $326/8 = 40.8$ pounds, and the shear area is 0.0085 in.² (Reference 17, page 165). The shear stress is $40.8/0.0085 = 4800$ psi. The tensile strength of each screw is 61,000 psi at 1200°F (Reference 19, page 61, 700°F to 1200°F section). Estimating the shear strength to be 0.6 of the tensile strength, the margin of safety is 0.16.

d. Analysis of Rigid Pressure Model. The pressure measurement model (Figure 49) is also sting-mounted, but is supported entirely at the rear. A sleeve is welded to the back half of the model, allowing it to thread into the sting. For purposes of determining the weight, the model can

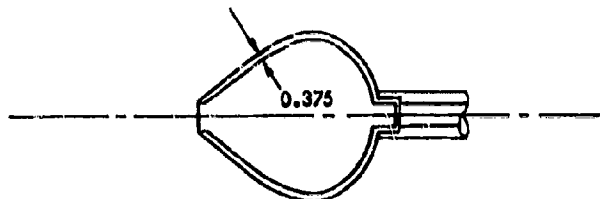
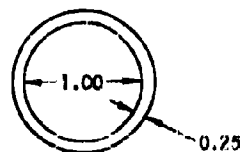


Figure 49. Rigid Pressure Model

be approximated by a sphere. The area is $4\pi R^2 = 314 \text{ in.}^2$, and the volume is $(314) (0.375) = 117.8 \text{ in.}^3$. The weight is approximately $(117.8) (0.285 \text{ lb/in.}^3) = 33.6 \text{ pounds}$. When positioning the model in the tunnel, the sting assembly can receive a maximum of 2g's loading vertically. Assuming the cg is located 5 inches in front of the support joint, the moment on the welded sleeve is $(33.6) (2) (5) = 336 \text{ in.-lb}$. The weakest cross section is shown in the following sketch:



The moment of inertia of this cross section is

$$I = \frac{\pi [(5/8)^4 - (1/2)^4]}{4} = 0.0708 \text{ in.}^4$$

The bending stress is

$$\frac{(336) (5/8)}{0.0708} = 2980 \text{ psi.}$$

The sleeve material is Type 321 stainless steel, with a tensile strength of 29,000 psi at 1400°F (Reference 19, page 73, 700° to 1200°F part). The margin of safety is 0.94.

The bending moment of 336 in.-lb must also be carried by the rear wall of the Ballute model. It can be conservatively assumed that the moment is carried only by a one-inch-wide strip of the rear wall, as shown in Figure 50.

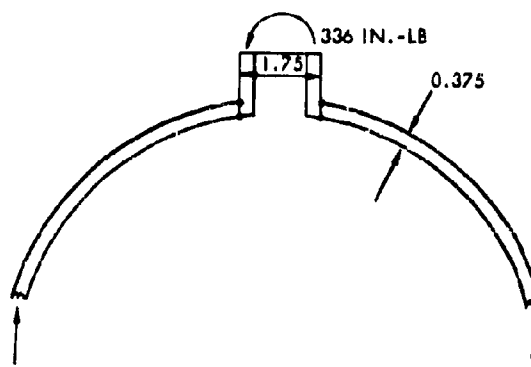
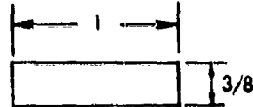


Figure 50. Bending Moment at Rear Wall

The maximum moment in the strip is $336/2 = 168$ in.-lb. The strip cross section is shown in the following sketch:



The section modulus is

$$\frac{I}{c} = \frac{(0.375)^2}{6} = 0.0234 \text{ in.}^3,$$

and the bending stress is $168/0.0234 = 7180$ psi. The material is Type 321 stainless steel, with a tensile strength of 44,000 psi at 1200°F (Reference 19, page 73, 700 to 1200°F part). The margin of safety is 0.22.

Under the direct drag load the rear half of the model can be approximated by a flat circular plate with a rigid plug at the center. This is case 8, page 62, Reference 18. $2a/2b = 10/1.75 = 5.72$. k is estimated to be 1.9. The maximum stress is therefore

$$\sigma_{\max} = \frac{kqa^2}{h^2} \text{ where } q = \frac{D}{2\pi a} = \frac{123}{10\pi} = 3.92 \text{ lb/in.}$$

$$\sigma_{\max} = \frac{(1.9)(3.92)(25)}{(0.375)^2} = 1320 \text{ psi.}$$

The 2-g loading condition analyzed previously gave a bending stress of 7180 psi. Under 1-g the stress is $7180/2 = 3590$ psi. Adding this to the stress from the drag load, the total is 4910 psi, which is less than the stress under the 2-g condition.

The front and rear halves of the pressure model are held together by six cap screws angled at 35 degrees to the center line. The screws are 1/4-20-NC and are made of Type 316 stainless steel.

The total pressure load at the equator is approximately

$$(4.15)(4.64)^2\pi = 278 \text{ lb.}$$

Subtracting the drag, the total load carried by the screws is $278 - 123 = 155$ pounds. The load in each one is then 19.4 pounds. This load has a tension component of $19.4 \cos 35^\circ = 15.9$ pounds and a shear component of $19.4 \sin 35^\circ = 11.1$ pounds. The stress area of this screw is 0.0317 in.² (Reference 17, page 165), giving a tensile stress of 501 psi and a shear stress of 351 psi. The margin of safety is very large.

e. Analysis of Model Support Sting. Figure 51 shows the model support sting with the weights and dimensions of the various sections. The 2 g vertical loading condition produces bending moments in the sting due to the weights and moment arms shown. If it is assumed that only the side walls are effective in bending at the joints, the critical sections are the two joints at the rear of the sting. The section modulus of the two sidewalls together is

$$\frac{I}{c} = \frac{(2)(0.109)(8)^2}{6} = 1.309 \text{ in.}^4$$

The maximum bending moment is $(2)(6+5)(61.5) + (2)(80)(30-3/4) = 6260$ in.-lb, and the bending stress is $6260/1.309 = 4790$ psi. The material is Type 321 stainless steel, with a tensile strength of 78,000 psi at 200°F. The margin of safety is large.

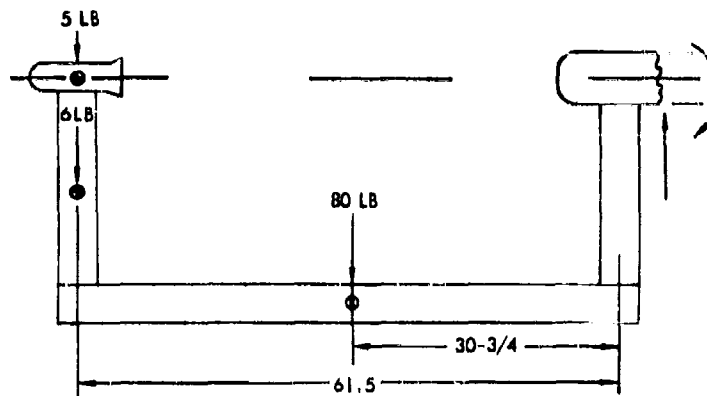


Figure 51. Model Support Sting

During tunnel operations it was anticipated that the model could be deflected as much as 15 degrees to the side, applying a side thrust to the sting. This side component is

$$123 \sin 15^\circ = 31.8 \text{ lb}$$

and is applied approximately 3 inches behind the shear center of the airfoil strut. The torque on this strut is $(31.8)(3) = 95.4 \text{ in-lb}$. The cross section dimensions are shown in Figure 52.

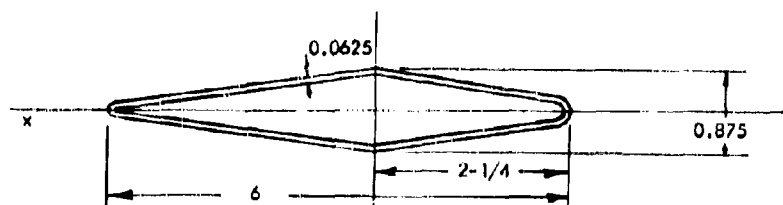


Figure 52. Strut Cross Section Dimensions

The enclosed area is approximately $(3/8)(5-7/8) = 2.2 \text{ in.}^2$, and the torsion shear stress is

$$\frac{95.4}{(2)(2.2)(0.063)} = 345 \text{ psi. The margin of safety is very large.}$$

The bending moment on the airfoil section from the side thrust is $(31.8)(18) = 575 \text{ in.-lb}$. The moment of inertia about the x-x axis can be conservatively estimated by assuming all the material is concentrated at a point midway between the axis of symmetry and the outer fiber. Thus $I_{x-x} = (2)(6)(1/16)(0.218)^2 = 0.0358 \text{ in.}^4$, and the bending stress is

$$S = \frac{(575)(0.438)}{0.0358} = 7080 \text{ psi.}$$

The margin of safety is $\frac{78,000}{(5)(7080)} - 1 = 1.21$.

The support sting is equipped with a pressurized system of passages through which water flows for cooling during tunnel operation. The highest pressure stresses occur in the six-inch side wall of the lower beam, which has the largest span of unsupported wall. The side wall is equipped with a row of 1/4-inch-diameter rods spaced evenly between the edges of the wall. The rods are 3-1/2 inches apart. The side wall can be conservatively analyzed as a large sheet supported by the rods spaced as shown in Figure 53.

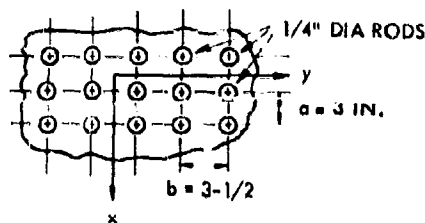


Figure 53. Rod Spacing

The wall is loaded by a uniform pressure of 25 psi as shown in Figure 54. The problem is discussed in detail in Reference 18, page 245. In this case $b/a = (3-1/2)/(3) = 1.168$.

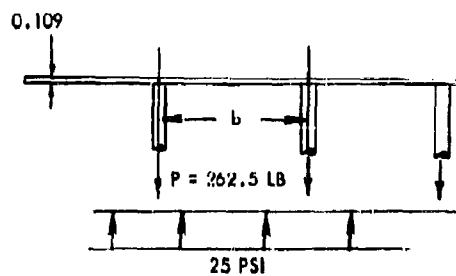


Figure 54. Wall Loading

The table on page 249 of Reference 18 gives $\beta = 0.0226$, $\beta_1 = 0.0359$. The moment, M_y , at the center of the panel is the larger. Its value is

$$M_y = (0.0359) (25 \text{ psi}) (3-1/2)^2 = 11 \text{ in.} \cdot \text{lb/in.},$$

and the bending stress is $(8) (11) / (0.109)^2 = 5500 \text{ psi}$. Using the conservative value of the ultimate strength of 78,000 psi at 200°, the margin of safety is large.

At the support points the moments M_x and M_y are given by Reference 18, Equations (157), page 149. M_x is the larger. The values substituted are $q = 25 \text{ psi}$, $a = 3$, $b = 3-1/2$, $c = 1/8$, $\gamma_1 = 0.384$, $\gamma_2 = 0.118$, $\nu = 0.3$, $\xi = a/2$. Using these values,

$$M_x = 66 \text{ in.} \cdot \text{lb/in.}$$

A first approximation to a limit design analysis indicates that the maximum ultimate moment (5.0 times the applied moment) would be $5.0 (66 + 11) (1/2) = 192.5 \text{ in.} \cdot \text{lb/in.}$ The modulus of rupture of annealed Type 321 stainless steel at 200°F is at least $78,000 \times 1.4 = 109,000 \text{ psi}$. (Since the

rectangular section shape-factor for a ductile material is close to 1.5.) The corresponding "stress" is

$$\frac{192.5 \times 6}{(0.109)^2} = 96,300 \text{ psi,}$$

which gives a margin of safety of

$$\frac{109000}{96300} - 1 = 0.13.$$

Yield loads would cause only local yielding at the posts - no general yielding.

The strain link assembly, located in the lower arm of the strut, receives twice the load that is produced by the drag device, or $(2)(123) = 246$ pounds. The strain link itself is a strip of Type 321 stainless steel 1/2-inch wide by 0.036-inch thick. The tensile stress is

$$\frac{246}{(0.5)(0.036)} = 13,680 \text{ psi.}$$

The tensile strength of Type 321 stainless steel is 85,000 psi at room temperature (Reference 19, page 73, 700 to 1200°F part), giving a margin of safety of 0.24.

The strain link is welded to the end plate, which is attached to the side plates by means of four No. 8-32 flat-head screws. The end plate can be conservatively analyzed as a fixed end beam with dimensions shown in Figure 55.

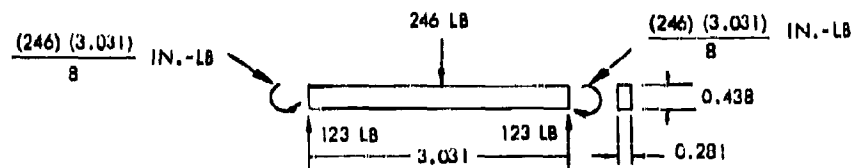


Figure 55. Radial Loads at Rear Fitting

The section modulus is

$$\frac{I}{c} = \frac{(0.281)(0.438)^2}{6} = 0.00895 \text{ in.}^3.$$

The maximum bending moment is

$$\left(\frac{246}{2}\right)\left(\frac{3.031}{2}\right) = 93.1 \text{ in. -lb. The bending stress is}$$

$$\frac{931}{0.00895} = 10,400 \text{ psi, and the margin of safety is 0.63.}$$

The four No. 8-32 screws have a stress area of 0.0139 in.² each. The screws are in double shear, giving a total area of $(8)(0.0139) = 0.111 \text{ in.}^2$. The shear stress is $163/0.111 = 1,470 \text{ psi}$, and the margin of safety is large.

The pulley pin is a 3/16-diameter slotted spring steel pin (MS 16562) having a strength in double shear of 4400 pounds. Its margin of safety is large.

G. SUBSONIC WIND TUNNEL TESTS

Wind tunnel tests of the most promising drag models were conducted in Goodyear Aircraft's subsonic wind tunnel prior to the testing of the identical models in the NASA Langley Unitary Supersonic wind tunnel. The purpose of these subsonic tests were as follows:

- (1) Obtain drag coefficient data at $M \approx 0.2$.
- (2) Observe towed stability.
- (3) Proof load wind tunnel models.

Figure 56 shows a model in GAC's subsonic tunnel. Data obtained is given in Table 7.

Table 7. Subsonic Performance Data

DATE	TYPE OF MODEL	DYNAMIC PRESSURE (lb/ft ²)	C _D	PERFORMANCE
Jan 1961	75° cone balloon with 6.3% fence	73	0.57 - 0.61	Coning $\approx 50^\circ$; stable.
Jan 1961	75° Ballute with 6.3% fence (open-front inlet)	73	0.56	Coning $\approx 50^\circ$; stable.
May 1961	100° Ballute with 6.25% fence (open-front inlet)	60	0.70 - 0.73	Coning $\approx 100^\circ$.
May 1961	Sphere with 6.25% fence	60	0.59 - 0.62	Coning less than 40° ; stable.
May 1961	80° Airmat cone	60	0.57 - 0.70	No coning; stable.
May 1961	100° Airmat cone	60	0.66 - 0.75	Coning less than 20° ; stable.
May 1961	80° Ballute with 6.25% fence (open front inlet)	60	0.56	Coning less than 60° ; stable.
May 1961	Torus and curtain	60	0.65	Coning = 18° .



Figure 56. Seventy-Five Degree Cone Balloon with 6.3-Percent Fence in GAC Subsonic Tunnel

SECTION 4

SUPERSONIC WIND TUNNEL TESTS AT NASA LANGLEY RESEARCH CENTER

A. GENERAL

The primary objective of these tests was to obtain drag and stability characteristics of the various towed configurations throughout the supersonic speed range.

The tests were conducted in the Langley Unitary Plan wind tunnel, which is a variable-pressure, return-flow tunnel. The tunnel has two test sections 4 feet by 4 feet square and approximately 7 feet long. The nozzles leading to the test sections are asymmetric sliding-block-type nozzles, and the Mach number may be varied continuously through a range from 1.57 to 2.87 in one test section and from 2.30 to 4.65 in the other. Reference 13 gives further details of the tunnel. Spark Schlieren photographs were taken for qualitative flow observations. High-speed Schlieren movies were taken to observe both flow and dynamic stability of the towed models. Drag coefficient data were recorded at various distances between the payload and towed drag body. The estimated accuracy of the measured test data is as follows:

C_D	± 0.02
L (towed line length - inches)	± 0.50
M_∞ (1.57 to 2.87)	± 0.02
M_∞ (2.30 to 4.65)	± 0.05

A typical model installation consisted of a payload and trailing towed drag body assembly as shown in Figure 57. The support system included two thin struts spanning the tunnel in the horizontal plane and holding the payload in the center of the tunnel (see Figure 58). Each towed drag model was attached to the payload with a 0.10-inch stainless steel cable from a drum mounted on a strain gage balance inside the payload. The balance with the motor-driven drum comprised a convenient system for testing towed decelerators since the distance between payload and drag model could be varied during the test run. Figures 59 through 62 show four models in the wind tunnel.

B. TEST PROGRAM

Figures 63 and 64 show some of the models used. Figure 65 shows detailed sketches of typical Ballute models. Table 8 lists the models tested, and Table 9 is a complete log of all of the supersonic tests.

Table 8. Supersonic Wind Tunnel Test Models

MODEL	RUN NO.
80-degree Ballute with 8.25% fence (open front inlet)	1, 14
75-degree Ballute with 8.30% fence (open front inlet)	2, 7, 9
80-degree Airmat cone (preinflated)	3, 16, 20, 26, 27, 28
Torus and curtain (flexible curtain, rigid torus)	4
Sphere with 8.25% fence (preinflated)	5, 10, 13, 21, 23, 24, 25
Hemisphere (preinflated)	6
100-degree Airmat cone (preinflated)	8
75-degree cone balloon with 8.3 % fence (preinflated)	11, 22, 29, 30, 31, 32
100-degree Ballute (open front inlet)	12, 17
80-degree tucked Ballute (open front inlet)	15
80-degree Ballute (front inlet with reed valves)	18
80-degree Ballute (front inlet with screen)	19
75-degree Ballute (side inlets with screen)	33, 34, 35, 36
80-degree Ballute (side inlets with screen)	37, 38
80-degree Ballute with 3.9% fence (side inlets with screen)	39, 40, 41, 42

Table 9. Log Sheet of Supersonic Tests

DATE	RUN NO.	MODEL	MACH NO.	DYNAMIC PRESSURE (lb/ft ²)	L/d	PERFORMANCE*
6-19-61	1	80-degree Ballute	1.77	173	2 - 4	Model inflated 50 percent, model rolled.
6-20-61	2	75-degree Ballute	2.66	97.6	---	Model partially inflated; model experienced some coning and flutter; model aft end ruptured.
6-20-61	3	80-degree cone	1.77 - 2.12	152 - 173	1 - 7	Stable generally; no coning; no roll.
6-20-61	4	Torus and curtain	1.62	153	6	High-frequency curtain flutter; model experienced some coning; curtain seam parted.
6-20-61	5	Sphere	2.0	155	---	Stable; model leaked.
6-21-61	6	Hemisphere	1.64 - 2.75	152 - 182	3 - 10	Stable; no coning; no roll.
6-22-61	7	75-degree Ballute	1.77	---	---	Stable; no coning.
6-22-61	8	100-degree cone	2.75	152	---	Unstable; 20-degree coning; tow cable broke.
6-22-61	9	75-degree Ballute	1.77	---	---	Model partially inflated; model experienced some coning and flutter; model aft end ruptured.
6-22-61	10	Sphere	2.75	152	---	Stable.
6-23-61	11	75-degree cone balloon	1.77 - 2.75	152 - 169	2 - 10	Stable.
6-23-61	12	100-degree Ballute	1.77	---	---	Model partially inflated; 20-degree coning.
6-23-61	13	Sphere	1.88 - 2.5	180	---	Stable generally.
6-23-61	14	80-degree Ballute	2.85 - 2.15	109 - 116	---	Model inflated partially; model rolled; model experienced fabric flutter; model aft end ruptured.
6-23-61	15	80-degree tucked Ballute	2.66	102	---	Model inflated; stable (no spinning or coning); model aft end ruptured.
6-27-61	16	80-degree cone	2.75	152	2 - 10	Stable; no coning; no roll.
6-27-61	17	100-degree Ballute	2.66	---	---	Tow cable broke; stopped test.
6-28-61	18	80-degree Ballute with front inlet and reed valves	2.5 - 3.5	150	3 - 8	No coning; high spin rate; model not fully inflated.
9-27-61	19	80-degree Ballute with front screened inlet	2.5 - 3.5	150	4 - 8	No coning; high spin rate; model not fully inflated.
4-16-62	20	80-degree Airmat cone	2.0 - 2.87	150	1 - 13	Stable.
4-17-62	21	Sphere with fence	2.0 - 2.87	150	1 - 12	Stable.
4-18-62	22	75-degree cone balloon	2.0 - 2.87	150	1 - 12	Stable.
6-14-62	23	Sphere with fence	2.5	150	2 - 9	Model rode a little rough in wake; stable; no roll.
6-14-62	24	Sphere with fence	3.5	150	1 - 9	Model stable; no roll.
6-14-62	25	Sphere with fence	3.96	150	1 - 9	At $L/d = 1 - 3$ and $7 - 9$, model stable; at $L/d = 4 - 6$, coning 10-degrees; lost model at $M = 4.65$; cable broke at payload when normal shock went through.
6-14-62	26	80-degree Airmat cone	2.5	150	3 - 12	Model stable; no roll.
6-15-62	27	80-degree Airmat cone	3.5	150	1 - 12	Cone rode rough at $L/d = 1, 2$; smooth ride at $L/d = 3 - 12$.
6-15-62	28	80-degree Airmat cone	4.65	150	1 - 8	Stable; no roll.
6-15-62	29	75-degree cone balloon with fence	2.5	250	1 - 8	Stable; zero roll; zero coning.
6-15-62	30	75-degree cone balloon with fence	3.5	250	1 - 8	Stable.
6-15-62	31	75-degree cone balloon with fence	3.96	250	1 - 8	Stable.
6-15-62	32	75-degree cone balloon with fence	4.65	250	1 - 8	Stable.
6-15-62	33	75-degree Ballute with side inlet	3.96	250	1 - 9	Stable.
6-15-62	34	75-degree Ballute with side inlets	4.65	250	1 - 9	Stable.
6-18-62	35	75-degree Ballute with side inlets	2.50	250	1 - 8	Stable.
6-18-62	36	75-degree Ballute with side inlets	3.5	250	1 - 9	Stable.

*Stable model performance is defined as visual observation of oscillatory coning less than 2 degrees.

Table 9. Log Sheet of Supersonic Tests (Continued)

DATE	RUN NO.	MODEL	MACH NO.	DYNAMIC PRESSURE (lb/ft ²)	L/d	PERFORMANCE *
6-18-62	37	80-degree Ballute with side inlets	2.5	250	7	Inlets misaligned; model rolled.
6-18-62	38	80-degree Ballute with fence and side inlets	2.5	250	-	Model swivel removed; inlets misaligned; model rolled slightly.
6-18-62	39	80-degree Ballute with fence and side inlets	2.5	250	2 - 9	Stable; zero roll; zero coning.
6-18-62	40	80-degree Ballute with fence and side inlets	3.5	250	2 - 9	Stable.
6-18-62	41	80-degree Ballute with fence and side inlets	3.96	250	2 - 9	Stable.
6-18-62	42	80-degree Ballute with fence and side inlets	4.65	250	4 - 9	Stable.

*Stable model performance is defined as visual observation of oscillatory coning less than 2 degrees.

During the series of tests in test section 1, runs 1 through 17 (Mach 1.64 to 2.75), it was evident that most models of the preinflated sphere, hemisphere, and cone models performed in a satisfactory manner. Drag coefficient data were obtained at various Mach numbers and at various L/d ratios (tow-line length divided by payload diameter). Schlieren still photographs and schlieren high-speed (1100 frames per second) movies were taken during the tests (see Figures 66 through 69). These schlieren stills were used to observe the supersonic flow patterns and to check the shape stability of the models under load.

Shape stability was verified by scaling the near optically-perfect schlieren photographs. These closed pressure-vessel models were not pressurized excessively for shape stability. The plan followed during the tests was to provide only enough internal inflating pressure to avoid wrinkling. The 80-degree Airmat cone and the hemisphere nose shapes did not change under load. The 75-degree cone balloon and the sphere did change shapes (see Figures 66 and 67). The apex angle of the cone balloon model was constructed to 75 degrees. Under load however, the apex angle was approximately 60 degrees.

The following results were obtained during this first series of tests of preinflated models:

- (1) Drag values obtained with cones are higher than spheres and hemispheres.
- (2) A towed 80-degree cone performs in a stable manner (little or no coning).
- (3) A towed 100-degree cone is unstable (violent pitching and coning greater than 10 degrees).

The ram-air Ballute models with open front inlets did not perform in a satisfactory manner. Most of these models experienced excessive coning and fabric flutter. Some of these models experienced high spin rates. All models subsequently experienced structural failure at the aft end. It was clear after a review of the high-speed schlieren movies that a pulsating mass flow or buzzing phenomenon existed which caused model shape changes and excessive structural oscillatory loading at a rate of approximately 70 cycles per second.

Prior to the scheduled test section 2 tests (Mach 2.5 to 4.65), a combined "in house" aerodynamic, structural, and design study was conducted. In addition consulting services were utilized. The details of this investigation are presented in Appendix I. Analytical studies and experimental water table tests were conducted. The net result of this investigation was reflected in model modifications as follows:

- (1) Provide a reed valve assembly type front inlet.
- (2) Provide a screened type front inlet.
- (3) Provide side inlets.

The 80-degree Ballute model with screened or reed valve front inlets was the first tested in test section 2 (test runs 18 and 19). The model performed in a stable manner although it did not fully inflate and experienced a high spin rate. A review of the schlieren still photographs and high-speed schlieren movies showed the following:

- (1) The model apex angle was between 63 and 68 degrees.
- (2) The model experienced no mass flow pulsations with the reed inlet.
- (3) The model experienced slight mass flow pulsations with the screened inlet.
- (4) The model experienced no significant shape change.

The final series of tests in test sect 2 (Runs 23 through 42) consisted of three preinflated model types and three ram-air Ballute model types.

All preinflated models performed in a satisfactory manner. The 75-degree Ballute with the 6.3-percent fence and screened inlet and the 80-degree Ballute with the 3.9-percent fence and screened side inlets also performed in a satisfactory manner. Both models remained motionless (no coning, no roll) in their towed positions during the test runs. A review of the high-speed schlieren movies revealed good shape stability and a complete absence of any mass flow pulsations. Internal static pressure readings were taken in the 75-degree Ballute model, utilizing a mercury manometer tube. A pressure transducer was used to measure the internal pressure pulsing magnitude and frequency of the 80-degree Ballute model. The output from the transducer was recorded on a visicorder type oscillograph. There was no measurable pulsing from the oscillograph trace.

C. SUMMARY OF RESULTS.

Figures 70 through 81 show the aerodynamic drag results. Drag coefficients were based on the fully inflated model design diameter of either 7 or 8 inches. The burble fence outside diameters were greater than their respective inflated design diameters. The rated size of a burble fence, for example a 3.9-percent fence, was based on the fence height divided by the model diameter. Note the hysteresis effect of the drag data in Figures 75 through 79. As the decelerator model is removed aft away from the forebody, the abrupt C_D change occurs at a larger L/d than when the decelerator is moved forward toward the forebody. At a small L/d (see Figure 68) the decelerator is in a divergent wake of the forebody with a corresponding low C_D . As the decelerator is moved aft, the divergent wake flow pattern of the forebody suddenly trips and changes to a convergent wake flow pattern normally experienced by a body in a free stream without being influenced by a trailing body. The corresponding higher C_D is obtained since decelerator is aft of this wake. Starting from a large L/d (see Figure 66), the forebody wake flow pattern is convergent. As the decelerator is moved forward, the wake flow pattern change from convergent to divergent is delayed and occurs at a smaller L/d . This tripping of the wake flow pattern at a smaller L/d occurs because of the larger pressure energy requirements to disturb the normal convergent wake pattern. This hysteresis effect is also shown in References 24, 25, and 26. The internal static pressure results taken during test runs 33, 34, 35, and 36 are shown in Figure 62. The results were correlated through the use of two ratios:

$$P_2/P_\infty \quad \text{and} \quad L/d$$

where

- P_2 = the inside static pressure
- P_∞ = the free stream static pressure
- L = the distance from the Ballute to the forebody
- d = the diameter of the forebody.

The magnitude of these ratios can be explained as being due to the presence of a combination of an oblique shock at the tip of the Ballute, and normal shocks at the side inlets.

To verify this explanation, theoretical predictions of the recovery ratios were made utilizing inviscid conical flow theory and taking into account the presence of both types of shocks. And,

as indicated by the graph, the theoretical results were close to, although higher than, the experimental results.

In summary the most significant results of all the supersonic tests are as follows:

- (1) Ballute models with side ram-air inlets do inflate fully and have drag values equivalent to preinflated models.
- (2) Ballute models with side inlets are stable in their towed position (no coning, no roll, no fabric flutter).
- (3) Good ram-air internal pressure readings were taken which will provide useful information for structural design.
- (4) Burble fences increase the drag values.
- (5) Conical-shaped models have higher drag values than spherical or hemispherical.

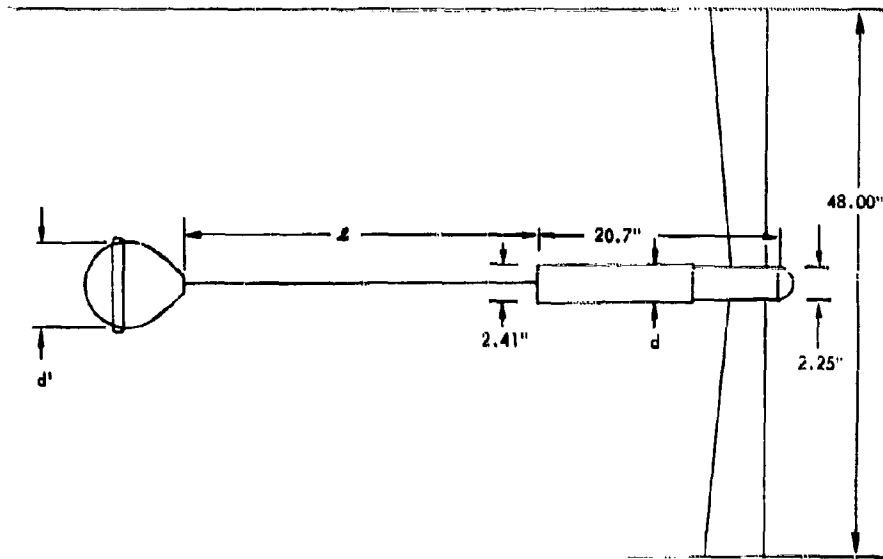


Figure 57. Typical Supersonic Wind Tunnel Installation

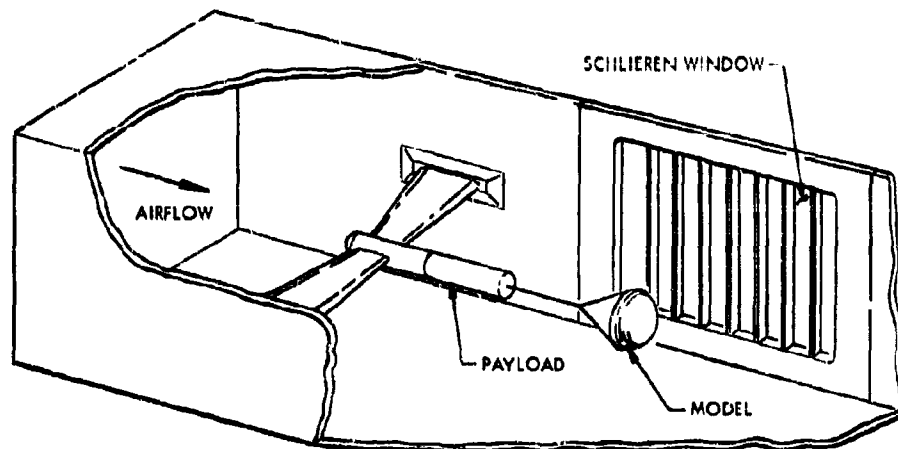


Figure 58. Supersonic Wind Tunnel Support Systems

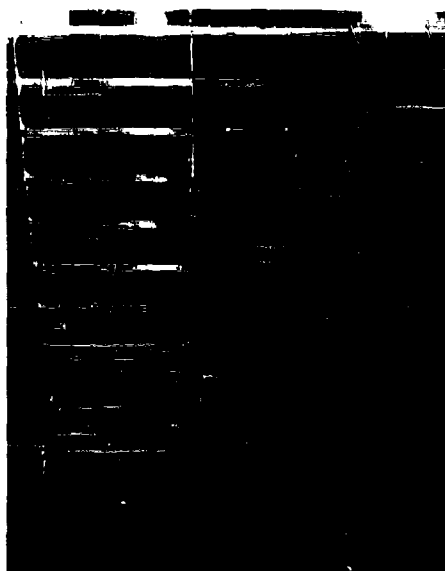


Figure 59. Sphere with 6.2-Percent Fence Trailing Payload in Supersonic Wind Tunnel

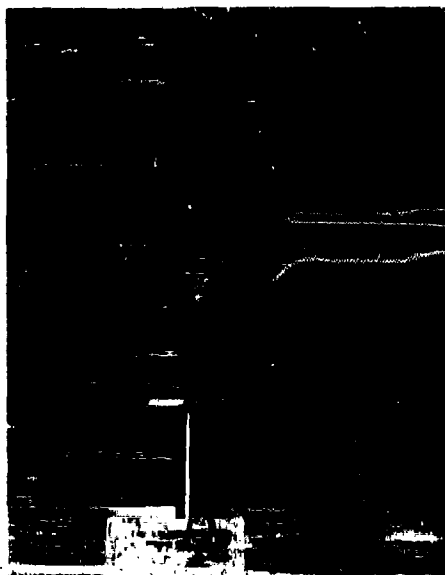


Figure 60. Torus and Curtain Trailing Payload in Supersonic Wind Tunnel

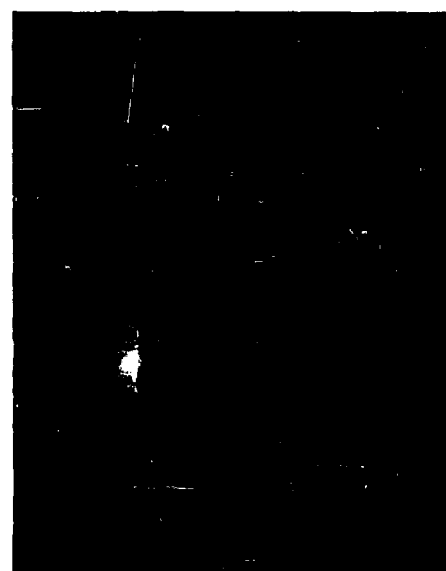


Figure 61. Eighty-Degree Airmat Cone Model Trailing Payload in Supersonic Wind Tunnel

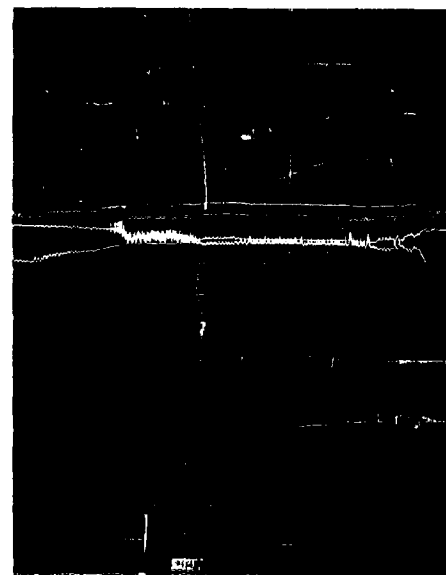


Figure 62. Seventy-Five Degree Cone Balloon with 6.3-Percent Fence Trailing Payload in Supersonic Wind Tunnel

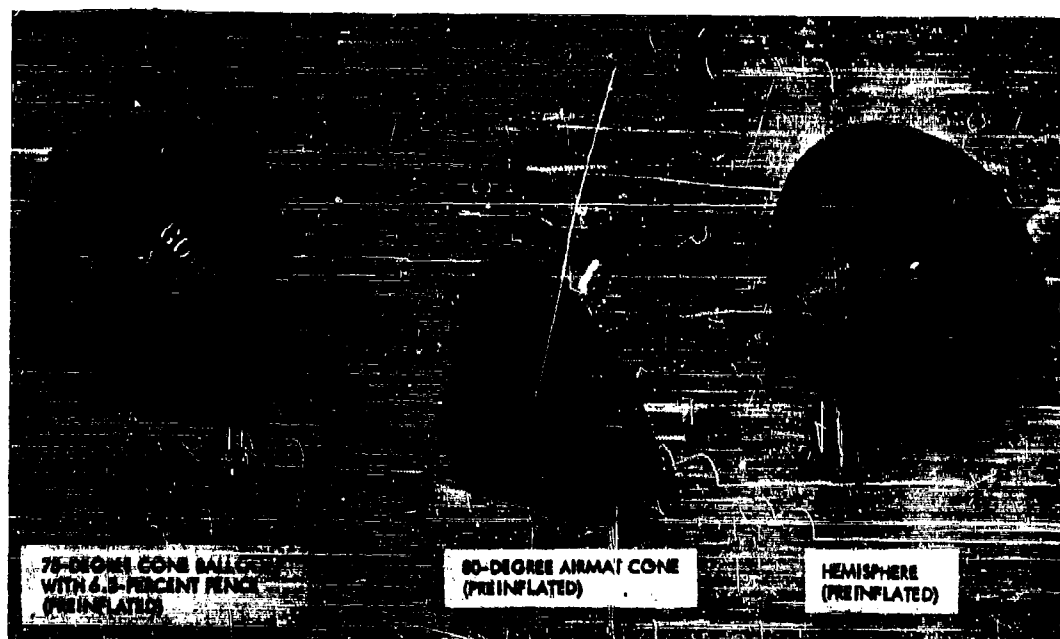


Figure 63. Preinflated Sample Supersonic Wind Tunnel Test Models

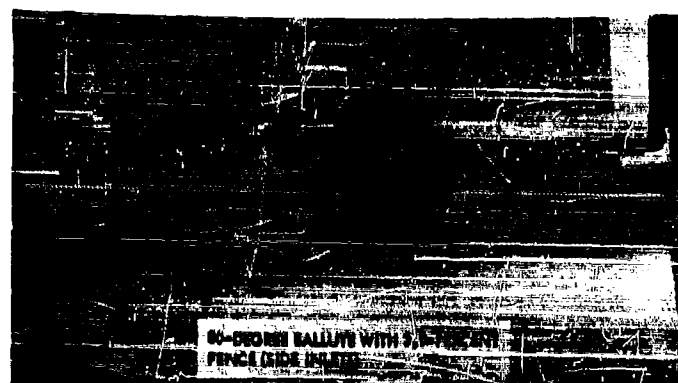
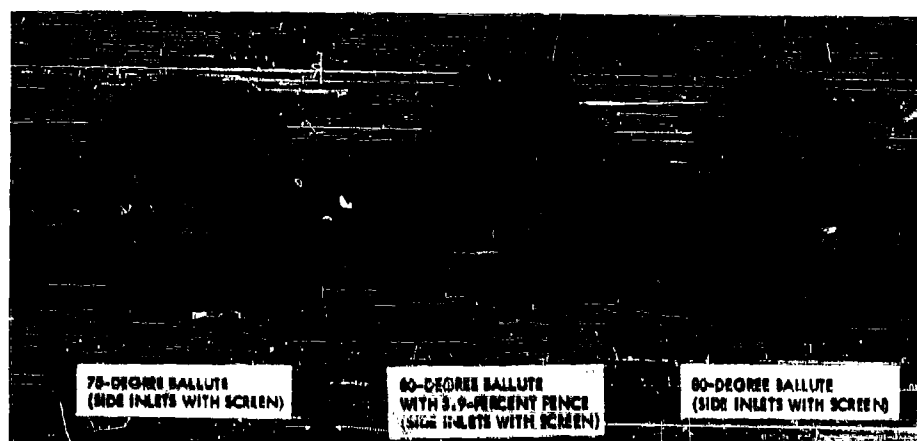


Figure 64. Ram-Air Sample Supersonic Wind Tunnel Test Models



Figure 66. Schlieren Photograph of Sphere with 0.25-Fence at $M = 2.5$

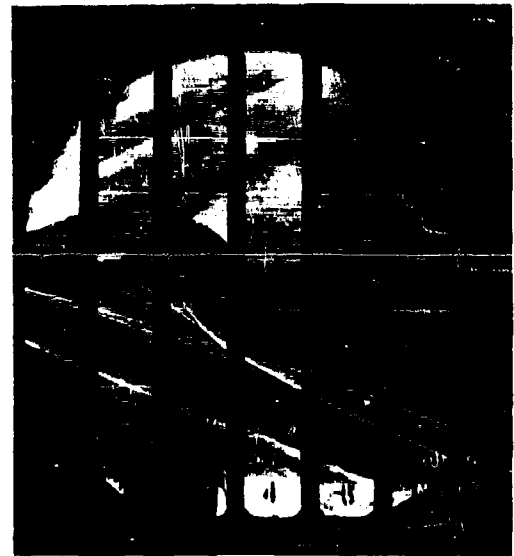


Figure 67. Schlieren Photograph of 75-Degree Cone Balloon at $M = 2.87$



Figure 68. Schlieren Photograph of Sphere with 0.25-Fence at $M = 2.87$

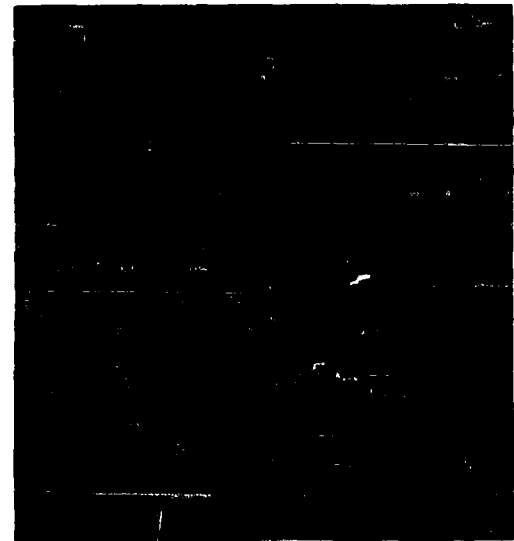
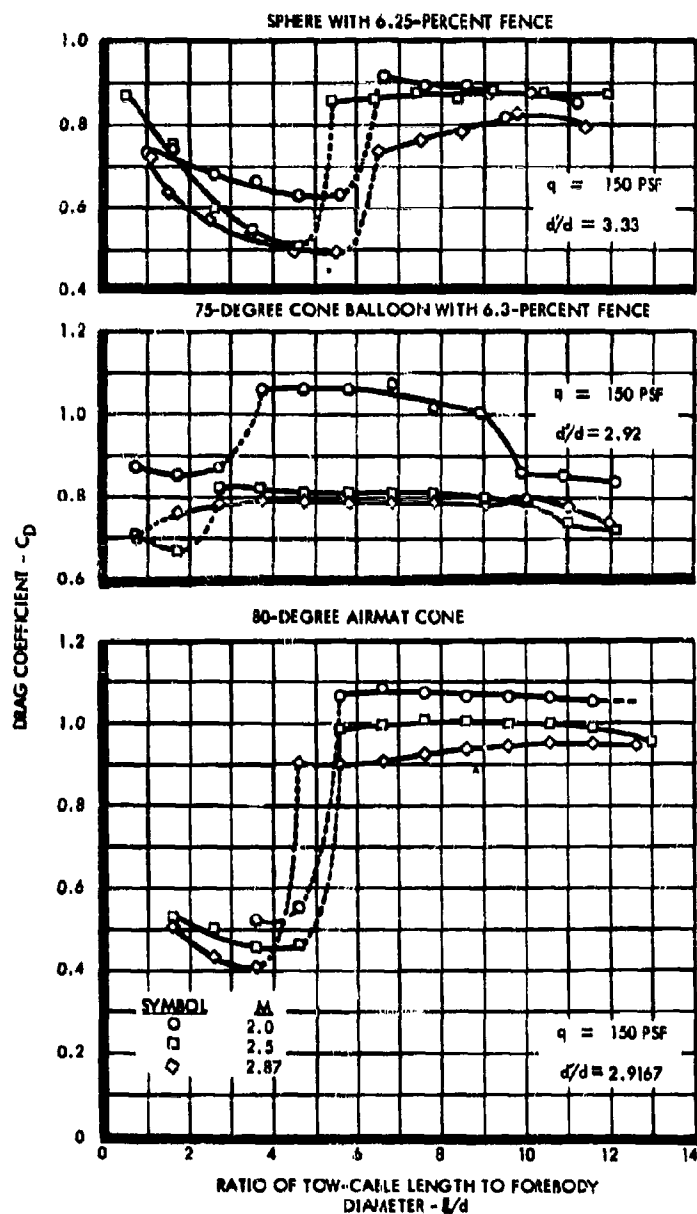


Figure 69. Schlieren Photograph of 80-Degree Ram-Air Ballute at $M = 2.5$



NOTE: d' - MODEL MAX DIAMETER (IN.)
 d - FOREBODY MAX DIAMETER (IN.)

Figure 70. Effect of the Tow-Cable Length on the Drag Coefficient of a Sphere with 6.25-Percent Fence, 75-Degree Cone Balloon, and 80-Degree Airmat Cone behind the Forebody

NOTE: d^* - MODEL MAX DIAMETER (IN.)
 d - FOREBODY MAX DIAMETER (IN.)
 $d^*/d = 3.33$

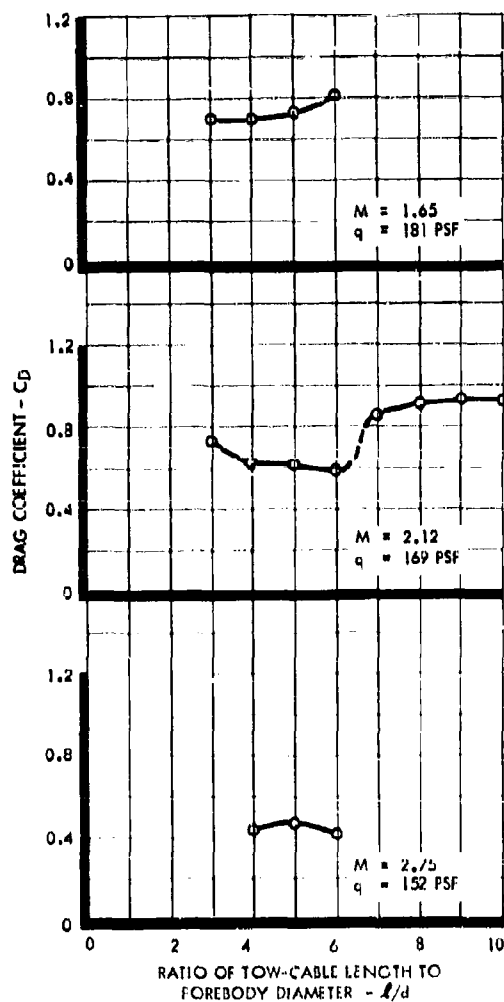


Figure 71. Effect of Tow-Cable Length on the Drag Coefficient of a Hemisphere

NOTE: d^* - MODEL MAX DIAMETER (IN.)
 d - FOREBODY MAX DIAMETER (IN.)
 $d^*/d = 2.92$

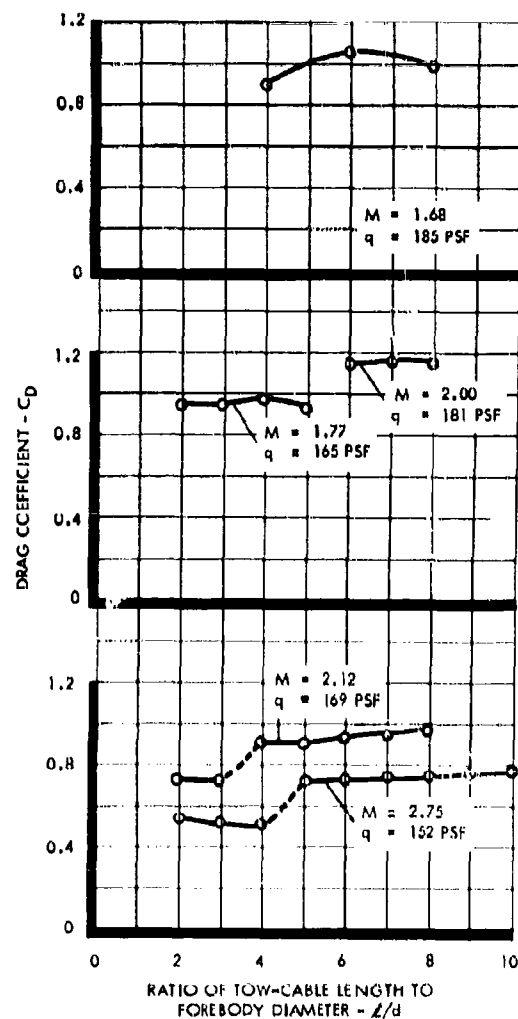


Figure 72. Effect of Tow-Cable Length on the Drag Coefficient of a 75-Degree Cone Balloon with 8.3-Percent Fence

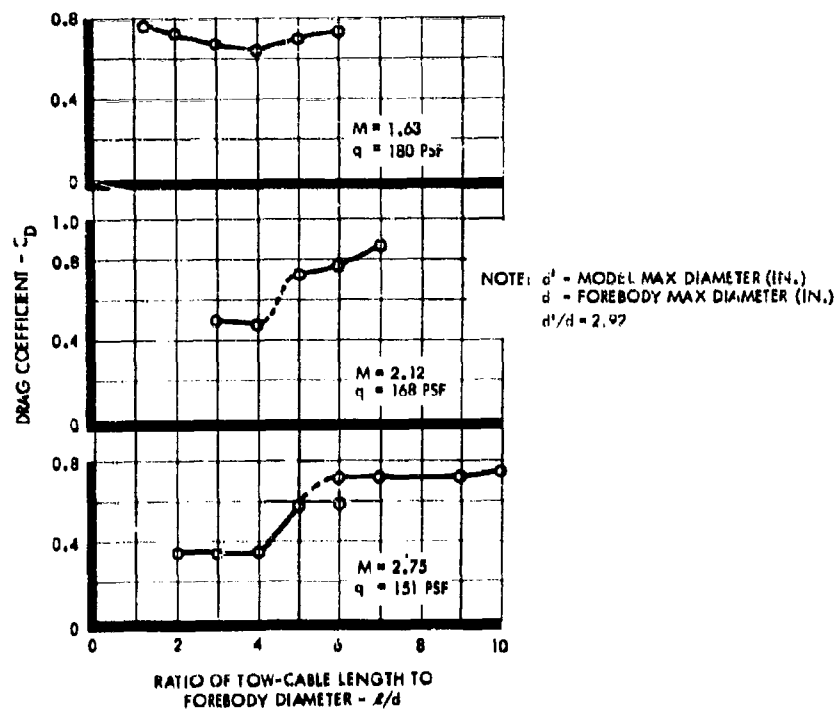


Figure 73. Effect of Tow-Cable Length on the Drag Coefficient of an 80-Degree Airmat Cone ($M = 1.63$ to 2.75)

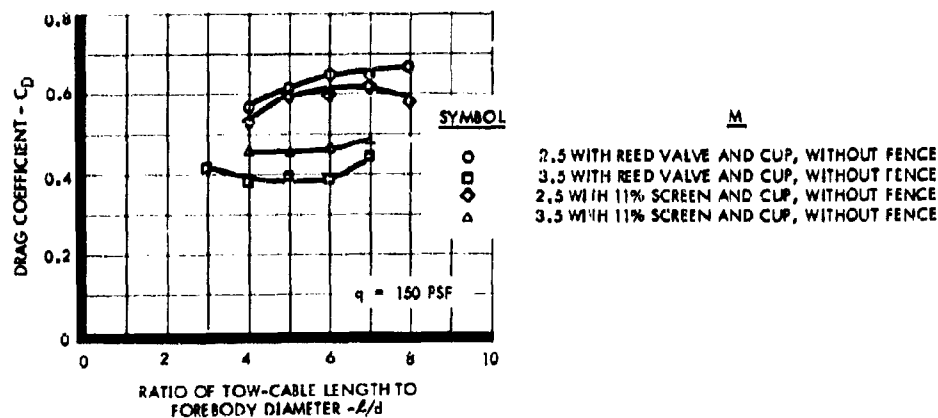


Figure 74. Effect of Tow-Cable Length on the Drag Coefficient of an 80-Degree Ballute without Fence (Ram-Air Inflated)

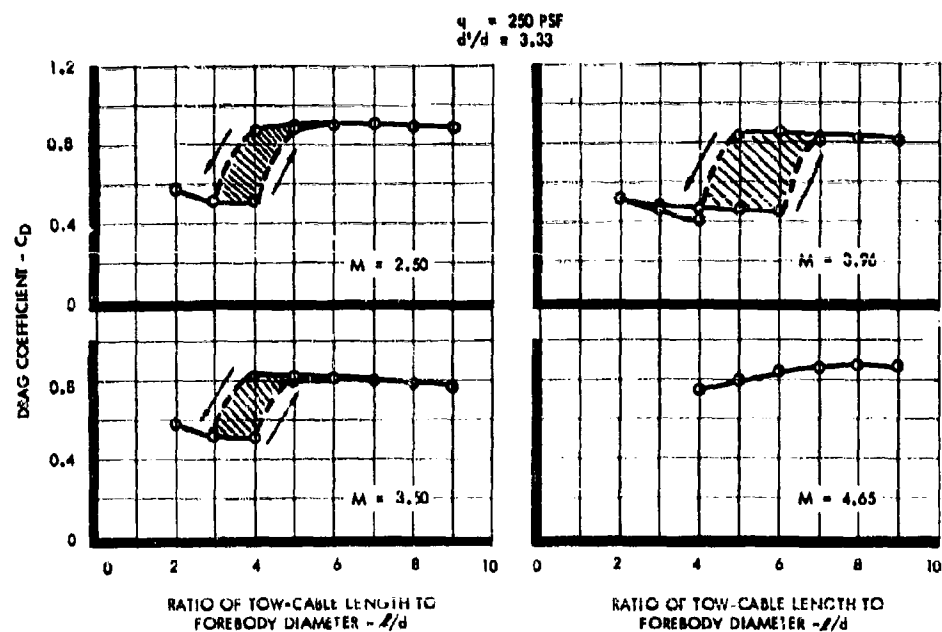


Figure 75. Effect of Tow-Cable Length on the Drag Coefficient of an 80-Degree Ballute with 3.9-Percent Fence (Ram-Air, Side Inlets)

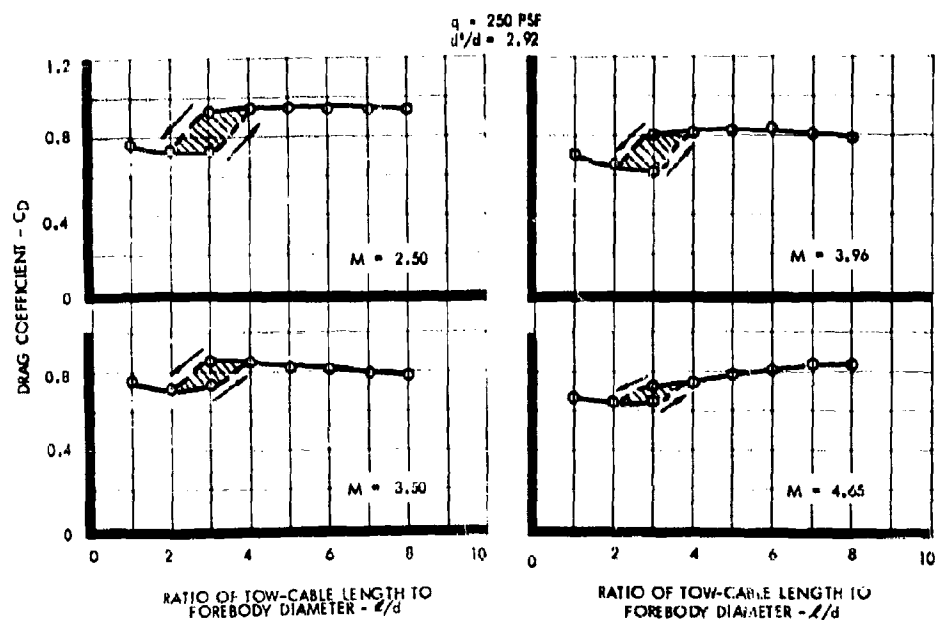


Figure 76. Effect of Tow-Cable Length on the Drag Coefficient of a 75-Degree Cone Balloon with 6.3-Percent Fence

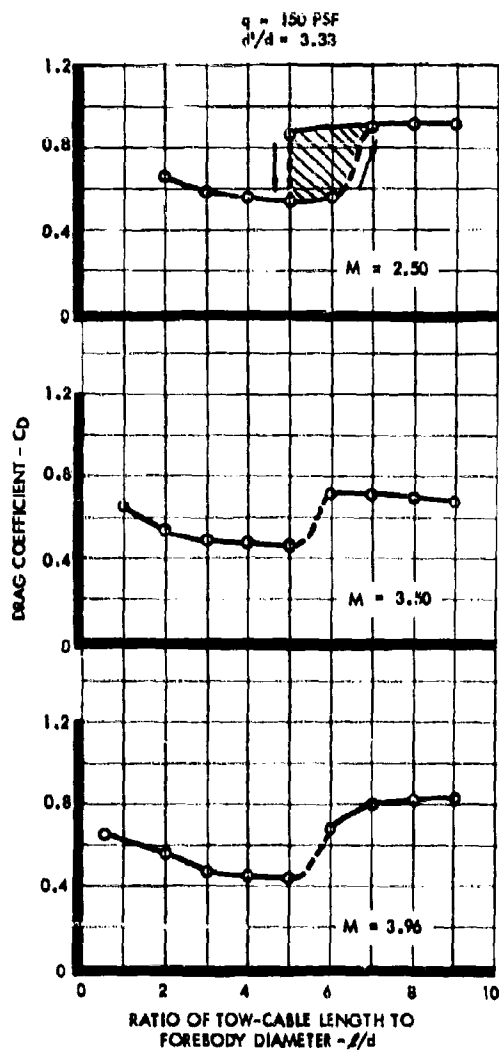


Figure 77. Effect of Tow-Cable Length on the Drag Coefficient of a Sphere with 6.25-Percent Fence

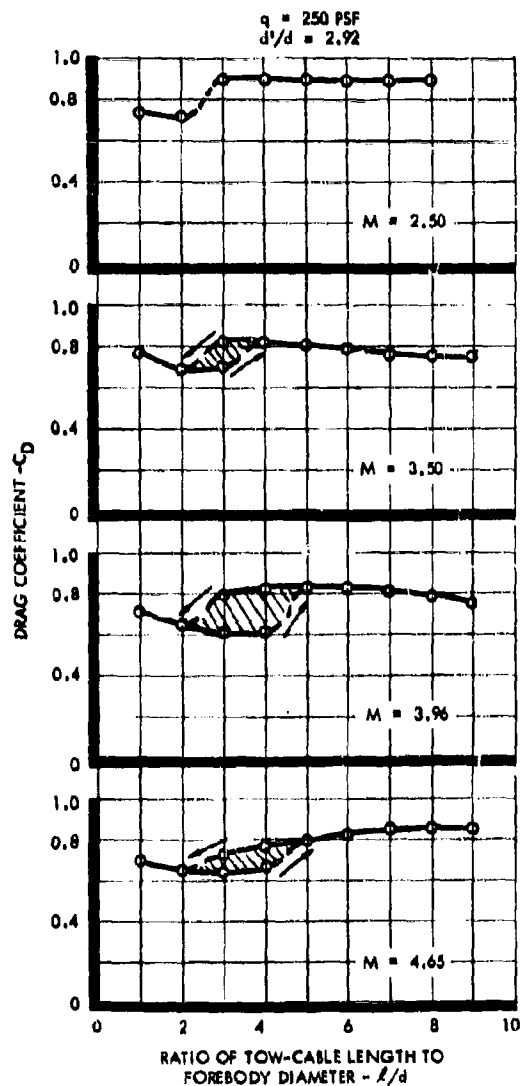


Figure 78. Effect of Tow-Cable Length on the Drag Coefficient of a 75-Degree Ballute with 6.3-Percent Fence with Side Inlets

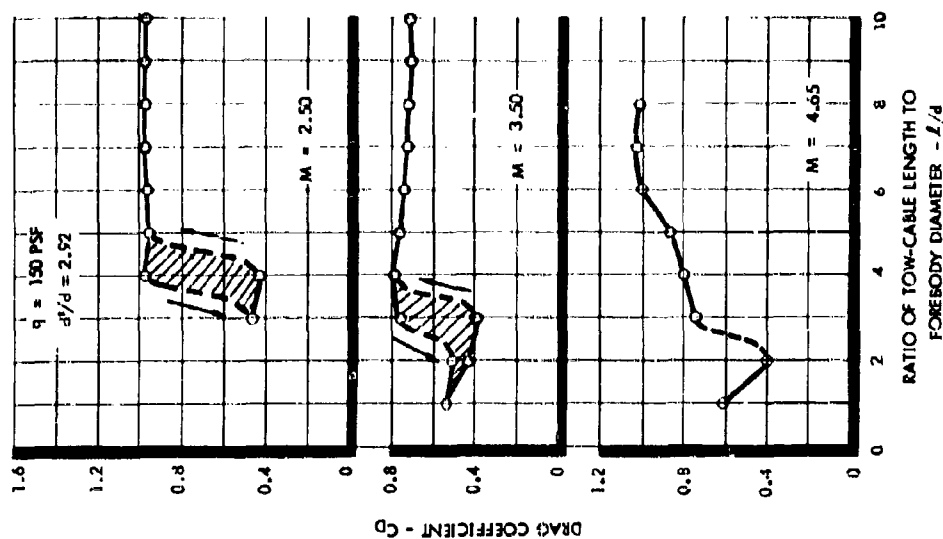


Figure 79. Effect of Tow-Cable Length on the Drag Coefficient of an 80-Degree Airmat Cone ($M = 2.50$ to 4.65)

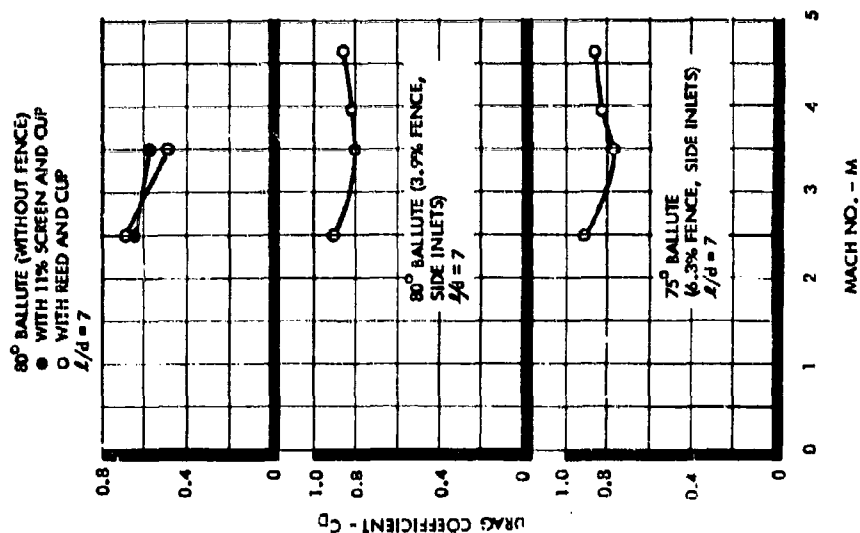


Figure 80. Effect of Mach No. on the Drag Coefficient (Ballutes)

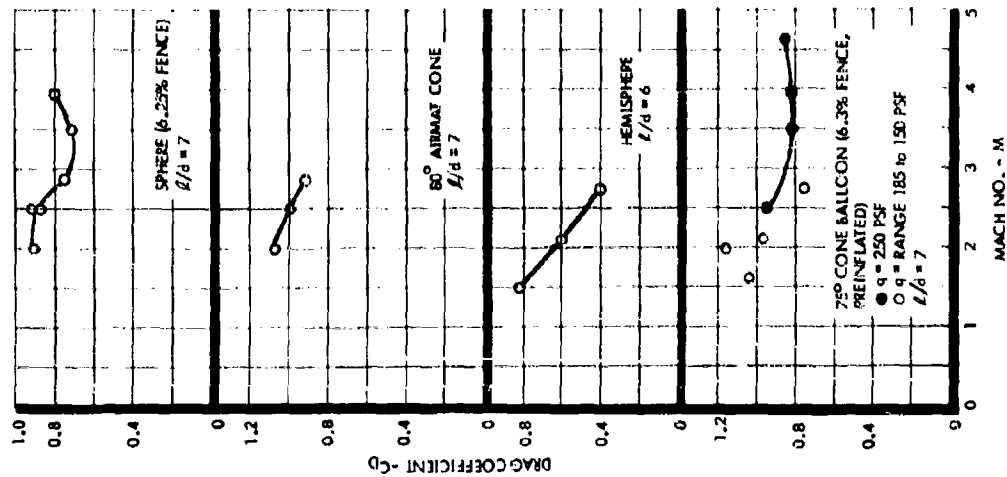


Figure 81. Effect of Mach No. on the Drag Coefficient (Closed Pressure Vessel)

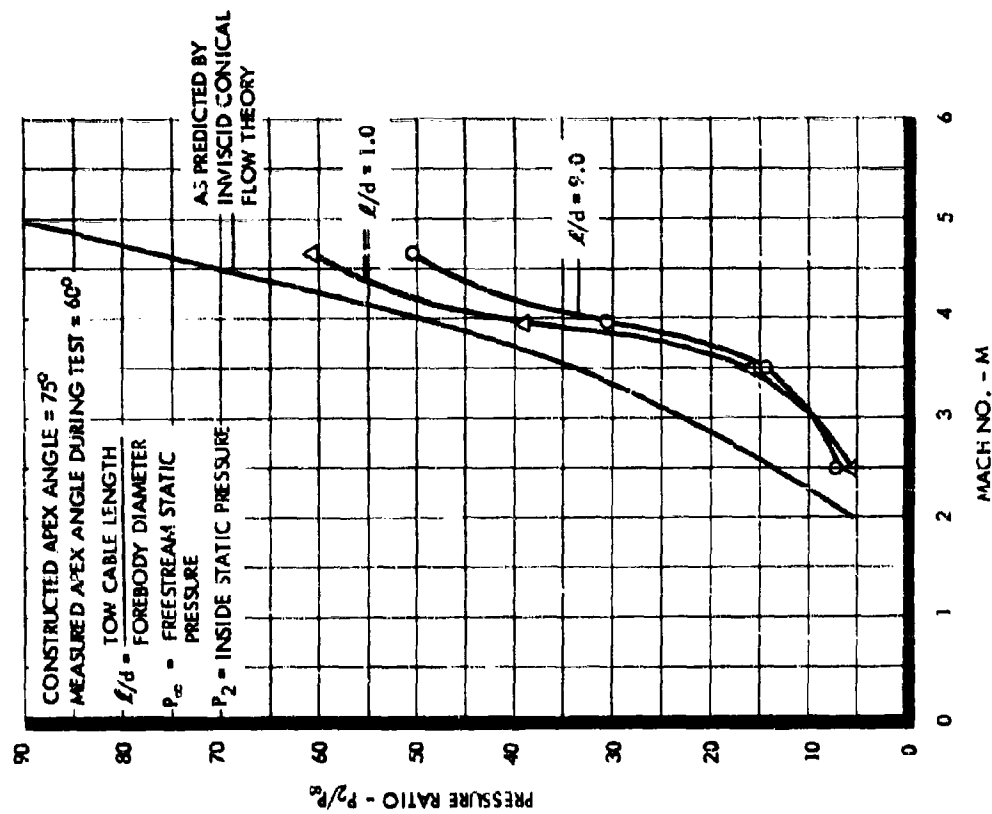


Figure 82. Side Inlet Pressure Recovery for 75-Degree Ballute with 6.3-Percent Fence

SECTION 5

HYPERSONIC WIND TUNNEL TESTS

A. GENERAL

The tests were conducted in the Arnold Von-Kármán, tunnel "C", at Arnold Air Force Station, Tennessee. The purpose of these tests was to obtain drag, pressure distribution, and heat transfer measurements of towed decelerators.

1. Description of Von-Kármán Tunnel "C"

The 50-inch Mach 10 tunnel is a continuous-flow, variable-density, hypersonic wind tunnel with a 50-inch-diameter test section. Because of changes in boundary layer thickness caused by changing pressure level, the Mach 10 contoured nozzle produces an average test section Mach number which varies from 10 at a stagnation pressure of 200 psia to 10.2 at 2000 psia. The centerline flow distribution is uniform within about 0.5 percent in Mach number. There is a slight actual gradient on the order of 0.01 Mach number per foot. The unique feature of the 50-inch Mach 10 tunnel is the model installation chamber below the test section which allows the entire pitch mechanisms (sting and model) to be raised into and lowered out of the tunnel. When the model is in the retractive position, the fairing doors and the safety doors can be closed allowing entrance to the tank for model changes while the tunnel is running. When the model is in the test section, only the fairing doors are closed leaving the tank at static pressure. Stagnation pressures of up to approximately 2000 psia are supplied through the 50-inch Mach 10 tunnel. The air is selectively valved through the compressor plant high-pressure dryers and the propane-fired heater, which raises the air temperature to a maximum of 800°F. The heated air then enters the electric heater, which increases the air temperature to a maximum of 1400°F, sufficient to prevent liquification of the air in the test section. From the electric heater the air flows through the nozzle, the diffuser, the cooler and back into the compressor system. For more detailed tunnel information see References 18 and 21.

2. Description of Test Setup and Models

The basic external geometry for all Ballute models is shown in Figure 83.

The heat transfer model was fabricated from Type 321 stainless steel (see Figure 84) and was formed by the spinning process. The skin thickness varied from 0.050 to 0.064 inch. Nineteen thermocouples were spot-welded on the interior surface and were located as shown in Figure 83. Two thermocouples were also mounted inside the model to measure the internal ambient temperature.

The pressure model was fabricated from Type 321 stainless steel (See Figure 85) and was instrumented with 17 static orifices on the surface as shown in Figure 83 and one internal orifice for measuring the internal model pressure.

Flexible drag models were fabricated from René 41 cloth. The seams of the model were joined by spot welding, and the model was impregnated with a high-temperature silicone ceramic elastomer to obtain an essentially gas-tight cloth. For added strength, eight longitudinal cables were connected from the nozzle to the base plate. A partially inflated Ballute is shown in Figure 86.

The basic inlet configuration is shown in Figure 87. This inlet was tested on the pressure model with screens covering the inlet slots, with reed valves (screen removed), and with open slots. In addition to the basic inlet, two types of total head inflating probes were used with the flexible models as shown in Figure 88.

The models were supported by the strut assembly as shown in Figures 89 and 90. The leading edges of the vertical sections and the sides and top of the horizontal section were water-cooled. The flexible drag models were connected to a 3/32-inch-diameter René cable which was routed around pulley wheels inside the strut. The cable could be extended or retracted by means of

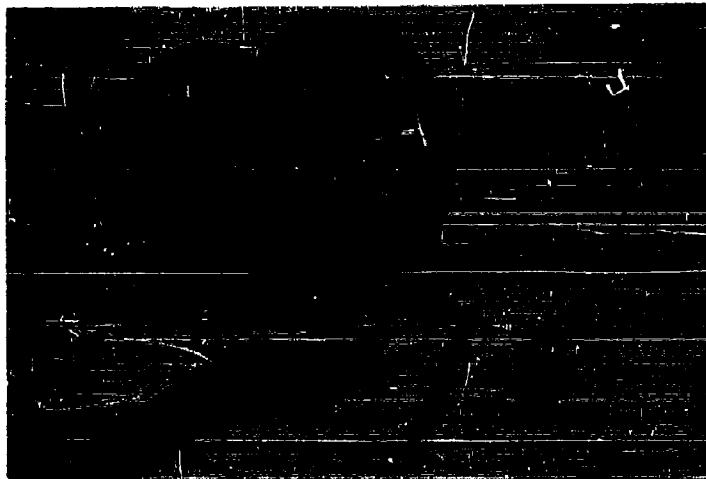


Figure 84. Heat Transfer Model

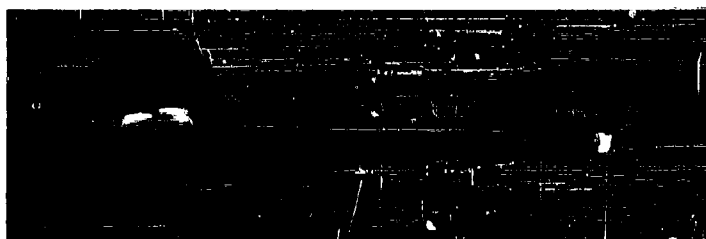


Figure 85. Pressure Model



Figure 86. Partially Inflated Ballute

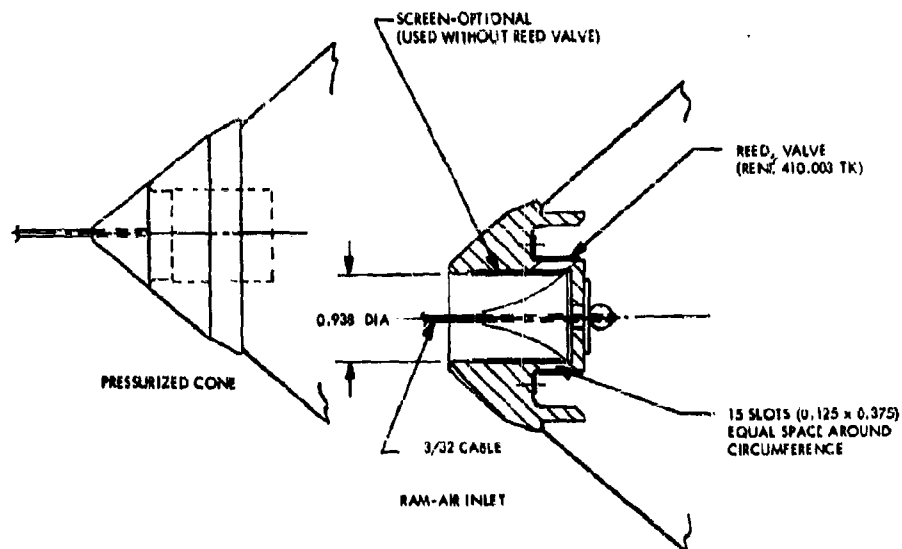


Figure 87. Typical Nose Configurations

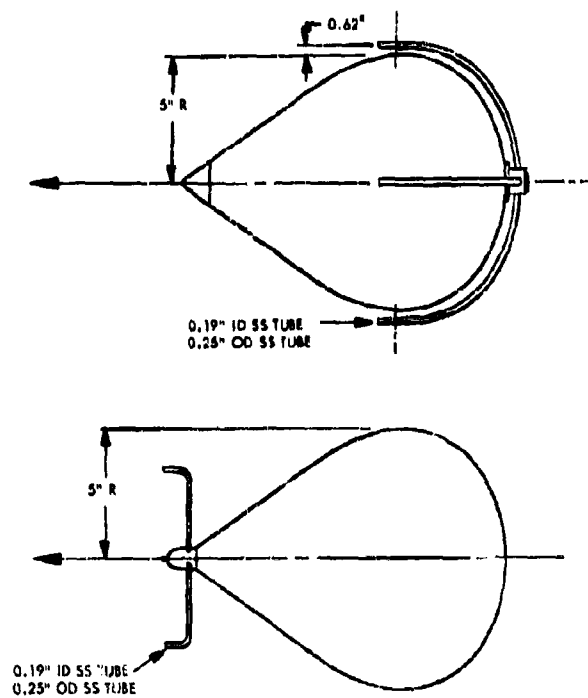


Figure 88. Front and Side Pitot Tubes

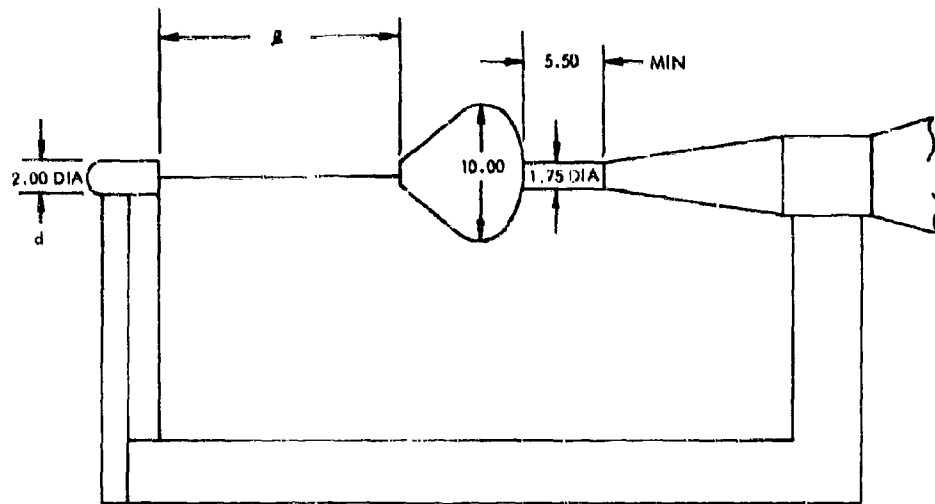


Figure 89. Pressure and Temperature Model Installation

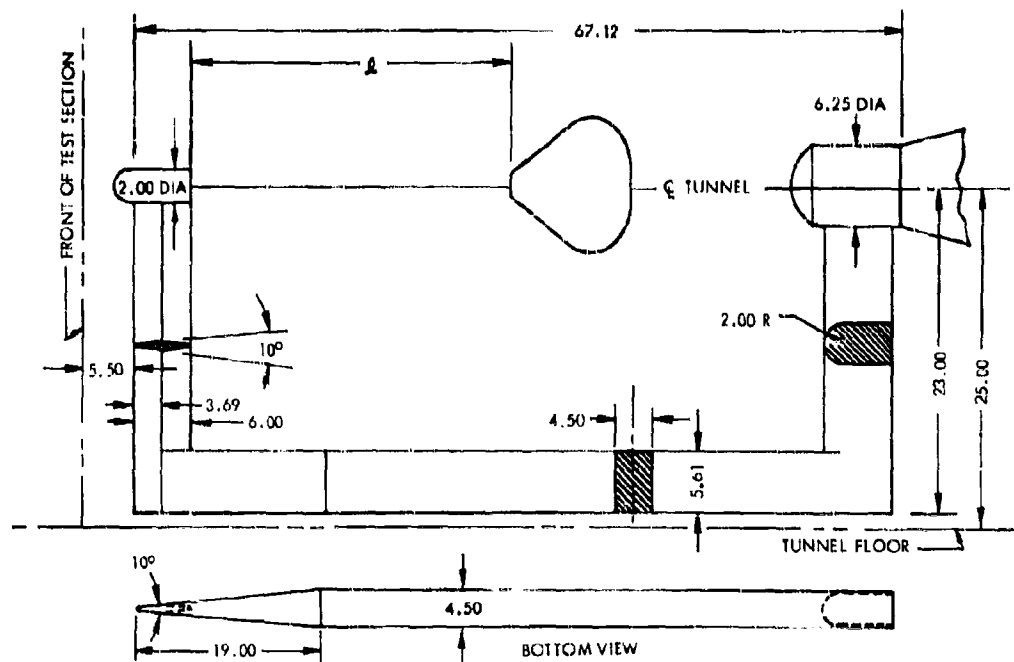


Figure 90. Drag Model Installation

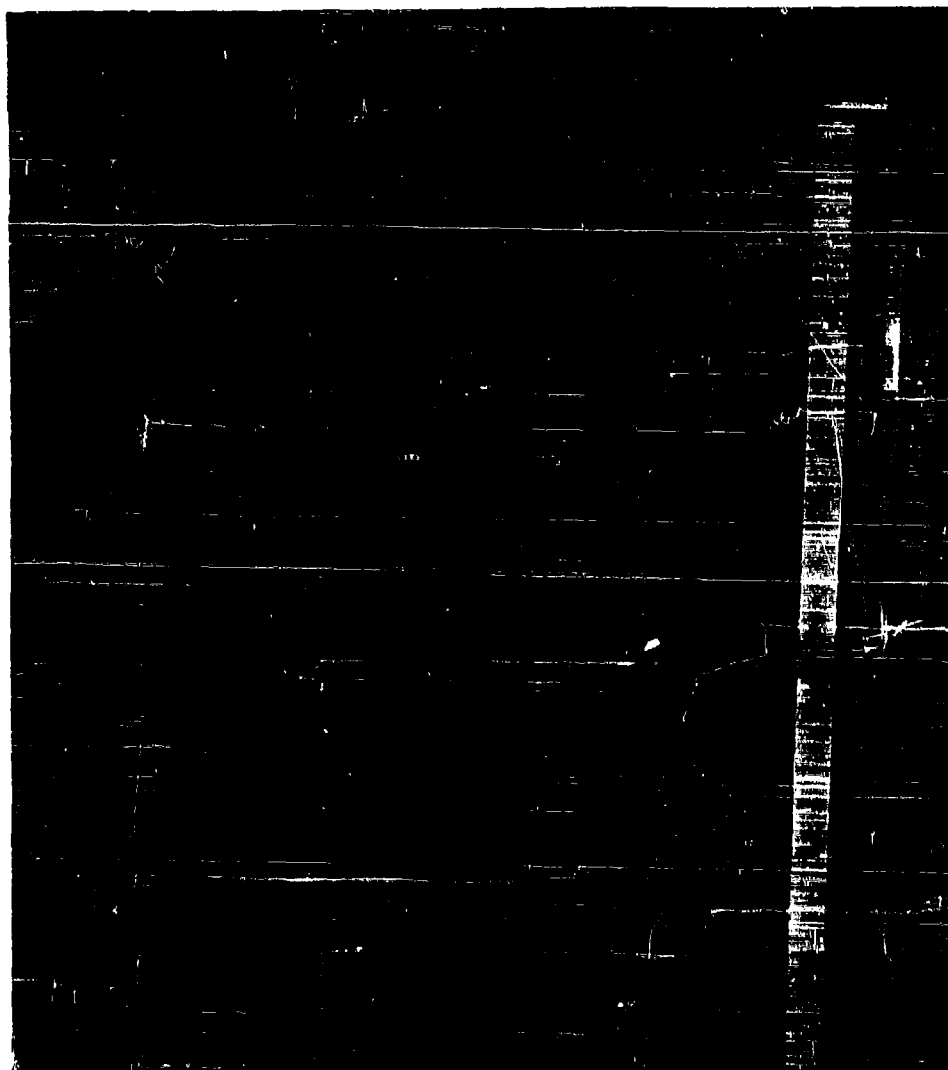


Figure 91. Pressure Model in Tunnel Installation Chamber

in conjunction with the transducers to obtain a differential count of 10,000. The resulting resolution is 0.0002 psi for the 1-psi transducer and 0.0015 psi for the 15-psid transducers. The accumulated count is stored in the binary counters, read out serially by the ERA scanner and punched on paper tape.

The P_g system contains two channels of frequency modulation pressure instrumentation, one with a range of 0 to 500 psia and the other with a range of 0 to 2500 psia.

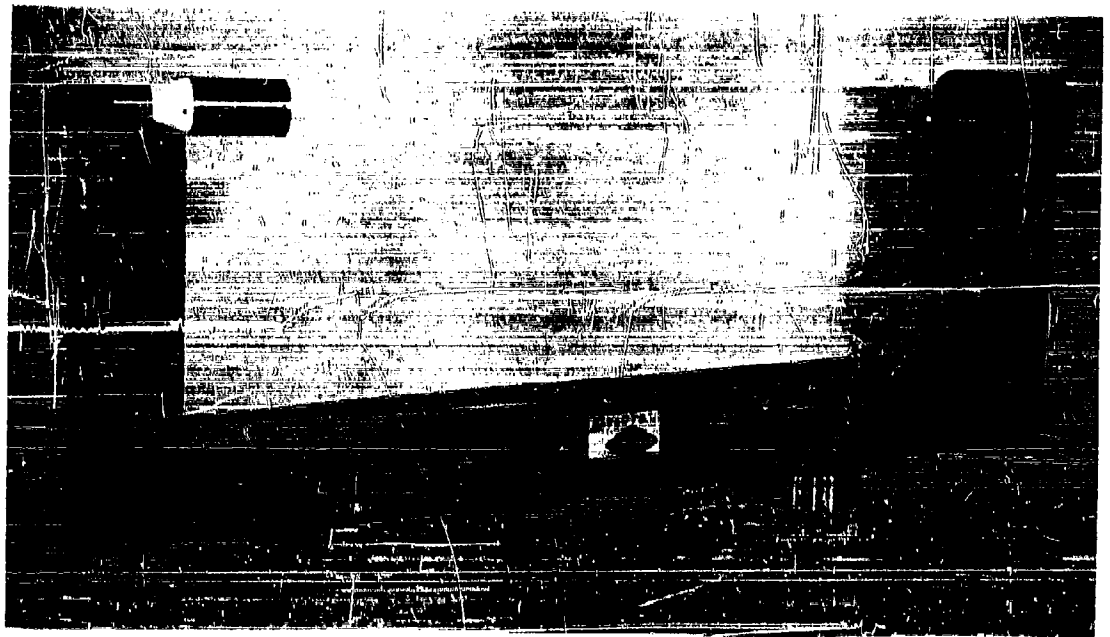


Figure 92. Water-Cooled Support Strut (Side View)

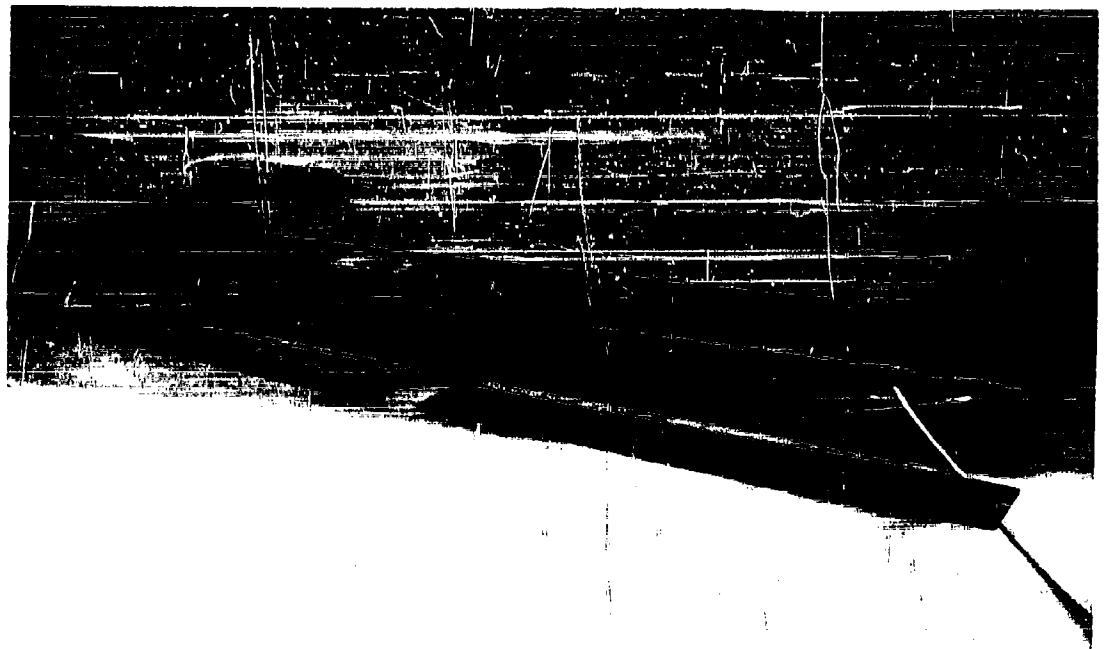


Figure 93. Water-Cooled Support Strut (Bottom View)

Table 10. Log Sheet of Mach 10 (± 0.187) Tests

DATE	RUN NO.	TYPE PAYLOAD	TYPE TRAILING MODEL	P _s (psi)	T _g (°F)	q (psi)	RN/FT x 10 ⁻⁶	λ/d	PURPOSE	RESULTS AND/OR DATA OBTAINED
11-9-61	1	2-in. dia	Pressure with conical plugged inlet	1394	769	294	3.17	7	Preliminary	Pressure distribution readings taken; tunnel heater not working properly
	2		Pressure with reed valve inlet	1190	956	267	2.31	8	Preliminary	
	3			1245	942	279	2.47	9	Contract data	Pressure distribution readings taken; tunnel heater not working properly. Still shadow-graph photo taken.
	4			1487	1418	314	1.80	9		Pressure distribution readings taken; trailing model in payload wake; internal pressure less than all external nose pressures.
11-9-61	5	2-in. dia		1402	1395	312	1.86	11		
11-10-61	6	2-in. dia		1455	1428	312	1.77	18		
	7	3-in. dia		1462	1418	313	1.79	12		
	8	4-in. dia		1997	1447	428	2.40	12	Contract data	
	9	2-in. dia with 15 small balls attached	Pressure with reed valve inlet	1424	1336	307	1.88	18	Attempt wake closure	
11-10-61	10	2-in. dia with boat tail	Pressure with reed valve inlet	1450	1430	313	1.78	18	Attempt wake closure	
11-10-61	11	2-in. dia with boat tail	Pressure with conical plugged inlet	235	1237	53.3	0.345	18	Contract data	
	12			415	1311	92.1	0.565	18		
	13			728	1354	158	0.943	18		
	14			1145	1380	240	1.43	18		
	15	2-in. dia with boat tail	Pressure with conical plugged inlet	1405	1418	314	1.79	18	Contract data	
	16	3-in. dia with aft scope (13 flaps)	Pressure with reed valve inlet	1402	1424	313	1.79	12	Attempt wake closure	
11-10-61	17	3-in. dia with aft scope (20 flaps)		1462	1427	313	1.77	12	Attempt wake closure	Pressure distribution readings taken; trailing model in payload wake; internal pressure less than all external nose pressures.
11-11-61	18	2-in. dia with boat tail	Temperature with conical plugged inlet	238	1207	---	0.36*	18	Contract data	Temperature distribution readings taken for 12.8 seconds.
	19			238	1220	---	0.36*	18		Repeat of run 18; 6 seconds of data.
	20			400	1264	---	0.60*	18		Temperature distribution readings taken for 6.9 seconds
11-11-61	21	2-in. dia with boat tail	Temperature with conical plugged inlet	559	1325	---	---	18	Contract data	Temperature distribution readings for 6.9 seconds.
11-11-61	22	2-in. dia with boat tail	Temperature with conical plugged inlet	679	1325	---	0.90*	18	Contract data	Repeat of run 21.
	23			1095	1381	---	1.44*	18		Temperature distribution readings for 6.9 seconds.

*Nominal values

Table 10. Log Sheet of Mach 10 (± 0.187) Tests (Continued)

DATE	RUN NO.	TYPE PAYLOAD	TYPE TRAILING MODEL	Pg (psi)	Tg (°F)	q (psf)	RN/FT x 10 ⁻⁶	L/d	PURPOSE	RESULTS AND/OR DATA OBTAINED
11-11-61	24	2-in. dia with boat tail		1375	1412	---	---	18	Contract data	Temperature distribution readings for 6.9 seconds.
	25		Temperature with conical plugged inlet							Repeat of run 24.
11-11-61	26	2-in. dia with boat tail	Bladder inflated 80° Ballute (cloth A)	715	1350	155	0.96	8.38	Contract data	Model in tunnel 8.2 seconds; $C_D = 0.328$; model was stable.
11-16-61	27	No payload	Pressure with conical plugged inlet	235	1235	53.5	0.347	---	Comparative data	Pressure distribution readings taken; still shadow graphs taken.
	28			415	1305	92.0	0.570	---		
	29			715	1350	155.0	0.926	---		
	30		Pressure with conical plugged inlet	1455	1435	311	1.75	---	Comparative data	Pressure distribution readings taken; still shadow graphs taken.
	31		Pressure with reed inlet	1464	1440	312	1.78	---	Contract data	Pressure distribution readings taken; both still and movie shadow graphs taken.
11-16-61	32	No payload	Pressure with open inlet	1458	1437	311	1.78	---	Contract data	
11-16-61	33	No payload	Pressure with screened inlet	1467	1429	314	1.78	---		Pressure distribution readings taken; still shadow graphs taken.
	34		Pressure with reed inlet	1465	1423	313	1.79	---		Pressure distribution readings taken; both still and movie shadow graphs taken.
	35		Temperature with conical plugged inlet	235	1230	---	0.36*	---		Temperature readings taken for 7 seconds.
	36			415	1280	---	0.60*	---		
	37			715	1340	---	0.98*	---		
	38			1140	1380	---	1.44*	---		
11-16-61	39	No payload	Temperature with conical plugged inlet	1465	1420	---	1.80*	---	Contract data	Temperature readings taken for 7 seconds.
11-28-61	40	2-in. dia with boat tail	Bladder inflated 80° Ballute (cloth B)	1468	1400	313	1.87	4-18	Contract data	Model in tunnel 74 seconds; fully inflated; peak temperature of cloth-1808°F; C_D varied 0.35 to 0.53; model stable; movies taken.
	41		80° Ballute with front inlets (cloth A)	1473	1428	313	1.78	---		Model aft end ruptured after 3 seconds; movies taken.
11-28-61	42	2-in. dia with boat tail	80° Ballute with side inlets (cloth A)	713	1375	153	0.785	8-9	Contract data	Model in tunnel 17.2 seconds; model fully inflated; stable; C_D varied 0.40 to 0.63; movies taken.
11-28-61	43	2-in. dia with boat tail	80° Ballute with side inlets (cloth A)	715	1364	153	0.920	---	Contract data	Used run 42 model; model aft end ruptured after 1 second.
11-28-61	44	2-in. dia with boat tail	80° Ballute with side inlets (cloth A)	714	1360	153	0.917	1-5	Contract data	Model fully inflated; stable; C_D varied 0.33 to 0.48; model aft end ruptured after 49.2 seconds.

*Nominal values

4. Temperature Model Instrumentation

The reference junction of each thermocouple was maintained at 132°F. Each thermocouple output was recorded in digital form on magnetic tape at a rate of 20 times per second by means of a Beckman 210 analog-to-digital converter. To monitor the temperatures at selected points on the models, nine of the thermocouple outputs were also recorded on strip charts by 0.25-second (full-scale travel) Brown servo-potentiometers.

5. Drag Model Instrumentation

A strain drag link furnished by GAC was used for drag measurements on the flexible models. The drag link was instrumented with two strain-gage bridges and mounted on the hydraulic cylinder piston rod. Power to the strain-gage bridges was supplied from a 400-cps carrier system. Output from one of the bridges was measured with a null-balance servo-potentiometer with a shaft positioning digitizer for recording on punched paper tape; the other strain-gage output was measured with a galvanometer-type oscillograph (visicorder). A cable positioning potentiometer was also mounted inside the strut assembly. Output from this potentiometer was also measured with the servo-potentiometer and visicorder.

6. Test Procedure

The tests were conducted as shown in Table 10. Figures 94, 95, and 96 show the inflated 80-degree Ballute models during the test runs.

Pressure data was obtained at various distances behind the forebody, and heat transfer data was obtained at an L/d of 18. All data was obtained at zero-degree angle of attack, and Reynolds number range covered was from 0.36×10^6 to 1.80×10^6 per foot. The forebody and strut assembly were removed, and additional heat transfer and pressure data were obtained over the same Reynolds number range.

The flexible models were installed as shown in Figure 90 and injected into the tunnel at the minimum desired L/d . The cable was then extended, and drag measurements were obtained over the desired L/d range. Some of the flexible models were preinflated with a neoprene bladder (Figure 96); other models were inflated with the ram-air devices shown in Figures 94 and 95. In order to keep the models relatively stable during the injection, a restraining cable was loosely connected from the model base to the hemispherical cover.

B. DISCUSSION OF RESULTS AND CONCLUSIONS

The pressure test results are shown in Figures 97 through 103. Note that Figure 103 presents a comparison of free-stream inviscid flow theory pressure distribution data and the actual wind tunnel pressure distribution data. The temperature test results are shown in Figures 104 and 105. Transient temperature distributions on the heat transfer model were recorded; computer reduction of this data with the total temperature of the air stream produced the heat transfer coefficient distribution. The drag test results of the inflatable metal cloth 80-degree Ballute models are shown in Table 10, test runs 26, 40, 41, 42, 43, and 44, and in Figures 106 and 107.

During the pressure tests the pressure distribution data indicated that the nose of the Ballute model was in an expanding wake of the payload from L/d of zero back to L/d 's of 18. During this test period it was not clear why forebody hypersonic wake phenomenon differed from supersonic wake phenomenon. Test runs 9, 10, 16, and 17 were unsuccessful attempts to collapse the wake. After these tests References 27 and 28 became available, and the following information obtained from these references is an indication of the phenomenon that may have occurred during these tests.

The shape of a hypersonic forebody wake depends on shape of the body in flow, but some features are typical for wakes in general. There is indication that each wake has a "neck" immediately behind the body where transition occurs. Air particles moving in the streamline above the stagnation streamline are decelerated and compressed at the neck. It is a region of narrow turbulence around the wake axis. This region has a tendency to spread out by engulfing the surrounding gas.

The important fact is that the inner wake is growing because of mixing and falling static pressure, thus the flow field is expanding. At some distance downstream, a process of diffusion

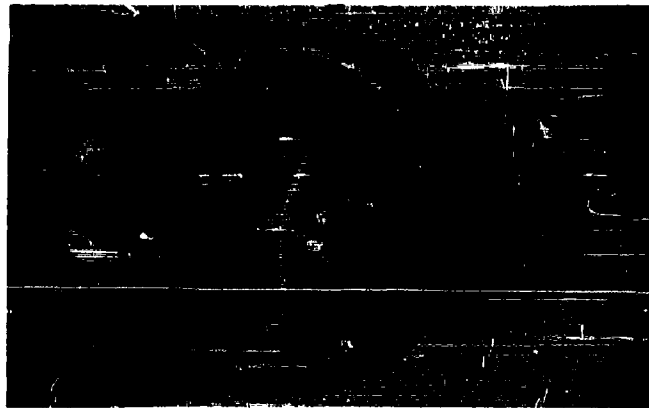


Figure 94. Eighty-Degree Ballute Model at $T_g = 1428^{\circ}\text{F}$
during Test Run (Front Inlets)

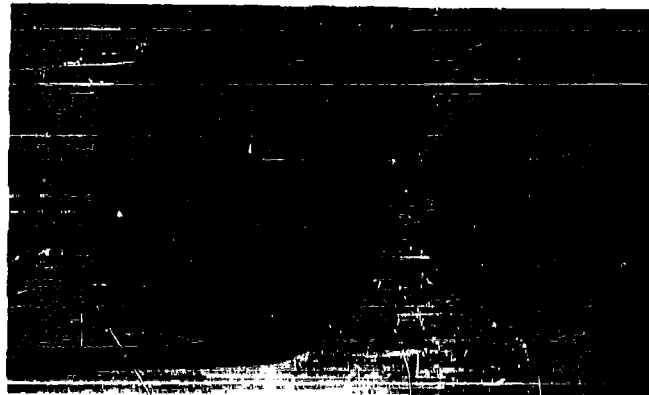


Figure 95. Eighty-Degree Ballute Model at $T_g = 1375^{\circ}\text{F}$
during Test Run (Side Inlets)

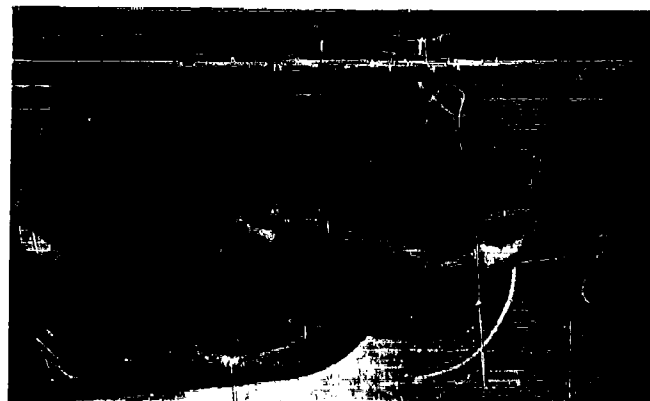


Figure 96. Eighty-Degree Ballute Model at $T_g = 1400^{\circ}\text{F}$
during Test Run (Bladder Inflated)

between the outer and inner wakes takes place. References 27 and 28 indicate that the diffusion occurs (25 to 50 diameters in a case of a ball), when turbulent, hot inner wake penetrates colder, denser outer wake.

The length and width of the wake are significant, especially if there is another body trailing the body which generates the wake. Problems of interference, drag variation, and drag hysteresis depend on behavior of the wake. Studies of the wakes, mainly in supersonic and hypersonic regions, are not complete, but the following is indicated by Reference 27. The relation of trail width (in ball diameters) to trail length (in ball diameters) is represented by a curve of the form (atmospheric pressure data):

$$L_d = D_d^2/10$$

where:

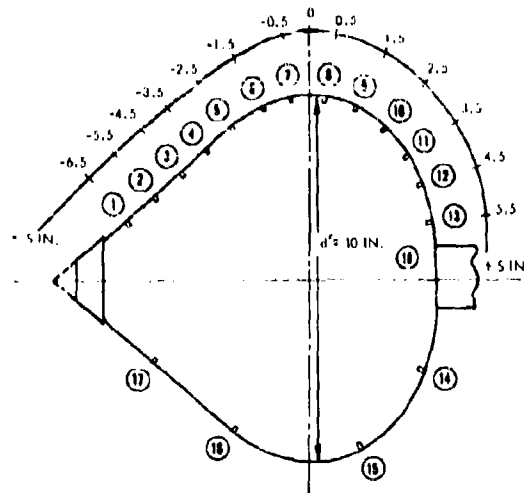
L_d = trail length

D_d = trail width

At transition point (For $L_d > 50$) 1/3 power law is recommended.

Both the side inlet inflation tube Ballute models and the bladder preinflated Ballute models performed in a satisfactory manner. Both types of configurations were fully inflated and were exceptionally stable in their towed position. A review of the high-speed movies of the test runs (1100 frames per second) reaffirmed this fact. There was no coning or roll of the model. In addition there was no indication of air mass pulsations of the self-inflated models. The review of the pressure distribution data was made with the following conclusions:

- (1) There is no pronounced effect in pressure distribution above the critical Reynold's number of approximately 500,000. Below this value the local pressure decreases with decreasing Reynold's number.
- (2) There is no pronounced effect in pressure distribution over the L/d range tested.



NOTES: ① - DISTANCE (INCHES) ALONG THE SURFACE (LONGITUDINAL)
② - TAP NUMBER (TYPICAL)

Figure 97. Ballute Pressure Tap Locations

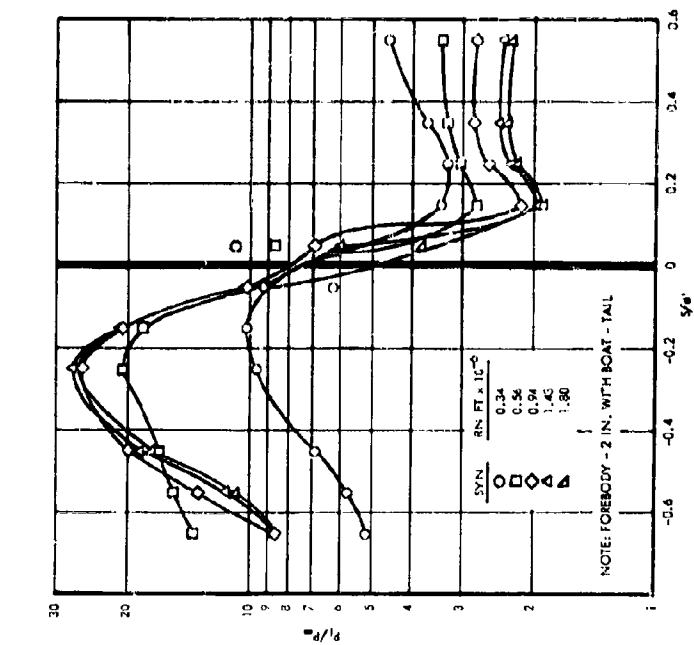


Figure 98. Ballute Longitudinal Pressure Distribution behind the Forebody (Plugged Inlet), $L/d = 18$

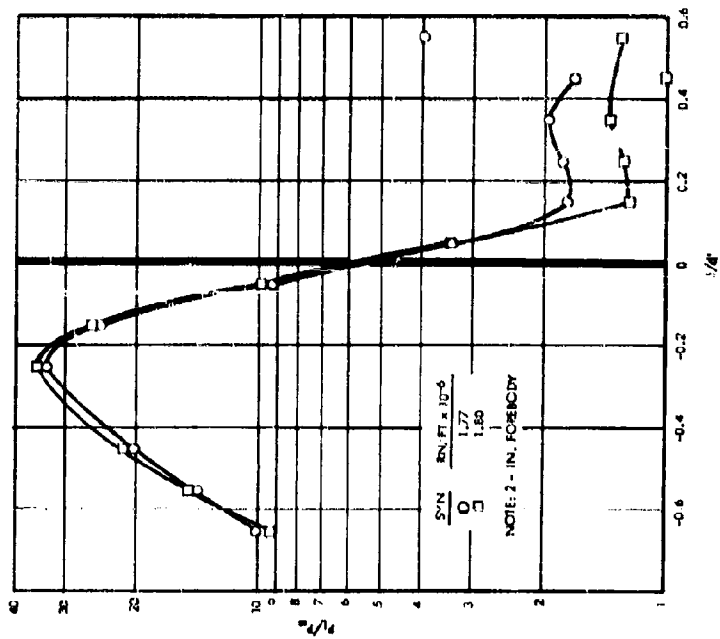


Figure 99. Ballute Longitudinal Pressure Distribution behind the Forebody (Ram-Air Inflation), $L/d = 9$

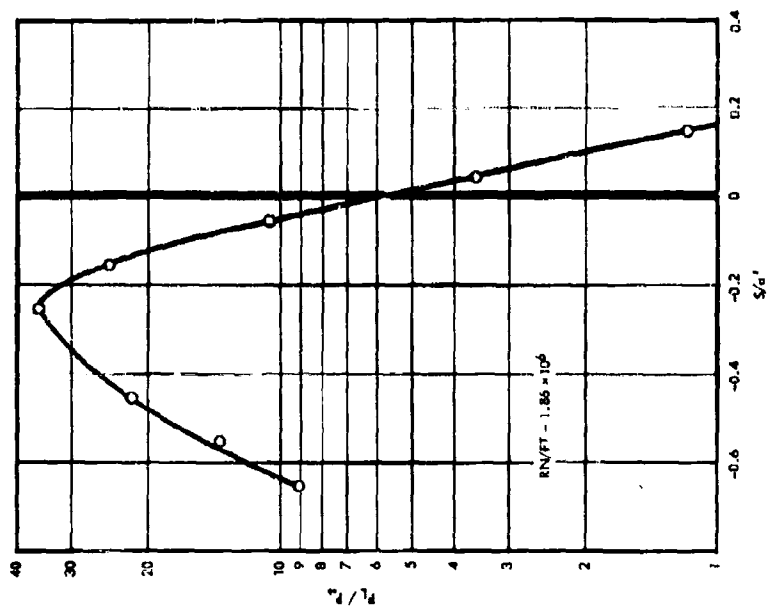


Figure 100. Ballute Longitudinal Pressure Distribution behind the Forebody (Ram-Air Inflation), $L/d = 11$

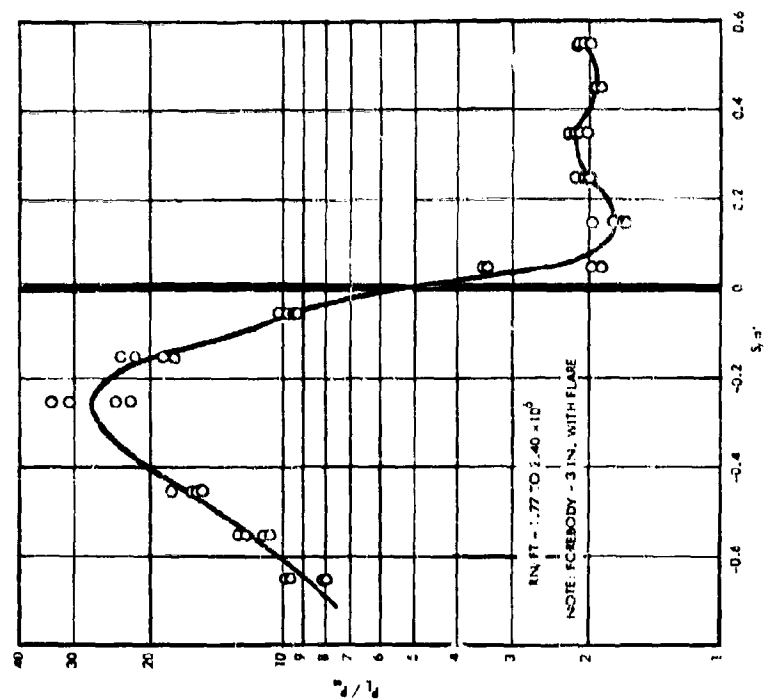


Figure 101. Ballute Longitudinal Pressure Distribution behind the Forebody (Ram-Air Inflation), $L/d = 12$

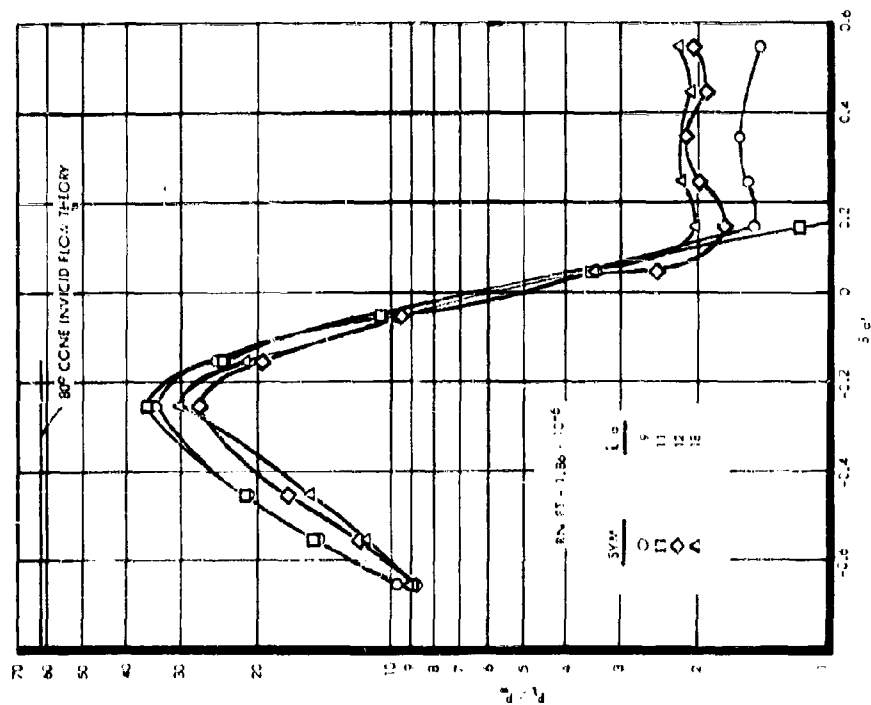


Figure 103. Ballute Longitudinal Pressure Distribution behind the Forebody (Ram-Air Inflation), Various Z/d 's

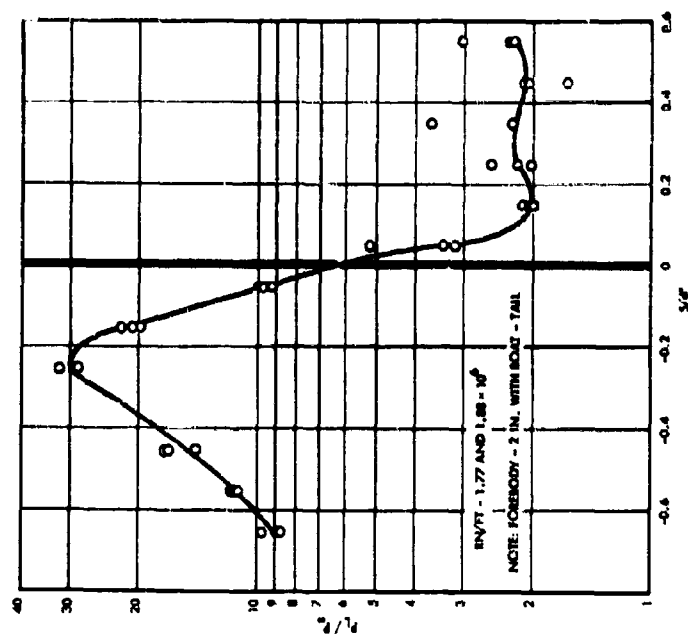


Figure 102. Ballute Longitudinal Pressure Distribution behind the Forebody (Ram-Air Inflation), $Z/d = 18$

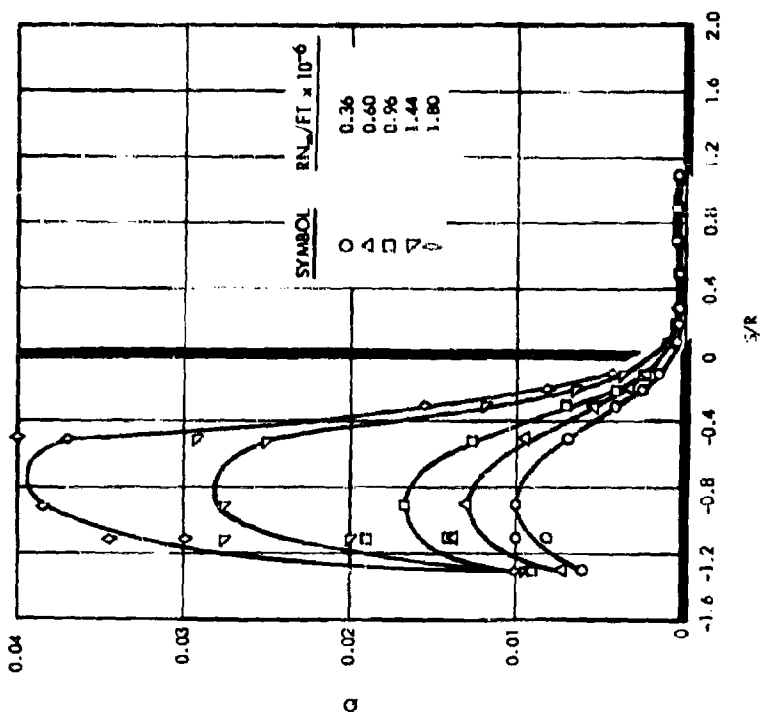


Figure 104. Heat Transfer Coefficients Obtained without the Presence of the Forebody and Strut Assembly (Plugged Inlet)

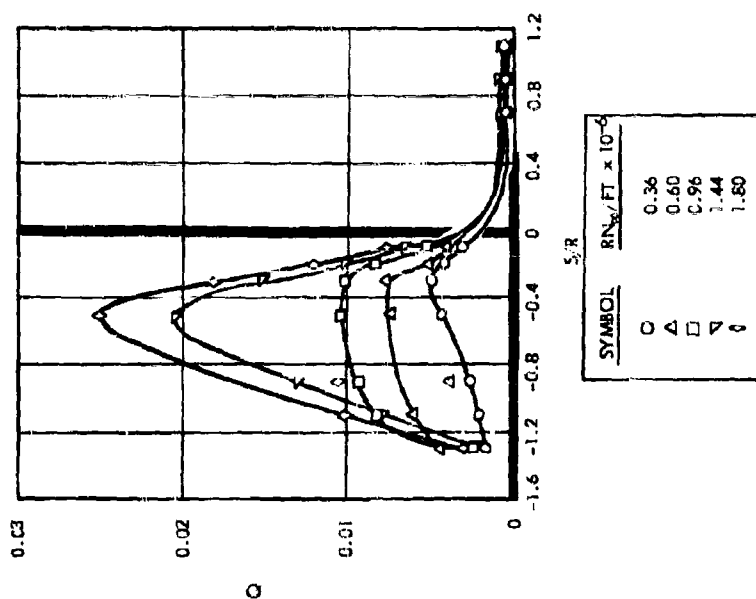


Figure 105. Heat Transfer Coefficients on the Ballute when Mounted behind the Forebody and Strut Assembly (Plugged Inlet)

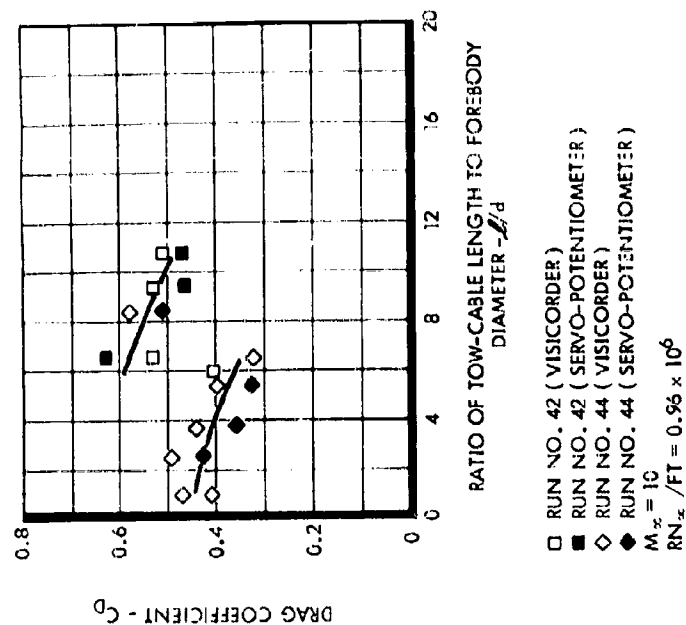


Figure 106. Effect of the Tow-Cable Length on the Drag Coefficient of an 80-Degree Ballute (Ram-Air Inflated)

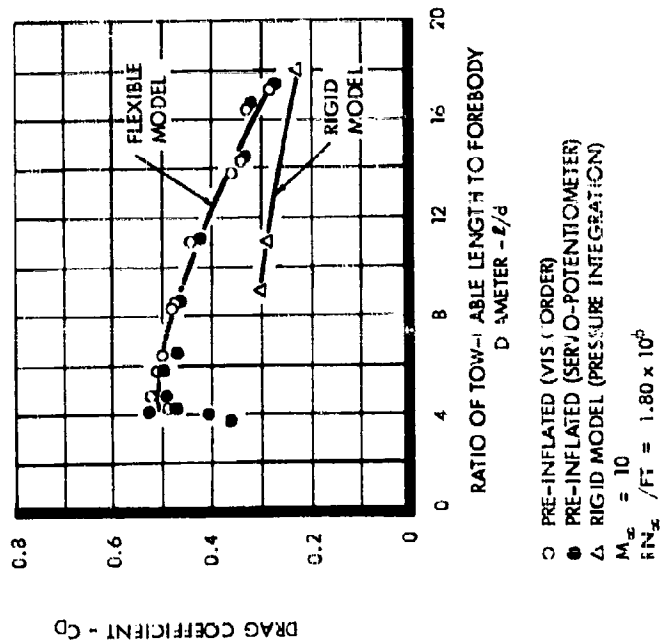


Figure 107. Effect of the Tow-Cable Length on the Drag Coefficient of an 80-Degree Ballute (Bladder Inflated and Rigid Tested behind a Forebody)

SECTION 6

MATERIALS INVESTIGATION

A. INTRODUCTION

1. Review of Available Materials

At the initiation of this program an investigation was conducted to appraise the state-of-the-art of materials applicable to the Ballute environment. The primary environment considered was temperature; this was set at a maximum of 1500°F. The material selected had to exhibit structural strength at this temperature.

The design criteria dictated that the material must also be flexible, permitting the structure to be packaged in small containers and subsequently deployed without damage to the material.

The third criteria demanded that the Ballute be capable of containing its pressurizing gas so that its shape could be maintained. In the case of the ram-air type of design, this criteria is not as critical.

Considering the above criteria, it was considered that a woven cloth would be required for the structural material. This type of material exhibits considerably more flexibility than does a sheet material. In order to approach the temperature requirement, it was evident that a super-alloy material would be required.

High-temperature metal cloths had previously been developed at GAC. Cloths woven of René 41 wire, 0.0016 inch in diameter and 200 wires per inch in both the warp and fill directions had previously been woven and evaluated. This cloth was not considered to be of sufficient weight and strength for the Ballute, however. Thus the existing material required advancement of cloth strength by weaving of heavier cloths. This involves decreasing flexibility. To alleviate this problem, weaving of stranded wire cloth instead of single wire cloth was investigated and incorporated into the program. Review of previous GAC developments on high-temperature coatings for metal cloths led to the selection of the GAC, CS-105 coating material. This coating is flexible at room temperature and exhibits gas tightness properties at the higher temperatures.

The basic ingredients in CS-105 are silicone elastomer and glass frits. CS-105 has 100 grams of S2077 and 100 grams of AW35. S2077 is the elastomer made by Dow-Corning Corporation, and AW35 is the glass frit made by Harshaw Chemical Company. The CS-105 coating acts and feels like a silicone elastomer at room temperature. As the temperature is raised, a thermal decomposition of the elastomer and a fusing of the glass frit occur. The rate of decomposition is a time-temperature phenomenon that progresses slowly at 800°F and increases as the temperature rises. The glass frit fuses before excessive decomposition of the silicone elastomer has taken place forming an adequate gas barrier.

Advanced development work on CS-105 coating was accomplished under GAC development projects. Thus any development work on coating material was not incorporated into this program. As CS-105 coating had not previously been applied to cloth designs used in this program, a minor effort was planned to evaluate coating applicability.

2. Formulation of Work Outline

Considering the presently available materials and the design requirements a work outline was formulated as follows:

a. Material Procurement. This work involved obtaining stronger but still flexible metal cloths woven of René 41 wire. Procurement of René 41 cable was also a requirement. For model work some stainless steel cloth was required.

b. Material Evaluation. The material obtained under item a was evaluated by testing at GAC. In addition a coating evaluation was performed to determine the coating adaptability to the new cloths.

c. Welding Investigation. Since the fabrication of models and full-scale Ballutes required a number of gores be joined together, a welding investigation was initiated to determine the welding criteria that would result in the highest joint efficiency.

d. Fabrication Investigation. Since the actual fabrication of a doubly curved Ballute presented a number of problems, it was considered desirable to first fabricate a 36-inch diameter model Ballute to check out detail processes. At the same time processes were developed for fabrication of the smaller wind tunnel models.

B. MATERIAL PROCUREMENT

It had previously been determined that a stronger cloth than the available René cloth was required for this program. The available cloth was woven of 0.0016-inch-diameter René wire and 200 x 200 wires per inch. The possibility of weaving René cloth to stainless steel fine wire tightness standards was investigated as a method of increasing the cloth strength.

The ability of a weaver to pack a larger diameter wire or more wires of the same diameter into a cloth is mainly dependent upon the softness of the wire. Stainless steel wire commonly used in weaving is "soft annealed" and has an ultimate strength of around 120,000 psi. Annealed René wire has an ultimate strength of about 180,000 psi. Thus it was apparent that the René weaving wire is somewhat "harder" than stainless steel weaving wire and that difficulty might be encountered in weaving René wire to stainless steel tightness standards.

The stainless steel standard cloth design of 0.0021-inch-diameter wires and 200 x 200 wires per inch was selected as the standard for weaving with René wire. The strength of this cloth woven of René wire would theoretically be increased 1.75 times over the previously woven René cloth. A weaving program was established to determine the practicality of weaving this item. This item was designated cloth A.

As it was considered desirable to further increase the cloth strength and to keep flexibility reasonable, a stranded wire cloth design was originated. The strand consists of six wires wound around a center wire for a total of seven wires. The design selected consisted of 0.0016-inch-diameter wires stranded together. These strands were to be woven 100 x 100 per inch. The strength of this cloth woven of René wire would theoretically be increased 3.50 times over the previously woven René cloth and 2.00 times over cloth A. This item was designated cloth B and a weaving program initiated. Cloth B was woven successfully after proper loom adjustments were made. The strand used has a theoretical diameter of 0.048 inch (3 x 0.0016) and the stainless steel single wire for 100 x 100 mesh is 0.0045. Thus it is apparent, at least in this case, that when using stranded René wire, weaving can be accomplished with stainless steel standards. Cloth A, however, using single wire could not be successfully woven to stainless steel standards.

The René wire used was procured from Hoskins Manufacturing Company. The weaving and stranding subcontract was performed by National Standard Company. Weaving was accomplished on conventional wire weaving looms. Considerable adjustment of the loom was required before satisfactory material was achieved. These loom adjustments were typical of the weaving industry and are formulated by experienced loom operators. Stranding was accomplished on conventional cabling equipment. This equipment is satisfactory although slow when using finer wires.

The weaving of cloth A proved to be most difficult. Sufficient quantities of "good" cloth wire were obtained to perform strength evaluations and to build wind tunnel Ballute models. It is not considered practical, however, to weave this particular cloth design to specifications required for production cloth. Thus it is further concluded that it is not practical to weave René wire to standards of stainless steel wire.

In connection with the weaving of cloth A, considerable investigation of the uniformity of the René wire was performed. It was concluded that as René is considered difficult to draw the wire uniformity is less than obtained with stainless steel and that this could be a major factor in the weaving difficulty.

The weaving of cloth B can be considered practical in production. Sufficient quantity of cloth was obtained to perform strength evaluations and to build wind tunnel Ballute models. Evaluation of the stranded cloth indicated that the theoretical strength estimates were achieved. Tear test evaluation showed this type of cloth to be greatly superior to monofilament cloth. Thus cloth B is recommended for future weaving programs.

C. MATERIAL EVALUATION

Cloth A and cloth B were evaluated for strength and stiffness characteristics. Tests were performed on the unwoven wire, the unwoven strand for cloth B, and on the woven cloth in both warp and fill directions. Efficiencies of the strand and cloth were calculated using the unwoven wire as 100 percent. This calculation shows the loss of strength and stiffness due to weaving.

Stress-strain curves were plotted showing the relationship in stiffness of the unwoven wire, strand, and woven cloth in both warp and fill directions.

In addition to the evaluation of cloth A and cloth B, three other evaluations were performed as follows:

- (1) The René 41 cable was checked for the specification strength requirement and reported.
- (2) The stainless steel cloth purchased for the three-foot model fabrication was tested to obtain tensile strength in the warp and fill direction.
- (3) The evaluation of the CS-105 coating when applied to the new cloths A and B is also reported.

The five evaluations listed are summarized in the following test reports.

1. Cloth A Evaluation

Cloth A is woven of 0.0021-inch-diameter wires and has a mesh of 200 per inch in both warp and fill. Test conditions are presented in Table 11. Test specimens were notched and torn; all wires were continuous.

Table 11. Cloth A Evaluation Test Conditions (Instron Machine)

	GAGE LENGTH (Inches)	CROSSHEAD SPEED (Inches /Minute)	
		FIRST 3 MINUTES	AFTER 3 MINUTES
WIRE	2	0.02*	0.20**
	6	0.08*	0.20
	10	0.10*	1.00
	14	0.14*	1.00
	18	0.18*	1.00
CLOTH***	GAGE LENGTH (Inches)	CROSSHEAD SPEED (Inches /Minute)	
	2	0.05	
	4	0.10	
	6	0.15	
	8	0.20	

*1.0 Percent /Minute Strain

**10 Percent /Minute Strain

***Specimen Width = 1 Inch.

Temperature = 73°F

Relative Humidity = 50 percent

Tests were performed on the wire used in weaving. All samples were obtained from the same spool, and 25 were tested in tension. Ultimate tensile strength, yield strength, modulus of elasticity, and percent elongation at failure are reported in Table 12.

Table 12. 0.0021-Inch-Diameter Reno Wire Tensile Tests

SPECIMENS	LOAD ULTIMATE (Pounds)	LOAD YIELD (Pounds)	STRESS ULTIMATE (psi)	STRESS YIELD (psi)	MODULUS OF ELASTICITY ($E \times 10^6$ in psi)	ELONGATION (Percent)
21	0.579	0.355	168,000	103,000	26	27
22	0.586	0.355	170,000	103,000	27	28
23	0.588	0.362	170,000	105,000	23	28
24	0.588	0.355	170,000	103,000	26	28
25	0.588	0.359	170,000	104,000	26	28
Avg	0.586	0.357	170,000	104,000	26	28
61	0.578	0.355	168,000	103,000	29	28
62	0.582	0.359	169,000	104,000	29	27
63	0.583	0.359	169,000	104,000	28	28
64	0.583	0.355	169,000	103,000	29	28
65	0.581	0.359	168,000	104,000	26	27
Avg	0.581	0.358	168,000	104,000	28	28
101	0.578	0.359	168,000	104,000	28	27
102	0.586	0.352	170,000	102,000	30	28
103	0.586	0.352	170,000	102,000	30	29
104	Jaw Break	---	---	---	---	---
105		0.359	169,000	104,000	29	28
Avg	0.583	0.356	169,000	103,000	29	28
141	0.579	0.359	168,000	104,000	30	26
142	0.582	0.359	169,000	104,000	29	28
143	0.582	0.359	169,000	104,000	27	26
144	0.583	0.359	169,000	104,000	30	28
145	0.579	0.359	168,000	104,000	30	27
Avg	0.581	0.359	169,000	104,000	29	27
181	0.581	0.359	170,000	104,000	30	28
182	0.580	0.356	168,000	103,000	30	20
183	0.581	0.355	169,000	103,000	29	19
184	0.581	0.356	169,000	103,000	29	19
185	0.583	0.358	169,000	104,000	30	19
Avg	0.581	0.357	169,000	103,000	30	21
Total	0.582	0.357	169,000	104,000	28	28

NOTE: Specimens coded as follows:
101 - 10-inch gage length specimen No. 1.

Tensile tests were performed on the woven cloth. Twenty specimens were tested in the warp direction, and 20 specimens were tested in the fill direction. Ultimate tensile strength, yield strength, modulus of elasticity and percent elongation at failure are reported in Tables 13 and 14.

Table 13. Cloth A Breaking Tests (Warp Direction)

NUMBER	LOAD ULTIMATE (Pounds per Inch)	LOAD YIELD (Pounds per Inch)	MODULUS OF ELASTICITY ($E \times 10^6$ in psi)	ELONGATION (Percent)	STRESS ULTIMATE (psi)	STRESS YIELD (psi)
W21	72	42	5.1	11.3	104,000	61,000
W22	69	41	5.7	9.8	100,000	59,000
W23	74	46	6.1	11.3	107,000	66,000
W24	71	42	6.0	10.5	103,000	61,000
W25	71	41	5.3	11.5	103,000	59,000
Avg	71	42	5.6	10.9	103,000	61,000
W41	67	42	6.5	7.6	970,000	61,000
W42	69	42	6.5	8.8	100,000	61,000
W43	72	44	6.4	8.9	104,000	64,000
W44	70	42	6.3	9.0	101,000	61,000
W45	71	43	6.4	9.0	103,000	62,000
Avg	70	43	6.4	8.7	101,000	62,000
W61	68	41	6.2	8.0	98,000	59,000
W62	69	41	6.0	9.0	96,000	59,000
W63	67	44	6.6	7.7	97,000	64,000
W64	68	42	6.1	8.4	98,000	61,000
W65	70	43	6.3	9.0	101,000	62,000
Avg	67	42	6.2	8.6	98,000	61,000
W81	66	42	6.1	8.1	95,000	61,000
W82	67	41	6.1	8.8	97,000	59,000
W83	63	40	6.0	6.2	91,000	58,000
W84	64	40	6.2	7.5	93,000	58,000
W85	66	42	5.8	7.8	95,000	61,000
Avg	65	41	6.0	7.7	94,000	59,000
Total	68	42	6.0	9.0	99,000	61,000

Table 14. Cloth A Breaking Tests (Fill Direction)

NUMBER	LOAD ULTIMATE (Pounds per Inch)	LOAD YIELD (Pounds per Inch)	MODULUS OF ELASTICITY ($E \times 10^6$ in psi)	ELONGATION (Percent)	STRESS ULTIMATE (psi)	STRESS YIELD (psi)
F21	99	71	14.1	6.4	143,000	101,000
F22	99	68	12.4	8.4	143,000	98,000
F23	98	69	14.1	7.0	142,000	100,000
F24	79	55	11.1	5.5	114,000	80,000
F25	77	53	13.4	7.0	111,000	77,000
Avg	90	63	13.0	6.9	130,000	91,000

Table 14. Cloth A Breaking Tests (Fill Direction) (Continued)

NUMBER	LOAD ULTIMATE (Pounds per Inch)	LOAD YIELD (Pounds per Inch)	MODULUS OF ELASTICITY ($E \times 10^6$ in psi)	ELONGATION (Percent)	STRESS ULTIMATE (psi)	STRESS YIELD (psi)
F41	110	84	19.4	5.0	159,000	122,000
F42	98	70	16.0	6.7	142,000	101,000
F43	97	68	15.3	7.5	140,000	98,000
F44	102	70	17.1	7.9	148,000	101,000
F45	105	72	17.2	8.0	152,000	104,000
Avg	102	73	17.0	7.0	148,000	105,000
F61	97	72	17.7	4.1	140,000	104,000
F62	97	68	16.1	7.3	140,000	89,000
F63	98	70	16.8	5.9	142,000	101,000
F64	77	55	12.4	4.9	111,000	80,000
F65	78	54	12.5	6.1	103,000	78,000
Avg	89	64	15.1	5.7	127,000	92,000
F81	113	81	20.8	6.5	164,000	117,000
F82	98	69	16.0	7.1	142,000	100,000
F83	95	66	16.4	6.4	138,000	96,000
F84	102	69	17.3	8.1	148,000	100,000
F85	102	70	18.2	8.1	148,000	101,000
Avg	102	71	17.7	7.2	148,000	102,000
Total	96	68	15.7	6.7	138,000	98,000

The target strength of this cloth is 87 pounds per inch in both the warp and fill directions. The openness factor of the cloth is 34 percent.

a. Test Results. The average results for wire are as follows:

Tensile - Ultimate = 0.582 pound
Tensile - Ultimate = 169,000 psi

Tensile - Yield = 0.357 pound
Tensile - Yield = 104,000 psi

Modulus = 26,000,000 psi
Elongation at failure = 26 percent.

The test results for the five different gage lengths are uniform except for modulus values. Actually the wire tends to slip a certain amount in the jaws, and the resulting computed modulus is generally low. Thus different gage lengths (2 to 18 inches) are used in testing to isolate the amount of slippage.

For cloth A, the breaking ultimate strengths in the warp direction are consistent and average 68 pounds per inch. This is 77 percent of the target strength.

The breaking ultimate strengths in the fill direction are quite inconsistent, ranging from a high of 113 pounds per inch to a low of 77 pounds per inch. This gives an average of 96 pounds per inch, which is 109 percent of the target strength.

The breaking yield strengths in the warp direction are consistent and average 42 pounds per inch, which is 62 percent of ultimate.

The tensile yield strengths in the fill direction vary about the same as the ultimate strengths. The average value is 71 percent of the ultimate average.

The average elongation at failure is 9.0 percent in the warp direction and 6.7 percent in the fill direction.

The average modulus in the warp direction is 6,000,000 psi. The average modulus in the fill direction is 15,700,000 psi.

b. Conclusions. The results of the wire tests are consistent and show an ultimate tensile value for the wire of 169,000 psi based on a nominal wire diameter of 0.0021-inch.

The results of the cloth tests in the warp direction show consistent results on an ultimate tensile strength of 68 pounds per inch. This value is less than the expected value.

The results of the cloth tests in the fill direction show inconsistent results, indicating that the fill wire used was inconsistent.

A further conclusion is apparent when comparison of warp and fill strength is made. More of the crimp is put into the warp wires; thus their strength is reduced. This is even more apparent when comparing modulus values as shown in Figure 108.

The structural efficiency data comparing cloth with the original wire is shown in Table 15.

Table 15. Structural Efficiency Data (Cloth A)

STRUCTURAL CONDITION	DIREC-TION	ULTIMATE (psi)	YIELD (psi)	MODULUS OF ELASTICITY (lb in psi)	ELONGA-TION (Percent)	YIELD ELONGA-TION (Percent)
0.0021 Wire	-	169,000	104,000	29,000,000	26.0	0.4
Cloth	W	99,000	61,000	6,000,000	9.0	1.1
Cloth	F	138,000	98,000	15,700,000	6.7	0.6
Cloth Efficiency	W	58 percent	58 percent	21 percent	33.0	- -
Cloth Efficiency	F	82 percent	95 percent	54 percent	25.0	- -

2. Cloth B Evaluation

Cloth B is woven of a strand (10 turns per inch) consisting of seven 0.0016 inch-diameter wires (six wires twisted about a center wire) and has a mesh of 100 per inch in both warp and fill. Test conditions are presented in Table 16.

Tests were performed on the wire used in weaving. All samples were obtained from the same spool, and samples were tested in tension. Ultimate tensile strength, yield strength, modulus of elasticity, and percent elongation at failure are reported in Table 17.

Tensile tests were performed on the strand used in weaving. All samples were obtained from the same spool and were tested in tension. Ultimate tensile strength, yield strength, modulus of elasticity, and percent elongation at failure are reported in Table 18.

Tensile tests were performed on the woven cloth. Twenty specimens were tested in the warp direction, and 20 specimens were tested in the fill direction. Ultimate tensile strength, yield strength, modulus of elasticity and percent elongation at failure are reported in Tables 19 and 20.

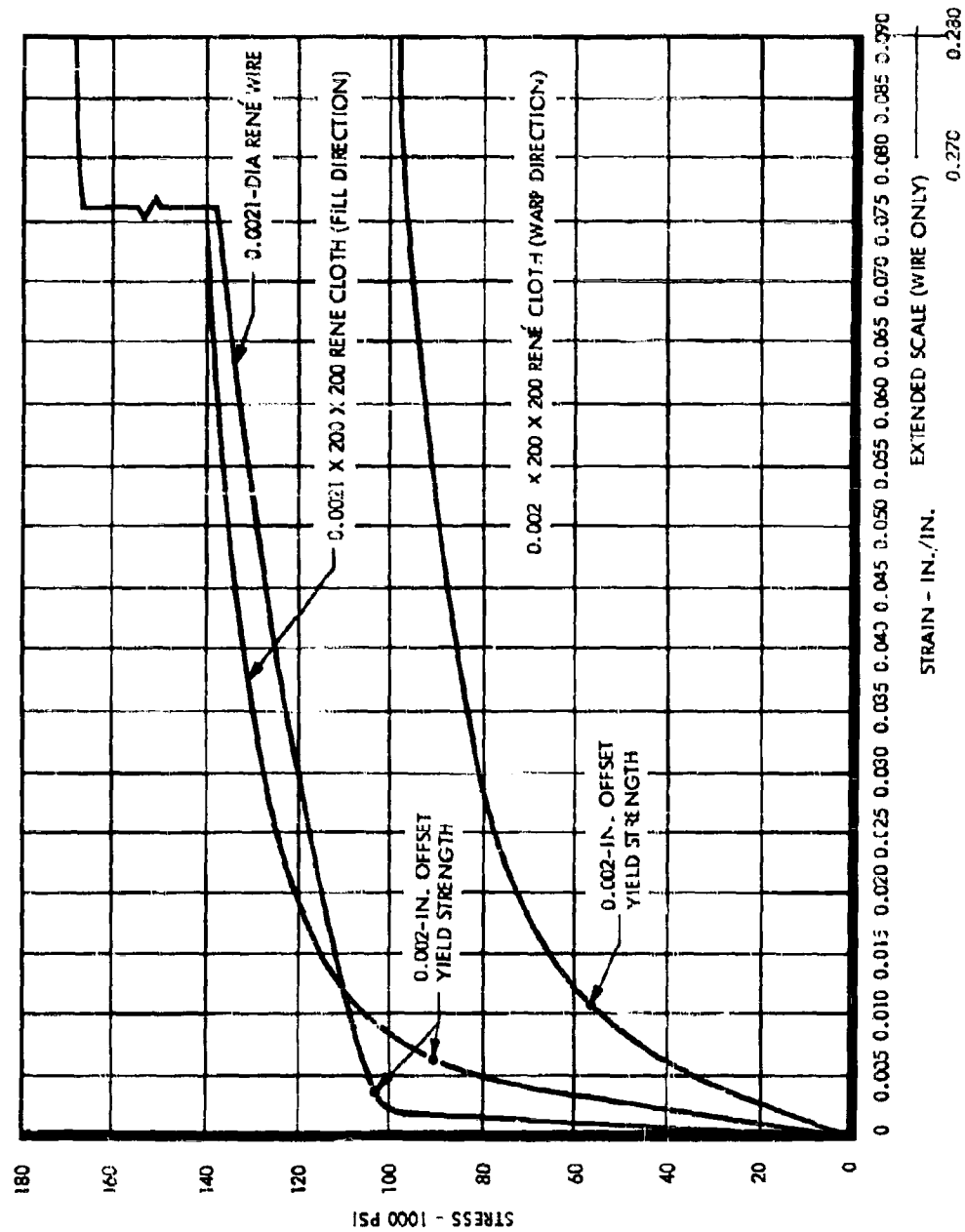


Figure 108. Cloth A Typical Stress-Strain Diagrams for René Wire and Cloth (Six-Inch Gage Lengths)

Table 16. Cloth B Evaluation Test Conditions (Instron Machine)

WIRE	GAGE LENGTH (Inches)	CROSSHEAD SPEED (Inches/Minute)			
		FIRST 4 MINUTES	AFTER 4 MINUTES		
	2	0.02*	0.20**		
	6	0.06*	0.20		
	10	0.10*	0.10		
14	0.14*	1.0			
16	0.18+ *	1.0			
†Run for 3 minutes instead of 4.					
STRAND	GAGE LENGTH (Inches)	CROSSHEAD SPEED (Inches/Minute)	CLOTH***	GAGE LENGTH (Inches)	CROSSHEAD SPEED (Inches/Minute)
	6	0.5		2	0.05
	10	0.250		4	0.10
	14	0.350		6	0.15
	18	0.45		8	0.20

* 1.0 Percent/Minute Strain

** 10 Percent/Minute Strain

***Specimen width = 1 inch; specimens were cut and raveled; edges trimmed after raveling.
Temperature = 73°F. Relative Humidity = 50 percent.

Table 17. 0.0015-Inch-Diameter René Wire Tension Tests

SPECIMEN	LOAD ULTIMATE (Pounds)	LOAD YIELD (Pounds)	STRESS ULTIMATE (psi)	STRESS YIELD (psi)	MODULUS OF ELASTICITY ($E \times 10^{-6}$ in psi)	ELONGATION (Percent)
21	0.312	0.209	176,000	118,000	30.5	22
22	0.321	0.207	181,000	117,000	31.2	25
23	0.320	0.207	181,000	117,000	31.5	23
24	0.316	0.214	178,000	121,000	28.3	23
25	0.318	0.203	179,000	115,000	30.2	24
Avg	0.317	0.208	179,000	117,000	30.3	23
61	0.313	0.205	177,000	116,000	30.1	24
62	0.311	0.205	176,000	116,000	29.2	23
63	0.313	0.200	177,000	113,000	28.6	23
64	0.316	0.203	178,000	115,000	29.5	24
65	0.315	0.205	173,000	116,000	30.7	22
Avg	0.314	0.203	177,000	114,000	29.6	23
101	0.316	0.209	178,000	118,000	31.4	22
102	0.317	0.209	179,000	118,000	29.4	22
103	0.317	0.205	179,000	116,000	31.7	23
104	0.314	0.203	177,000	115,000	31.4	22
105	0.317	0.209	179,000	116,000	31.7	23
Avg	0.316	0.207	178,000	116,000	31.1	22

Table 17. 0.0015-Inch-Diameter René Wire Tensile Tests (Continued)

SPECIMEN	LOAD ULTIMATE (Pounds)	LOAD YIELD (Pounds)	STRESS ULTIMATE (psi)	STRESS YIELD (psi)	MODULUS OF ELASTICITY ($\text{E} \times 10^{-6}$ in psi)	ELONGATION (Percent)
141	0.314	0.209	178,000	116,000	32.2	22
142	0.318	0.203	179,000	115,000	31.8	23
143	0.319	0.207	180,000	117,000	32.2	23
144	0.319	0.203	180,000	115,000	32.6	24
145	0.318	0.203	179,000	115,000	32.8	24
Avg	0.318	0.205	179,000	115,000	32.3	22
181	0.313	0.209	177,000	116,000	32.2	17
182	0.316	0.203	178,000	115,000	32.2	23
183	0.311	0.209	176,000	116,000	32.2	21
184	0.317	0.209	179,000	116,000	31.5	22
185	0.317	0.209	179,000	116,000	32.2	23
Avg	0.315	0.208	178,000	116,000	32.1	21
Total Avg	0.316	0.206	178,000	116,000	32	22

Table 18. René Strand Tensile Tests (Seven 0.0015-Inch-Diameter Wires)

SPECIMEN	LOAD ULTIMATE (Pounds)	LOAD YIELD (Pounds)	STRESS ULTIMATE (psi)	STRESS YIELD (psi)	MODULUS OF ELASTICITY ($\text{E} \times 10^{-6}$ in psi)	ELONGATION (Percent)
61	2.45	1.54	198,000	124,000	28	24
62	--	1.53	--	123,000	28	--
63	2.47	1.54	199,000	124,000	27	23
64	2.42	1.50	195,000	121,000	30	24
65	2.42	1.50	195,000	121,000	26	24
Avg	2.44	1.52	197,000	123,000	28	24
101	--	1.50	--	121,000	28	--
102	--	1.50	--	121,000	29	--
103	2.44	1.50	197,000	121,000	29	22
104	--	1.50	--	121,000	29	--
105	2.37	1.53	191,000	123,000	28	19
106	2.46	--	198,000	--	--	--
107	2.46	--	198,000	--	--	--
108	2.45	--	198,000	--	--	--
109	2.43	--	196,000	--	--	--
1010	2.45	--	198,000	--	--	--
1011	2.46	--	198,000	--	--	--
1012	2.44	--	197,000	--	--	--
1013	2.44	--	197,000	--	--	--
1014	2.46	--	198,000	--	--	--
Avg	2.44	1.50	197,000	121,000	29	20

Table 19. Cloth B Breaking Tests (Fill Direction)(Continued)

SPECIMEN	LOAD ULTIMATE (Pounds)	LOAD YIELD (Pounds)	STRESS ULTIMATE (psi)	STRESS YIELD (psi)	MODULUS OF ELASTICITY ($E \times 10^{-6}$ in psi)	ELONGATION (Percent)
F81	185	86	183,000	76,000	6.2	8.8
F82	193	88	171,000	78,000	5.8	11.6
F83	199	86	175,000	76,000	5.6	15.0
F84	204	99	170,000	83,000	5.0	11.3
F85	205	105	175,000	90,000	4.8	8.5
Avg	197	95	171,000	81,000	5.5	11.0
Total Avg	193	88	172,000	78,000	5.3	12.0

Note: The ultimate and yield psi values shown are corrected for the fact that specimens had mesh counts of less than 100 per inch.

Table 20. Cloth B Breaking Tests (Warp Direction)

SPECIMEN	LOAD ULTIMATE (Pounds)	LOAD YIELD (Pounds)	STRESS ULTIMATE (psi)	STRESS YIELD (psi)	MODULUS OF ELASTICITY ($E \times 10^{-6}$ in psi)	ELONGATION (Percent)
W21	183	61	146,000	49,000	2	20
W22	186	62	149,000	50,000	2	19
W23	183	61	146,000	49,000	2.2	17
W24	184	62	147,000	50,000	2.3	17
W25	185	60	148,000	48,000	2	17
Avg	184	61	147,000	49,000	2.1	18
W41	184	62	147,000	50,000	2.5	15
W42	185	61	148,000	49,000	2.5	15
W43	177	62	142,000	50,000	2.5	14
W44	188	62	149,000	50,000	2.6	15
W45	184	61	147,000	49,000	2.5	15
Avg	183	61	147,000	50,000	2.5	15
W61	188	61	150,000	65,000	2.7	14
W62	189	64	151,000	51,000	2.6	14
W63	181	64	145,000	51,000	3.2	13
W64	184	65	147,000	52,000	2.6	14
W65	185	64	148,000	51,000	2.6	15
Avg	185	68	148,000	52,000	2.7	14
W81	184	74	147,000	59,000	2.9	13
W82	180	61	144,000	49,000	2.8	13
W83	177	65	142,000	52,000	3.0	13
W84	179	65	143,000	52,000	2.8	13
W85	190	65	152,000	52,000	2.9	14
Avg	182	66	145,000	52,000	2.9	13
Total Avg	183	64	147,000	50,000	2.5	15

Note: The ultimate and yield psi values shown are corrected for the fact that specimens had mesh counts of less than 100 per inch.

The target strength of this cloth is 175 pounds per inch in both the warp and fill directions. The openness factor of the cloth is 27 percent. The actual measured diameter of the wire is 0.0015 inch and hereafter is referred to as 0.0015 inch instead of the manufacturer's 0.0016-inch diameter callout.

a. Test Results. The average results for wire are as follows:

Tension - Ultimate = 0.316 (lb)
Tension - Ultimate = 178,000 (psi)
Tension - Yield = 0.206 (lb)
Tension - Yield = 116,000 (psi)
Modulus = 32×10^6 (psi)
Elongation at Failure = 22 (percent).

The average results for strand are as follows:

Tension - Ultimate = 2.43 (lb)
Tension - Ultimate = 196,000 (psi)
Tension - Yield = 1.51 (lb)
Tension - Yield = 122,000 (psi)
Modulus = 29×10^6 (psi)
Elongation at Failure = 22 (percent).

For cloth the tensile ultimate strengths in the warp direction are consistent and average 183 pounds per inch. This is $183/175 = 1.04$ or 104 percent of the target strength.

The tensile ultimate strengths in the fill direction are not as consistent and average 193 pounds per inch. This is $193/175 = 1.10$ or 110 percent of the target strength.

The tensile yield strengths in the warp direction are consistent and average 64 pounds per inch, which is 35 percent of ultimate.

The tensile yield strengths in the fill direction average 88 pounds per inch, which is 45 percent of the ultimate average.

The average elongation at failure is 15 percent of ultimate in the warp direction and 12 percent of ultimate in the fill direction.

The average modulus in the warp direction is 2.5×10^6 psi. The average modulus in the fill direction is 5.3×10^6 psi.

b. Conclusions. The structural efficiency data comparing cloth and strand to the original wire is shown in Table 21.

Table 21. Structural Efficiency Data (Cloth B)

STRUCTURAL CONDITION	DIRECTION	STRESS ULTIMATE (psi)	STRESS YIELD (psi)	MODULUS OF ELASTICITY ($E \times 10^{-6}$ in psi)	ELONGATION (Percent)	YIELD ELONGATION (Percent)
0.0015-In. -Dia Wire	- -	178,000	116,000	32	22	0.4
0.0015-In. -Dia Strands	- -	196,000	122,000	29	22	0.7
Cloth	Warp	147,000	90,000	2.5	15	1.8
Cloth	Fill	172,000	78,000	5.3	12	1.4
Strand Efficiency	- -	110%	105%	90%	100	- -
Cloth Efficiency	Warp	82%	43%	8%	68	- -
Cloth Efficiency	Fill	96%	67%	16%	55	- -

A comparison of modulus values is shown in Figure 109.

3. René Cable (1/32 and 3/32) Tension Tests (Standard Aircraft Cable Configuration)

The minimum ultimate tensile strengths specified on the order were 110 pounds for the 1/32 cable and 920 pounds for the 3/32 cable. The 1/32 value was later reduced to 100 pounds. Tests were performed on the delivered cable as follows:

1/32 Cable (3 x 7 Construction 0.0048 Wire)

Specimen No. 1 = 102 lb
Specimen No. 2 = 104 lb
Specimen No. 3 = 103 lb
Specimen No. 4 = 103 lb
Average = 103 lb

3/32 Cable (7 x 7 Construction 0.0104 Wire)

Specimen No. 1 = 990 lb
Specimen No. 2 = 929 lb
Specimen No. 3 = 884 lb.

Strain rate was one percent per inch per minute for 1/32 cable; gage length was 10 inches for 1/32 cable.

Strain rate for 3/32 cable was 25 percent per inch per minute for specimen No. 1 and 2.5 percent per inch per minute for specimens No. 2 and 3.

For 3/32 cable it was necessary to swage ends on the cable; approximately a 9-inch gage length resulted. Specimen No. 3 slipped in the jaws, was reloaded and was not considered a good test.

4. Stainless Steel Cloth Evaluation

A quantity of stainless steel cloth was purchased for use in constructing the three-foot model. Upon receipt of this cloth, tests were performed to determine its strength properties. The cloth tested was Type 304, 0.0021-inch diameter wire, 200 x 200 mesh, and plain woven.

Tension tests performed were as follows:

10 specimens in the warp direction.
10 specimens in the fill direction.

Testing conditions were as follows:

room temperature
specimen size = 1 x 6 inches
grip length = 3 inches
crosshead speed = 0.2 inch per minute
chart speed = 2 inches per minute.

A summary of the stainless steel cloth tension tests is presented in Table 22.

5. CS-105 Coating Evaluation

A limited test program was performed to approximate the amount of leakage that may occur in the Mach 10 wind tunnel test.

a. Hot Roc Tests. Four specimens were tested as indicated in Table 23.

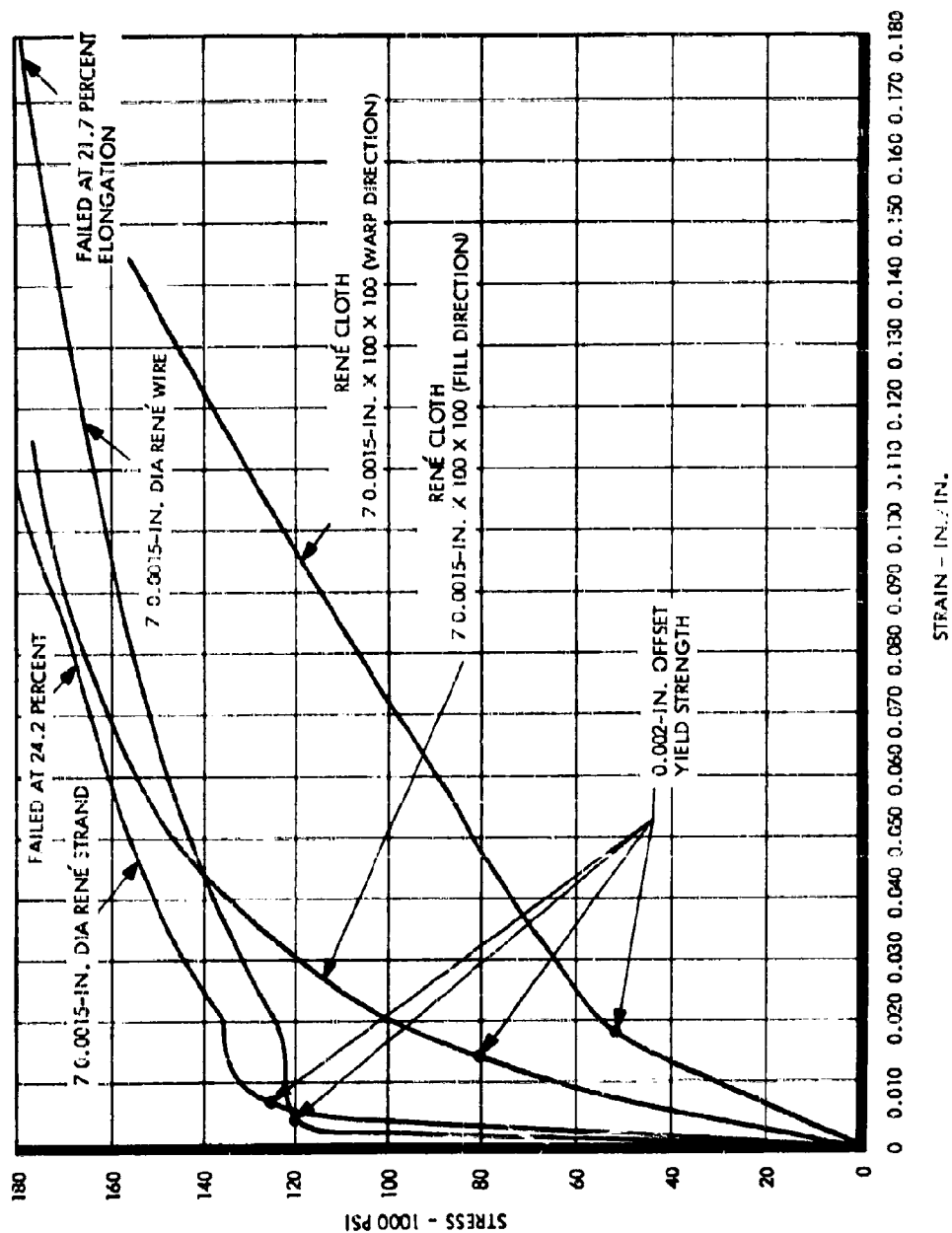


Figure 109. Cloth B Typical Stress-Strain Diagrams for René Wire, Strand, and Cloth (Six-Inch Gage Lengths)

Table 22. Summary of Stainless Steel Cloth Tension Tests

WARP DIRECTION		FILL DIRECTION	
SPECIMEN NO.	ULTIMATE LOAD (Lb/in.)	SPECIMEN NO.	ULTIMATE LOAD (Lb/in.)
W1	50	F1	57
W2	43	F2	57
W3	50	F3	60
W4	49	F4	57
W5	49	F5	56
W6	51	F6	58
W7	48	F7	62
W8	40	F8	59
W9	50	F9	58
W10	52	F10	58
Average	49	Average	58

Table 23. Hot Roc Tests

TEST NO.	TYPE OF CLOTH	NUMBER OF COATS	BACK-UP PRESSURE (psi)	TEMP (°F)	TIME AT TEMP
1	A	12	4	1275	2
2	A	12	4	1275	10
3	B	12	4	1275	2
4	B	12	4	1275	10

One coat of CS-105 approximates 1 oz/sq yd.

Outside of some flaking, the coating did not appear porous after testing. It was not necessary to adjust the pressure during test, indicating that leakage was less than the accuracy of the equipment.

b. Permeability Tests. Six specimens were tested in the environmental laboratory as shown in Table 24. Four specimens were fabricated by welding together two halves. This was done as an attempt to check if more leakage would occur at the welds.

Table 24. Permeability Tests

TEST NO.	TYPE OF CLOTH	WELD OR CONTROL	NUMBER OF COATS	BACK-UP PRESSURE (psi)	TEMP (°F)	TIME AT TEMP
3	A	Control	12	2	1500	20
1	A	Welded	10	2	1500	20
5	A	Welded	10	4	1275	20
8	B	Control	12	4	1275	20
6	B	Welded	10	4	1275	--
2	B	Welded	10	2	1500	60

The leak rates are plotted in Figure 110.

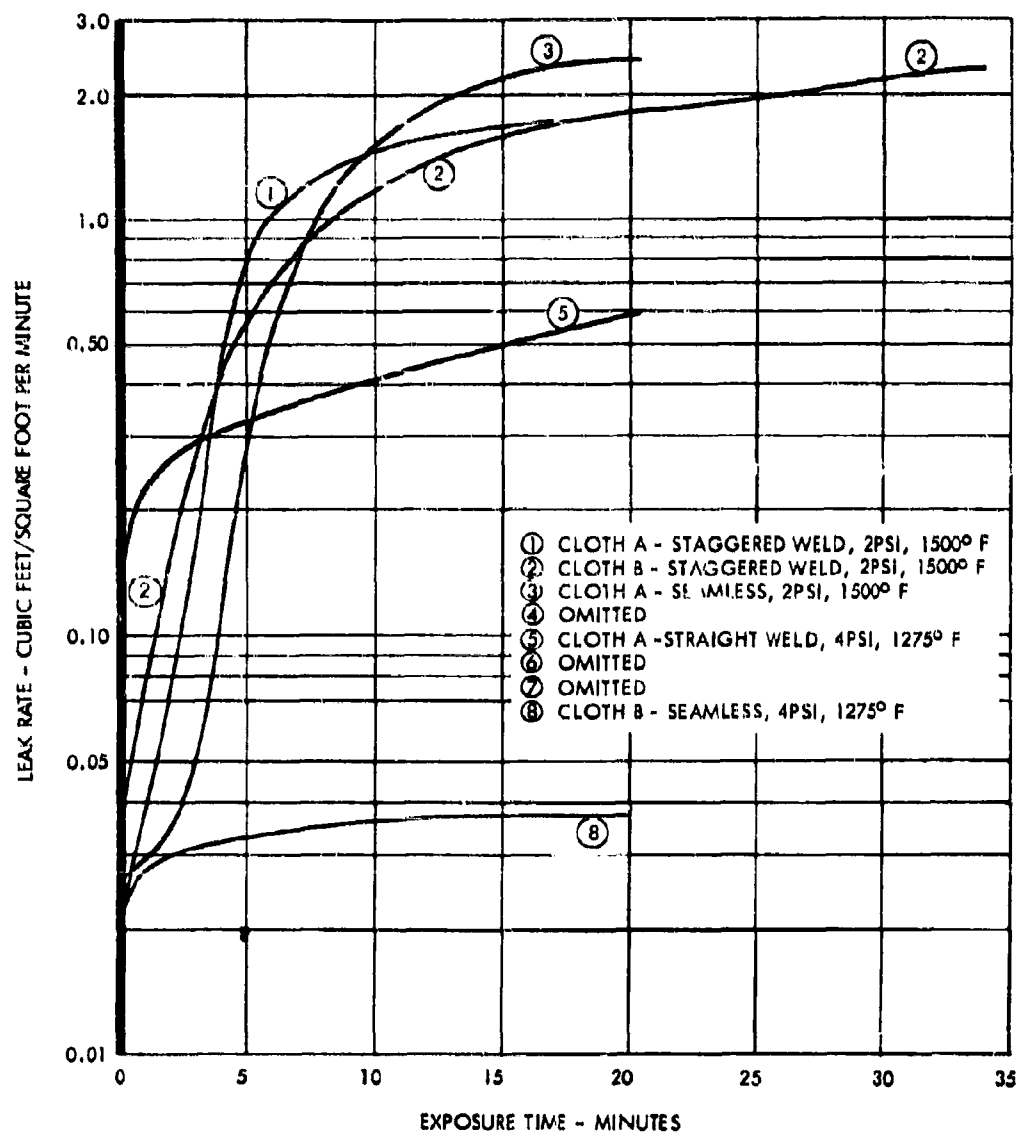


Figure 110. Leak Rates

Specimen No. 3 blistered opposite the heated side. Apparently only one or two coats were lost, however, as pressure was maintained.

Specimen No. 6 could not be tested to completion as a major leak developed in the weld area.

Considerable more charring of the CS-105 occurs at 1500°F than at 1275°F.

D. WELDING INVESTIGATION

1. Equipment

The following resistance welding machines were available and deemed worthy of consideration for welding of metal cloth such as that proposed for use for the subject contract.

- (1) Spot Welder (Federal Machine and Welder Co). 100-kva, a-c, single-phase 42-inch throat, welding force range 100 to 3000 pounds.
- (2) Seam Welder (Sciaky Bros, Inc). 200-kva. 3-phase, 54-inch throat. welding force range 600 to 4500 pound.
- (3) Seam Welder (Resistance Welder Corp). 150-kva, a-c, single-phase, 48-inch throat, welding force range 300 to 2300 pound.
- (4) Seam Welder (Thomson Electric Welder Co). 50-kva, a-c, single-phase, 22-inch throat, welding force range 10 to 500 pounds.
- (5) Spot Welder (United Corporation - Weldmatic). 40-watt-second, capacitor-discharge, pincer and probe-type electrodes; for tack welding.

2. Equipment Evaluation

For equipment evaluation the material used was René 41 0.0015-inch diameter, 200 x 200 wires per inch since this material was available and there was welding background information at hand.

Initial seam welding was done on the Sciaky machine. It was found that consistent strength welds could be obtained at weld speeds up to 80 inches per minute. This could be either a seam weld or roll-spot weld. It was necessary to sandwich the cloth between foil strips to prevent sticking of the cloth to the electrodes. The foil was peeled off after welding. Because of the inherent high weld force of this machine, parts had to be securely clamped and little guiding was possible during welding. This machine's use would be limited to flat, straight joints.

The resistance seam welder was found to have only slight advantage over the Sciaky welder. Guiding of parts was easier due to narrower wheels and lower weld force. Foil was required on only one side of the cloth. The weld strengths were comparable, but it was felt that small contoured parts would be difficult to handle here also.

Preliminary welding on the Thomson seam welder indicated that machine alterations and development time would be required to gain any appreciable advantages over the larger machines.

The Federal spot welder, although a low production machine (inches of weld per unit time), had over-balancing advantages. There was a minimum of clamping and fixturing required. Accessibility was good for welding of either size Ballute model. There was less danger of having hard-to-repair defects. The weld tensile-shear and slit-tear strengths were superior to those of seam welds. Foil sandwiching was required. Table 25 shows the results of welding, using the two machines showing the greatest promise.

Table 25. Welded Strengths of 0.0016-Inch-Diameter, 200 x 200 Mesh Rend 41

MACHINE MAKE	TYPE OF WELD	NO. OF ROWS	SPOTS/ IN. /ROW	TRAVEL (In. /Min)	TENSILE-SHEAR		SLIT TEAR	
					(Lb/In. Avg)	Efficiency	Lb	Efficiency
Sciaky	Roll-spot	2	8	80	44	80%	4.5	60%
Sciaky	Roll-spot	2	6	80	36	66%	5.0	67%
Sciaky	Seam	1	12	72	35	64%	4.3	57%
Sciaky	Seam	1	15	18	--	--	5.0	67%
Federal	Spot	2	7	--	41	75%	6.7	89%

The spot welds were fairly good in tensile-shear and by far the best in slit-tear. The tests were performed in the fill direction.

3. Joint Design

Since spot welding was preferable to seam welding, optimum joint design was determined. Previous work indicated that every wire normal to the direction of loading must be welded and that tear resistance is best when spots are separated. This dictated a two-row staggered pattern with the spot spacing dependent upon the size spot obtainable for a given cloth.

In preparation for welding the 36-inch Ballute, a weld schedule was established on the Federal spot welder for Type 304 stainless steel 0.0021-inch diameter, 200 x 200 cloth. Welds were made in two-row patterns at different spacings normal to the direction of loading. This was also done on two and three thickness combinations with the weld rows at 45 degrees to the direction of loading. Results of these tests are shown in Table 26.

Table 26. Spot Weld Strengths in Stainless Steel Cloth (Fill)

DIRECTION OF WELD ROWS	NO. OF ROWS	SPOT/ INCH/ROW	TENSILE-SHEAR STRENGTH (lb avg)	PERCENT EFFICIENCY
Normal	2	8	48	83
Normal	2	6	44	76
Normal	2	4	37	64
Normal	2	2	21	31
3 Thickness	2	6	50	86
2 Thickness	2	6	42	72

The two-row staggered pattern with eight spots per inch per row was selected as the standard for welding of the 36-inch Ballute.

4. Weld Strength Evaluation (Cloths A and B)

A summary of weld strength evaluation test results is presented in Table 27.

After consideration of the tensile strength, tear resistance, fabrication costs, and reliability, it was decided to use a two-row staggered pattern of seven spots per inch per row and a row spacing of 3/32 to 1/8 inch for both A and B cloths.

Table 27. Summary of Weld Strength Evaluation Test Results

CLOTH	DIRECTION	SPOT-WELD INFORMATION		TENSILE STRENGTH 70°F (Lb./In.)	JOINT EFFICIENCY (Percent)	STRENGTH AT 1500°F (Lb./In.)	JOINT EFFICIENCY (Percent)	TENSILE TEAR STRENGTH 70°F (Lb./In.)	JOINT EFFICIENCY (Percent)
		No. of Rows	No. of Spots/Inch/Row						
A	Fill	1	9	59	63	26	54	18	95
A	Fill	1	11	61	66	--	--	19	100
A	Fill	2	7	64	69	--	--	21	100
A	Fill	2	9	76	92	33	69	21	100
A	Fill	Control		93	--	48	--	19	--
A	Warp	1	9	67	94	27	93	20	105
A	Warp	1	11	68	96	--	--	20	100
A	Warp	2	7	70	99	--	--	20	100
A	Warp	2	9	68	96	29	100	20	100
A	Warp	Control		71	--	29	--	20	--
B	Fill	1	7	143	80	--	--	58	97
B	Fill	2	7	172	94	--	--	53	88
B	Fill	Control		183	--	--	--	60	--
B	Warp	1	7	147	84	--	--	50	100
B	Warp	2	7	175	100	--	--	55	98
B	Warp	Control		174	--	--	--	56	--

E. FABRICATION TECHNIQUES

Preparation of gores and the welding sequence of all models was similar. Marking and cutting templates shown at the top of Figure 111 were made from the developed gore drawings. With the template on the cloth at 45 degrees to the warp, the material was marked and cut. Cable locating loops were first seam tack welded, located, and taped in place as shown at the bottom of Figure 111, then welded in place using the Federal welder, with the first spot as close as possible to the rod along the gore center line.

The gores were then loaded into coating frames and clamped as shown in Figure 112 with the match points coinciding with holes in the top frame which was a mask for the weld area. Both sides of the gore were sprayed with five coats of high-temperature silicone elastomer CS-105. Each coat was cured.

For the 36-inch model, gores were welded in pairs; then pairs were added one at a time to form a hemisphere. Pairs of gores were mounted on a formed tacking template and tack-welded every six inches with the Federal welder. Prior to tacking, sandwiching foil was taped in place covering the overlapped weld area. Spot spacing was uniformly controlled by the indexing attachment as shown in Figure 113. As each joint was welded, the foil was peeled off and the excess overlap material trimmed. Figure 114 shows the welding together of subassemblies. Welded joints were brush-coated with CS-105 and put through the normal coat and cure cycle.

When the two halves of the Ballute were ready for joining, one side was welded from the polar cap opening to the tangent point and the other side from the opening for about six inches. The inside polar cap was tacked in place and the hole cut out to provide the correct overlap. The outer cap was added and the three-thickness combination welded. The welded polar cap and joints were coated and cured. Figure 115 shows the joining of the Ballute halves. Match points were superimposed, and two tack welds made about five inches apart. The area to the first weld was filled in with spots and then another tack weld added. Welding was alternated from one side of the Ballute to the other. During the final closure, welding was interrupted for coating. Final few inches of welding was done with a special arm which was tapered out to a button electrode. Figure 116 shows the assembled model.

Fabrication of the ten-inch cloths A and B Ballutes generally followed the same processing. Tack welding of the gores up to the point of joining the halves was done on a plywood form made to the developed contour at the joint. Copper attached to the form was the conductor to which the welding lead was clamped.

The heavier and stiffer cloth B was easier to handle and weld. Figure 117 shows the welding of two gores with cable loops and match points visible. Cloth B can be welded without foil. Foil was used on one side when convenient to speed the welding process.

F. SUMMARY OF RESULTS

The development weaving program involved design procurement and evaluation of two new René cloths. These cloths would be stronger than the available René cloth. Cloth A was woven to commercial stainless steel cloth standards. Cloth B was woven of stranded wires to maintain flexibility of the heavier cloth.

Results of the weaving program show that the Cloth A design is too tight a weave to be woven of René wire in production quality. Cloth B, however, was woven successfully and is recommended for procurement on future phases of work.

Results of strength tests are summarized in Table 28.

The welding program was planned to determine the processing that would obtain the highest weld efficiency. Staggered rows of spot welds were concluded to be most efficient strengthwise and also most reliable tearwise.



Figure 111. Fabrication Templates

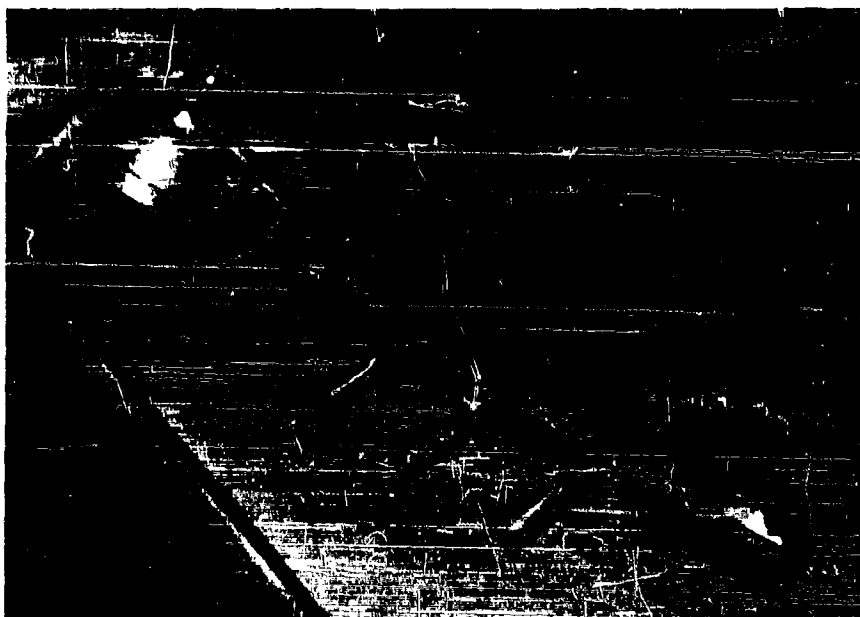


Figure 112. Clamping Gore in Coating Frame

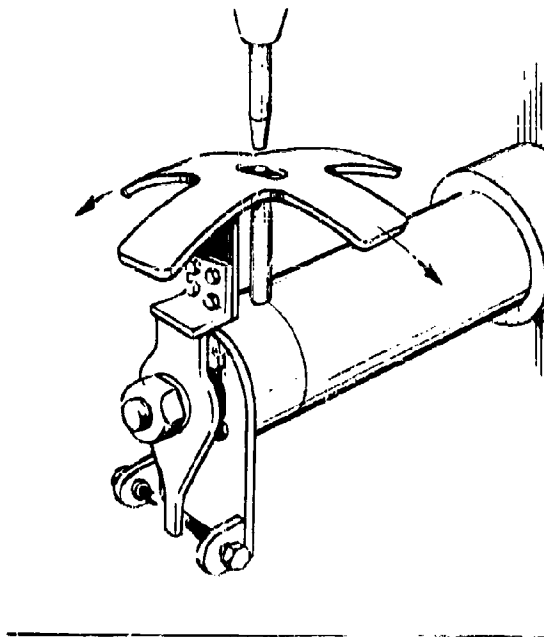


Figure 113. Indexing Attachment



Figure 114. Welding Subassemblies

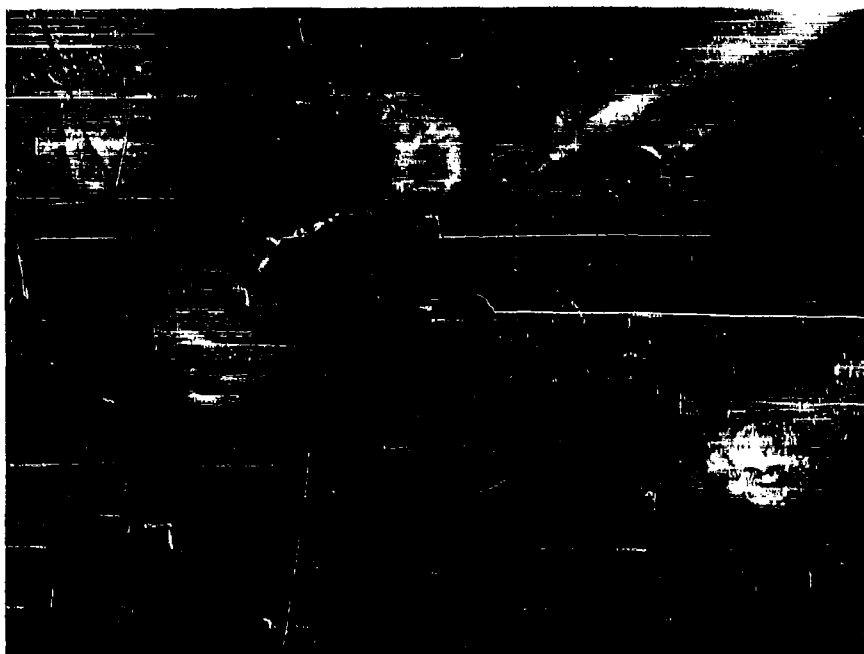


Figure 115. Joining Ballute Halves



Figure 116. Thirty-Six Inch Diameter Stainless Steel Ballute Model

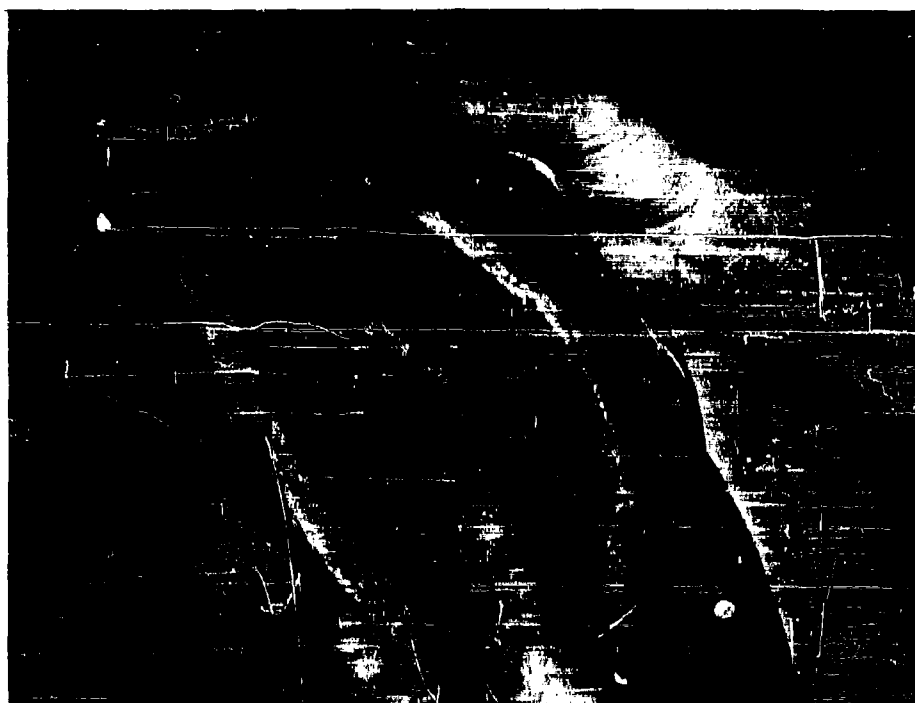


Figure 117. Welding Two Cloth B Gores

Table 28. Summary of Strength Tests

MATERIAL	CLOTH DESIGNATION	WIRE DIAMETER	MESH PER INCH	ULTIMATE TENSILE (Lb/In.)	
				WARP	FILL
Rene' 41	Original	0.0016	200 x 200	47	61
Rene' 41	Cloth A	0.0021	200 x 200	68	96
Rene' 41	Cloth B	7 - 0.0016	100 x 100	183	193
Stainless steel	Commercial	0.0021	200 x 200	48	64

Table 29 summarizes the most efficient weld results.

Table 29. Summary of Weld Results

MATERIAL	WARP DIRECTION			FILL DIRECTION		
	CONTROL	WELDED	PERCENT EFFICIENCY	CONTROL	WELDED	PERCENT EFFICIENCY
Cloth A	71	70	98	93	76	82
Cloth B	174	174	100	183	172	94

A summary comparison of weights is presented in Table 30.

Table 30. Summary Comparison of Weights

MATERIAL	CLOTH DESIGNATION	WIRE DIAMETER	MESH PER INCH	CLOTH WEIGHT (Oz/Yd ²)	ESTIMATED COATING REQUIRED (Oz/Yd ²)	ESTIMATED TOTAL WEIGHT (Oz/Yd ²)
René 41	--	0.0016	200 x 200	5.01	8	13
René 41	Cloth A	0.0021	200 x 200	8.75	8	17
René 41	Cloth B	7 - 0.0016	100 x 100	17.50	10	27

SECTION 7

INFLATION SYSTEMS STUDY

A. GENERAL

The function of a Ballute inflation system is to provide sufficient internal pressure P to maintain a symmetrically rigid decelerator.

Since the Ballute can be used in so many stabilization and deceleration applications each of which has peculiar thermal and structural considerations as well as a variety of altitude velocity regimes, optimization of the inflation system must be conducted separately for each mission. As in any airborne system, weight is one of the prime considerations in the determination of an optimum design. For this reason, a graphic summary of the most feasible methods of Ballute inflation versus weight is present in Figure 118.

The following systems were found to be worthy of detailed analysis:

- (1) Compressed gas in pressure vessels
- (2) Residual air within the Ballute
- (3) Gas generation by burning fuel
- (4) Chemically generated gas
- (5) Airborne compressors
- (6) Ram-air inflation.

B. COMPRESSED GAS IN PRESSURE VESSELS

Probably the most widely used method of producing large volumes of gas at relatively low pressures is storage at high pressures and small volumes in steel, wire-wound, fiberglass, etc bottles. The state-of-the-art in this area is progressing with the development of higher strength metals and compression equipment. Associated hardware in the form of tubing, solenoid, and pyrotechnic valves is available in the form of off-the-shelf items. Inflation rates may be easily controlled by metering with standard hardware.

The weight curves for the steel bottle systems and the fiberglass bottle systems shown in Figure 118 are based on catalogue weights for commercially available bottles. The titanium sphere weight curve was calculated from data obtained from a nomograph published by the Titanium Metals Corporation of America. Heat treated Ti-6Al-4V alloy was selected, and the design conditions for the bottles were assumed to be 7000 psi pressure and 100,000 psi design stress. This stress level gives a safety factor of 1.6 at 70°F.

In the three gas bottle systems the total system weight was determined by adding the weight of the compressed air and the weight of the control valve. The control valve was assumed to be simple, and its weight was estimated to vary from 1 to 3 pounds over the range of bottle sizes.

C. RESIDUAL AIR WITHIN THE BALLUTE

In certain high-altitude missions where the Ballute is relatively small and the altitude decrement is small, it is feasible to make use of the air trapped within the packaged Ballute as the inflation medium. If it is necessary to eliminate the predeployment stresses on the Ballute, the packaging canister may be hermetically sealed, creating a zero pressure differential across the Ballute fabric. This system insures rapid inflation and good reliability and eliminates the pressure vessel and valve requirements. However, it is limited to high-altitude applications.

D. GAS GENERATION BY BURNING SOLID FUEL

Chemical generation of gas by burning "explosive" type materials is a very reliable system that is being continually refined. Hot-gas and cool-gas generators are now available in some small

sizes as off-the-shelf items. Custom-made gas generators may be procured to fulfill almost any pressure volume requirement. Firing of these devices can be done either electrically or mechanically.

The gas generator curve in Figure 118 was calculated from the equation

$$Pv = wrT$$

where

Pv = energy in lb-ft

w = propellant weight in pounds

T = gas temperature in $^{\circ}F$

r = energy constant = 55 ft/ $^{\circ}R$ (a good average value for present-day ballistic generators)

The total weight of the gas generator systems was determined by arbitrarily multiplying the propellant weight by 1.5 to include the weight of the case and hardware. The 1.5 factor was estimated from limited data on hot-gas generators, and it assumes that the gas is generated hot and then cooled down to 70 $^{\circ}F$ within the balloon.

Two points are shown on the graph which indicate the weights of two cool-gas generator systems which were proposed by McCormick-Selph Associates, Hollister, California for use in specific inflatable devices.

E. CHEMICALLY GENERATED GAS

Re-entry recovery missions that allow inflation of the Ballute at extremely high altitudes permit the use of subliming solids or vaporizing liquids as the gas source. Since only very low pressures can be effected by this method, application is limited to orbital decay and high-altitude missions or as initial inflation of ram-air Ballutes in comparable altitude regimes.

Two examples of sublimating powder systems are shown in Figure 118. The points were calculated from the following data on the ECHO I and ECHO II balloon inflation systems:

	<u>Sublimating Solid</u>	<u>Weight</u>	<u>Density</u>	<u>Pressure</u>	<u>Volume</u>
ECHO I	Benzole acid	10	79		
	Antraquinone	20	89		
		30 lb	85 lb/ft ³	0.06 mm	525,000 ft ³
ECHO II	Acetanide	50 lb	72 lb/ft ³	0.2 mm	1,290,000 ft ³

F. AIRBORNE COMPRESSORS

A cursory examination of the feasibility of airborne compression equipment was conducted revealing several unfavorable attributes. The compression of rarified gases such as those encountered at higher altitudes imposes severe tolerance restrictions on the moving parts of the compressor. The rate at which large volumes of low-density gases can be pumped into an inflatable device renders the inflation time required prohibitive. The weight and volume of airborne compressors compare unfavorably with those of other systems.

G. RAM-AIR INFLATION

The practicability of the ram-air inflation concept had been proven in the subsonic velocity regime prior to the work accomplished under this contract. However, during the wind tunnel tests

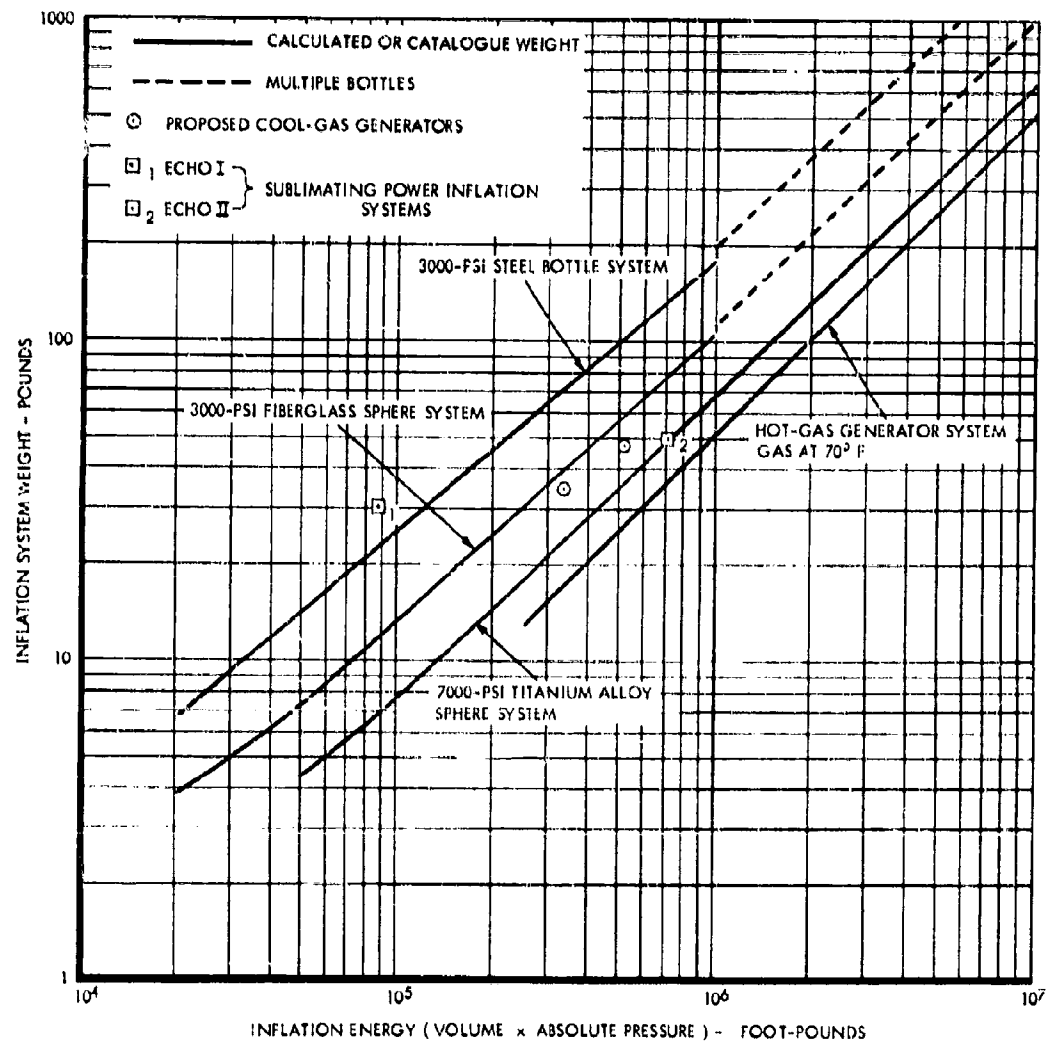


Figure 118. Inflation System Weights for Various Types of Systems

described in this report, data was obtained indicating feasibility from subsonic through hypersonic velocities.

Basically the ram-air concept converts the kinetic energy of the external dynamic pressure to internal static pressure by presenting an orifice or orifices normal to the air stream. The inflation aperture may be located at the nose of the Ballute or in the area of the equator. Internal pressures one to four times greater than the dynamic pressure have been noted in the supersonic velocity range when the side inlets were used. This indicates that configurations requiring inflation pressures greater than q may also be ram-air inflated.

Contrary to closed Ballute inflation the ram-air system may operate in a wide range of altitude-velocity combinations without over-pressurizing the Ballute or programming the inflation gas, thus reducing the structural requirements of the fabric.

Both the rate of inflation and the g forces imposed on the payload can be controlled by the size of the inflation orifice.

H. PACKAGE BULK FACTORS FOR THE VARIOUS INFLATION SYSTEMS

The package density, or the ratio of inflation system weight to volume of the inflation system, was calculated for each type of system as follows:

TYPICAL PACKAGING FACTORS

<u>Type of System</u>	<u>Density (lb/ft³)</u>
Hot-gas generator	60
Cool-gas generator	95
Fiberglass sphere, air at 3000 psi	35
Titanium sphere, air at 7000 psi	59
Steel bottle, air at 3000 psi	63
Sublimating powders	
ECHO I (benzoic acid and antraquinone)	85
ECHO II (acetanide)	72

The density of a typical hot-gas generator was determined from limited data on a generator proposed by the Frankford Arsenal. The density of the cool-gas generator system was determined from data on a McCormick-Solph proposal drawing. Bottle volumes were estimated from catalogue data, and the total weights, including the weight of the compressed air, were used in determining densities.

SECTION 8

CONFIGURATION INVESTIGATION

A. GENERAL

The purpose of this investigation was to evaluate all the analytical and experimental data and to conduct an optimum configuration design study.

Figure 119 is presented to assist in the description of the design study conducted. Major parameters affecting the towed inflatable decelerator design include:

- (1) The descent initial conditions (altitude, velocity, W/C_{DA} , flight angle.
- (2) The ballistic coefficient after decelerator deployment (W/C_{DA}).
- (3) The drag area, which is influenced by the size and drag coefficient (C_D) (efficiency).
- (4) The drag coefficient (C_D), which is influenced by L/d (tow-line length divided by payload diameter), d/d (decelerator diameter divided by payload diameter), and the decelerator nose shape.
- (5) The aerodynamic stability, which is influenced in part by decelerator shape.

Factors affecting the structural and weight design include:

- (1) The peak loading condition, which is influenced by all performance parameters.
- (2) The peak stress condition, which is influenced by the loading, size, and shape of the decelerator.
- (3) The stress-to-weight ratio, which is influenced by the aerodynamic heating temperatures and the type of material selected.
- (4) The weight of the decelerator, which is influenced by the design parameters plus the miscellaneous hardware weights such as the inflation system, if required.

Prior to showing the optimum configuration design details, the final stress, thermodynamic, and aerodynamic results are presented. These results were used for this specific design configuration study.

B. STRESS

1. Spherical Ballutes with Meridian Cable Suspension System

The meridian cable spherical type of drag body is composed of a fabric envelope and a cage of meridian cables to which the riser line is attached. The fabric envelope is fabricated from gores of a single-ply fabric, usually cut with the thread sets at 45 degrees to the gore center lines, and seamed together along the meridians of the sphere.

Structural analysis of the spherical drag body is greatly dependent upon a number of design details which have little or no effect on thermodynamic or aerodynamic considerations. Because the sphere is a stable pressure vessel with the fabric envelope alone, the meridian cables do not need to be in contact over the entire surface, but can depart on a tangent at some angle at the nose. The nose angle then becomes a structural parameter. In such a design the behavior under load is governed by the presence or absence of a shear bond between the meridian cables and the fabric. If there is no shear bond, the bias angle of the fabric can change, resulting in a change in the meridian arc lengths and a corresponding change in the circumference of the equator.

If the meridian cables are bonded to the fabric, or if the seam tapes have significant lengthwise stiffness, the meridian arc lengths cannot change very much under load, requiring a different analysis than the case of no shear bond. A similar restrictive effect, although more localized, is produced by the stiffness of the burlap fence in the hoop direction.

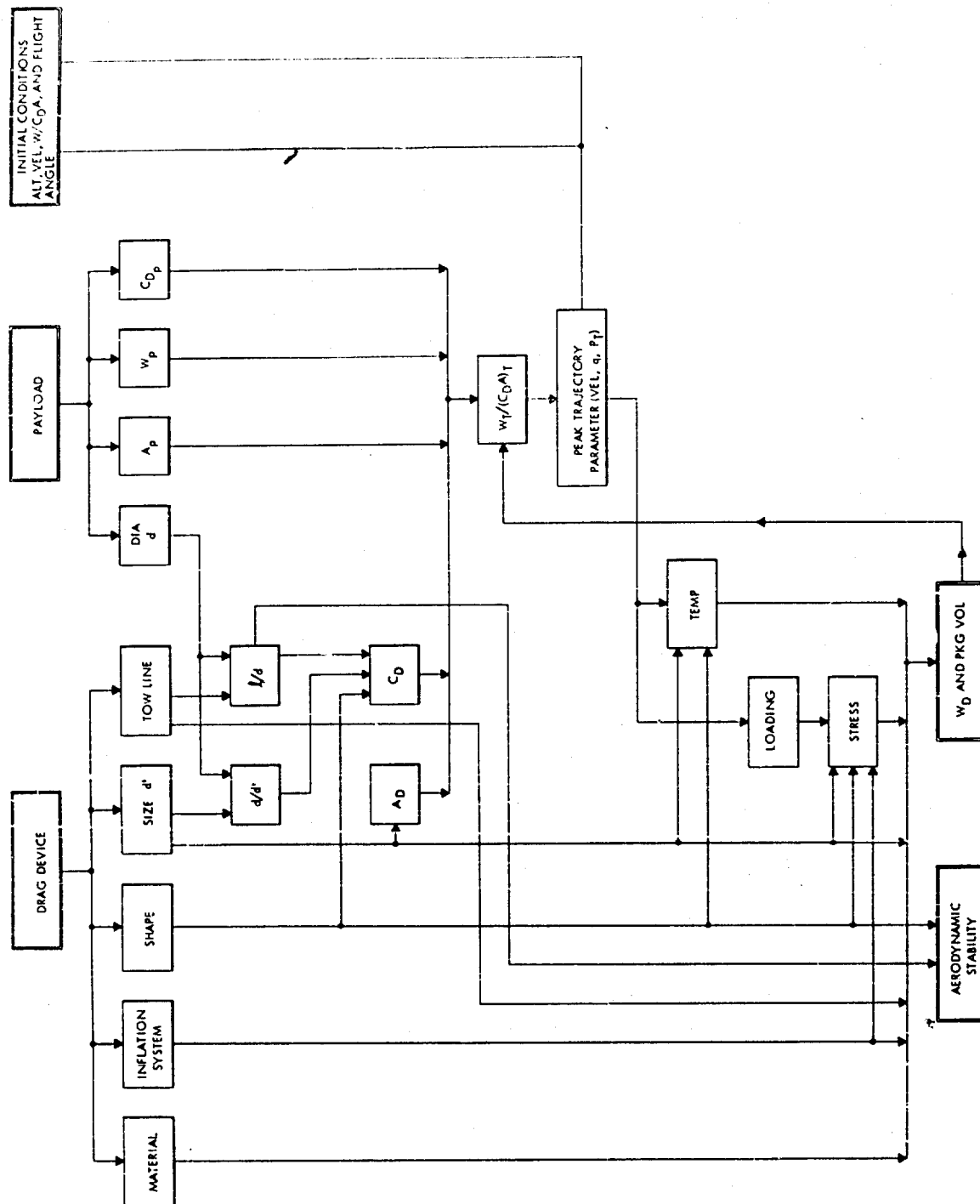


Figure 119. Parameters Affecting Drag Device Design

Another parameter affecting the analysis of a spherical drag body is the presence or absence of a center cable connecting the front and rear poles. If there is a center cable, the length of the drag body must remain constant under load, and part of the drag force is taken out at the rear pole. If there is no center cable, all of the drag force is taken out at the nose, and the length of the drag body can change under load.

Another variation in the spherical shape is obtained by tailoring the fabric envelope to one of the isotenoid curves of Figure 8A, Reference 14. For small values of k , these curves are nearly circular, yet produce some tension in the meridian cables without any drag load.

Because the number of combinations of the various parameters is very large, investigation of all types of spherical drag bodies is not attempted here (refer to Appendix III for a discussion of various sphere drag shapes). The following analysis applies to the type of sphere of which models were built for the Langley tests. It is believed that the resulting weights are typical of other types of spherical drag bodies.

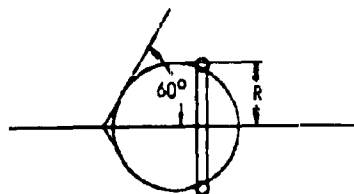


Figure 120. Sphere Geometry with No Drag Load

The model (Figure 120) is tailored to a spherical shape and is fitted with a number of meridian cables to which the riser line is attached. It is assumed that there is no shear bond between the meridian cables and the fabric. The cables are cut long enough to provide a 60-degree angle at the nose with no load on the model.

The sphere is a member of the isotenoid family of membranes derived in Reference 14, Appendix A, for the special case where the meridian cable tension is zero. In order to carry any drag, of course, the meridians must have some tension, causing the shape to deviate from the circular profile. If the deviation is small, the new profile is approximately one of the family of curves shown in Figure 8A, Reference 14. The approximate shape is obtained as a function of the drag loading by means of the following structural model:

Suppose a cage of n meridian cables, each carrying load, T_m , is applied to the outside of the above described fabric sphere, carrying pressure, P . Defining the quantity

$$\frac{nT_m}{P\pi(R)^2} \text{ as } k,$$

the pressure vessel formed by the fabric and cables takes the shape of one of the profile curves of Figure 8A, Reference 14, with outer radius, R' . (It is assumed that the burble fence does not restrict the deformation of the fabric.) In order to determine R' in terms of R , it is assumed that the fabric threads and the meridian cables are inextensible. It is further assumed that the bias angle can change slightly without causing any change in the one to one ratio of the principal stresses in the fabric. For small changes in the bias angle, the elongations in the hoop and meridian directions are equal in magnitude and of opposite sign. If the change in bias angle is assumed to be constant throughout the surface, the sum of the meridian circumference and equatorial circumference must remain constant as k increases. For $k = 0.1$, Figure 3C, Reference 14, gives the length of the meridian between the equator and the pole as $1.530R'$. The length of one quarter of the equator

Now suppose the meridian cables on one end are cut at some radius, x_1 , from the axis of symmetry and the forces T_m are applied to each cable as shown in Figure 121. In order to maintain the equilibrium of the structure, the loading between the removed sections of cable and the fabric must be supplied by some external means. This load on a circle of radius, x , is equal to $-T_m \sin \theta$ (the second term of Equation 2A, Reference 14). From Equations 5A and 16A, Reference 14,

$$-aT_m \sin \theta = \frac{kP_1 R'^2 [x^2/(R')^2]}{k + x/R'(1-k)}$$

and

$$d(-nT_m \sin \theta) = k p \pi (R')^2 \frac{\left[k + (x/R') (1-k) \right] \left(\frac{2x}{(R')^2} \right) - \frac{x^2}{(R')^2} \left(\frac{1-k}{R'} \right)}{\left[k + (x/R') (1-k) \right]^2} dx.$$

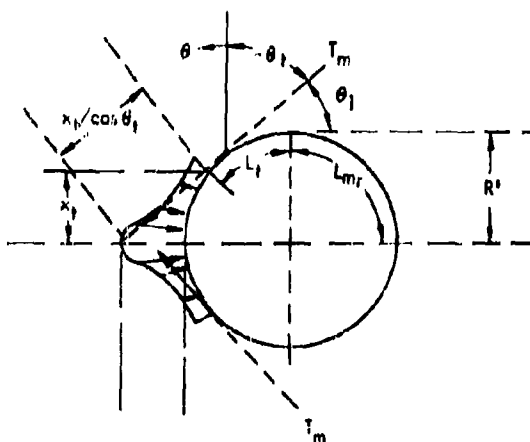


Figure 121. Structural Model with Cables Partially Replaced by External Loads

$$\frac{kP \left| \left| k + (x/R') (1-k) \right| - \frac{x(1-k)}{2R'} \right|}{\left| k + (x/R') (1-k) \right|^2}$$

The structure with cables partially removed and external loads applied is shown in Figure 121. It is seen that the external pressure is similar to the aerodynamic loading on a drag body, in which case the shape closely approximates the shape the drag body of Figure 120 takes under load.

The tangency point, x_t , is determined from the assumption that the meridian cables are inextensible. From Figure 120, the length of each meridian is seen to be

$$R \left[\frac{150\pi}{180} + \tan 30^\circ \right] = 3.197R.$$

From Figure 121, the length is

$$R' \left(\frac{L_{m_r}}{R'} + \frac{L_t}{R'} + \frac{x_t}{R' \cos \theta_t} \right)$$

where L_t is the length of arc between the tangency point and the equator. Equating these two lengths,

$$3.197R = R' \left(\frac{L_{m_r}}{R'} + \frac{L_t}{R'} + \frac{x_t}{R' \cos \theta_t} \right),$$

Equations 5A and 16A of Reference 14 give

$$\sin \theta_t = \frac{-x_t^2/R^2}{k + x_t/R(1-k)}.$$

For any value of k , x_t/R' is determined by trial from the above two equations and from Figure 8A, Reference 14. When $k = 0.1$, it was previously found that $R' = 1.0132R$. From Figure 8A, Reference 14, $L_{m_r}/R' = 1.53$ and for a value of $x_t/R' = 0.60$, $L_t/R' = 0.90$. The above values satisfy the above two equations for $\theta_t = -34.2$ degrees. Similarly, for $k = 0.2$ and 0.3 , x_t/R' is found to be 0.67 and 0.71 and θ_t is -37.5 and -39.2 degrees. The deflected shapes for $k = 0, 0.1, 0.2$, and 0.3 are shown in Figure 122.

The drag on the drag body is found from equilibrium of the joint between the meridian cables and the riser line:

$$D = nT_m \cos \theta,$$

where

$$\theta_1 = \theta_t + 90^\circ.$$

Dividing by $P_n R'^2$,

$$\frac{R^2 j}{(R')^2} = k \cos \theta_1 = k \cos (\theta_t + 90^\circ) = -k \sin \theta_t$$

where

$$j = \frac{D}{P_n R'^2}$$

Using the previously determined values of θ_t and R'/R , j is obtained from the above equation for various values of k :

j	k
0	0
0.0578	0.1
0.128	0.2
0.204	0.3

The required pressure is determined by the allowable distortion of the drag body. Figure 122 indicates that at $k = 0.3$ the cross section has departed considerably from the original circle and this value is chosen arbitrarily as the limiting value. k is plotted as a function of j in Figure 123.

2. Hemispherical Ballutes with Tucked Back

In the hemisphere model, (Figure 124) the front half is a fabric hemisphere with no meridian cables. The riser line passes through a sliding fitting at the nose and is attached to the rear pole of

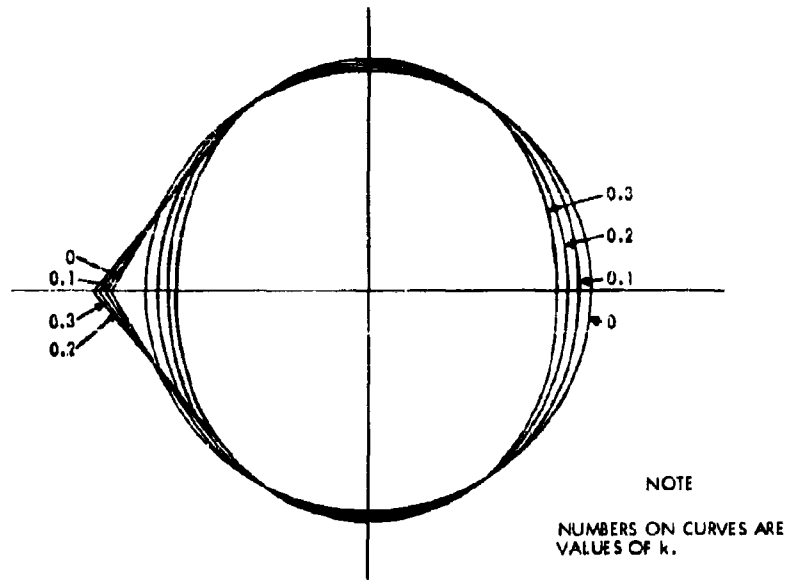


Figure 122. Deflected Shape of a Spherical Drag Body under Various Loadings

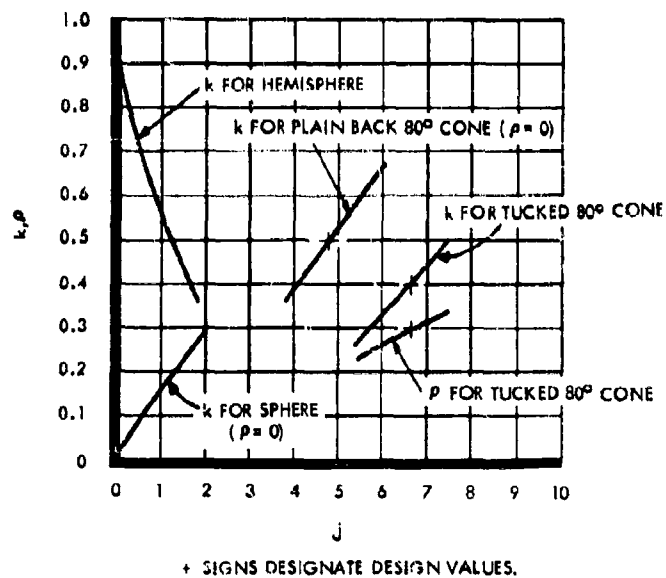


Figure 123. Cable Tension Parameters versus Drag to Pressure Force Ratio for Four Drag Body Configurations

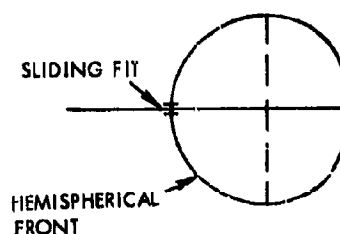


Figure 124. Hemisphere Model Geometry

the model. It is necessary, therefore, for the rear half to have meridian straps in order to carry the riser line load. Because the straps do not extend beyond the equator, they must be bonded to the fabric envelope. It is desirable that the model be a stable pressure vessel with no drag load ($j = 0$), avoiding the necessity of controlling the pressure throughout the trajectory.

The above requirements can be satisfied by making the rear profile one of the curves of Figure 8A, Reference 14, except that such a shape would cause a discontinuity between the front half and the rear half of the model at the equator. (In the front half all the meridian stress is carried by the fabric; in the rear half, part would be carried by the fabric and part by the meridian straps. In addition, the gore radii of the rear half would not match the circular cross section of the front hemisphere.) What is needed is a rear profile in which most of the meridian stress is carried by the straps near the pole and by the fabric near the equator. Such a membrane is not an isotensoid, but can be formed with the results of the isotensoid analysis of Appendix A of Reference 14, by letting k vary with x/R .

Table 1A of Reference 14 gives values of the derivative of the profile curve in the case of $\rho = 0$ for various values of x/R and k . In the case of an isotensoid, the derivative is plotted versus x/R for a constant value of k and the profile curve is obtained by graphical integration. A curve for variable k can be obtained in the same way by choosing the proper values of the derivative. The following values are selected for the rear profile:

x/R	k	dy/dx
0	0.9	0
0.1	0.9	-0.011
0.2	0.9	0.0435
0.3	0.9	-0.0972
0.4	0.9	-0.1727
0.5	0.9	-0.2728
0.6	0.9	-0.4045
0.7	0.9	-0.5853
0.8	0.6	-0.9863
0.9	0.4	-1.6981
0.95	0.2	-2.7579
1.0	0	∞

Between $x/R = 1$ and $x/R = 0.95$, the curve is closely approximated by a circular arc of radius, R . Between $x/R = 0.95$ and $x/R = 0.7$, the derivatives are plotted and the curve is obtained by graphical integration. Between $x/R = 0.7$ and $x/R = 0$, the curve is the isotensoid for $k = 0.9$ and is traced from Figure 8A, Reference 14. The resulting curve is shown in Figure 125.

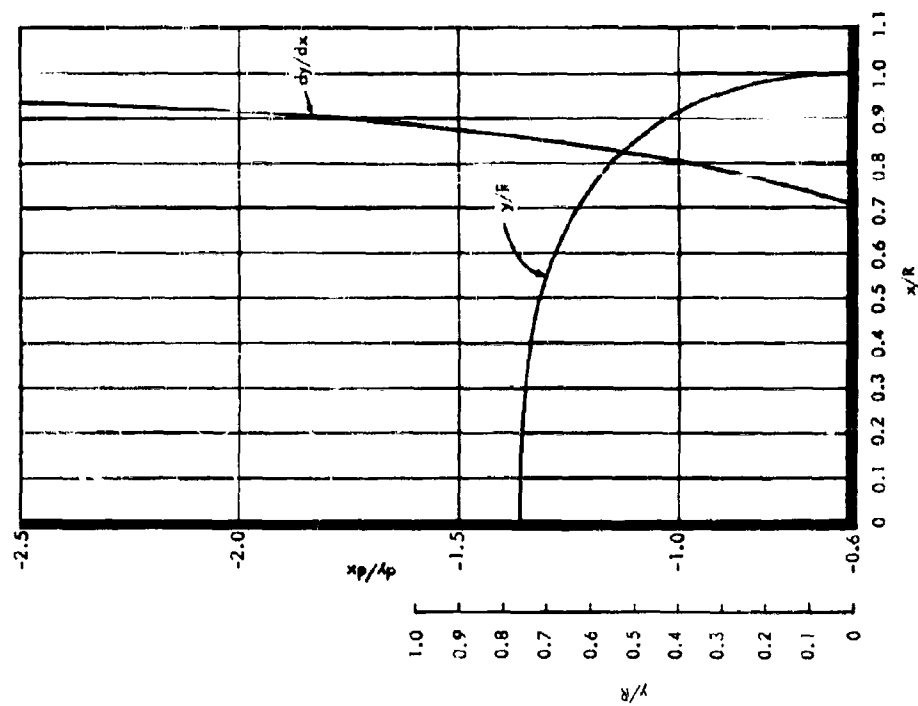
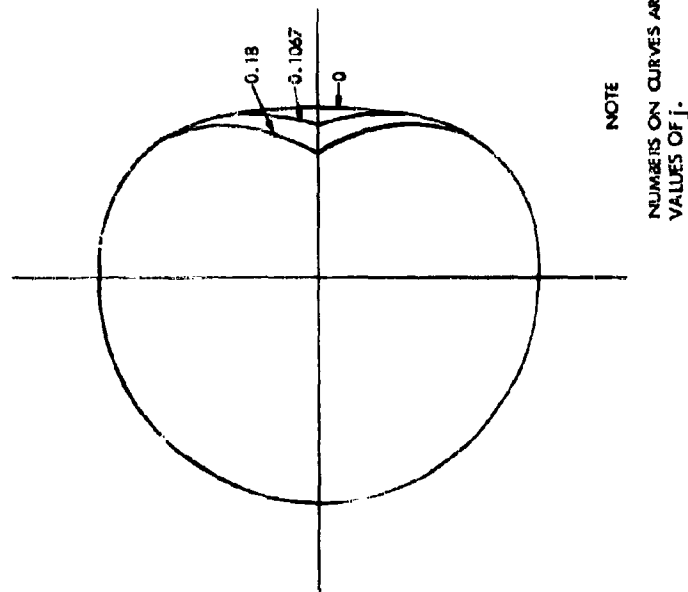


Figure 125. Profile Curve for $\rho = 0$ for Various Values of x/R and k



NOTE
NUMBERS ON CURVES ARE
VALUES OF j .

Figure 126. Equilibrium Shape of Hemisphere for Various Values of j

When a load is applied to the riser line, the rear half of the drag body must deform. Because the deformation takes place primarily between $x = 0$ and $x/R = 0.7$, where the rear profile is an isotensoid, the approximate deflected shape for any given load can be obtained from the perturbation analysis of Reference 14. Entering Figure 3C of Reference 14 for $k = 0.9$ and $\rho = 0$, the following values are obtained:

$$L_m/R = 1.325$$

$$y_0/R = 0.615.$$

It is assumed that as the membrane deflects, the arc length of the meridians remains constant. Suppose the deflection is such that $\rho/k = 1/5$. Entering Figure 3C of Reference 14 for $\rho/k = 1/5$ and $L_m/R = 1.325$, it is estimated that $k + \rho = 0.64$ and $y_0/R = 0.543$. The equations $k + \rho = 0.64$ and $\rho/k = 1/5$ give $k = 0.533$, $\rho = 0.1067$. The deflection at the pole is equal to $(0.615 - 0.543)R = 0.072R$. Similarly for $\rho/k = 1/2$, the curve is defined by $k = 0.36$ and $\rho = 0.18$, and the deflection is $0.197R$.

Using the method of estimating profile curves described in Reference 14, the deflected shapes are obtained and are shown along with the undeflected shape of the drag body in Figure 126. Because all the riser line tension is taken out of the rear pole, $\rho = j$ for this model. Using the above values of $\rho = j$ and k , j is plotted versus k in Figure 123.

The curve for $j = 0.18$ is chosen as the maximum useful deflection.

3. Optimum Design Ballutes

The optimum design is a two-pole type drag body, discussed in Reference 14. Equation 7 of Reference 14 becomes

$$j = k \cos \theta_1 + \rho$$

$$k = \frac{j - \rho}{\cos \theta_1}.$$

For a ram-inflated design, the definition of j becomes

$$j = \frac{C_D}{C_{F_1}} \frac{C_D}{C_{P_r}}$$

where the drag coefficient and pressure coefficients are obtained from aerodynamic analysis for various points in the trajectory. The values of j thus obtained in general are not equal for all points in the trajectory. If this is the case, the value that is used to determine k is either a mean value or the value at maximum dynamic pressure, whichever gives the lower drag body weight.

The value of θ_1 that is chosen depends on the desired shape of the front half of the drag body. If the nearly straight portion of front profile is desired to have a given cone angle, then a value of θ_1 smaller than the desired cone angle must be chosen.

Knowing j and θ_1 , k is obtained from the above equation and the rear profile shape is derived using the analysis of Reference 14, Appendix A. The pressure distribution over the front of the drag body must be known in order to derive the exact front profile, but an estimated shape can be obtained easily as described in Reference 14.

After the design shape of the drag body is obtained for the chosen value of j , the perturbation analysis of Reference 14 is necessary to determine the behavior of the drag body for different values of j .

The above method is now applied to two typical design conditions. It is desired that the angle of the straight part of the front profile be 40 degrees:

For the first condition the following values are given:

$$C_D = 0.75$$

$$C_{P_i} = 1.0$$

$$C_{P_r} = 0$$

$$\rho = 0.$$

It follows that $j = 0.75/1.0 = 0.75$. Choosing a value of $\theta_1 = 30^\circ$, $k = 0.75/0.866 = 0.866$.

For the second condition the given values are

$$C_D = 0.75$$

$$C_{P_i} = 1.0$$

$$C_{P_r} = 0$$

$$\rho = 0.75k$$

It follows that $j = 0.75/1.0 = 0.75$. Choosing a value of $\theta_1 = 25^\circ$, $k = 0.453$ and $\rho = 0.34$.

4. Conical Ballutes

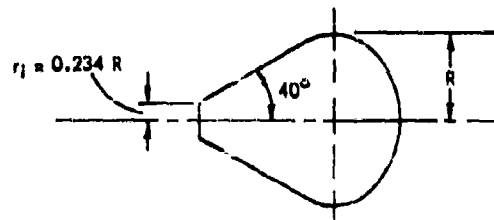


Figure 127. Tailored Geometry of Plain Back 80-Degree Cone

a. Convex Back 80-Degree Cone. The 80-degree cone (Figure 127) is constructed with a single-ply fabric and meridian cables in much the same way as the spherical design. Inflation pressure is maintained by ram air, which enters the drag body through a metal ring at the nose or through inlets at the equator. The metal ring also serves to transmit the riser line load to meridian cables and fabric.

The rear half of the drag body is an isotenoid membrane having the parameters $k = 0.5$ and $\rho = 0$. The derivation of this curve is given in Reference 14, Appendix A, and the curve is shown in Figure 8A, Reference 14. The front-half profile is formed by the mirror image of the rear curve between the equator and the point where this curve is tangent to an 80-degree cone, which forms the rest of the front profile. This particular shape is analyzed here because it matches the wind tunnel models that GAC has tested.

In operation the pressure loading on the outside of the drag body varies from the nose to the equator and is constant from the equator back. The pressure distribution therefore satisfies the constant pressure assumption that was made in the derivation of the rear profile.

Present design practice is to derive an isotensoid surface for the front half by approximating the variable pressure with a step-function distribution as shown in Appendix B of Reference 14. A typical curve resulting from such a derivation is shown in Figure 3B, Reference 14. This curve has a concave portion at the nose, a portion that is nearly straight, and then a convex portion at the equator. When a curve of this type is used for the profile of a drag body, the radius of curvature at the equator must be the same as the curvature of the rear profile at the equator in order for the two curves to be compatible. Although the front profile curve of Figure 127 was not derived as an isotensoid, it has the same characteristics in that the curvature of the equator is the same as that of the rear profile and the remainder of the curve is a straight line. The concave portion of the curve is missing, but most or all of this portion would be in front of the inlet diameter and would therefore be cut off anyway. By choosing the proper pressure distribution and nose angle, therefore, the front profile of Figure 127 can be approximated by an isotensoid surface with the same stresses as the rear surface. If it is assumed that the required pressure distribution is close to the actual pressure distribution that the drag body receives in operation, it remains to determine the nose angle, θ_1 , of the extended curve.

The nose angle is determined from the requirement that the slope of the curve is 40 degrees at the nose ring radius of 0.234R. Summing forces on the nose ring,

$\left[nT_m + 2\pi (0.234R)t \right] \cos 40^\circ = D$, or dividing by $P\pi R^2$ and substituting for f from Equation 1A of Reference 14,

$$\left[k + (0.234)(1-k-\rho) \right] (0.766) = j.$$

For $k = 0.5$, $\rho = 0$, and $j = 0.474$, Equation 7 of Reference 14 then gives

$$\cos \theta_1 = j/k = 0.948, \text{ or } \theta_1 = 19^\circ.$$

The value of 19 degrees is consistent with the requirement that the nose portion of the curve is concave.

The value of $j = 0.474$ is the only value for which the configuration of Figure 127 is structurally stable. If j deviates from this value, the drag body changes shape until a new equilibrium is reached. The perturbation analysis of Reference 14 is now applied to determine the changes in j corresponding to small changes in the shape of the drag body. For this analysis, the radius, R , is assumed to remain constant. Let

$$\frac{dy_0}{R} = 0.05. \text{ Equation 20 of Reference 14 gives } \frac{dL_{mr}}{R} = -0.0383.$$

Figure 3C of Reference 14 gives

$$\frac{L_{mr}}{R} = 1.402 \text{ for } k = 0.5, \rho = 0.$$

Adding

$$\frac{dL_{mr}}{R}, \text{ the new value of } \frac{L_{mr}}{R} \text{ is } 1.364,$$

which corresponds to a value of $k = 0.68$, $\rho = 0$. It follows that $dk = 0.68 - 0.5 = 0.18$. Substituting $r_1/R = 0.234$, $dk = 0.18$, $\cos \theta_1 = 0.766$, $k = 0.5$, and

$\frac{dy_0}{R} = 0.05$ into Equation 21 of Reference 14,

$$dj = (1 - 0.234) \left[(0.18)(0.766) - (0.5)(0.05)(0.265) \right] - \left[(0.234)(0.05)(0.265) \right]$$

$$dj = 0.097,$$

and the new value of j is $0.474 + 0.097 = 0.571$.

Let $\frac{dy_0}{R} = -0.05$. Equation 20 of Reference 14 give $\frac{dL_{m_r}}{R} = 0.0383$.

The new value of

$$\frac{L_{m_r}}{R} \text{ is } 1.402 + 0.0383 = 1.440.$$

Figure 3C gives $k = 0.36$, or $dk = 0.36 - 0.5 = -0.14$. Substituting into Equation 21 of Reference 14,

$$dj = (1 - 0.234) \left[(-0.14)(0.766) - (0.5)(-0.05)(0.265) \right] - \left[(0.234)(-0.05)(0.265) \right]$$

$$dj = 0.074,$$

and the new value of j is $0.474 - 0.074 = 0.40$.

Figure 128 shows the equilibrium shapes for various values of j . k is plotted as a function of j for the 80-degree cone with plain back in Figure 123.

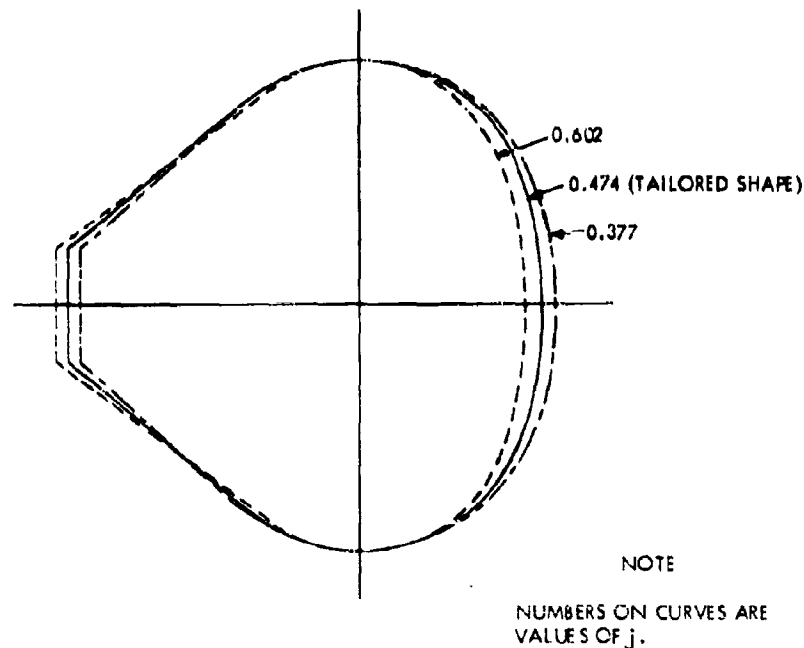


Figure 128. Equilibrium Shape of Plain Back 80-Degree Cone for Various Values of j

b. **Tucked Back 80-Degree Cone.** The tucked design (Figure 129) is similar to the plain back, except that the rear profile has values of $k = 0.4$ and $\rho = 0.3$ (see Figure 5A, Reference 14). Again summing forces on the nose ring,

$[nT_m + 2\pi (0.234R)f] \cos 40^\circ + T_c = 0$, or dividing by πR^2 and substituting for f from Equation 1A of Reference 14,

$$[k + (0.234)(1 - k - \rho)] 0.766 + \rho = j.$$

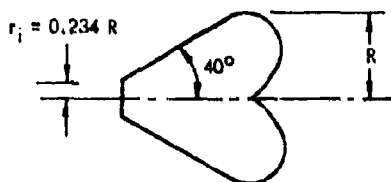


Figure 129. Tailored Geometry of 80-Degree Tucked Cone

Substituting $k = 0.4$ and $\rho = 0.3$ and $j = 0.660$, Equation 7 of Reference 14 gives

$$\cos \theta_1 = \frac{j - \rho}{k} = 0.901, \text{ or } \theta_1 = 25.9^\circ.$$

As in the case of the plain back cone model, the tucked 80-degree cone (Figure 129) is structurally stable for only one value of $j = 0.660$. Changes in j corresponding to small changes in shape are now determined from the perturbation analysis of Reference 14.

Let $\frac{dy_{0r}}{R} = 0.10$. Equation 17 of Reference 14 gives $\frac{dL_{mr}}{R} = 0.0766$. For $k = 0.4$ and $\rho = 0.3$, Figure 3C of Reference 14 gives

$$\frac{y_{0r}}{R} = 0.128, \quad \frac{L_{mr}}{R} = 1.335. \quad \text{The new value of } \frac{y_{0r}}{R} \text{ is } 0.128 + 0.10 = 0.228,$$

and the new value of

$\frac{L_{mr}}{R} = 1.335 + 0.0766 = 1.412$. These values correspond to $k + \rho = 0.488$ and $\rho/k = 0.885$, or $k = 0.259$ and $\rho = 0.229$. $dk = 0.259 - 0.4 = -0.141$ and $d\rho = 0.229 - 0.3 = -0.071$. Substituting $dk = -0.141$, $d\rho = -0.071$, $k = 0.4$, $\rho = 0.3$, $\theta_1 = 40^\circ$, $r_i/R = 0.234$, and

$$\frac{dy_{0f}}{R} = 0.10 \text{ into Equation 19 of Reference 14,}$$

$$dj = -0.071 - [(0.141)(0.766)] + [(0.4)(0.10)(0.265)] - (0.234)[(-0.212)(0.766) + (0.3)(0.265)(-0.10)]$$

$$dj = -0.128, \quad j + dj = 0.532.$$

Let $\frac{dy_{0r}}{R} = 0.05$. Equation 17 of Reference 14 gives $\frac{dL_{mr}}{R} = -0.0353$.

The new value of

$\frac{y_{0r}}{R}$ is $0.128 - 0.05 = 0.078$, and the new value of $\frac{L_{mr}}{R}$ is 1.297 .

Figure 3C of Reference 14 gives $k + \rho = 0.84$, $\rho/k = 0.680$, or $k = 0.5$, $\rho = 0.34$. $dk = 0.5 - 0.4 = 0.1$, and $d\rho = 0.34 - 0.30 = 0.04$. Equation 19 of Reference 14 gives

$$dj = 0.04 + [(0.1)(0.786)] - [(0.4)(0.05)(0.265)] - [(0.234)(0.14)(0.766) + (0.3)(0.265)(0.05)]$$

$$dj = 0.085, j + dj = 0.745.$$

Figure 130 shows the equilibrium shapes for various values of j . k is plotted as a function of j for the 80-degree cone with tucked back in Figure 123.

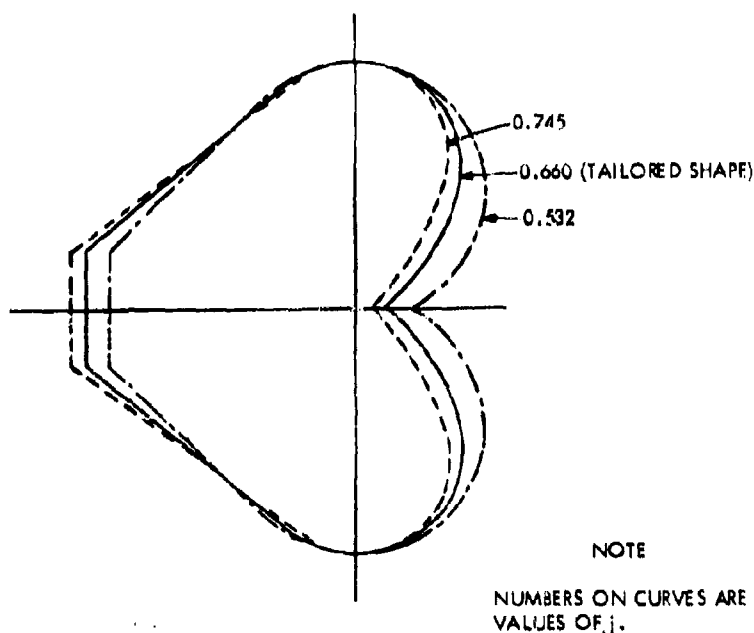


Figure 130. Equilibrium Shape of Tucked 80-Degree Cone for Various Values of j

5. Eighty-Degree Airmat Cone

The dimensions of the Airmat cone are shown in Figure 131.

The Airmat cone is formed by two fabric cones which have the same apex but different cone angles and are connected at the outer radius by a segment of a torus of cross section radius, r . The

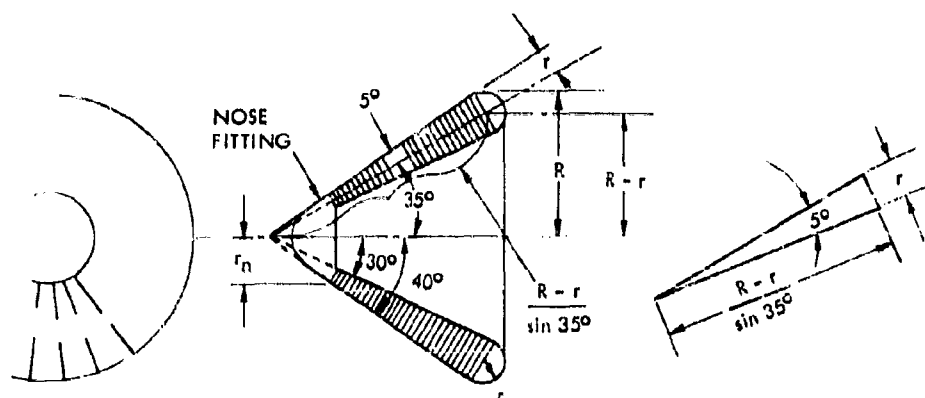


Figure 131. Airmat Cone Dimensions

fabric cones are connected together over the remainder of their areas by a system of closely spaced threads called drop threads. The drop threads are perpendicular to the 35-degree line, and if extended would pass through the axis of symmetry of the drag body.

From the geometry of Figure 131, it is seen that

$$\frac{r \sin 35^\circ}{R - r} = \sin 5^\circ, \text{ or } \frac{r}{R} = 0.1318.$$

It is assumed that the drag results from a uniform aerodynamic pressure, P_i , over the front of the cone. It follows that $P = C_D q$. Figure 132 shows a segment of the drag body cut in such a way as not to cut any drop threads.

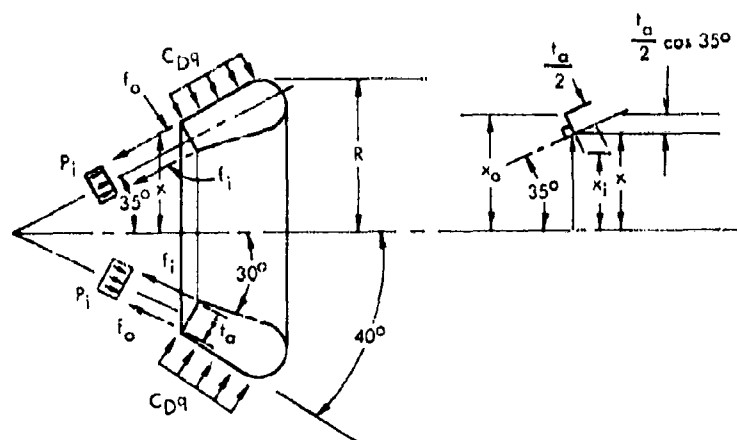


Figure 132. Loads Acting on a Segment of an Airmat Cone

The thickness, t_a , of the Airmat at any radius, x , is given by

$$t_a = \frac{2x \tan 5^\circ}{\sin 35^\circ} = 0.304x.$$

The outer radius, x_o , is equal to

$$x + \frac{t_a}{2} \cos 35^\circ = x + \frac{0.304x}{2} \cos 35^\circ = 1.125x, \text{ and the inner radius, } x_i, \text{ is equal to } x - t_a/2 \cos 35^\circ = 0.875x. \text{ Summing forces horizontally in Figure 132,}$$

$$C_D q \pi (R^2 - x_o^2) + P_i A_x = 2\pi (x_o f_o \cos 40^\circ + x_i f_i \cos 30^\circ)$$

where A_x is the frontal projection of the annular area over which the internal pressure, P_i , acts. A_x is equal to $\pi(x_o^2 - x_i^2) = \pi x^2 (1.125^2 - 0.875^2) = \pi x^2/2$.

Substituting for x_o , x_i and A_x ,

$$C_D q \pi (R^2 - 1.266x^2) + \frac{P_i \pi x^2}{2} = 2\pi x (0.861f_o + 0.758f_i).$$

Determination of the stresses f_o and f_i is a statically indeterminate problem which is beyond the scope of this work. For purposes of determining the weight of the drag body, it is sufficiently accurate to assume that they are equal. The above equation then becomes

$$C_D q \pi (R^2 - 1.266x^2) + \frac{P_i \pi x^2}{2} = 3.24\pi x f_i$$

where f_i is the meridian stress in one skin. Treating the Airmat as simply a conical shell, the hoop stress caused by the external pressure, $C_D q$ is equal to approximately $-C_D q x / \cos 35^\circ$. The sum of the hoop stresses in the inner and outer cones is $P_i t_a$ due to the internal pressure, P_i . Using a factor of safety of 1.5 on wrinkling,

$$P_i t_a = \frac{1.5 C_D q x}{\cos 35^\circ}$$

Substituting $t = 0.304x$, $P_i = 6.02 C_D q$.

Substituting for P_i into the equation of horizontal equilibrium,

$$C_D q (R^2 + 1.74x^2) = 3.24 x f_i$$

or

$$f_i = \frac{C_D q (R^2 + 1.74x^2)}{3.24x} = \frac{C_D q}{3.25} (R^2/x + 1.74x).$$

Suppose an element is taken out of the free body, as shown in Figure 133.

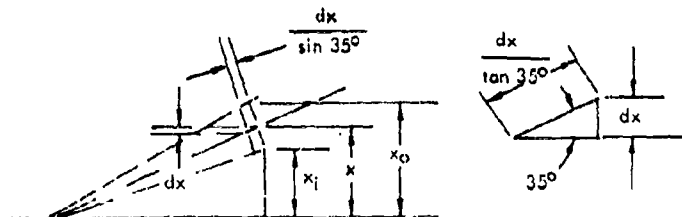


Figure 133. Taking Element from Free Body

The total fabric area of this element is approximately $2\pi(x_1 + x_0) dx/\sin 35^\circ$, or $2\pi x (1.125 + 0.875) dx/0.574 = 6.99\pi x dx$. The weight of this element (meridian threads only) is

$$dW_m = \frac{f_1 (FS) dA}{2k_f}$$

(assuming a constant factor of safety throughout the drag body) where k_f is the strength to weight ratio of the fabric as though it had two identical thread sets. Substituting for dA and f_1 , and using a FS of 2.0,

$$dW_m = \frac{(2) C_D q (R^2/x + 1.74x) (6.99\pi x dx)}{(2) (3.24 k_f)}$$

or

$$dW_m = \frac{6.77 C_D q (R^2 + 1.74x^2) dx}{k_f}$$

The actual drag body must have a rigid fitting at the nose. If the weight of this fitting is the same as the fabric it replaces, the total weight of the meridian elements of the drag body is

$$W_m = \int dW_m = \int_0^R \frac{6.77 C_D q}{k_f} (R^2 + 1.74 x^2) dx$$

or

$$W_m = \frac{6.77 C_D q (1.58) R^3}{k_f} = \frac{10.7 C_D q R^3}{k_f}$$

The sum of the hoop stresses in the inner and outer skins was given previously as $P_{it} = 1.5 C_D q x / \cos 35^\circ = 1.83 C_D q x$. Again assuming that the hoop stress divides evenly between the inner and outer skins, $f_2 = P_{it}/2 = 0.915 C_D q x$ where f_2 is the hoop stress in one skin. The weight of the hoop threads in this element is

$$dW_H = \frac{f_2 (FS) dA}{2 k_f}$$

Substituting $dA = 6.99\pi x dx$, $FS = 2$, $f_2 = 0.915 C_D q x$,

$$dW_H = \frac{20.1 C_D q x^2 dx}{k_f}$$

Again integrating from 0 to R,

$$W_H = \frac{20.1 C_D q}{k_f} \int_0^R x^2 dx = \frac{6.7 C_D q R^3}{k_f}$$

The total weight of the Airmat cone is

$$W = \frac{17.4 C_D q R^3}{k_f}$$

6. Torus With Curtain

A general analysis of the torus with curtain is given in Reference 14. For simplicity, a uniform pressure is assumed to be acting over the front side, producing a drag equal to $D = P\pi R_4^2$.

It follows that $P = CDq$.

The curtain profile chosen is a constant pressure isotensoid membrane having the parameter $k = \rho = 0.45$. Equation 24 of Reference 14 gives

$$R_4/R = \sqrt{\rho} = 0.671.$$

The torus cross section radius is chosen equal to $R_4/12$, and the nose radius is equal to $R_4/8$. The resulting drag body profile is shown in Figure 134, in which the eccentricity of the curtain load on the torus is made approximately zero by placing the center line of the torus cross section on the skirt profile curve. The profile curve intersects the torus at $x/R = 0.51$ and $\theta = 22.3^\circ$. The meridian stress at any radius, x , is

$$f_1 = f + \frac{nT_m}{2\pi x}$$

or

$$\frac{2f_1}{PR} = \frac{2f}{PR} + \frac{nT_m}{P\pi xR}.$$

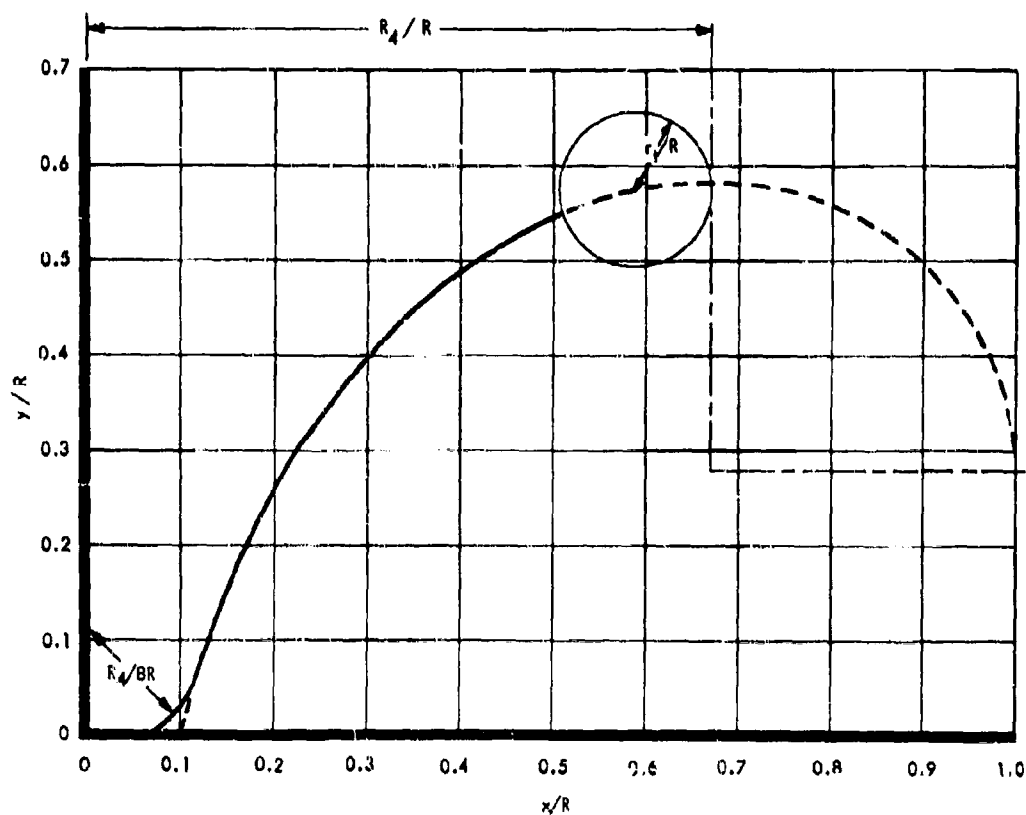


Figure 134. Profile Curve of Torus with Curtain Drag Body

Substituting $2f/PR = 1 - k - \rho$ (Equation 1A of Reference 14) and $k = nT_m/P\pi R^2$,

$$\frac{2f_1}{PR} = 1 - k - \rho + \frac{kR}{x}$$

Substituting $k = \rho = 0.45$ and $x/R = 0.51$,

$$\frac{2f_1}{PR} = 0.1 + \frac{0.45}{0.51} = 0.982$$

or

$$f_1 = 0.491 PR.$$

The radial component of this stress is $f_1 \cos 22.3^\circ = 0.455 PR$. The radial loading produces a compressive load in the torus equal to $(0.455PR)(0.51R)$. The pressure load on the torus cross section is $P_t \pi r_t^2$, where P_t is the torus pressure. Using a factor of safety of 1.5 to prevent wrinkling,

$$P_t \pi r_t^2 = (1.5)(0.455PR)(0.51R).$$

It was previously given that $r_t = R_4/12$ and $R_4 = 0.071R$, which gives $r_t = 0.056R$. Substituting into the above equation,

$$P_t = \frac{(1.5)(0.455)(0.51)P}{\pi(0.056)^2} = 35.3 P = 35.3 C_D q.$$

The principal pressure stresses in the torus are approximately equal to $P_t r_t = (35.3P)(R_4)/12 = 2.94 PR_4$ and $P_t r_t/2 = 1.47 PR_4$. In any specific design, the torus would have to be checked for elastic stability under the radial load. Elastic stability is not considered in this parametric study because of the difficulty of predicting the elastic properties of the materials in parametric form. This is not believed to affect the total weight of the drag body, however, because if buckling is encountered it can be corrected by increasing the value of r_t/R_4 . A higher value of r_t/R_4 would result in more torus area, but this would be compensated by a lower torus pressure, resulting in approximately the same torus weight.

7. Weight Analysis

a. General. In analyzing the weights of the various configurations, it is assumed that the critical point in the trajectory occurs at maximum dynamic pressure.

b. Isotensoid Shapes. The weight analysis of isotensoid drag bodies is given in Reference 14. Equation 35 of Reference 14 gives the weight of the fabric envelope as

$$W_f = \frac{RD(A_f/\pi R^2)(1 - k - \rho)(FS)}{2k_f}.$$

For the isotensoid shapes considered here, the fabric area, A_f , is approximately $4\pi R^2$ and a factor of safety of 2.0 is used. Substituting $j = D/P\pi R^2$, the fabric weight expression becomes

$$W_f = \frac{4P\pi R^3(1 - k - \rho)}{k_f}.$$

Equation 37 of Reference 14 gives the cable weight as

$$W_c = \frac{RD(FS) \sum \left[\left(\frac{L}{R} \right) \left(\frac{T}{D} \right) \right]}{k_c}.$$

Substituting $D = jP\pi R^2$, and $FS = 2.0$,

$$W_c = \frac{2jP\pi R^3 \sum \left[\left(\frac{\ell}{R} \right) \left(\frac{T}{D} \right) \right]}{k_c}$$

The total weight is given by

$$W = P\pi R^3 \left[\frac{4(1-k-\rho)}{k_f} + \frac{2j \sum \left[\left(\frac{\ell}{R} \right) \left(\frac{T}{D} \right) \right]}{k_c} \right]$$

(1) Sphere. For the sphere that is analyzed in the Stress and Deflection Analysis section, $\rho = 0$, $k = 0.3$, and $j = 0.204$. The sphere is equipped only with meridian cables, whose tension is T_m and whose length is $3.197R$. The quantity

$$\sum \left[\left(\frac{\ell}{R} \right) \left(\frac{T}{D} \right) \right] \text{ is therefore equal to } (3.197) \frac{nT_m}{D} \text{ or } (3.197) \left(\frac{k}{j} \right). \text{ The expression for total}$$

weight becomes

$$W = P\pi R^3 \left[\frac{(4)(0.7)}{k_f} + \frac{2(3.197)(0.3)}{k_c} \right]$$

$$W = P\pi R^3 \left[\frac{2.8}{k_f} + \frac{1.92}{k_c} \right]$$

(2) Eighty-Degree Cone with Plain Back. For the plain back cone, $\rho = 0$. It too has only meridian cables the length of which is approximately πR . The quantity

$$\sum \left[\left(\frac{\ell}{R} \right) \left(\frac{T}{D} \right) \right] \text{ becomes approximately } \frac{\pi k}{j}. \text{ The total weight expression becomes}$$

$$W = P\pi R^3 \left[\frac{4(1-k)}{k_f} + \frac{2\pi k}{k_c} \right]$$

(3) Eighty-Degree Cone with Tucked Back. The tucked back cone has a center cable as well as meridian cables. The center cable length is approximately $1.2R$, and its load is equal to $\rho P\pi R^2$. The quantity $\sum [(1/R)(T/D)]$ for the center cable and the meridian cable is equal to $(1.2\rho)(j) + (\pi k)/(j)$. The total weight expression becomes

$$W = P\pi R^3 \left[\frac{4(1-k-\rho)}{k_f} + \frac{2(1.2\rho + \pi k)}{k_c} \right]$$

(4) Hemisphere. The spherical surface of the hemisphere (all of the front half and the rear half between $x/R = 0.95$ and 1.0) has a stress of approximately $PR/2$ if the aerodynamic pressure is small compared to the internal pressure. The rear surface of the drag body requires lighter fabric than the spherical area, but must have meridian straps also. If it is assumed that the weight of the rear surface between $x/R = 0$ and 0.95 is the same as the weight of a spherical segment of fabric alone, the weight of the drag body is the same as the weight of a sphere containing pressure, P . The fabric weight per unit area is equal to $PR(FS)/2k_f$, and the area is $4\pi R^2$. Using a factor of safety of 2, the total weight of the fabric is

$$W = \frac{4P\pi R^3}{k_f}$$

where

$$P = \frac{C_D q}{j} = \frac{C_D q}{0.18}$$

14. (5) Torus With Curtain. The fabric stress in the curtain is given by Equation (1A) of Reference

$$\frac{2f}{PR} = 1 - k - \rho = 0.1 \text{ or } f = \frac{PR}{20}.$$

The curtain area is approximately $0.5\pi R^2$. Using a factor of safety of 2.0 for the fabric, the fabric weight is

$$W_f = \frac{(PR/20) (0.5\pi R^2) (2)}{k_f} = \frac{P\pi R^3}{20k_f}.$$

The meridian cable tension is equal to $nT_m = kP\pi R^2 = 0.45P\pi R^2$ for all cables. The length of one cable is approximately $0.85R$. Again using a factor of safety of 2.0, the cable weight is

$$W_c = \frac{(0.45P\pi R^2) (0.85R) (2)}{k_c} = \frac{0.585P\pi R^3}{k_c}.$$

The total weight of the curtain is

$$W_{\text{curtain}} = P\pi R^3 \left(\frac{1}{20k_f} + \frac{0.585}{k_c} \right) = PR_4^3 \left(\frac{0.519}{k_f} + \frac{8.07}{k_c} \right).$$

The torus area is approximately equal to $(2\pi) (0.59R) (2\pi r_t)$,

or

$$2\pi (0.59) \left(\frac{R_4}{0.671} \right) (2\pi) \left(\frac{R_4}{12} \right) = 2.9 R_4^2.$$

The stresses in the torus were found respectively to be $2.94 PR_4$ and $1.47 PR_4$. The weight required is the same as if both stresses were equal to the average value of $2.2 PR_4$. Using a factor of safety of 2, the torus weight is

$$W_{\text{torus}} = \frac{(2.2 PR_4) (2.9R_4^2) (2)}{k_f} = \frac{12.8 PR_4^3}{k_f},$$

and the total weight is

$$W = PR_4^3 \left(\frac{13.3}{k_f} + \frac{8.07}{k_c} \right)$$

where

$$P = C_D \dot{q}.$$

(6) Airmat Cone. The weight analysis of the Airmat cone is given in C4 of this section.

C. THERMODYNAMIC CONFIGURATION ANALYSIS

1. General

Aerodynamic heating of thermally thin spheres and blunted 40-degree half-angle cones at altitudes from 60,000 to 200,000 feet and at Mach numbers from 2 to 10 was analyzed. The analysis included the effects, if any, of a forebody and considers turbulent and laminar flow. Test data from GAC Mach 10 Ballute tests at the von Kármán Gas Dynamics Facility, Arnold Engineering Development Center, was used to determine effects of a forebody on aerodynamic heating.

The objective was to provide temperature information to assist in functional, structural, and environmental design optimization of a Ballute used in the specified initial flight envelope where the initial velocity is downward.

Re-entry trajectories were obtained from computer studies conducted by GAC aerodynamicists for ballistic coefficient $W/C_D A$ of 1, 10, 50, and 100 lb/ft² for each of the four corners of the initial flight envelope.

2. Method of Analysis

a. Connection To a Drag Body. Two configurations were analyzed for the drag body (Ballute): (1) a sphere and (2) a blunted cone with a half angle of 40 degrees. The drag body will be attached by a long cable to a forebody of unknown configuration.

The effect of the forebody on the aerodynamic heating of the drag body is presented in Figure 135 and is based on a review of the data obtained during the GAC Mach 10 Ballute tests at the von Karman Gas Dynamics Facility, Arnold Engineering Development Center. The heat flux to the forward portions of the drag body is reduced due to the forebody and cable reduction of air velocity, while the heat flux to the waist and trailing edge of the drag body is increased due to the added turbulence. The data presented in Figure 135 is presumed to apply to the sphere as well as the blunted cone in either turbulent or laminar flow throughout the flight envelope.

b. Transition to Turbulent Flow. Figure 136 presents the transition point from laminar to turbulent flow, based on a transition Reynold's number of 500,000 for the flight envelope. Note that turbulent flow is a very definite possibility. The 1959 ARDC Model Atmosphere is used in all calculations involving atmospheric properties.

c. Laminar Heat Flux and Temperature Distribution. The laminar heat flux and temperature distributions on a blunted cone and sphere are presented in Figures 137 and 138 respectively. The heat flux distribution without forebody are based on Reference 25; Figure 135 was then used to obtain the heat flux distributions with forebody. The temperature distributions were based on a thermally thin Ballute without internal radiation. The base point for the heat flux and temperature distributions is the stagnation point.

d. Turbulent Heat Flux and Temperature Distribution. The turbulent heat flux and temperature distributions on a blunted cone and sphere are presented in Figures 139 and 140 respectively. The heat flux distributions without forebody are based on Reference 26; Figure 135 was then used to obtain the heat flux distributions with forebody. The temperature distributions, as previously mentioned, were based on a thermally thin ballute without internal radiation. The base point for the heat flux and temperature distributions is an S/R_0 of two for the blunted cone and an S/R_0 of one for the sphere.

e. Base Point Heat Fluxes and Temperatures. The base point heat fluxes and temperatures are presented as a function of the altitude and velocity in Figures 141 and 142 respectively. These figures also show the effects of body size on heat flux and temperature and the effect of emissivity on temperature.

The laminar flow base point heat flux is based on Reference 3 and may be summarized as

$$Q_0 R_0^{0.5} = f_1 (\text{altitude, velocity}). \quad (6)$$

Since the Ballute is thermally thin and internal radiation is neglected, the above heat flux must be radiated from the Ballute, therefore:

$$Q_0 = \sigma \epsilon T_0^4 \quad (7)$$

or

$$Q_0 R_0^{0.5} = \sigma \epsilon R_0^{0.5} T_0^4 = f_1 (\text{altitude, velocity}) \quad (8)$$

and

$$(\epsilon R_0^{0.5} T_0^4)^{0.25} = \epsilon^{0.25} R_0^{0.125} T_0 = f_2 (\text{altitude, velocity}). \quad (9)$$

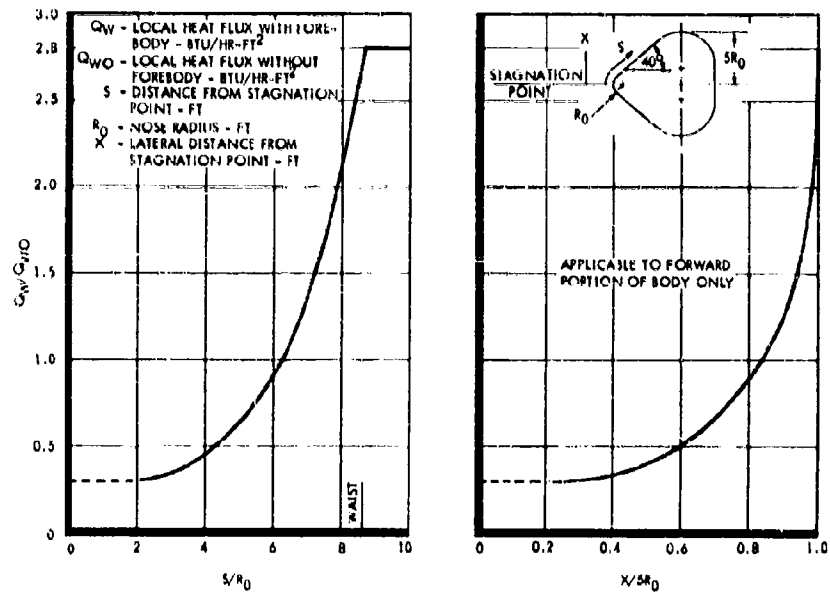


Figure 135. Effect of Forebody on Heat Fluxes

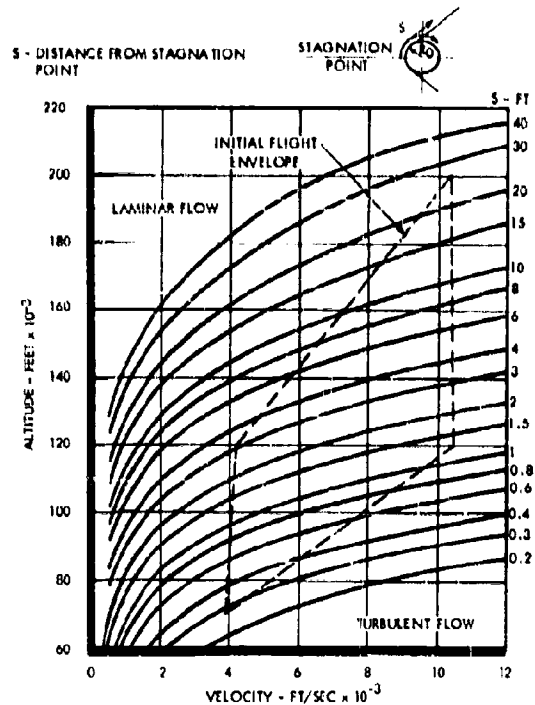


Figure 136. Transition from Laminar to Turbulent Flow

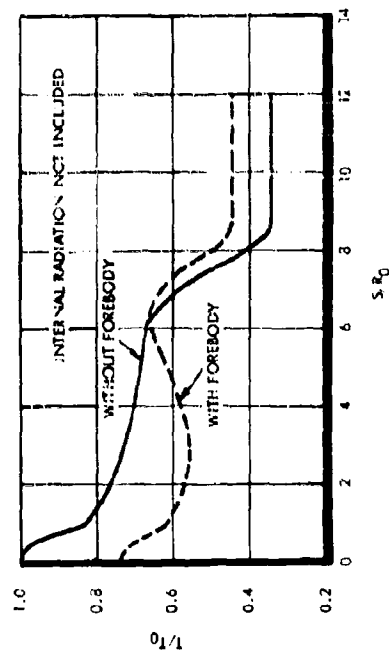
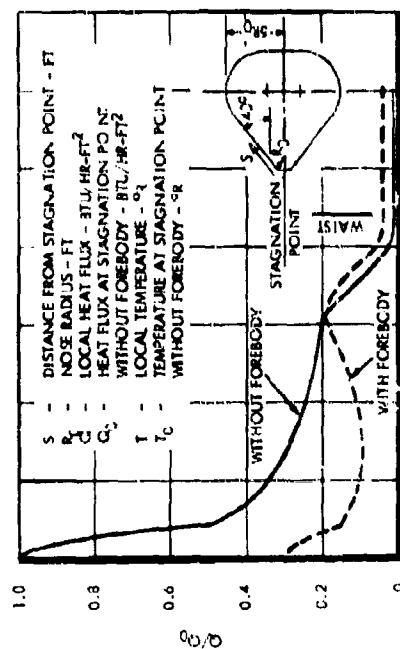


Figure 137. Laminar Heat Flux and Temperature Distribution on a Blunted Cone

- s - DISTANCE FROM STAGNATION POINT - FT
 R_0 - RADIUS - FT
 q - LOCAL HEAT FLUX - BTU/HR-FT²
 q_0 - HEAT FLUX AT STAGNATION POINT
 T - LOCAL TEMPERATURE - °F
 T_0 - TEMPERATURE AT STAGNATION POINT
 WITHOUT FOREBODY
 WITH FOREBODY
 WITH INTERNAL RADIATION
 WITHOUT INTERNAL RADIATION

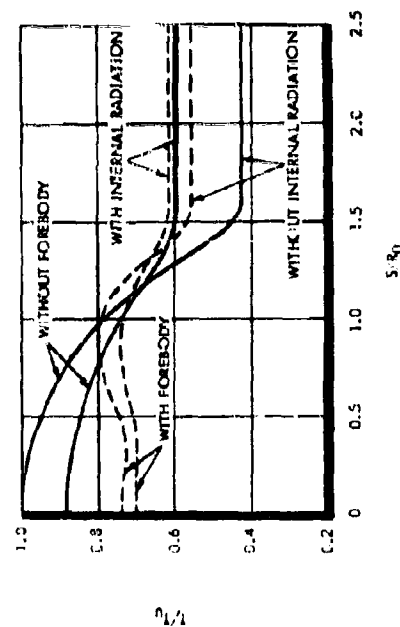
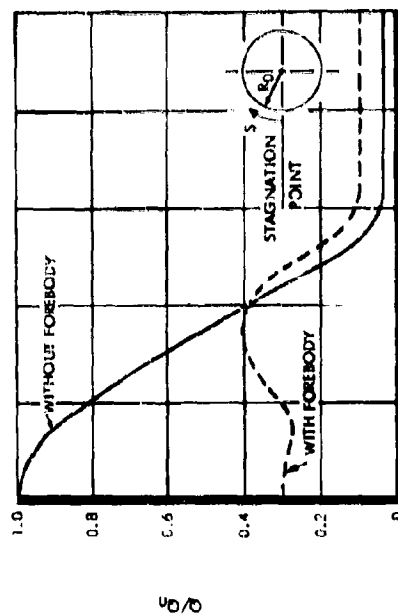


Figure 138. Heat Flux and Temperature Distribution on a Sphere in Laminar Flow

S - DISTANCE FROM STAGNATION POINT - FT
 R_0 - NOSE RADIUS - FT
 Q_c - LOCAL HEAT FLUX - BTU/HR-FT²
 Q_c - HEAT FLUX AT $S/R_0 = 2$ WITHOUT FOREBODY - BTU/HR-FT²
 T - LOCAL TEMPERATURE - °R
 T_c - TEMPERATURE AT $S/R_0 = 2$ WITHOUT FOREBODY - °R

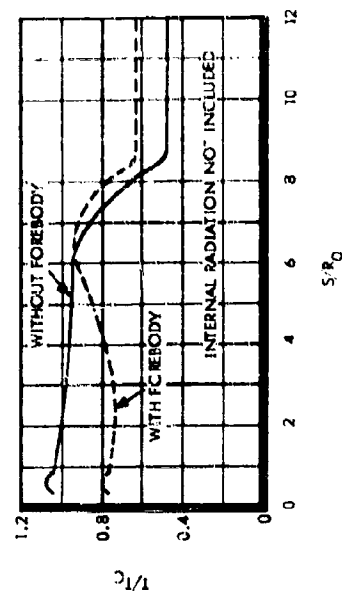
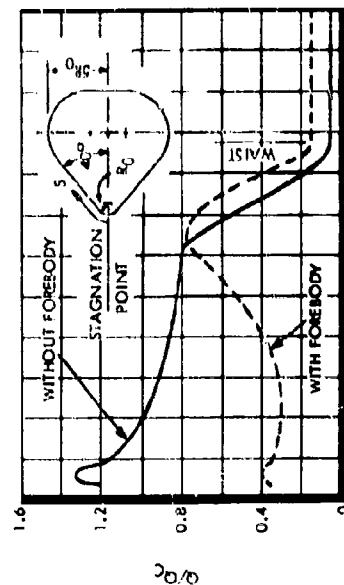


Figure 139. Turbulent Heat Flux and Temperature Distribution on a Blunted Cone

S - DISTANCE FROM STAGNATION POINT - FT
 R_0 - RADIUS - FT
 Q_c - LOCAL HEAT FLUX - BTU/HR-FT²
 Q_c - HEAT FLUX AT $S/R_0 = 1$ WITHOUT FOREBODY - BTU/HR-FT²
 T - LOCAL TEMPERATURE - °R
 T_c - TEMPERATURE AT $S/R_0 = 1$ WITHOUT FOREBODY - °R

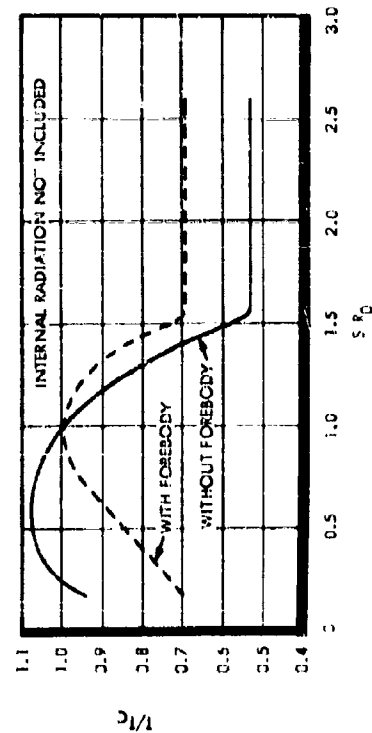
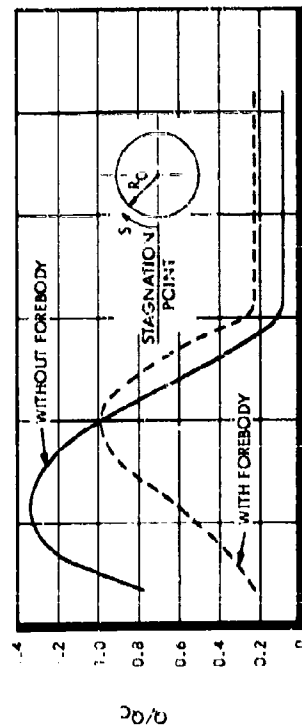


Figure 140. Heat Flux and Temperature Distribution on a Sphere Turbulent Flow

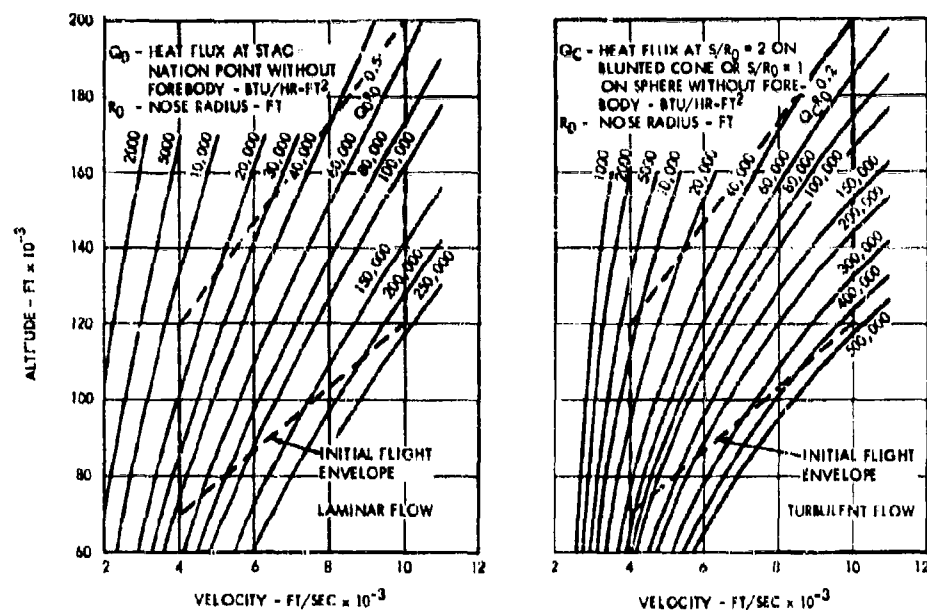


Figure 141. Laminar and Turbulent Heat Fluxes

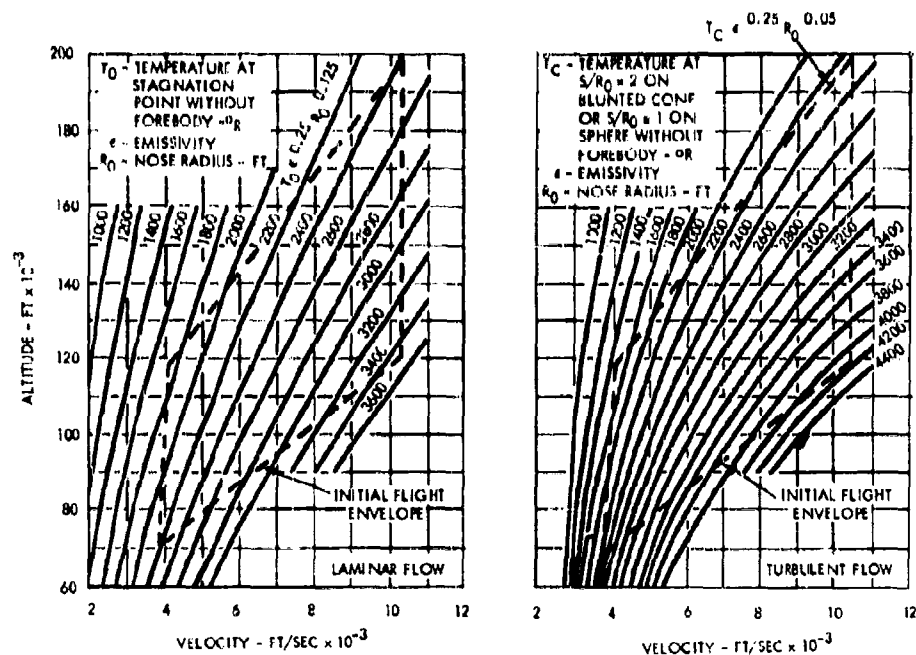


Figure 142. Laminar and Turbulent Temperatures

Equations (8) and (9) are plotted in Figures 141 and 142 respectively.

The turbulent flow base point heat flux is based on Reference 23 for a 40-degree half-angle cone at a distance from the nose of 2 feet, and may be summarized as $Q(S = 2 \text{ ft}) = f_3$ (altitude, velocity). (10)

The specified heat flux in the above equation is equal to the general heat flux (any value of S) multiplied by a distance correction factor (to correct to an S of 2 feet):

$$Q_S \left(\frac{S}{2} \right)^{0.2} = f_3 \text{ (altitude, velocity).} \quad (11)$$

For the condition wherein $S/R_0 = 2$, or $S/2 = R_0$,

$$Q(S/R_0 = 2) (R_0)^{0.2} = Q_C R_0^{0.2} = f_3 \text{ (altitude, velocity)} \quad (12)$$

Note that Q_C is based on an S/R_0 of 2 for the blunted cone. Reference 22 indicates that the heat flux, Q_C , at an $S/R_0 = 2$ on the blunted cone is equal to the heat flux, also Q_C , at an $S/R_0 = 1$ on the sphere. Again taking the Ballute as thermally thin and neglecting internal radiation, the above heat flux must be radiated from the Ballute, therefore

$$Q_C = \sigma \epsilon T_C^4 \quad (13)$$

or

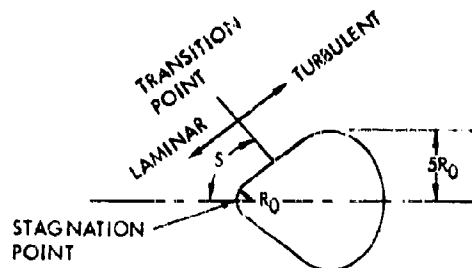
$$Q_C R_0^{0.2} = \sigma \epsilon R_0^{0.2} T_C^4 = f_3 \text{ (altitude, velocity)} \quad (14)$$

and

$$\left(\epsilon R_0^{0.2} T_C^4 \right)^{0.25} = \epsilon^{0.25} R_0^{0.05} T_C = f_4 \text{ (altitude, velocity)} \quad (15)$$

Equations 12 and 15 are plotted in Figures 141 and 142 respectively.

f. Example Problem. First it must be determined if the flow is laminar or turbulent at the desired point, S/R_0 of 6.5. This may be determined with the aid of Figure 136. Entering this chart at the altitude and velocity stated in the problem, 130,000 feet and 8000 ft/sec respectively yield a value of 2.6 feet for S, the distance between the stagnation point and the transition point on the body where this flow change occurs.



In this problem, the waist radius given was 5 feet. Considering blunt cone Ballute configurations, this then fixes the nose radius at 1 foot. At the point of investigation, $S/R_0 = 6.5$. With $R_0 = 1$, S is, therefore, equal to 6.5 feet. Since this distance is greater than the chart value 2.6 feet (location of the transition point) the flow is turbulent.

The temperature at point $S/R_0 = 6.5$ can now be found by using the turbulent flow curve of Figure 142. Entering this curve at given velocity-altitude points gives a $T_{C,0.25} R_0^{0.05}$ value equal to $3000^\circ R - ft^{0.05}$. Using the given value of emissivity ($\epsilon = 0.9$) and the nose radius of 1 foot, the base temperature is found to be

$$T_{C(0.9)}^{0.25} (1)^{0.05} = 3000^\circ R$$

$$T_{C(0.974)} (1) = 3000^\circ R$$

$$T_C = 3080^\circ R.$$

Using Figure 139 and the S/R_0 value of 6.5, T/T_C is found to be 0.940. The local temperature is therefore $0.940 \times 3080^\circ R = 2895^\circ R$ ($2435^\circ F$).

g. Trajectory and Temperature Limit Parameters. The temperature limit parameters shown in Figures 143 and 144 indicate the available safe margin of operation attainable for particular Ballute drag systems deployed within the intended flight envelope. The equilibrium temperature limits represent the thermally critical areas on each of the Ballute configurations in laminar and turbulent flow. Transition Reynold's number for these studies, as was previously mentioned, was assumed at 5×10^5 based upon freestream conditions.

Increasing the reference radius is reflected in increased altitude margin of operation with substantial benefits being realized in laminar flow. The plots are seen to terminate in the vicinity of Mach 4.5, the total temperature at this velocity being insufficient to create a thermal problem. Internal radiation was not taken into account in preparing the temperature limit parameters. Radiation interchange studies show that the radiation equilibrium surface temperatures can be reduced in excess of 100° for those applications, with the resulting limiting altitude parameter being lowered approximately 5000 feet for a $1500^\circ F$ limiting temperature.

h. Comparison with Preliminary Study. A spiked body was used for the preliminary analysis (Section 3) in the absence of definite information concerning drag bodies. Subsequent testing of drag bodies demonstrated that spiked body data is not applicable to drag bodies. The initial shock wave from the spike generally impinged upon the spiked body, producing a highly turbulent region with resulting high heat flux. The shock wave from the forebody did not impinge upon the drag body, while the wake prevented the airstream from recovering free-stream velocity downstream of the forebody, thereby partially shielding the drag body from the higher energy flow.

3. Conclusions and Recommendations

Figures 135 through 144 may be used to predict the local fabric temperature for Ballute configurations deployed within the flight envelope under consideration.

The wind tunnel tests conducted indicate a reduction in the heat transfer rates to the drag bodies in the presence of forebodies. However, additional testing is recommended to determine the conditions causing turbulent flows and to encompass the velocity regime between supersonic flow and Mach 10.

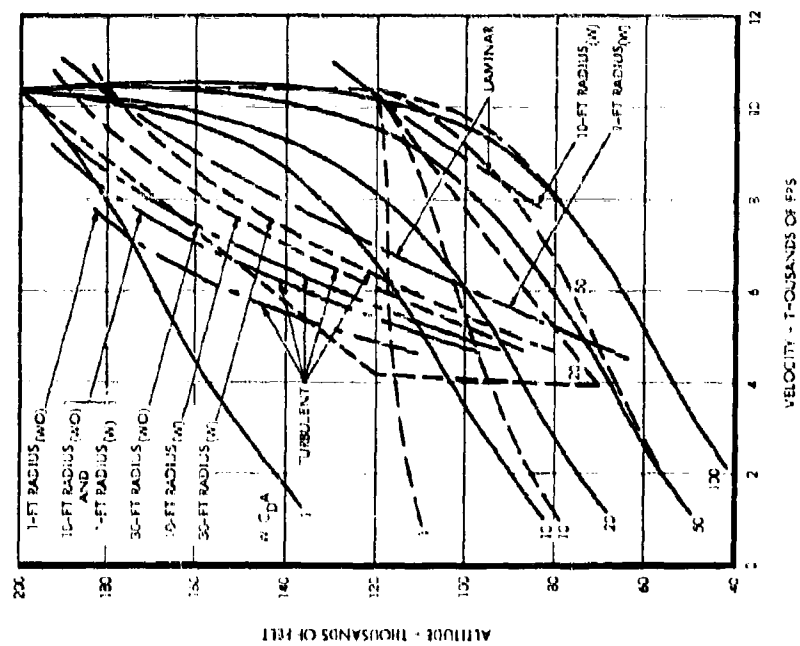
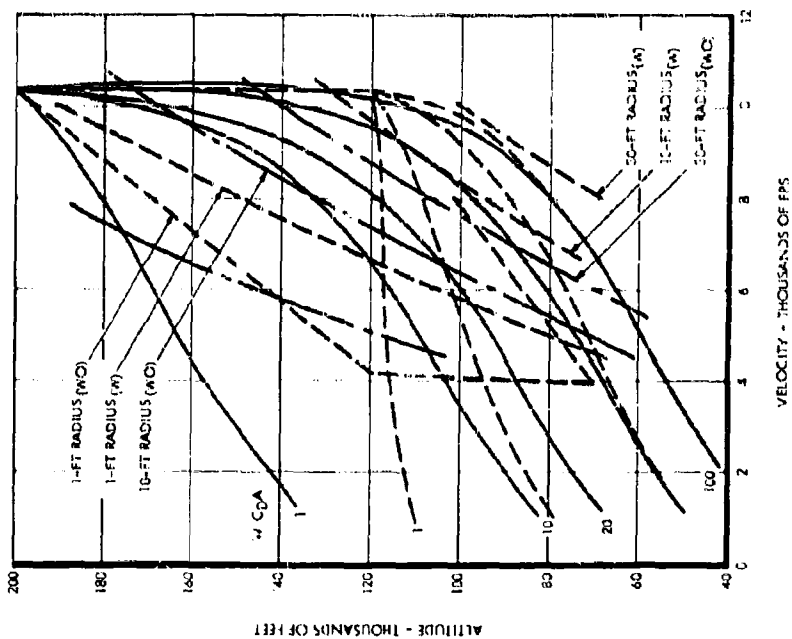
More precise thermal calculations should be in order for any specific Ballute configuration, with design optimization being desirable in cases of marginal heating.

D. AERODYNAMICS

1. General

A final aerodynamic discussion of the combined results of all of the contract wind tunnel tests is presented. Data from Reference 24 plus recent unpublished data of wind tunnel tests conducted by the Large Supersonic Tunnels Branch personnel at NASA Langley Station, Virginia, is also presented. These recent NASA tests (Reference 25) were supplemental to References 24 and 2, plus this contract effort and consisted of supersonic tests of towed solid conical models. The NASA tests were conducted between this contract's schedule tests of September 1961 and 1962.

As required per contract, analytical and experimental aerodynamic data was obtained over a range of Mach 0.2 and Mach 10. The Reynolds number range was between RN/ft equal to 0.96×10^6 to $6 \times 10^6/ft$. This range of wind tunnel test Reynold's numbers that would be experienced in the contract flight performance envelope is shown in Figure 145.



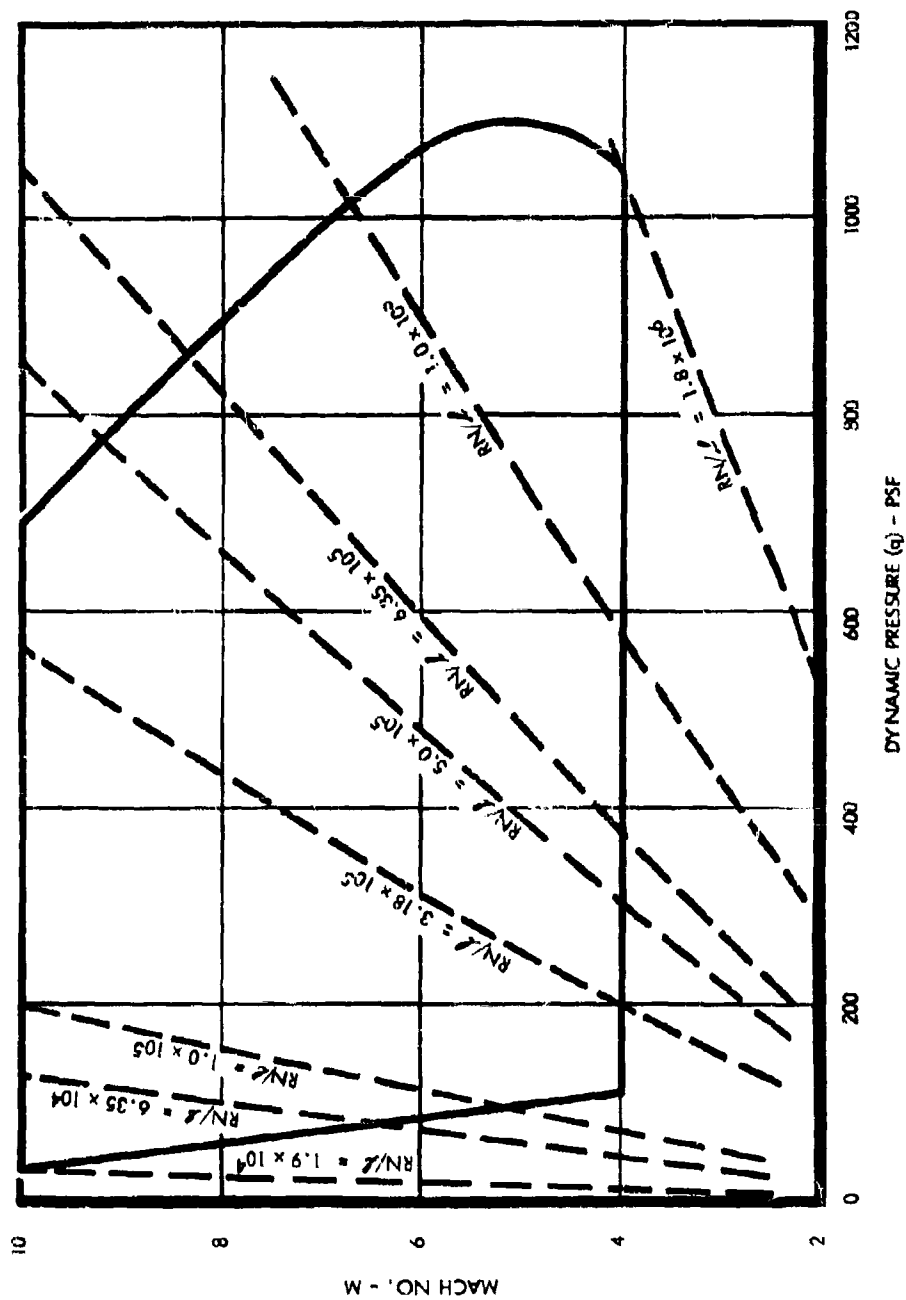


Figure 145. Reynold's Number Range in Performance Envelope

2. Flow Behavior

The concept of the boundary layer is used to explain the flow behavior around the model.

Boundary layer experiences transition from laminar to turbulent under the influence of Reynold's number and Mach number among other factors. The tests were conducted in a range of RN and Mach numbers that suggest turbulent state of boundary layer with possible transitional region occurring at certain times. Separation of the boundary layer is produced either by the changes in geometry of a model or by shock wave intersection. The configurations investigated indicate separation due to fence and shock-boundary layer interaction. Large adverse pressure gradient imposed by the shock thickens the boundary layer, makes it turbulent, and separates it from the model, which in turn increases the thickness of the wake. Increase in drag is realized which has frictional nature.

After the separation occurrence the turbulent (or laminar) separated region is steady provided the turning angle of the flow (or surface deflection angle) is not high.

The 3.9 or 6.25 percent fence achieves separation at a point (30 degrees aft of a model equator) of the most aft position. This position is significant because of the force equilibrium existing there, which assures the steadiness of the region. As a result the drag is constant for a given model configuration within the supersonic velocity range. The increase in the height of a fence may favorably influence the drag of a model, but stability will decrease due to unsteadiness of the separated region.

The pressure rise in the steady separated region is close to that in inviscid flow behind the expanded shock since downstream of the region the flow is again parallel to the bounding surface. Thus inviscid flow pressure rise can be used to estimate the pressure rise across a separated region.

Generally the drag of the configurations considered consists mainly of the pressure drag with small contributions from the skin-friction drag.

3. Drag Results

A summary curve of all of the applicable drag data is presented in Figure 146. The shaded portions indicate the envelope of experimental wind tunnel data. The inflatable model data falls within the shaded area. The envelope limits of the supersonic tests were obtained from the solid model data in References 25 and 2.

Figure 147 presents data from Reference 25; the data shows the effect of increasing the size of the burble fence up to 10 percent. A 15-percent burble fence was also tested. The data is not shown because of reported questionable stability in its towed position.

The combined results of all applicable tests indicate the following:

- (1) Inflatable model results show reduced drag coefficients at L/d ratios below 5.
- (2) Inflatable model results show peak drag coefficients at L/d ratios of 6 to 8.
- (3) Inflatable model results show percent increase (or decrease) at L/d ratios greater than 8 is small in the supersonic range.
- (4) Drag data results of inflatable (rain-air and preinflated) models is equivalent to solid models which demonstrates feasibility of inflatable devices.

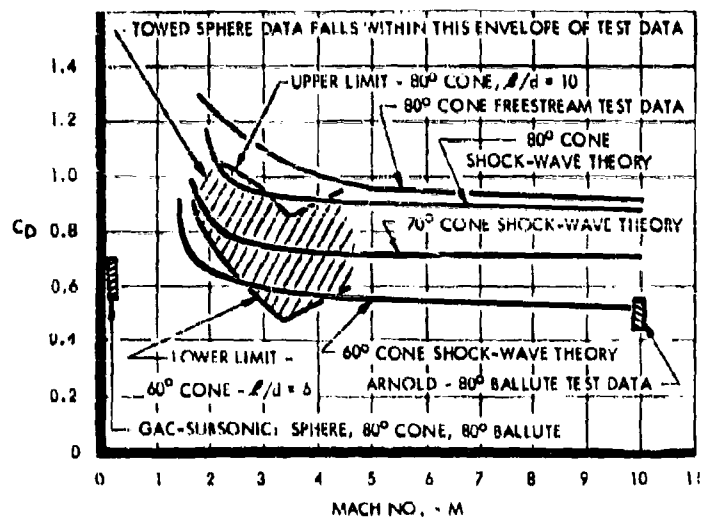


Figure 146. Towed Blunt Body Drag Data

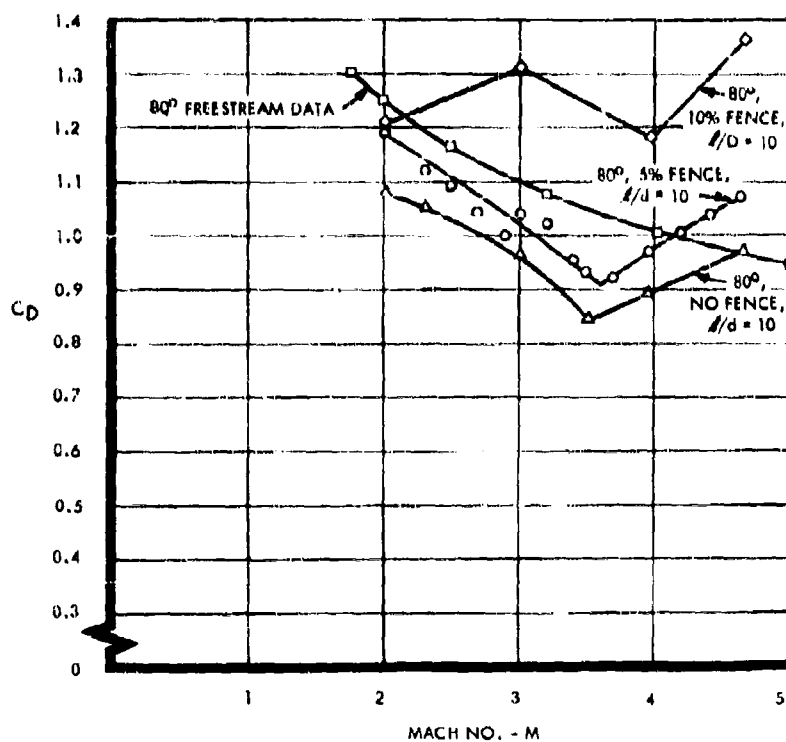


Figure 147. Towed Cone, Fence Drag Data

E. DESIGN

1. Design Conditions and Assumptions

The weight and bulk study of the various configurations was made utilizing the trajectory data of three of the four starting points of the performance envelope as presented in Figure 1. These starting conditions were:

- (1) $M_0 = 10$ at 200,000 feet
- (2) $M_0 = 4$ at 120,000 feet
- (3) $M_0 = 4$ at 70,000 feet.

The materials considered in the study were coated René 41 cloth and Dacron-neoprene fabric. In condition 1, where the temperature would be high, the temperature was arbitrarily chosen to always be at 1500°F. In conditions 2 and 3, at $M_0 = 4$, the temperature was assumed low enough to use either Dacron-neoprene or René 41. The strength-weight ratios used in these conditions were therefore:

<u>Condition 1</u>	$k_f = 2920$ feet	René 41 at 1500°F
	$k_c = 32,100$ feet	
<u>Condition 2 and 3</u>	$k_f = 7920$ feet	René 41 at 1000°F
	$k_c = 61,600$ feet	
	$k_f = 26,700$ feet	Dacron at 350°F
	$k_c = 37,500$ feet	

A factor of safety $FS = 2$ was used throughout the study. Based on the wind tunnel results at Mach numbers 4 and 10, it was estimated that at the conditions of peak (q) along the trajectories the drag coefficient would be approximately 0.75. Therefore, for consistency, a $C_D = 0.75$ was chosen for all cases. It is pointed out that the C_D value chosen for the design defines the shape and stresses in the particular configuration (see Section 8).

Total weights (W) chosen for the study were 250 pounds and 750 pounds. The four ballistic coefficients ($W/C_D A$) of 1, 10, 50, and 100, as used in the trajectory analysis, were also chosen. Since the payload drag area ($C_D A$)_P is small compared to the decelerator drag area ($C_D A$)_D, the remainder of the design discussion assumes $CDA = (C_D A)_T = (C_D A)_D$.

The inflation pressures used for the closed pressure vessel configuration, namely sphere, hemisphere, Airmat cone, and torus with curtain, are a function of a peak dynamic pressure (q) as defined for each particular case in the examples presented in Section 8-B. For the rain-air configurations the inflation pressure was assumed as $P = q$, which is adequate to assure full inflation of the model. Since the Langley wind tunnel tests indicated that higher internal pressure values of q were obtained, it is further assumed that a gage pressure relief valve will be provided to hold the maximum internal pressure equal to the peak q along the trajectory. In addition it was assumed that the static pressure in the wake aft of the Ballute is equal to zero. Therefore, the internal pressure is equal to the pressure differential across the fabric.

Since the pressure differential across the fabric, which is equal to q , is the peak structure design load, the selection of the weight of the decelerator structure is based on a specific high-level dynamic pressure. For the remainder of the design study it is important to note the following:

- (1) Ballute weights in Table 31 were based on the q load at a peak temperature of 1500°F, which was the most critical condition.

Table 31. Weights of Various Concepts for One Trajectory Condition (Sheet 1)

CONFIGURATION	WEIGHT EQUATION	P/q	k	ρ	INFLATION PRESSURE - P (psf)
80-Degree Ballute, Plain Back	$W_D = P\pi R^3 \left[\frac{4(1-k)}{k_f} + \frac{2\pi k}{k_c} \right]$	1.0	0.865	-	230
80-Degree Ballute, Tucked Back	$W_D = P\pi R^3 \left[\frac{4(1-k-\rho)}{k_f} + \frac{2(1.2\rho + \pi k)}{k_c} \right]$	1.0	0.453	0.34	230
Sphere	$W_D = P\pi R^3 \left[\frac{4(1-k)}{k_f} + \frac{2\pi k}{k_c} \right]$	3.68	0.3	-	847
Hemisphere	$W_D = \frac{4P\pi R^3}{k_f}$	4.16	--	--	956
80-Degree Airmat Cone	$W_D = \frac{17.4 C_D q R^3}{k_f}$	4.52	--	--	1040
Torus with Curtain	$W_D = P\pi R^3 \left[\frac{13.3}{k_f} + \frac{6.07}{k_c} \right]$	26.5	--	--	6100

CONDITIONS

$W/C_D A = 40$

$M_0 = 4.96$

$h_0 = 133,000 \text{ ft}$

$C_D = 0.75$

Diameter = 10 ft

$W = 2355 \text{ lb}$

$A = 78.5 \text{ ft}^2$

$q = 230 \text{ psf}$

FS = 2

$k_f = 2920 \text{ ft}$

$k_c = 32,100 \text{ ft}$

Coated Reno 41 at 1500°F

Package factor = 28.8 lb/ft³

(2) Design curve weights (Figures 140 and 140) were based on the peak q occurring at a peak temperature of 1500°F along the descent trajectory. This assumption is conservative since the peak q usually occurs after peak temperature, and hence the decelerator structure does not have to support this peak load at its lowest strength-to-weight ratio.

2. Configuration Weight and Bulk Comparison

The weight and package volumes as presented in Table 31 were calculated for the six concepts considered at one trajectory condition of

$M_0 = 4.96$

$h_0 = 133,000 \text{ feet}$

$\frac{W}{C_D A} = 40$

$W = 2355 \text{ pounds.}$

This trajectory condition, which is different from the conditions stated above and different from the conditions chosen for the aerodynamic analysis, was arbitrarily chosen for this particular weight

Table 31. Weights of Various Concepts for One Trajectory Condition (Sheet 2)

CLOTH & CABLE DECELER- ATOR WT (lb)	VOLUME (ft ³)	PV (lb-ft)	INFLATION GEAR WT (lb)	TOTAL DECELER- ATOR WT - W _D (Pour is)	PACKAGE VOLUME (FT ³)		
					DECELER- ATOR	INFLATION GEAR	TOTAL
32	--	--	---	32	1.2	--	1.2
36	--	--	--	36	1.3	--	1.3
278	523	443,000	49	327	9.7	1.5	11.2
420	477.3	456,000	49	469	14.6	1.5	16.1
106	109.1	113,700	14.9	124.0	3.7	0.3	4.0
84	15.62	95,400	11.7	95.7	3.0	0.3	3.3

and bulk table in order to select a point within the prescribed performance envelope where the temperature would fall within the 1500°F limit. See Figure 150.

The minimum limiting diameter of 10 feet, as determined in Section 8-C, was chosen. This diameter and the W/C_{DA} , for which data was available, determined the weight (W), of 2355 pounds.

Coated René 41 at 1500°F was the material considered and as previously stated, $C_D = 0.75$. From the trajectory data of Reference 1, the q at peak temperature = 230 psf, which occurs at 110,000 foot altitude.

The packaging factor used for calculating volumes of the Ballute alone is 29.9 lb/ft³. This value was obtained for metal cloth packaging tests.

Weight and volume of the inflation gear were estimated on the basis of 3000-psi fiberglass sphere bottles with compressed air.

From Table 31 the ram-air configurations offer the lowest weight and package volume. Based on this and on the satisfactory wind tunnel results, the remainder of the weight study is confined to the 80-degree ram-air Ballute. The Ballute with a tucked back was not considered further in the weight study because of limited experimental data. During a subsonic wind tunnel test run here at GAC, the tucked Ballute did not remain conical in shape. The model took the shape of a torus. During run No. 15 (see page 56) of the supersonic tests, the tucked Ballute did remain conical in shape. The reason for the shape instability at subsonic speeds can not be clearly defined. However, one suggested reason is that the tie-line inside the Ballute, which ties the model nose to the back end,

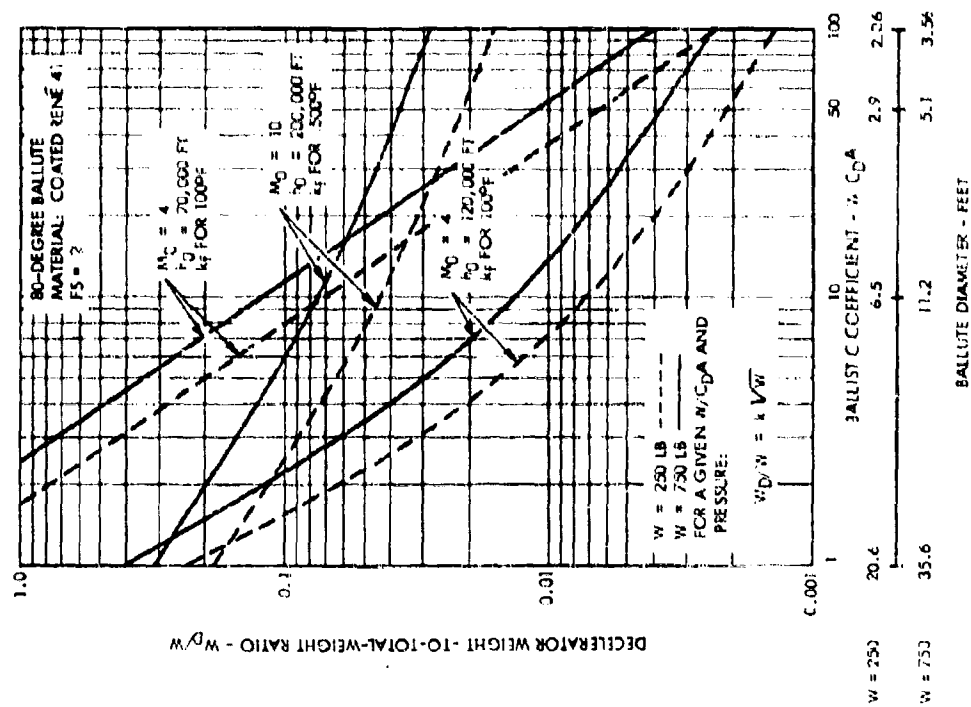


Figure 148. Decelerator Weight-to-Total-Weight Ratio (w_D/w) versus Ballistic Coefficient ($w C_D A$)

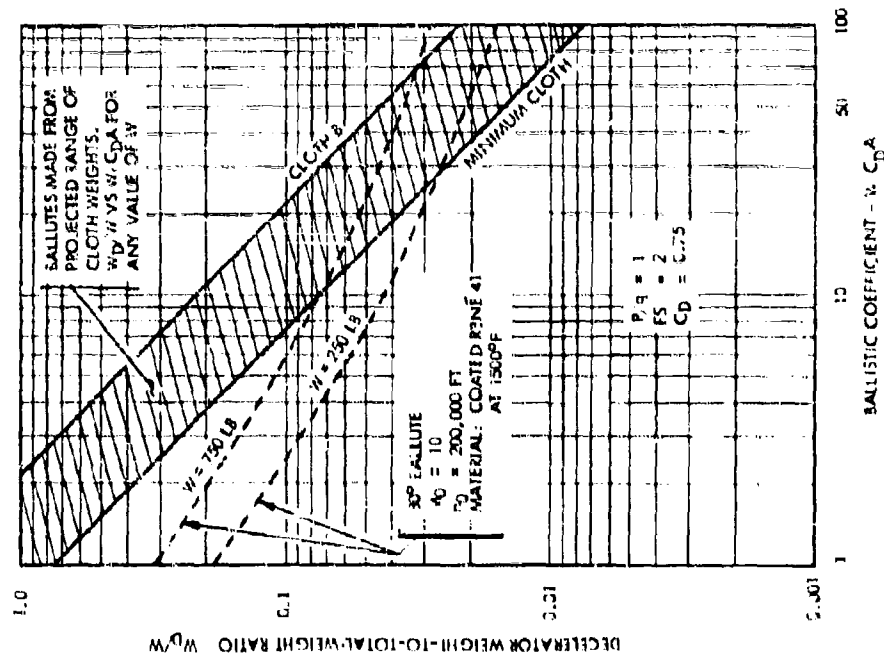


Figure 149. Projected Weight Range for 80-Degree Ballute of Coated René 41 at 15000F

restricted the length shape change, and hence if the internal pressure load is in excess of the external air load the inflated model takes the shape of a body-of-revolution, in this case a torus.

3. Design Curves

Figure 151 shows the penalty of the 80-degree Ballute made of René 41 at 1500°F compared to Dacron at 350°F. The inflation pressure chosen is 230 psf, and the parameters $P/q = 1$, $C_D = 0.73$, and $FS = 2$ are as were discussed above.

The contour shape factor for the 80° Ballute is

$$K = \frac{nT_m}{P\pi R^2} = 0.865 \text{ (Reference Section 8-B)}$$

The strength-weight ratios for these materials are

$$k_f = 2920 \text{ feet} \quad \text{René 41 at 1500°F}$$

$$k_c = 32,100 \text{ feet}$$

$$k_f = 26,700 \text{ feet} \quad \text{Dacron at 350°F}$$

$$k_c = 37,600 \text{ feet}$$

Figure 152 is plotted for Ballutes designed for the pressure relationship of $P/q = 1$. The graph may be used to determine weights at any pressure P by direct proportion since

$$W_D = \text{constant} \times (PR^3)$$

In Figure 152 the weight of a René 41 80-degree Ballute is shown versus size at various q 's at a temperature of 1500°F. Superimposed on this graph is a plot of weights of Ballutes constructed of cloth B and a minimum-weight cloth. Cloth B (see Section 6) represents nearly the maximum-weight single-ply cloth that can be made. The minimum-weight cloth is a 0.0016-inch diameter woven 200 x 200 mesh cloth with the coating weight of 5 oz/yd, giving a total weight of 10 oz/yd². Although cloth weights may be reduced with the development of cloths utilizing 0.0006-inch projected diameter wire, it is assumed here that coating weights cannot be reduced substantially below 5 oz/yd². The Ballute weights were calculated with the addition of meridional cable weights compatible with each diameter.

The band between the weight curves of cloth B and the minimum cloth represents the projected range of Ballute size which can be built for the 1500°F.

In Figure 153 the membrane stress level of an 80-degree Ballute is shown versus size at various inflation pressures.

Figure 148 presents the René 41 80-degree Ballute weight to total system weight ratio, W_D/W versus $W/C_D A$, for 3 starting conditions. Payload weights of 250 and 750 pounds were assumed. The strength-weight ratio employed in calculating weights was based on 100°F for the Mach 4 conditions and 1500°F for the Mach 10 condition. The curves indicate a reduction in weight with increasing $W/C_D A$ since the R^3 term decreases more than the pressure P increases in the weight equation:

$$W_D \text{ (decelerator weight)} = \text{constant} \times (PR^3).$$

The curves also indicate a reduction in weight ratio with decreasing total weight for a given $W/C_D A$ and pressure. It can be shown from the weight equation that for a given $W/C_D A$ and pressure P

$$\frac{W}{C_D A} = \text{constant} \times W.$$

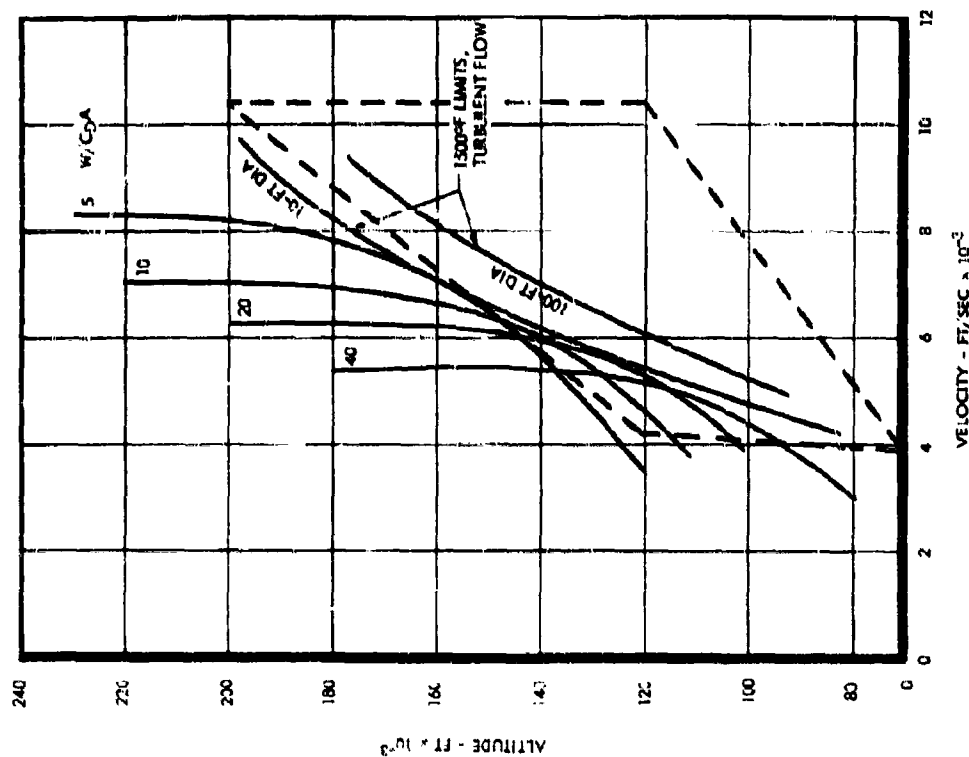


Figure 150. Vertical Trajectories within the 1500°F Limit for 10-Foot-Diameter Ballute in Turbulent Flow

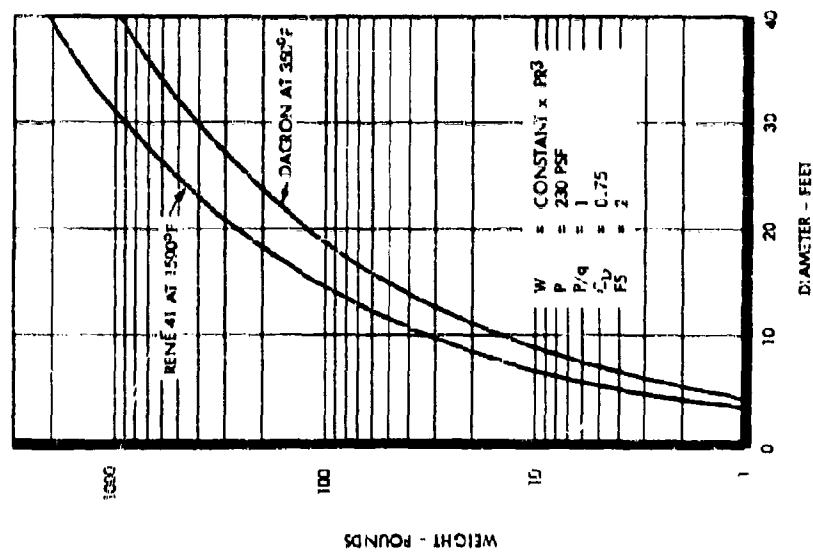


Figure 151. Weight of 80-Degree Ballite versus Diameter at One Pressure for Two Material Conditions

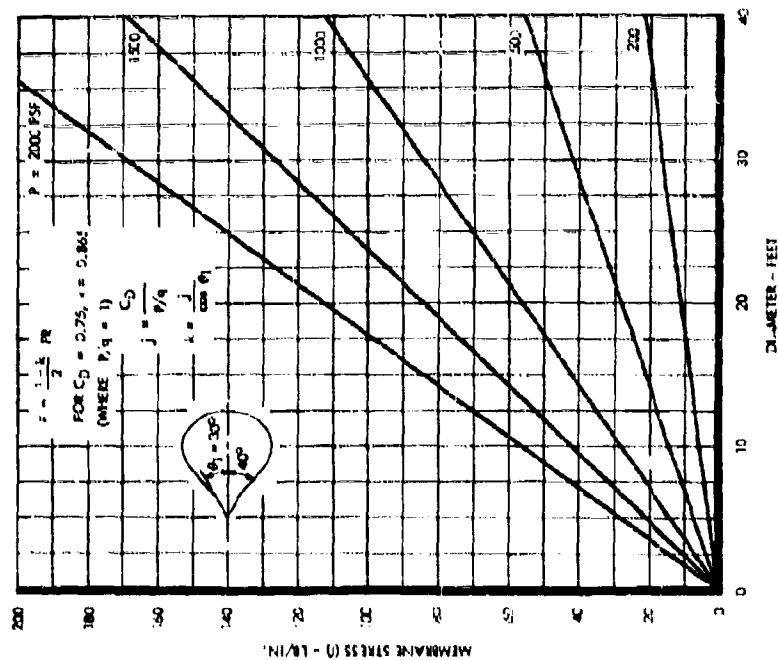


Figure 153. Membrane Stress in 80-Degree Balloon at Various Inflation Pressures

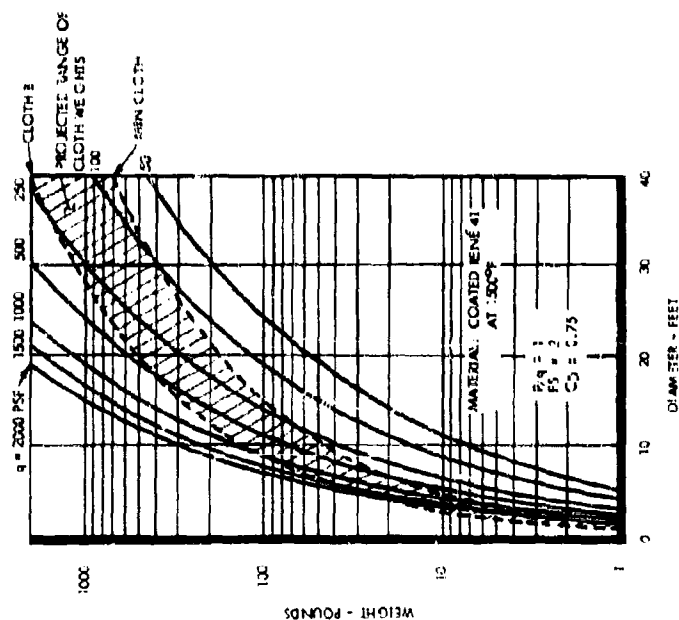


Figure 152. Weight of 80-Degree Balloon versus Diameter at Various Dynamic Pressures

The curves further indicate that the W_D/W ratio becomes prohibitively high at low values of $W/C_D A$.

Figure 149 presents the band of Ballute weight ratios of Ballutes made from the same range of cloth weights as shown in Figure 152 except that the data is plotted as W_D/W ratio versus $W/C_D A$. It can be shown that in dividing the Ballute weight W_D for a given cloth, which is proportional to $(d')^2$, by the total weight W , which is proportional to $W/C_D A \times (d')^2$, the $(d')^2$ term cancels out leaving

$$W_D/W = (\text{constant } x)1/(W/C_D A).$$

This indicates that the W_D/W ratio for a particular cloth is a function of $W/C_D A$ only and is independent of the total weight W . Included in the graph are the two W_D/W ratio curves for the $M_0 = 10$ starting condition which were presented in Figure 148. The intersection of either of these curves with a cloth curve gives the corresponding $W/C_D A$, which defines the Ballute size for that particular total weight W and cloth material. This graph indicates that the ballistic coefficient $W/C_D A$ must be fairly large in order to obtain a reasonably low W_D/W ratio.

Figure 150 shows two of the temperature limit curves shown previously in Section 8-C. They show the 1500°F limit for the turbulent flow condition for a 10-foot diameter and for a 100-foot diameter conical decelerator. Above the 10-foot diameter curve are drawn four trajectories which fall just within the 1500°F limit for this size Ballute. The trajectory for $W/C_D A = 40$ was taken from Reference 1. The other three trajectories for $W/C_D A = 5, 10, \text{ and } 20$ were calculated by a hand iteration process (successive incremental approximation). The estimated error of these altitude velocity trajectories is less than 4 percent of the computer results.

SECTION 9

CONCLUSIONS AND RECOMMENDATIONS

A. GENERAL

It is concluded from the design and performance information obtained during this investigation that an inflatable balloon is a feasible stabilization and deceleration device and will perform satisfactorily.

Since the main objective of the program was to obtain optimum drag device design information, the following concluding statements are presented.

B. DESIGN REQUIREMENTS (CONSIDERED OPTIMUM)

The following list of design requirements was based on the results of the analytical study, the experimental tests, and the subsequent final design study.

- (1) Use a ram-air Ballute configuration with a plain isotenoid aft end.
- (2) Provide an apex nose angle of 80 degrees.
- (3) Provide a 10-percent burble fence located on the decelerator equator.
- (4) Provide side ram-air screened inlets (inlets may be orifices on the burble fence).
- (5) Make the diameter of the Ballute greater than the diameter of the payload.
- (6) Make the length of the tow line 6 to 8 times the payload diameter to obtain maximum drag.
- (7) Design the fabric structure based on the most adverse of the following loading conditions:
 - (a) Fabric differential pressure load at peak temperature conditions.
 - (b) Fabric differential pressure load at peak q condition.
- (8) Provide pressure relief valve to control internal Ballute pressure when required.

C. REASONS FOR DESIGN PARAMETER SELECTIONS

- (1) Ram-air inflation eliminates heavy, bulky hardware.
- (2) Ram-air inflation eliminates near 100 percent gas-tight material requirements.
- (3) An 80-degree apex nose angle is the most blunt (high drag) body that exhibits excellent stability in its towed position behind a forebody.
- (4) A 10-percent burble fence provides maximum drag (up to $C_D = 1.3$ in the Mach 2 to 5 speed range) without penalizing stability.
- (5) Side ram-air inlets provide pressure for full inflation of the Ballute at subsonic, supersonic, and hypersonic speeds.

D. RECOMMENDATIONS

Since Ballute decelerator performance has been shown feasible, it is recommended that

actual free-flight Ballute demonstration tests be conducted in the Mach 4 to Mach 10 flight regime.

In addition there is need for other development programs to obtain usable system hardware in the field of inflatable structures for re-entry and recovery. They are as follows:

- (1) Obtain additional René cloth information.
- (2) Investigate further the use of refractory and super-alloy materials.
- (3) Investigate inflatable trailing drag bodies at $L/d = 0$.

APPENDIX I

RAM-AIR BALLUTE SHAPE STABILITY ANALYSIS

The instabilities exhibited by the ram-air inflated Ballute and its ultimate failure during the Series I wind tunnel tests at NASA Langley prompted an investigation of the phenomenon and means by which it can be mitigated. This phenomenon is quite familiar to the ram-jet designer since this is a problem encountered in off-design operation. The presence of the Ballute in a turbulent wake of the payload and the broad Mach number band of operation not a rather complex problem.

In an effort to initiate this study, the consulting services of Dr. S. Ostrach of Case Institute of Technology were obtained. His function was to review the general problem area plus the specific NASA Langley wind tunnel results, namely the high-speed schlieren movies, and investigate and submit reasons for the buzzing phenomenon, the incomplete model inflation, and the subsequent model fabric rupture. In addition he was to confirm GAC's suggested solution of providing inlet damping with screens or reed valves or suggest other possible solutions. A summary of his comments is as follows:

- (1) Sudden opening of the model could cause fabric rupture.
- (2) Insufficient inflation pressure due to the presence of a forebody low-pressure wake could cause incomplete model inflation.
- (3) Cyclic flow circulation (in and out of the front inlet) or mass flow pulsations caused by a pressure variation across the inlet due to shock wave curvature near the inlet could cause fabric rupture.
- (4) Inlets with reed valves or oblique shock inducers could alleviate problems.

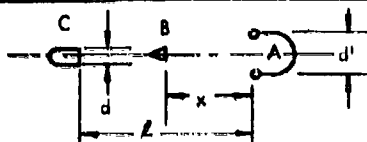
An experimental approach to the problem was undertaken concurrently with the analytical approach. A water flow table was employed in this investigation with various two-dimensional models inserted in the stream flow to simulate supersonic flow conditions. This hydraulic analog of supersonic flow is well known to be exact at $M = 2.0$ with deterioration on either side of this exact Mach number. It was felt, however, that the study by this simulation would have merit even though two-dimensional models would be employed, and the flow simulation would not be exact in some cases. A qualitative evaluation of factors affecting this phenomenon was undertaken using this experimental technique.

Tables 32 and 33 document the various configurations and flow conditions that were tested, and a typical test setup is shown in Figure 154.

The water table used is a commercially available device known as the Aerodynalog. In order to measure the instability possessed by the Ballute, attention was given to the characteristics of the internal flow. By the insertion of a colored dye in the cavity of the model Ballute, the time of its dissipation was indicative of the internal flow stability - the longer time duration of the dissipation, the superior the flow stability.

Series I tests were conducted to determine the effectiveness of a flow separator placed forward of the afterbody. The function of the flow separator was to stabilize the concave afterbody inlet flow. This method was successfully employed by the University of Minnesota parachute group to stabilize supersonic parachutes. As the result of this series of tests, it is concluded that the flow separator does contribute to internal flow stability when it is located some distance upstream, not adjacent to the concave body. With the addition of the payload located 5 diameters forward, the flow stability deteriorated somewhat; however, it was not ascertained whether the flow separator remained effective in this arrangement. In the series II tests where the flow separator was tested both in and out of the wake of the payload, the effectiveness of the flow separator was not significant. It is therefore concluded that, at least for these short coupled arrangements of payload and Ballute, the flow separator is not effective; however, it may have merit for the long coupled arrangements.

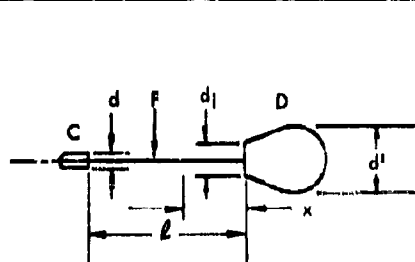
Table 32. Water Table Test Log - Series I Configuration



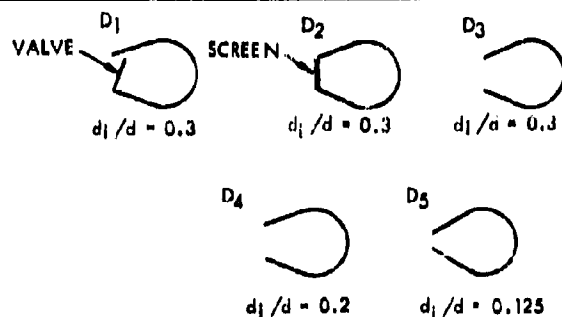
SERIES I CONFIGURATION

RUN NO.	TYPE CONFIGURATION	MACH NO.	l/d	x/d'	RUN NO.	TYPE CONFIGURATION	MACH NO.	l/d	x/d'
1	A	2	-	-	11	A + B + C	3	-	0.81
2	A + B	3	-	-	12		2	5	0
3		2	-	0	13		2	5	0.18
4		2	-	0.18	14		2	5	0.25
5		2	-	0.22	15		2	5	0.31
6		2	-	0.25	16		3	5	0
7		2	-	0.31	17		3	5	0.18
8		3	-	0	18		3	5	0.25
9		3	-	0.18	19		3	5	0.31
10		3	-	0.31	20		3	5	1.38

Table 33. Water Table Test Log - Series II Configuration



SERIES II CONFIGURATION



SERIES II DECELERATOR VARIATIONS

RUN NO.	TYPE CONFIGURATION	MACH NO.	l/d	x/d'	RUN NO.	TYPE CONFIGURATION	MACH NO.	l/d	x/d'
1	D ₁	2	-	-	11	D ₁ + F	3	6	-
2	D ₁ + C	3	-	-	12		5	1	-
3		5	-	-	13		5	4	-
4		2	1	-	14		5	5	-
5		2	4	-	15		5	6	-
6		2	5	-	16		2	5	-
7		2	6	-	17		2	6	-
8		3	1	-	18		3	5	-
9		3	4	-	19		3	6	-
10		3	5	-	20		5	5	-

Table 33. Water Table Test Log - Series II Configuration (Continued)

RUN NO.	TYPE CONFIGURATION	MACH NO.	L/d	x/d'	RUN NO.	TYPE CONFIGURATION	MACH NO.	L/d	x/d'
21	D ₁ + F + C	5	6	-	41	D ₂ + F + C	5	4	-
22		2	5	-	42		5	5	-
23		2	8	-	43		3	5	-
24		3	5	-	44		5	5	-
25		3	6	-	45	D ₅	3	-	-
26	D ₃	5	5	-	46	D ₅ + C	5	-	-
27		5	6	-	47		3	1	-
28		2	-	-	48		3	2	-
29		3	-	-	49		3	4	-
30		5	-	-	50		3	5	-
31	D ₃ + C	3	4	-	51	D ₄	2	-	-
32		3	5	-	52		3	-	-
33		5	4	-	53		5	-	-
34		5	5	-	54		5	3	-
35		3	5	-	55	D ₄ + C	5	4	-
36	D ₃ + F + C	5	5	-	56		5	5	-
37		3	-	-	57		5	0	-
38		5	-	-	58		3	5	-
39		3	4	-	59		3	5	0.14
40	D ₂ + C	3	5	-	60		2	5	-
					61		2	5	0.14

The series II tests were conducted on more realistic Ballute models with various inlet diameter ratios, payload location, and internal flow damper systems. Internal flow damping investigation was of particular concern in this test series since it was believed that if this flow should be adequately damped, the Ballute would then become fully effective. To this end the results were most gratifying since both the Ballute inlet screen damper and the flap valve damper contributed the stability desired. The screen-type damper exhibited superior qualities in this demonstration due to the fine-mesh fabric screen employed with its significant capillary forces. The valve system employed in this demonstration was a simple metal flapper valve without an adequate seal around its edges. It was concluded that either system would provide the necessary internal flow stability.

Additional observations of the flow characteristics around the Ballute are worthy of mention. The tests of various inlet ratios where the dampers were not employed indicated the internal stability superiority of the largest inlet diameter ratio ($d_i/d = 0.3$) over the lesser values of 0.2 and 0.125. The inlet ratio of 0.2 proved to be the most inferior.

The presence of forebodies (in this case, payloads) results in a relative increase in internal flow stability over the totally exposed and undamped Ballute case which was caused by the payload's turbulent wake.

In the test cases where spikes were employed without the payload, superior stability was demonstrated over the totally exposed Ballute cases. When the payload was added, the spike became a line and no significant contribution to the stability was apparent.

As far as the effect of proximity of the payload to the Ballute and Mach number effects are concerned, nothing significant can be reported from the test observation.

These tests confirmed the analytical studies and demonstrated qualitatively the stable performance of the Ballute with a flow damping system installed in the annular inlet. This encouraged its employment in the remaining wind tunnel tests.

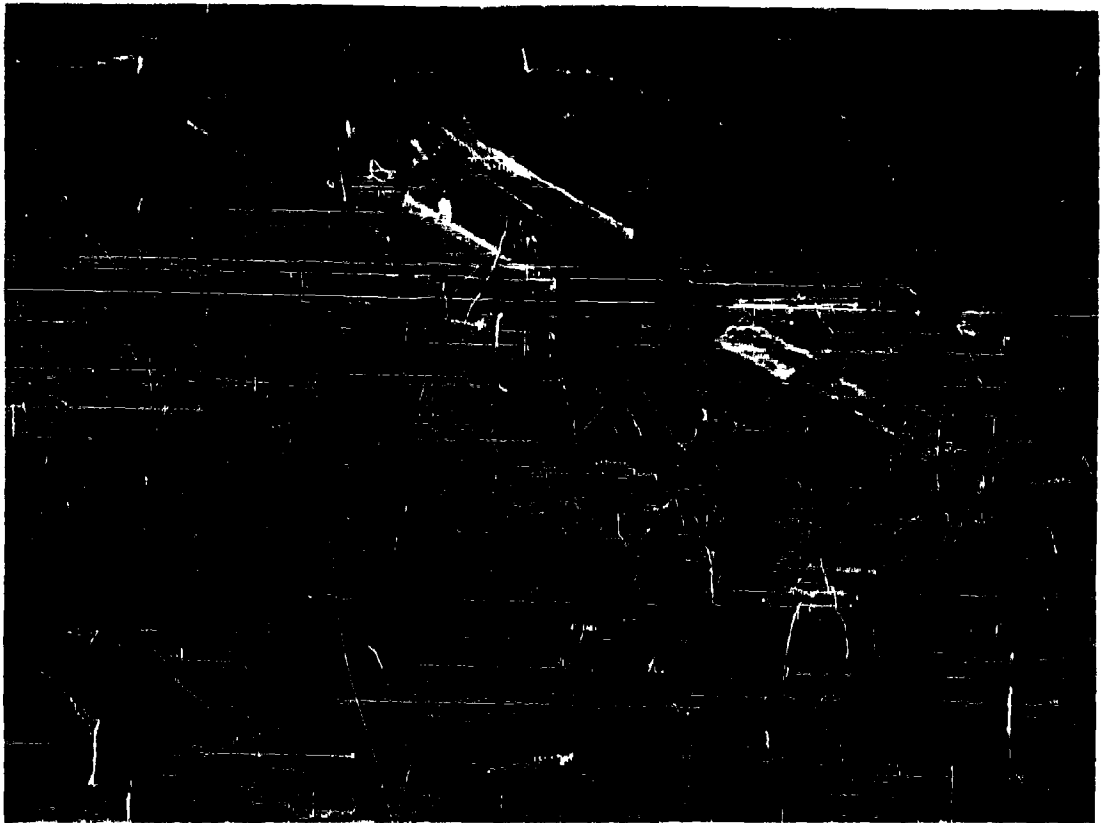


Figure 154. Water Table Test Setup

APPENDIX II

VARIABLE DRAG BALLUTES

A. GENERAL

The deceleration of a payload along a given descent trajectory sometimes poses requirements which seem to be best solved by altering the drag force. For example, a given Ballute may provide the required terminal velocity at the proper altitude, but the maximum g loads along the trajectory may be excessive for the mission. Reducing the effective drag area during this period with subsequent reduction in g's is one possible solution. Likewise, when the magnitude of the predicted impact area is unreasonably large, programming of the braking forces during the recovery phase can reduce the search effort by shrinking this target area.

The evolution of the several methods varying the drag of a payload-decelerator system has been the result of reviewing the test results of the contract study. It was evident during the wind tunnel tests that the drag coefficients of the various configurations varied considerably by changing the riser line length between the payload and the decelerator. The investigation was divided into two major categories: multiple decelerators and variable geometry decelerators.

The systems to be discussed in this section are therefore

- (1) Variable riser line Ballutes
- (2) Clustered Ballutes
- (3) Variable geometry Ballutes.

B. VARIABLE RISER LINE BALLUTES

Figures 71 thru 79 illustrate graphically the variation in the drag of a Ballute in and out of the wake of the forebody. Two significant characteristics of this phenomenon are noted: the total drag of a Ballute trailing within the wake of the payload may often be doubled by deploying it to a position aft of the payload wake, and the change of the drag coefficient value occurs through a relatively short riser line length variation.

The application of these facts to variable drag is obvious, as are the limits of drag variation. If the range of the required deceleration force variation for a particular mission does not exceed a ratio of 2:1, the variable riser line concept is feasible.

The additional equipment required to make use of this system of drag variation is twofold. Sensing equipment is required to monitor the critical parameters (maximum g loading, velocity, impact area length, etc). The output of the sensing equipment must then be coupled to the riser line length actuator (winch or similar device).

C. CLUSTERED BALLUTES

Over 100 tests of clustered Ballutes have been conducted in the Goodyear Aircraft Corporation subsonic wind tunnel at velocities up to 260 ft/sec. The models were spheres 1.5 inches in diameter with 7-percent barble fences. Drag readings were recorded in clusters of one to seven. The significant data is summarized as follows:

No. of Ballutes in Cluster	Mean C_D
1	0.48
2	0.58
3	0.75
4	0.80

It is evident that in the subsonic velocity regime the efficiency of the Ballute may be increased substantially by clustering.

Coupled with the increase of the value of the C_D , it is noted that the addition or subtraction of Ballutes from a deceleration system would vary the total drag by a factor greater than the linear increase or decrease of frontal area.

Since the frontal area of a Ballute is πR^2 and the surface area is $4\pi R^2$, the ratio of the drag area to the fabric required is 1:4 and the same amount of fabric is required for a given drag area for a single Ballute as for several.

An analysis of the structural requirements of clustered Ballutes as compared to a single Ballute of the same drag area is described numerically as follows:

Let R_1 = radius of single Ballute.

R_2 = radius of each Ballute in cluster.

n = number of Ballutes in cluster.

P = Internal Ballute pressure in lb/in.²

f = fabric stress in lb/in.

Then

$$\text{Area of single Ballute} = \pi R_1^2$$

$$\text{Area of Ballute Cluster} = n\pi R_2^2$$

$$\pi R_1^2 = n\pi R_2^2$$

$$R_1^2 = nR_2^2$$

$$R_2^2 = \frac{R_1^2}{n}$$

$$R_2 = \sqrt{\frac{R_1^2}{n}} = \frac{R_1}{\sqrt{n}}$$

Likewise

$$f_1 = \frac{PR_1}{2}$$

$$f_2 = \frac{P\left(\frac{R_1}{\sqrt{n}}\right)}{2}$$

For example, if $R_1 = 10$ in. and $n = 4$,

$$R_2 = \frac{R_1}{\sqrt{n}}$$

$$= \frac{10}{\sqrt{4}}$$

$$R_2 = 5 \text{ in.}$$

Let

$$P = 10 \text{ psi.}$$

Then

$$f_1 = \frac{PR_1}{2} = \frac{10 \times 10}{2} = 50 \text{ lb/in.}$$

$$f_2 = \frac{PR_2}{2} = \frac{10 \times 5}{2} = 25 \text{ lb/in.}$$

Assuming linear relationship of fabric weight to strength, the weight of a cluster of four Ballutes (disregarding C_D change) is one half of a single Ballute of equivalent drag area.

D. VARIABLE GEOMETRY BALLUTES

The third method for varying the deceleration characteristics of a Ballute system is by changing the geometry of a single Ballute so as to affect both a change of frontal area and drag coefficient value. Since the Ballute is essentially a pressure vessel, its geometry is fixed for a given set of aerodynamic loading conditions. The geometry of a single Ballute can be varied by using a combination of fabric pressure vessels which may be inflated separately or together. Two schematics of how this might be accomplished are shown in Figures 155 through 159. Figures 155, 156, and 157 depict a closed pressure Ballute consisting of a 12-sided pyramid constructed of Airmat panels to which has been added an outer skin attached to the pyramid at the panel juncture lines. These pockets are capable of being inflated independently, forming a series of tangent cones. Since both the base diameter and the cone angle of this Ballute can be varied, the frontal area and the drag coefficient change in unison, resulting in a considerable change in the total effective drag.

The second concept (Figures 158 and 159) is a modification of the first, differing in that the Airmat is replaced with a ram-air Ballute. The system geometry is controlled by a ram-air valve which, actuated through a 90-degree arc, diverts the ram air from full to zero with respect to the inner Ballute while opening the outer Ballute orifice simultaneously from zero to full.

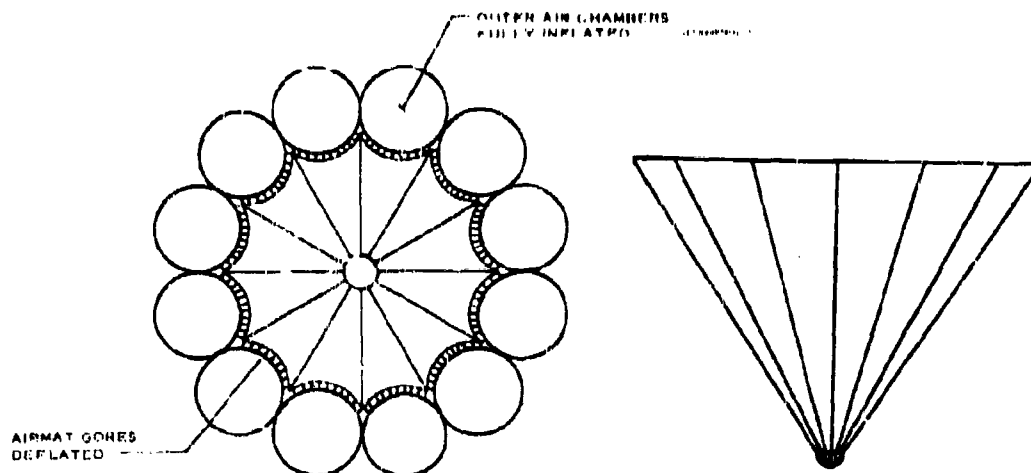


Figure 155. Dual-Chambered Inflated Variable-Drag Cone (Smallest Drag)

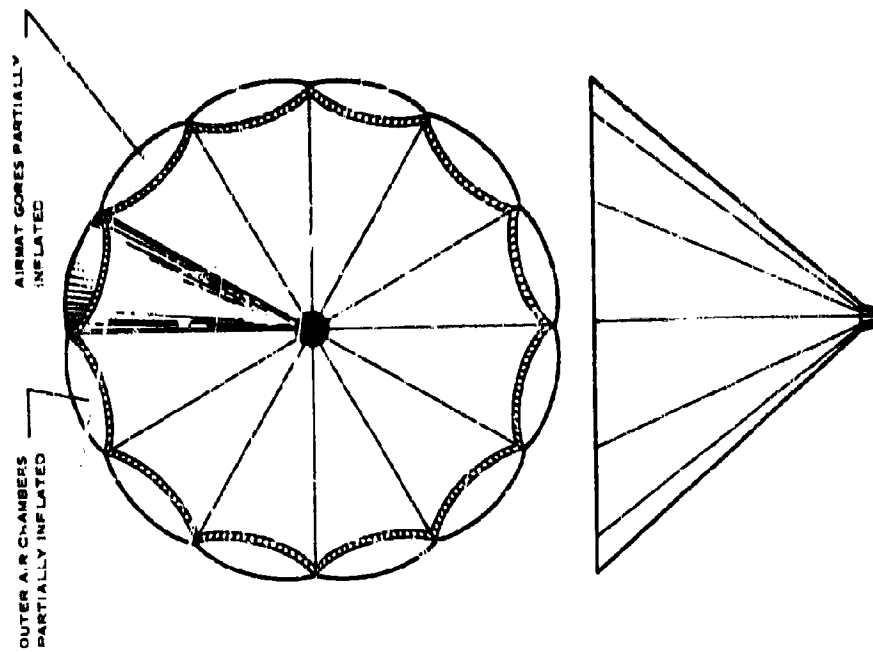


Figure 156. Dual-Chambered Inflated Variable-Drag Cone (Intermediate Stage)

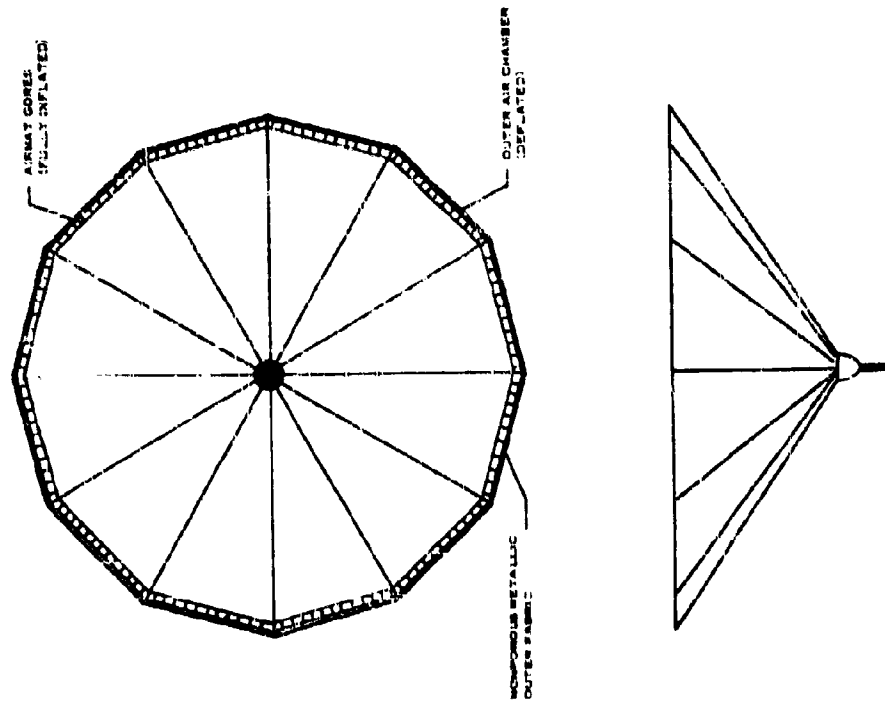


Figure 157. Dual-Chambered Inflated Variable-Drag Cone (Maximum Drag Area Shown)

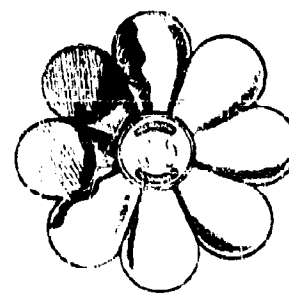
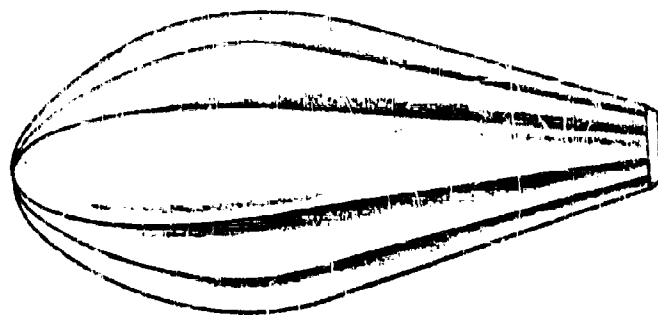


Figure 159. Ram-Air Double-Skin Ballute
(Outer Chambers Inflated)

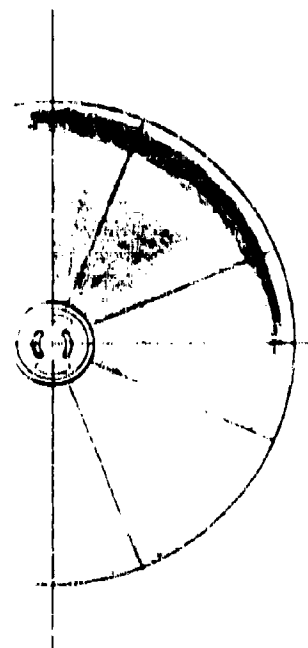
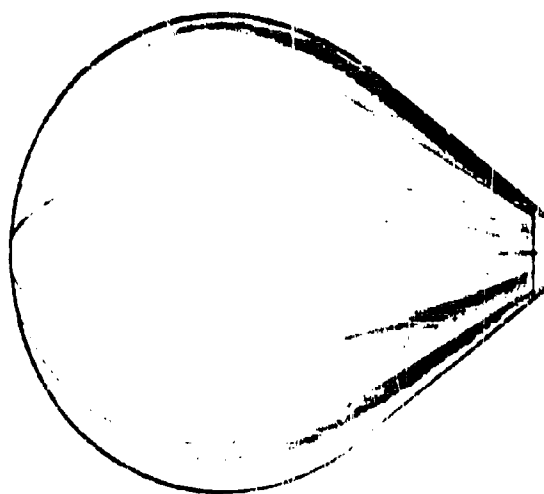


Figure 158. Ram-Air Double-Skin Ballute (Inner Chamber Inflated)

APPENDIX III

VARIOUS SPHERE DRAG SHAPES

The sphere has long been known as an efficient shape for pressure vessels, providing the lowest weight structure for a given volume and pressure. This is true, however, only when the loading is symmetrical about any plane containing a great circle. In the case of a drag body the loading is not symmetrical about the equatorial plane. The optimum shape is not a sphere, therefore, as is shown in the following analysis.

Consider first the meridian-type drag body. If the body is a perfect sphere, the meridian cables are perpendicular to the riser line at the nose of the drag body and therefore cannot resist any riser-line load. Also, if there is any tension in the meridian cables, they cause the sphere to assume a new shape, either by wrinkling or by elongation of the envelope material. For these two reasons, therefore, the structure must deviate from its spherical shape to function as a drag body. For a given size and loading, the structural weight depends on the amount of deviation from a spherical shape that can be tolerated. The minimum weight is obtained with some form of pear-shaped or heart-shaped body. As the drag body becomes more spherical, the weight increases until for a perfect sphere the pressure and weight theoretically go to infinity.

It can be shown that the same is true of any other type of suspension of the spherical drag body. Any type of unsymmetrical loading, results in unsymmetrical deflections, causing the shape to deviate from a sphere. It is not possible to say which type of sphere is the best unless the amount of deviation from a true sphere is specified. In any case, a nearly spherical shape will be heavier than a pear-shaped or heart-shaped type.

APPENDIX V

REFERENCES

1. Krause, R., and Hadman, W. F., Vertical Descent Trajectories Including Re-Entry into the Atmosphere, Air Force Missile Development Center Technical Report AFMDC TR60-4, AFMDC TR60-4, AFMDC TR60-4.
2. Nelaker, F. R., Feasibility Study of an Inflatable Type Deceleration System for High-Altitude and High-Speed Recovery, WADC Technical Report 54-182, December 1961.
3. Fay, J. A., and Riddell, F. R., "Theory of Stagnation Point Heat Transfer in Dissociated Air," Journal of the Aeronautical Sciences, Volume XXV, No. 2, February 1958.
4. Lees, L., "Laminar Heat Transfer over Blunt-Nosed Bodies at Hypersonic Flight Speeds," Jet Propulsion, April 1950.
5. Van Driest, E. R., "The Problems of Aerodynamic Heating," Aeronautical Engineering Review, October 1956.
6. Stalder, J. R., and Nielsen, H. V., Heat Transfer from a Hemisphere-Cylinder Equipped with Flow-Separation Spikes, NACA TN287, 1954.
7. Bogdonoff, S. M., and Vas, I. E., Preliminary Investigations of Spiked Bodies at Hypersonic Speeds, WADC TN 58-7, March 1958.
8. Chapman, D. R., A Theoretical Analysis of Heat Transfer in Regions of Separated Flow, NACA TN3792, 1960.
9. Crawford, D. H., Investigation of the Flow over a Spiked-Nose Hemisphere-Cylinder at a Mach Number of 0.8, NACA TN 3114, December 1959.
10. Stress Analysis of the Balloon Stabilization Equipment for the Cree Missile Test, Phase III, AF 33(816)-6010, Goodyear Aircraft Corporation, 8 M-7814, February, 1960.
11. MIL-HDBK-5, Strength of Metal Aircraft Elements, Armed Forces Supply Support Center, Washington, D. C., March 1959.
12. D'Allura, J. E., Discussion with NASA Personnel: Low Reynolds Number Research on the Problem of Pulsation or Buzzing Encountered within the Ram-Air Inlet System during Wind Tunnel Testing, AAD-304, 20 July 1961.
13. Manual for Users of the Unitary Plan Wind Tunnel Facilities of the National Advisory Committee for Aeronautics, NACA, Washington, 1956.
14. Houtz, N. E., The Application of Isotensoid Membranes to the Design of Inflatable Drag Bodies, OER 10770, July 1962.
15. United States Air Force Parachute Handbook, WADC Technical Report 55-265, Wright Air Development Center, December, 1956.
16. Arnold Center Test Facilities Handbook, Vol. 4, United States Air Force, Arnold Air Force Station, Tennessee, January 1961.
17. Spotts, M. F., Design of Machine Elements, Prentice-Hall, Inc., New York, 1953.
18. Timoshenko, S., and Woinowsky-Krieger, S., Theory of Plates and Shells, Second Edition, McGraw-Hill, N. Y., 1959.

19. Shinkus, R. P., Materials for High Temperature Service 400°F and Over, Engineering Report, Goodyear Aircraft Corporation.
20. Timoshenko, S., Theory of Elastic Stability, McGraw-Hill, New York, 1936.
21. Kayser, L. D., Pressure Distribution, Heat Transfer, and Drag Tests on the Goodyear Dallute at Mach 10, Arnold Engineering Development Center, AEDC-TDR-62-39, March 1962
22. "Analysis of the Aerodynamic Heating for a Re-Entrant Space Vehicle," ASME Journal of Heat Transfer, August 1959.
23. A Manual for Determining Aerodynamic Heating of High Speed Aircraft, AD 229 434, June 1950.
24. Charczenko, N., and McShera, J. T., Aerodynamic Characteristics of Towed Cones Used as Decelerators at Mach Numbers from 1.5 to 4.65, NASA TN D-994, December 1961.
25. Unpublished NASA Langley Unitary Tunnel Drag Results of 80° Cones with Disks Protruding Beyond the Cone Base Diameter at Various L/d 's and at Mach Numbers of 1.57 to 4.65. Tests conducted in 1961 and 1962.
26. Coats, J. D., Static and Dynamic Testing of Conical Trailing Decelerators for the Pershing Re-Entry Vehicle, Arnold Engineering Development Center, AEDC-TN-60-188.
27. Lees, L., and Freeman, L., Turbulent Diffusion in the Wake of a Blunt-Nosed Body at Hypersonic Speeds, IAS Paper No. 62-71, January 1962.
28. Slattery, R. E., and Clay, W. G., "Width of the Turbulent Trail behind a Hypervelocity Sphere," Physics of Fluids, Volume 4, No. 10, October 1961.

APPENDIX VI

BIBLIOGRAPHY

A. THERMODYNAMICS

1. Beastall, D., and Turner, J., The Effect of a Spike Protruding in Front of a Bluff Body at Supersonic Speeds, R & M No. 3007 ARC Technical Report, 1957.
2. Becker, J. V., and Konyeinski, P. F., Heat Transfer and Pressure Distribution at a Mach Number of 6.8 on Bodies with Conical Plates and Extensive Flow Separation, NACA RM L56 F22, August 1956. (CONFIDENTIAL Report)
3. Bloom, M. H., Shroud Tests of Pressure and Heat Transfer over Short Afterbodies with Separated Wakes, WADC TN 58-185, ASTIA AD-155690.
4. Bloom, M. H., On Heat Transfer Effects of Flow-Separation Spikes on Blunt Noses, General Applied Science Lab Inc Technical Report No. 122, ASTIA AD No. 227409, September 1959.
5. Bogdonoff, S. M., and Vas, I. E., Preliminary Investigation of Spiked Bodies at Hypersonic Speeds, WADC TN 58-7, March 1958.
6. Burbank, P. B., and Stalling, R. L., Jr., Heat-Transfer and Pressure Measurements on a Flat Face Cylinder at a Mach Number Range of 2.49 to 4.44, NASA TM X-19, August 1959. (CONFIDENTIAL Report)
7. Burrows and Jones, The Effects of the Curved Shock from a Blunt Nosed Cone on the Heat Transfer to the Conical Surface, ASTIA AD-200 003.
8. Champney, W. B., Athons, J. B., and Mayerson, C. D., A Study of Hypersonic Aerodynamic Drag Devices, WADC TR 59-324 Part II, December 1960.
9. Chapman, D. R., A Theoretical Analysis of Heat Transfer in Regions of Separated Flow, NACA TN 3702, October 1956.
10. Crawford, D. H., Investigation of the Flow over a Spiked-Nose Hemisphere-Cylinder at a Mach Number of 6.8, NASA TN D-118, December 1959.
11. Crawford, D. H., and McCauley, W. D., Investigation of the Laminar Aerodynamic Heat-Transfer Characteristic of a Hemisphere-Cylinder in the Langley 11-Inch Hypersonic Tunnel at a Mach Number of 6.8, NACA Report 1323, 1957.
12. Creger, M. O., Effects of Leading-Edge Blunting on the Local Heat Transfer and Pressure Distributions over Flat Plates in Supersonic Flow, NACA TN 4142, December 1957.
13. Eckert, E. R. G., Survey on Heat Transfer at High Speeds, WADC TR 54-70, April 1954.
14. Fay, J. A., and Riddell, F. R., "Theory of Stagnation Point Heat Transfer in Dissociated Air," Journal of the Aeronautical Sciences, Vol XXV, No. 2, February 1958.
15. Ferri, A., Zolkay, V., and Libby, P. A., A Theoretical and Experimental Analysis of a New Method of Reducing Aerodynamic Heating, AFOSR TN 57-113, March 1957. (CONFIDENTIAL Report)
16. Fisher, R., The Effects of Variations of Nose Cone Bluntness of the Turbulent Heat Transfer to the Conical Portion of a Spherical-Nose Cone, ASTIA AD-200 004.

18. Lees, L., "Laminar Heat Transfer over Blunt-Nosed Bodies at Hypersonic Flight Speeds," Jet Propulsion, April 1956.
19. Stadler, J. R., and Nielsen, H. V., Heat Transfer from a Hemisphere-Cylinder Equipped with Flow-Separation Spikes, NACA TN 3287, September 1954.
20. Van Driest, E. R., "The Problems of Aerodynamic Heating," Aeronautical Engineering Review, October 1950.
21. Zokkay, V., Heat Transfer Experiment with Flow Separation Spikes at Mach 7.9, PIBAL Report No. 525, October 1959.
22. An Experimental Investigation at Mach 3.09 on Heat Transfer Reduction by the Use of Upstream Probes, ASTIA AD-313 652, PIBAL 527, AFOSR TN59-1167.
23. Factors Affecting the Temperature of Components within Orbiting Space Vehicles, WADC TN 58-232.
24. The Naval Supersonic Laboratory Aerodynamic Spike, Fourteenth Quarterly Progress Report MIT NSL WTR188, October-November 1956.

B. AERODYNAMICS

1. Beckwith, I. E., and Gallagher, J. J., Heat Transfer and Recovery Temperatures on a Sphere with Laminar, Transition and Turbulent Boundary Layers at Mach No. of 2.00 and 4.15, NASA TN 4125, December 1957.
2. Bowditch, D. N., and Wilcox, F. A., Dynamic Response of a Supersonic Diffuser to Bypass at Spike Oscillation, NASA TM X-10, August 1959.
3. Champney, W. B., Athans, J. B., and Mayerson, C. D., A Study of Hypersonic Aerodynamic Drag Devices, WADC Technical Report 59-324 Part II.
4. Charczenko, N., and Hennossey, K. W., Investigation of a Retro-Rocket Exhausting from the Nose of a Blunt Body into a Supersonic Free Stream, NASA TN D 751, June 1961.
5. Charczenko, Nikolai, and McShera, John T., Aerodynamic Characteristics of Towed Cones Used as Decelerators at Mach Numbers from 1.67 to 4.65, NASA TN D-084.
6. Coats, J. D., Static and Dynamic Testing of Conical Trailing Decelerators for the Pershing Re-Entry Vehicle, Arnold Engineering Development Center, AEDC-TN-60-188.
7. Crane, J. F. W., The Use of Woollen Felt Screens as Air Cleaners for Supersonic Wind Tunnels, CP No. 538.
8. Evvard, J. C., and Blakey, J. W., The Use of Perforated Inlets for Efficient Supersonic Diffusion, NASA RM MO. E7C20, June 1947.
9. Fisher, L. R., Equations and Charts for Determining the Hypersonic Stability Derivatives of Combinations of Cone Frustums Computed by Newtonian Impact Theory, NASA D-149, November 1959.
10. Freman, N. C., On the Newtonian Theory of Hypersonic Flow for a Blunt Body, Princeton University, Report No. 467 May 1959.
11. Goddard, F. E., Jr., Effect of Uniformly Distributed Roughness in Turbulent Skin-Friction Drag at Supersonic Speeds, Jet Propulsion Laboratory, Report No. 20-113, ASTIA AD 152714, September 1957.

12. Johnston, G.W., An Investigation of the Flow about Cones and Wedges at and beyond the Critical Angle, Institute of Aerophysics, University of Toronto, UTIA Report No. 24, December 1952.
13. Johnson, R.H., "Instability in Hypersonic Flows about Blunt Bodies," The Physics of Fluids, Volume 2, 5 November 1959.
14. Kantrovitz, A., Theory and Experiments on Supersonic Inlets and Diffusers, Material Presented at the NACA Conference on Supersonic Aerodynamics at AMES Aeronautical Laboratory, 4 June 1946.
15. Kennedy, Ernest D., Method of Calculating Pressure Distributions of Various Nose Shapes at Zero Angle of Attack in the Range of Mach Numbers from 0.9 to 7.0, Scientific Report No. 1, Period: March 15, 1957 to June 15, 1957, Gruen Applied Science Laboratories, Inc, ASTIA 137494.
16. Krause, R., and Haldeman, W.F., Vertical Descent Trajectories Including Re-Entry into the Atmosphere, AFMDC TR 56-4, Holloman Air Force Base, 1958.
17. Lehnert, R., Base Pressure of Spheres at Supersonic Speeds, NAVORD Report 2774.
18. Linnell, R.D., Vertical Re-Entry of Very Lightweight Bodies into the Earth's Atmosphere, Convair Scientific Research Laboratory, Research Note 9, October 1957.
19. Love, E.S., Base Pressure at Supersonic Speeds on Two-Dimensional Airfoils and in Bodies of Revolution with and without Fine Having Turbulent Boundary Layers, NASA TN 3010, January 1957.
20. Maynard, Julian D., Aerodynamics of Decelerators at Supersonic Speeds, Paper Given at Recovery of Space Vehicles Symposium, Los Angeles, California, 31 August - 1 September 1960.
21. McLean, F.E., and Rennemann, C. Jr., Supersonic Flow past Non-Lifting Bumped and Indented Bodies of Revolution, NASA TN 3744, September 1956.
22. Nichols, James, H., Wind Tunnel Investigation of Stabilization Parachutes for the B-58 Crew Escape Capsule, AEDC-TN-59-107.
23. Rainey, R.W., Working Charts for Rapid Prediction of Force and Pressure Coefficients on Arbitrary Bodies of Revolution by Use of Newtonian Concepts, NASA TN D-176, December 1950.
24. Sopezak, S.S., Jr., Drag and Pressure Distribution Coefficient of Spheres in the Wake of Various Bodies at Mach No. of 1.5, 2.0, 2.5 and Dynamic Stability of Tethered Spheres and Balloons, AAD-214, 18 December 1959.
25. Sterbentz, W.H., and Davids, J., Amplitude of Supersonic Diffuser Flow Pulsations, NASA TN 3572, October 1955.
26. Sterbentz, W.H., and Evvard, J.C., Criteria for Prediction and Control of Ram-Jet Flow Pulsations, NASA RM E51C27, May 1951.
27. Syverson, C.A., and Dennis, D.H., A Second-Order Shock-Expansion Method Applicable to Bodies of Revolution Near Zero Lift, NASA TN 3527, January 1956.
28. Van Hise, V., Investigation of Variation in Base Pressure over the Reynolds Number Range in Which Wake Transition Occurs for Two-Dimensional Bodies at Mach No. from 1.95 to 2.20, NASA TN D-167, November 1959.

29. Whitfield, J. D. , and Potter, J. L. , On Base Pressure at High Reynold's Numbers and Hyper-sonic Mach Numbers, Arnold Engineering Development Center, AEDC-TN-60-61, March 1960.
30. Wyatt, D. D. , and Hunczak, H. R. , An Investigation of Convergent-Divergent Diffusers at Mach No. 1.85, NASA RM No. E8K21, April 1947.

1. Space capsules
2. Re-entry aerodynamic
3. Drag
4. Balloons
5. Recovery
6. AFE Project 6065
7. Task 606506
8. Contract AF 33
9. (616-8015)
10. Goddard Aircraft
11. Corp., Akron, Ohio
12. W. C. Alexander
13. Re. eval for GDS
14. In AF 33
15. Release

Aeronautical Systems Division, Mr. Aeromachid, Flight Accessories Lab, Wright-Patterson AFB, Ohio.
 Re: Mr. ASD-TR-60-72, Pt. II. INFORMATION TO DETERMINE THE FEASIBILITY OF USING INFLATABLE BALLOON TYPE DRAG DEVICES FOR RECOVERY APPLICATIONS IN THE TRANSONIC, SUPERSONIC, AND HYPERSONIC FLIGHT REGIONS. Mach 4 to Mach 10 Feasibility Investigation. Final report, Dec 62, 1967. Incl. illus., tables, 28 refs.

Unclassified Report
 Analytical and experimental data was obtained on a number of inflatable balloon type drag device configurations in the subsonic, super-

Aeronautical Systems Division, Mr. Aeromachid, Flight Accessories Lab, Wright-Patterson AFB, Ohio.
 Re: Mr. ASD-TR-60-72, Pt. II. INFORMATION TO DETERMINE THE FEASIBILITY OF USING INFLATABLE BALLOON TYPE DRAG DEVICES FOR RECOVERY APPLICATIONS IN THE TRANSONIC, SUPERSONIC, AND HYPERSONIC FLIGHT REGIONS. Mach 4 to Mach 10 Feasibility Investigation. Final report, Dec 62, 1967. Incl. illus., tables, 28 refs.

Unclassified Report
 Analytical and experimental data was obtained on a number of inflatable balloon type drag device configurations in the subsonic, super-

1. Space capsules
2. Re-entry aerodynamic
3. Drag
4. Balloons
5. Recovery
6. AFE Project 6065
7. Task 606506
8. Contract AF 33
9. (616-8015)
10. Goddard Aircraft
11. Corp., Akron, Ohio
12. W. C. Alexander
13. Re. eval for GDS
14. In AF 33
15. Release

sonic and hypersonic flight regimes. On the basis of this data it has been concluded that an inflatable conical balloon is a feasible stabilization and deceleration device for recovery from high-altitude, high-speed flight regimes (up to Mach 10 at 20,000 feet). The practicality of these inflatable decelerators was based on satisfactory performance for a

FIVE WEIGHT AND BURN PROFILE; TECHNIQUE OF MANUFACTURING, AND AVAILABILITY OF STRUCTURALLY COMPATIBLE MATERIALS WITHIN A TEMPERATURE RANGE UP TO 1500°F. The Ballute (inflated conical balloon) configuration was selected as optimum for best meeting the contract requirements.

sonic and hypersonic flight regimes. On the basis of this data it has been concluded that an inflatable conical balloon is a feasible stabilization and deceleration device for recovery from high-altitude, high-speed flight regimes (up to Mach 10 at 20,000 feet). The practicality of these inflatable decelerators was based on satisfactory performance for a

FIVE WEIGHT AND BURN PROFILE; TECHNIQUE OF MANUFACTURING, AND AVAILABILITY OF STRUCTURALLY COMPATIBLE MATERIALS WITHIN A TEMPERATURE RANGE UP TO 1500°F. The Ballute (inflated conical balloon) configuration was selected as optimum for best meeting the contract requirements.